EFFECTS FROM ALKALI-SILICA REACTION AND DELAYED ETTRINGITE FORMATION ON REINFORCED CONCRETE COLUMN LAP SPLICES

A Thesis

by

MARY KATHLEEN ECK

Submitted to the Office of Graduate Studies of
Texas A&M University
in partial fulfillment of the requirements for the degree of

MASTER OF SCIENCE

May 2012

Major Subject: Civil Engineering

EFFECTS FROM ALKALI-SILICA REACTION AND DELAYED ETTRINGITE FORMATION ON REINFORCED CONCRETE COLUMN LAP SPLICES

A Thesis

by

MARY KATHLEEN ECK

Submitted to the Office of Graduate Studies of
Texas A&M University
in partial fulfillment of the requirements for the degree of

MASTER OF SCIENCE

Approved by:

Chair of Committee,	Joseph M. Bracci
Committee Members,	Paolo Gardoni
	Harry A. Hogan
Head of Department,	John M. Niedzwecki

May 2012

Major Subject: Civil Engineering

ABSTRACT

Effects from Alkali-Silica Reaction and Delayed Ettringite Formation on Reinforced Concrete Column Lap Splices. (May 2012)
Mary Kathleen Eck, B.S., Texas A&M University
Chair of Advisory Committee: Dr. Joseph M. Bracci

Reinforced concrete bridge columns can deteriorate prematurely due to the alkali-silica reaction (ASR) and/or delayed ettringite formation (DEF), causing internal expansion and cracking on the surface of the concrete. The performance of the longitudinal reinforcement lap splice in deteriorated concrete columns is the focus in this research.

This thesis presents the results from the deterioration of large-scale specimens constructed and placed in an environment susceptible to ASR/DEF deterioration, the experimental results from four-point and three-point structural load tests, and an analytical model based on bending theory characterizing the specimen behavior during the structural load tests.

Fourteen large-scale specimens were constructed, placed in an environment to accelerate the ASR/DEF deterioration mechanisms, and instrumented both internally and externally to measure the internal concrete expansions, and surface expansions and crack widths. In addition, two control specimens were constructed and kept in a laboratory, preventing ASR/DEF deterioration. Post-tensioning was used to simulate axial load on a bridge column. Structural load tests were performed on eight specimens with no ASR/DEF damage to late stage ASR and minimal DEF damage. Comparing the specimen behaviors during the loading testing, it was found that the yield strength increased about 5-15%, and post-cracking stiffness up to first yielding of the deteriorated specimens was about 25-35% stiffer than the control specimens. The increased specimen strength and stiffness likely occurred from volumetric expansion due to ASR/DEF damage which

engaged the reinforcement, further confining the concrete and causing a beneficial increase in the axial post-tensioning load. The analytical model matched the control specimens well and matched the non-control specimens when the axial load was increased.

ACKNOWLEDGEMENTS

I would like to thank my committee chair, Dr. Bracci, and my committee members, Dr. Gardoni and Dr. Hogan for their guidance. I especially want to thank Dr. Bracci for his exceptional support throughout the course of this research.

I would like to thank Texas A&M University for the Graduate Diversity Fellowship and those in the civil engineering department for the nomination. Thanks also go to the civil engineering faculty at Texas A&M University for the knowledge they bestowed on me. I also want to extend my gratitude to the Texas Department of Transportation and the Federal Highway Administration through the Texas Transportation Institute for providing the research project and funding. I want to acknowledge Ryan Alberson for his work documenting the project up until the testing of the control specimens. I am grateful for the graduate and undergraduate student researchers involved in the design, construction, and data collection of the specimens before I was involved with the project. I also want to thank Jason Zidek and Marcus Schniers for their contributions, in particular for data collection, cylinder tests, and structural load tests.

I wish to acknowledge Dr. Peter Keating and Mr. Matt Potter of the Civil Engineering High-Bay Structural and Materials Laboratory at Texas A&M University for their technical and logistical assistance during in the construction and structural testing of the large-scale specimens.

Finally, thanks to my family and friends for the love and support they provided.

NOMENCLATURE

ASR	Alkali-Silica Reaction
DEF	Delayed Ettringite Formation
TxDOT	Texas Department of Transportation

TABLE OF CONTENTS

Page

Page

LIST OF FIGURES

Page

Page

Page

Page

Page

Page

Page

LIST OF TABLES

Page

1. INTRODUCTION

1.1 Background and Problem Statement

The Texas Department of Transportation (TxDOT) has been dealing with an expanding road system due to the growing population in the state, especially in metropolitan areas. A significant amount of large construction projects have been taken on in order to satisfy the increased traffic demands. In addition to aggressive scheduling and aggressive resource allocations, it is believed that some contractors proportioned concrete mixtures to achieve high early strengths so that forms can be removed early, allowing the construction to be completed in an expedited fashion. It is believed that this practice to decrease construction costs and time for the project, also contributed to the early cracking of many structures (premature concrete deterioration). The concrete member sizes of the systems have also increased for many reasons. The large concrete placements can experience elevated temperatures during hydration, which can later lead to cracking and deterioration of these concrete structures. The chemical constituents in the cement and aggregate also contribute to the deterioration of the concrete members. This premature concrete deterioration has occurred from the alkali-silica reaction (ASR) and delayed ettringite formation (DEF). This research assesses adequacy of column lap splice regions once the cracking from premature deterioration has occurred. Figure 1-1 shows the cracking on an existing bridge column in Houston, TX.

Alkali-silica reaction (ASR) occurs when reactive forms of silica (commonly found in aggregates in Texas), sufficient alkalis (from the cement), and sufficient moisture (within concrete and externally from rain, etc.) are present. The reaction between the silica in the aggregates and the alkalis form a gel usually at the aggregate and cement interface, which expands with more water and causes the surrounding concrete to crack.

This thesis follows the style of *Journal of Structural Engineering*.

Once the constituents are consumed, the ASR process will stop (Folliard et al. 2006). Berube et al. (2002) reported specimens subjected to wetting and drying cycles have less ASR deterioration than specimens exposed to more humidity. However, the cycles promote map-cracking on the surface. Members with little confining reinforcement have a greater tendency to crack from the ASR expansion.

(a) Column Elevation View **(b) Close-up View of a Typical Crack**

Figure 1-1. Column with Pronounced Effects from ASR in Houston, TX [taken from Alberson (2009)].

Delayed ettringite formation (DEF) occurs when there are high concrete temperatures (150°F or greater) during the curing process for several hours (Petrov et al 2006). High heat can occur from large concrete placements and amplified from external temperatures (common in Texas). The increase in concrete member sizes has necessitated large concrete placements causing high heat during the concrete hydration. There are different hypotheses about how the delayed ettringite formation (DEF) occurs. (Folliard et al. 2006) and (Bauer et al. 2006) summarized that temperatures of 158°F and higher inhibit ettringite ($C_4AS_3H_{32}$) (usually formed at hydration) from forming. Instead, calcium silicate hydrate (C-S-H) is formed, releasing sulfate and aluminum. After the concrete hardens and usually in the presence of water, the sulfate and aluminum ions react with monosulfate hydrate to form ettringite. This delayed ettringite formation causes expansion, thus cracking is observed. The delayed ettringite formation often occurs in previously formed microcracks. Therefore, cracks previously formed from ASR can lead to DEF.

The research presented in this thesis is a continuation of the research documented by Alberson (2009). The previous research and execution includes four main areas: the design and construction of the large-scale specimens, deterioration program, analytical model, and structural load test procedure. The large-scale specimens were designed with a lap splice similar to the existing cracked bridge columns and proper internal instrumentation was installed to monitor the strains in the concrete and reinforcing steel. The specimens were placed in an environment to accelerate the deterioration and a program to monitor the specimen's expansion and deterioration was developed. An analytical model was developed to calculate the flexural capacity of the specimens during the structural load test. The structural load test procedure and external instrumentation was established and the control specimens (non-deteriorated) were tested. Alberson (2009) documented the results from the initial deterioration of the non-control specimens and the structural load test results from the control specimens.

1.2 Research Objectives and Tasks

The major objectives covered in this thesis are to:

- Evaluate the condition of the concrete column lap splice during the structural load test exposed to varying levels of deterioration, and
- Develop an analytical model to measure the capacity of the splice region during the structural load test which accounts for the varying levels of deterioration.

The tasks to execute the objectives given as follows:

- Monitor the deterioration of the reinforced concrete specimens internally and externally with the previously developed program adjusting as needed, illustrate the results, and form conclusions;
- Further develop the analytical model initiated by Alberson (2009) to measure the flexural capacity of the specimens during the structural load testing;
- Perform the structural load tests on specimens with varying levels of deterioration;
- Compare the results of the experimental data to the analytical model and modify the model for the deterioration as needed;
- Assess the performance of the column lap splice on varying levels for premature concrete deterioration due to ASR/DEF.

1.3 Scope of Thesis

This thesis includes data and results from the deterioration program, an analytical model of structural load tests, and experimental data and results from the structural load tests.

- Section 1: Introduction (current section)

- Section 2: Specimen Design and Construction. This is a summary of Alberson's work to familiarize the reader with the specimens design and internal instrumentation.
- Section 3: Deterioration of Large-Scale Specimens. The environment used to accelerate the deterioration and the results from the gages monitoring the deterioration are discussed in this Section.
- Section 4: Analytical Model for Structural Load Tests. This section describes the new theory and equations used to calculate the flexural-deformation relationships for the four-point and three-point structural load tests, which were significantly enhanced from Alberson (2009).
- Section 5: Experimental Testing and Results. This section includes results from the control specimens and six specimens with varying levels of deterioration. The analytical model is compared to the experimental results in this section.
- Section 6: Conclusions and Future Testing. This section discusses the conclusions reached from the research to date and identifies the future work and experimental testing of the research project.

2. SPECIMEN DESIGN AND CONSTRUCTION

The specimens were designed to replicate the steel lap splice in the joint between the concrete column and foundation in non-seismic regions. The design of the construction of the specimens is not the focus in this thesis; it is presented as a background for deterioration and structural load testing of the specimens. For a more detailed description of the design and construction see Bracci et al. (2011).

A total of 16 LSC specimens were cast between January 2008 and September 2008. The concrete mix was designed for a compressive strength of 5 ksi (34 Mpa) using cement with alkali and aggregate with silica to promote ASR.

2.1 Reinforcement Design

The large-scale concrete specimens were designed 25 ft (7.62 m) long with a 2 ft (0.61 m) by 4 ft (1.22 m) cross section. The reinforcing and lap splice was designed similar to a bridge column with #11 longitudinal bars spliced at 9 ft (2.74 m) and #5 bars for the transverse reinforcement. Post-tensioning strands were used to simulate the axial load in concrete bride columns. Figure 2-1 shows the reinforcement layout of the specimens 2 ft (0.61 m) side as the height and the 4 ft (1.22 m) side as the width (into the page) since this is the orientation of the specimen during the structural load tests. Three #11 bars, located on top and bottom are spliced in the center of the specimen and hook at each end. Additional straight #11 bars are placed outside of the splice length. The alphabetical bar labels are explained later.

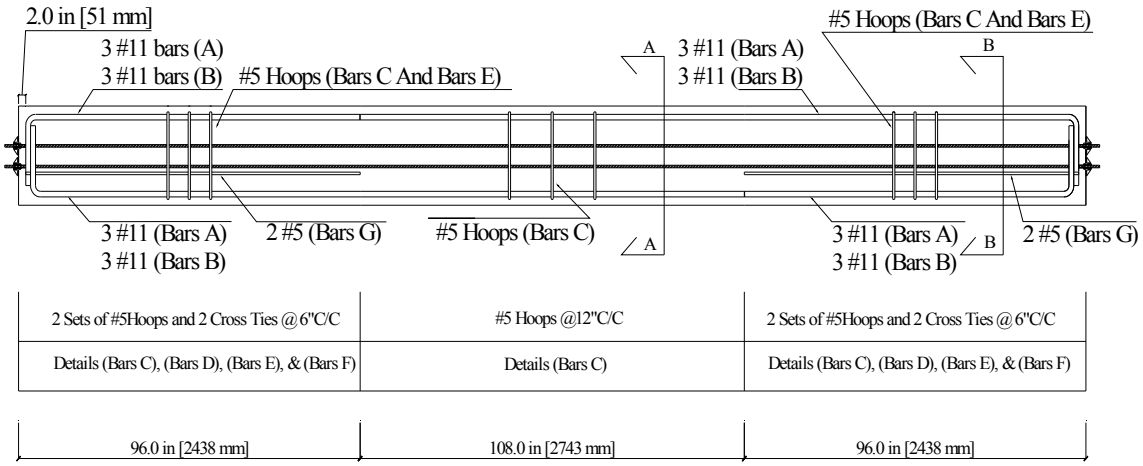

Figure 2-1. Reinforcement Layout [taken from Alberson (2009)].

Figure 2-2 shows the cross section of the specimens in the splice region and the end region. The spliced bars are illustrated with a filled circle and the straight bars located only in the end region are illustrated with an open circle.

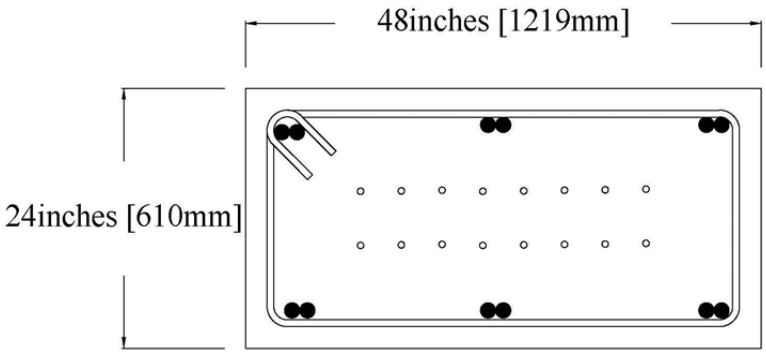

Section A-A Splice Region

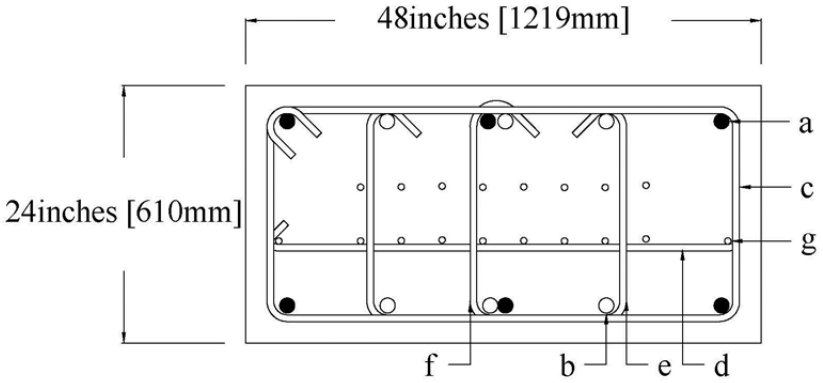

Section B-B End Region

Section B-B Parts	
a	6 #11 Bars A [marked with fill]
b	6 #11 Bars B [marked without fill]
c	#5 Hoops @ 6" C/C (Bars C)
d	#5 Cross Ties @ 6" C/C (Bars D)
e	#5 Hoops @ 6" C/C (Bars E)
f	#5 Cross Ties @ 6" C/C (Bars F)
g	2 #5 Bars (Bars G)

Figure 2-2. Cross Section View of the Reinforcement Layout [taken from Alberson (2009)].

Figure 2-3 shows the reinforcement details for the different longitudinal and transverse bar types. The location of the bars is referenced with the alphabetical labels in Figure 2-1.

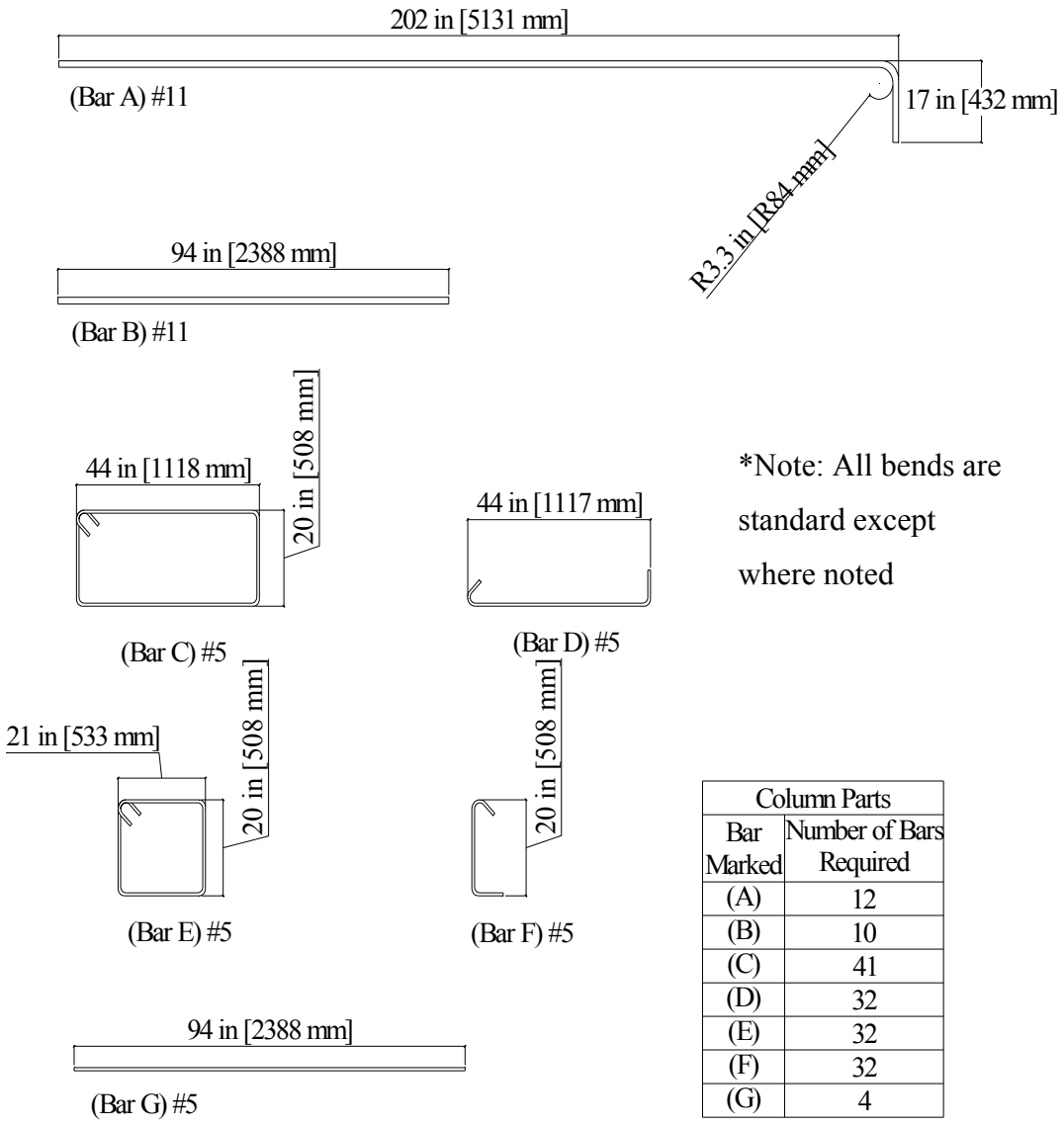

Column Parts	
Bar Marked	Number of Bars Required
(A)	12
(B)	10
(C)	41
(D)	32
(E)	32
(F)	32
(G)	4

Figure 2-3. Reinforcement Types, Quantities, and Dimensions [taken from Alberson (2009)].

2.2 Internal Instrumentation

Strain gages were mounted to the reinforcing steel and the surrounding concrete to monitor the internal effects of deterioration and the structural load testing. The reinforcing steel was smoothed at the location of instrument placement and the strain gages were attached with an adhesive. The concrete embedment gages (KM) measured in the strains in the concrete. Ten strain gages were placed on the longitudinal reinforcing bars in the splice region and two were placed on the transverse reinforcement. Figure 2-4 shows the location of the ten strain gages (SG1 – SG10) on the longitudinal reinforcement. During the structural load test, the bottom bars are in tension and the top bars are in compression; therefore they are labeled accordingly in this figure. The cross section in the figure shows SG1 through SG4 were placed on the edge of the tension side, SG5 through SG8 were placed at the center of the tension side, and SG9 and SG10 were placed at the center of the compression side. Each group of strains gages such as SG1 through SG4 were placed on the same splice bar therefore the bar has the least available anchorage at location of SG4. The splice bar with no gages is illustrated in the figure with a dashed line.

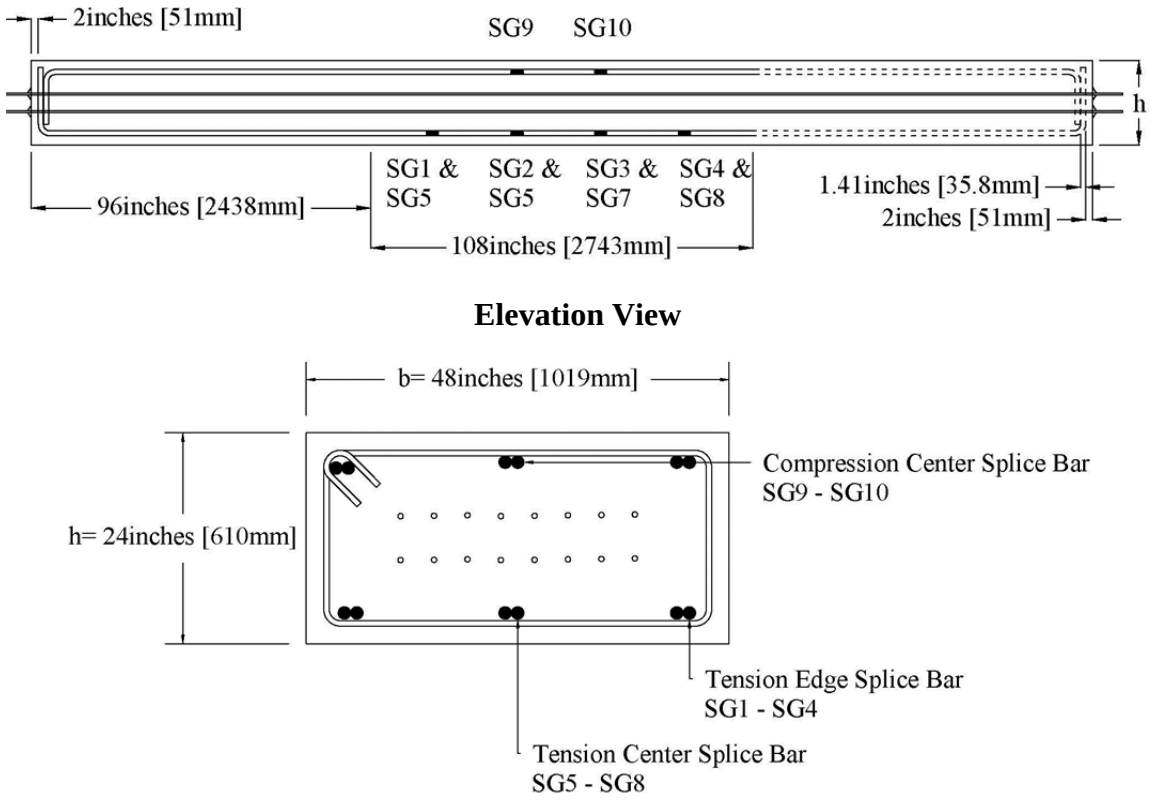

Figure 2-4. Internal Strain Gage Locations on Longitudinal Reinforcement [taken from Alberson (2009)].

Figure 2-5 shows the location of the strain gages on the transverse steel (SG11 – SG12), in the concrete cover (KM1 and KM3), in the concrete core (KM2 and KM4), and perpendicular to the transverse steel (KM5). Figure 2-5 also shows face labels used throughout this thesis.

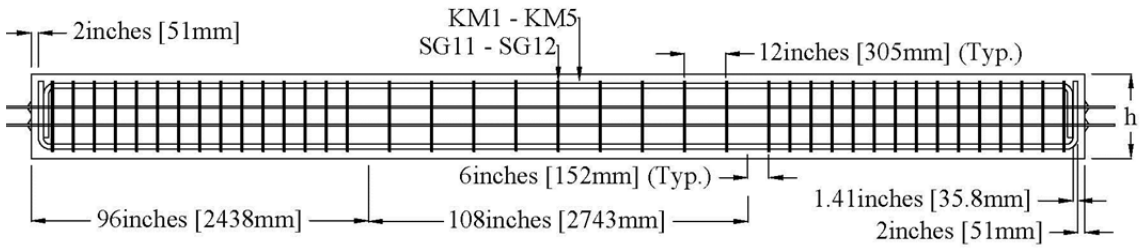

Elevation View

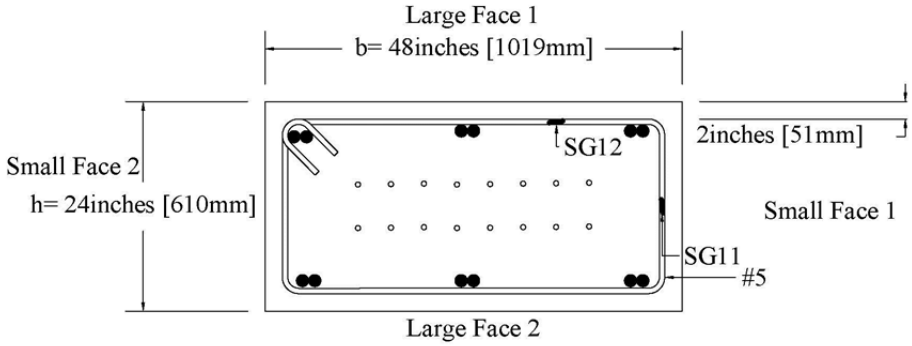

Cross Section with SG11 – SG12

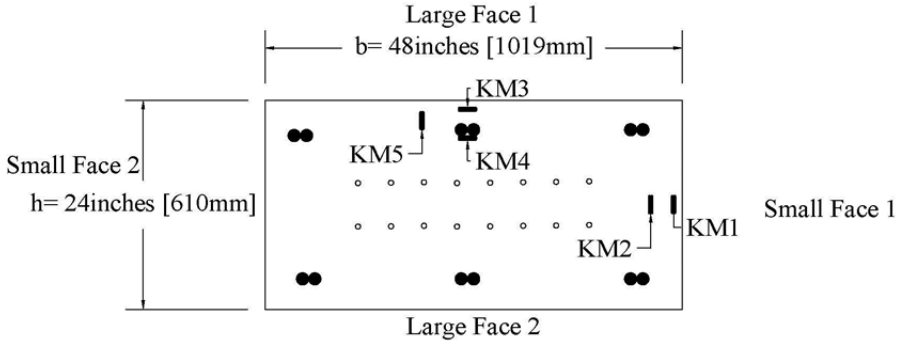

(c) Cross Section with KM1 – KM5

Figure 2-5. Internal Strain Gage Locations on Transverse Reinforcement, Concrete Core, and Concrete Cover [taken from Alberson (2009)].

2.3 Simulated Axial Load

The post-tensioning strands were placed in the formworks with a plastic sleeve to prevent bonding between the concrete and strand. Once the concrete had cured, the 16 strands in two layers of eight (Figure 2-5) were jacked to 36.3 kips (161 kN) per strand which is a total of 580.5 kips (2582 kN).

2.4 Supplemental Heat

Since high temperatures during the casting of the concrete promote DEF, heat was supplied to the by Electrical Resistive Wiring (ERW) to raise the temperature above 160 °F (71.1 °C) during the casting the early stages of concrete curing. The design of the supplemental heating system for the large-scale specimens is fully described in the final report the TxDOT project (5997) by Mander et al. (2011). The same supplemental heating system was successfully used in both projects.

2.5 External Instrumentation

DEMEC points were mounted to the surface of the LSC specimens to monitor the surface expansion during the deterioration process. The DEMEC points allowed a caliper to measure the change in the distance between the points to find the surface expansion throughout the deterioration program with a precision of 0.0005 inch (12.7 μm). A hole was drilled into the specimen creating space for a brass insert with a measurement tip. Epoxy held the brass insert in place. Figure 2-6 shows the brass insert, measurement tip, and the epoxy holding the DEMEC within the hole, 1 inch (25.4 mm) deep and 7/16 inches (11.11 mm) in diameter. A grid of DEMEC points was installed at 10 inches (254 mm) intervals which provided distances in the transverse and longitudinal directions for surface strain calculations.

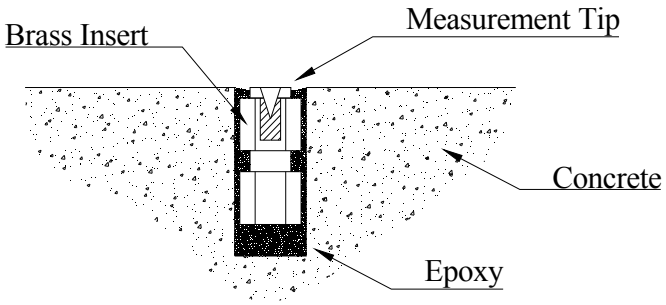

Figure 2-6. Brass Insert with Tip Installed in the Surface of the LSC [taken from Alberson (2009)].

The LSC specimens were initially oriented during the deterioration process with the smaller face on top. Each face of the specimen excluding the ends was labeled to further explain the instrumentation. Figure 2-7 illustrates the initial orientation and LSC specimen face labels.

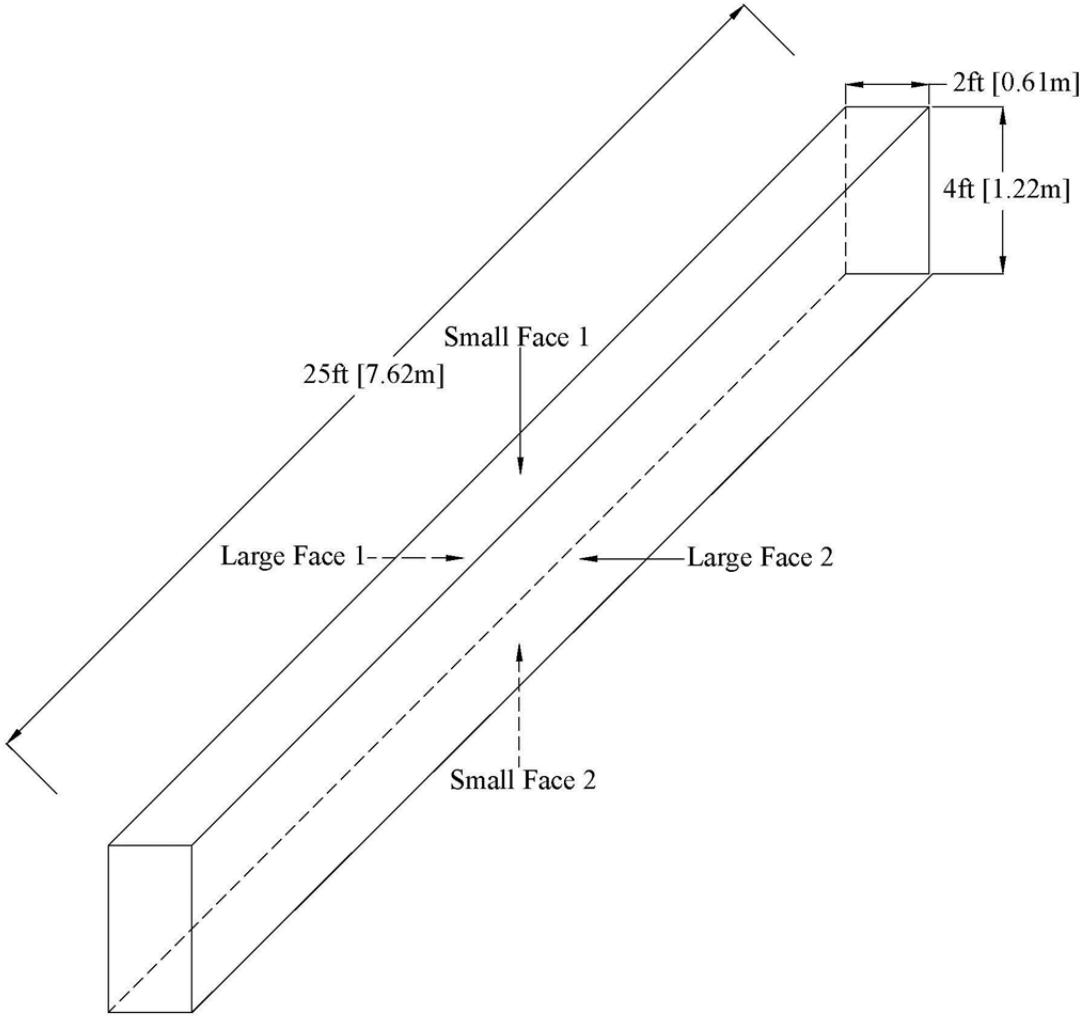

Figure 2-7. Initial LSC Specimen Orientation and Face Labels.

A grid of DEMECs was installed on top, Small Face 1, and on one side, Large Face 1, of the LSC specimens along the splice region. On Small Face 1, the 3x12 grid consisted of 36 DEMECs spaced at 10 inches (254 mm). A 5x12 grid of 60 DEMECs was installed on Large Face 1. Figure 2-8 shows the DEMEC layout on Small Face 1 and Large Face 1. Figure 2-1 shows the 108 inches (2.74 m) long splice region centered longitudinally. The DEMECs completely cover this area on Small Face 1 and Large Face 1.

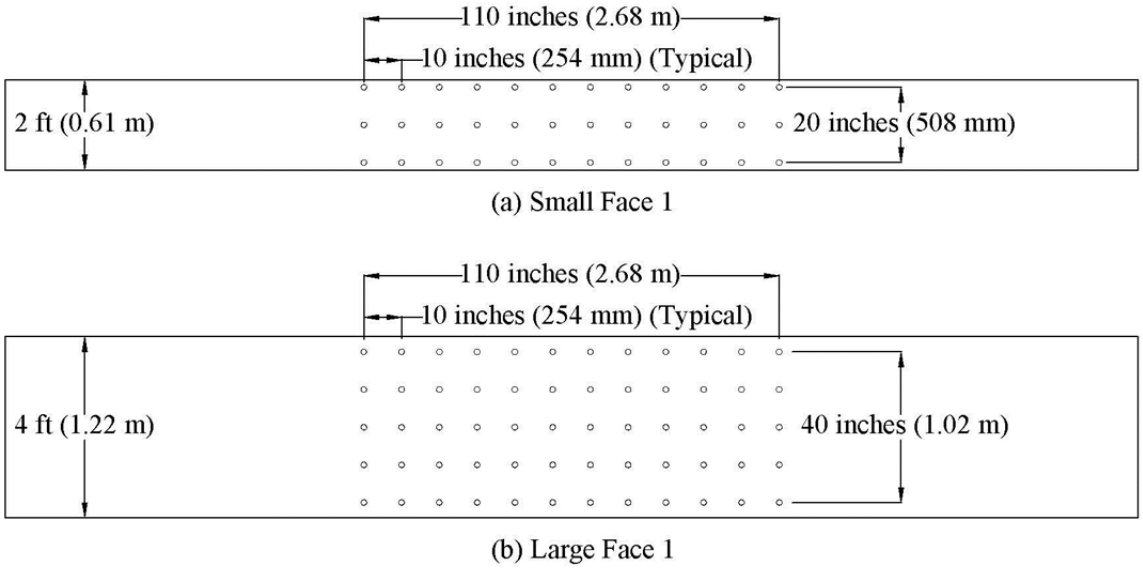

Figure 2-8. DEMEC Layout in the Splice Region [taken from Alberson (2009)].

2.6 Summary

The specimens were designed similar to a concrete bridge column with concrete mix properties that promote ASR and temperature during the cast was increased to promote DEF. Internal and external instrumentation was placed to monitor the behavior during the deterioration process and the structural load test.

3. DETERIORATION OF LARGE-SCALE SPECIMENS

3.1 Introduction

This section describes the process of evaluating the deterioration of the LSC specimens. The exposure conditions, internal and external instrumentation, and specimen behavior due to ASR/DEF are included. The monitoring of the specimen expansions during the deterioration process is extremely important since there is only limited capability of measuring the effects of ASR/DEF in field structures. A petrographic analysis report (summarized in Bracci et al. (2011)) conducted on cores taken from specimens following the structural load test assessed that the specimens experienced late stage ASR and minimal DEF.

3.2 Specimen Exposure Condition

Shortly after the construction of LSC specimens and their preloading to replicate service conditions, the specimens were placed outside at the Texas A&M University Riverside Campus in Bryan, TX where they were exposed to the environmental weather conditions of the area and supplemental water to accelerate the Alkali Silica Reaction (ASR) and Delayed Ettringite Formation (DEF) deterioration mechanisms. The supplemental water was supplied by a sprinkler system activated four times a day and for 15 minutes each time. Figure 3-1 and Figure 3-2 show the average temperatures and precipitation in Bryan, TX according to the Weather Channel (2011). The values in the figures are an average of all recorded data, not specific to a year.

The 14 specimens were placed next to each other with the smaller face on top as shown in Figure 3-3. A clear space of about 2 - 3 ft (0.6 - 0.9 m) was between each LSC specimen, which allowed the LSC specimens' Small Face 1 to experience direct sunlight. Since Large Face 1 and Large Face 2 were on the sides of the specimen, only

the top of each side experienced significant direct sunlight, while the bottom of each side was mostly in the shade of the adjacent LSC specimen. Figure 3-3 shows the LSC specimens at the Riverside Campus with Small Face 1 on top. Figure 3-4 shows the sprinkler system between two specimens. This system wetted the specimens on the three outer faces.

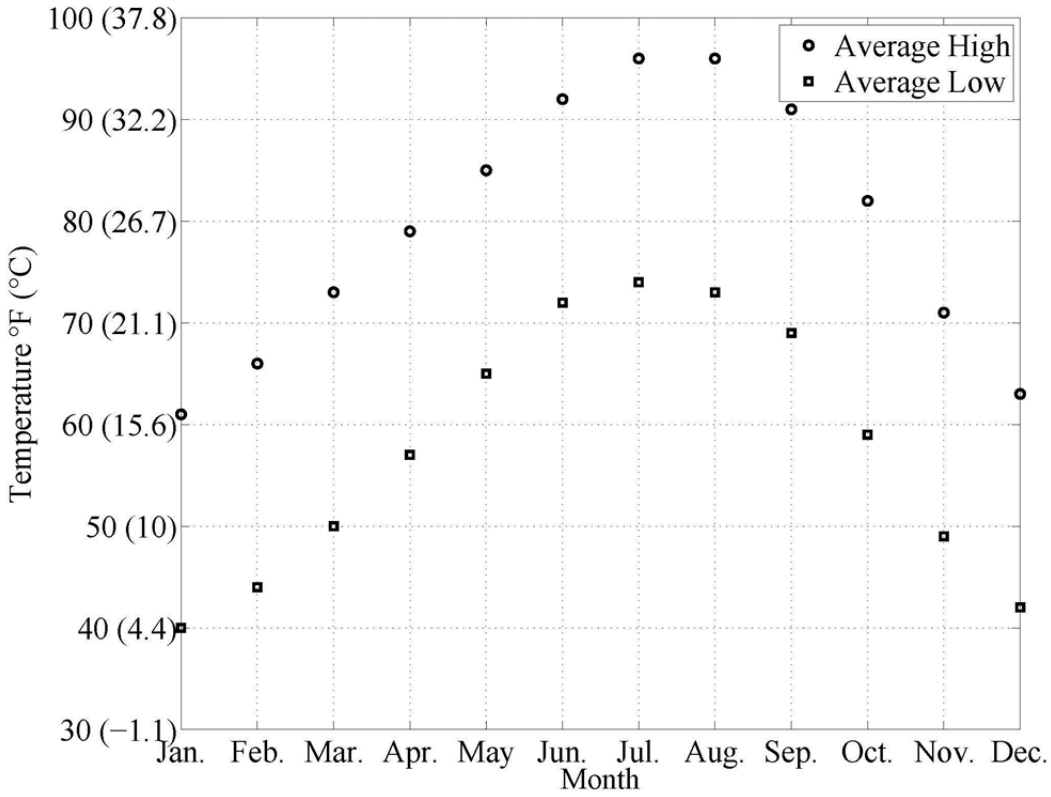

Figure 3-1. Average Temperatures at Riverside Campus in Bryan, TX (Weather Channel, 2011).

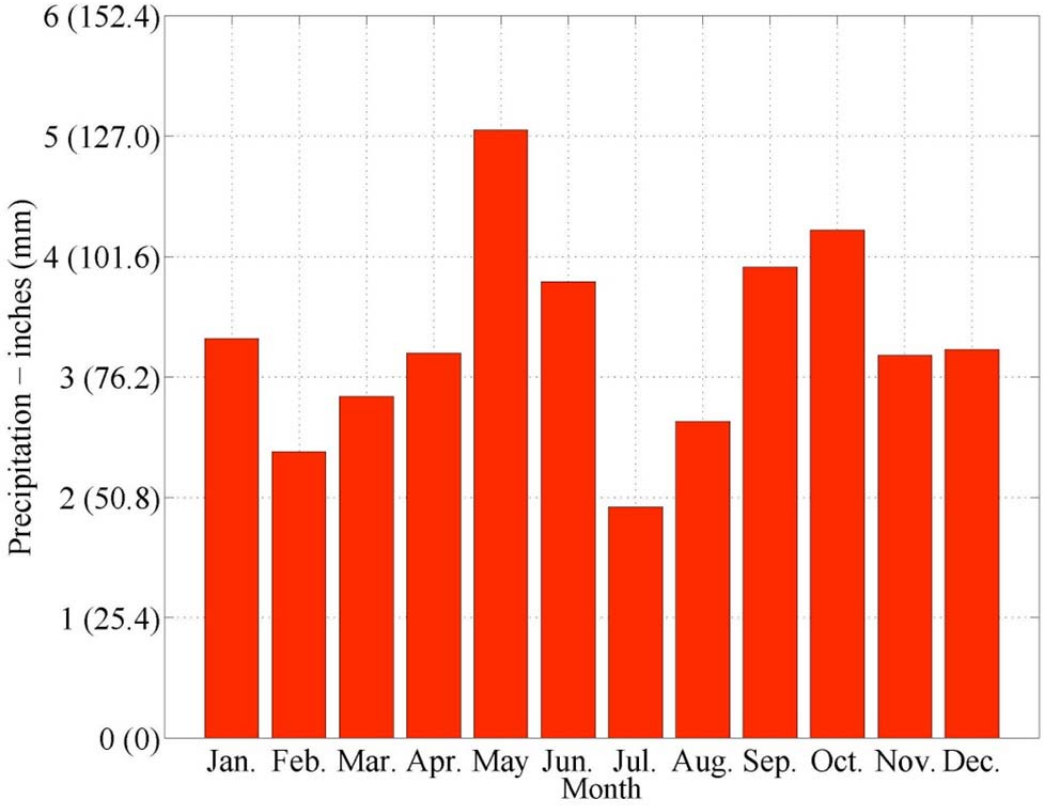

Figure 3-2. Average Precipitation at Riverside Campus in Bryan, TX (Weather Channel, 2011).

Figure 3-3. LSC Specimens Exposed to the Environment at the Riverside Campus [taken from Alberson (2009)].

Figure 3-4. Sprinkler System between Two LSC Specimens [taken from Alberson (2009)].

From measured expansion data on the specimens that will be further described later, it was found that the largest surface expansions resulted on the top or sunny side of the specimen. Therefore to provide more uniform expansion throughout the specimens, the LSC specimens were rotated twice during the deterioration program. Figure 3-5 shows the three orientations and the label for each face. The length of the specimens is 25 ft (7.62 m), which is not shown to scale in the figure. Since Small Face 2 had not experienced any direct sunlight or water, the first rotation positioned this face on top. The second rotation was 90° which positioned Large Face 2 on top, which was the critical tension side in the subsequent structural load testing. Figure 3-6 shows the specimens during the 3rd orientation.

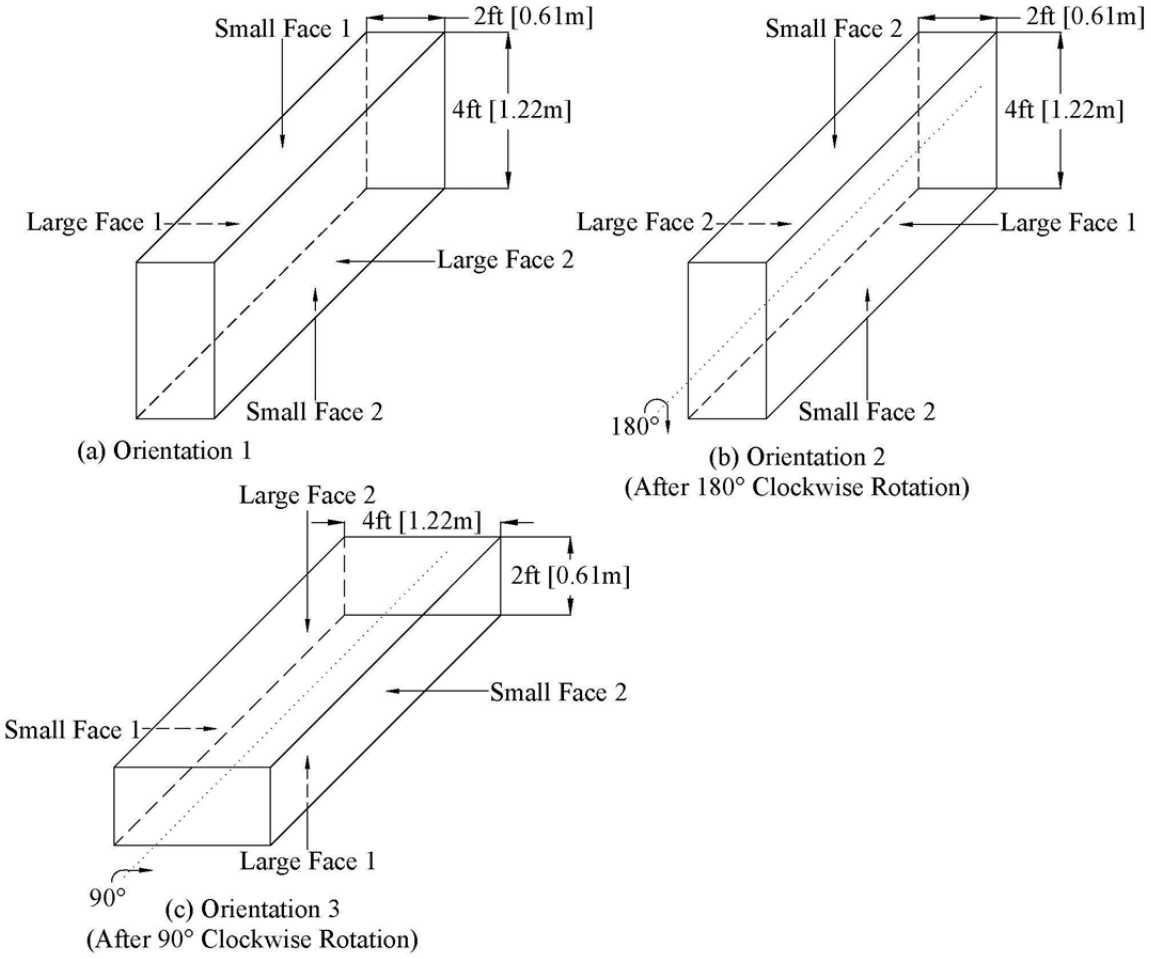

Figure 3-5. Orientations of the LSC Specimens.

Figure 3-6. LSC Specimens at the Riverside Campus during the 3rd Orientation.

Table 3-1 lists the month and year of the specimen casting, first exposure to the environmental conditions with supplemental water, 180° rotation, 90° rotation, and structural load test. As a note, LSC1 through LSC4 were transported at the Riverside Campus before May 2008. However, the sprinkler system providing supplemental water was not installed until May. Therefore, these specimens had some time without supplemental water from the sprinkler system. Since water is a necessary component for ASR (Folliard et al. 2006), it was decided to define the initial exposure as the time when the specimens were first exposed to the supplemental water.

Table 3-1. Dates of Exposure, Rotations and Structural Load Testing.

LSC Specimen #	Date of Casting	Date of Initial Exposure	Date of 180° Clockwise Rotation	Date of 90° Clockwise Rotation	Date of Structural Load Test
1	1/2008	5/2008	7/2009	N/A	8/2010
2	2/2008	5/2008	7/2009	7/2010	TBD
3	2/2008	5/2008	7/2009	N/A	8/2010
4	3/2008	5/2008	7/2009	7/2010	TBD
5	4/2008	5/2008	7/2009	7/2010	7/2011
6	4/2008	5/2008	7/2009	7/2010	TBD
7	4/2008	7/2008	7/2009	7/2010	TBD
8	5/2008	7/2008	7/2009	7/2010	7/2011
9	6/2008	7/2008	7/2009	N/A	2/2010
10	6/2008	7/2008	7/2009	N/A	2/2010
11	6/2008	9/2008	2/2010	7/2010	TBD
12	7/2008	9/2008	2/2010	7/2010	TBD
13	7/2008	9/2008	2/2010	7/2010	TBD
14	8/2008	9/2008	2/2010	7/2010	TBD

3.3 Specimen Behavior during Deterioration Phase

The behavior of the LSC specimens during the environmental exposure conditions was monitored with external surface and internal strain measuring devices. Demountable mechanical (DEMEC) points were mounted on the surface of the specimens and provided a way to measure the external surface expansion during the deterioration process. Electronic strain gages were placed on the reinforcing steel and concrete embedment gages were placed within the concrete specimen to measure the internal deformations during the deterioration process. The placement of the internal instrumentation was described in 0. The usage and results of the instrumentation is explained below.

3.3.1 Surface Strains between DEMEC Points

Figure 2-8 shows the grid of DEMEC points installed on Small Face 1 and Large Face 1 at the critical splice region. A caliper with a 0.0005 inches (0.0127 mm) precision was used to measure the distance between two DEMEC points in the transverse and longitudinal directions. The surface strain between two points was calculated as follows:

$$\varepsilon_d = \frac{l_d(t) - l_d(0)}{l_d(0)} \qquad \text{(Eq. 3-1)}$$

where $l_d(t)$ is the distance between two DEMECs at time, t, and $l_d(0)$ is the initial distance. Transverse and longitudinal distances were measured on Small Face 1 and Large Face 1 and used to calculate a surface strain for each distance measured, ε_d. Each distance, d, is numbered 1 through 160. Figure 3-7 shows the grid of DEMECs and numerical labels for the distances used to calculate the strains. Average strains were calculated to give an overall strain along the length of the LSC specimens to help summarize the results. The average strains are labeled by face (Small Face 1 or Large Face 1), strain type (transverse or longitudinal), and strain number. The face name is abbreviated to SF1 and LF1 for Small Face 1 and Large Face 1. The strain type is abbreviated to TS and LS or transverse strain and longitudinal strain. The strain number is given since a few average strains are calculated on each face. The first average transverse strain on Small Face 1 is calculated as follows

$$\text{SF1 TS1} = \text{average}(\varepsilon_{1,\ldots 12}) \qquad \text{(Eq. 3-2)}$$

where ε_1 through ε_{12} is calculated in Eq. 3-1 for each distance, 1 through 12. The other average strains are calculated in the same way using different ε_d values. For instance, the first longitudinal strain on Large Face 1 (LF1 LS1) is an average of strain values ε_{106}

through ε_{116}. The strain values, ε_d, used to calculate the other average strains are shown in Figure 3-7. Note that the length of the face is not shown to scale in Figure 3-7.

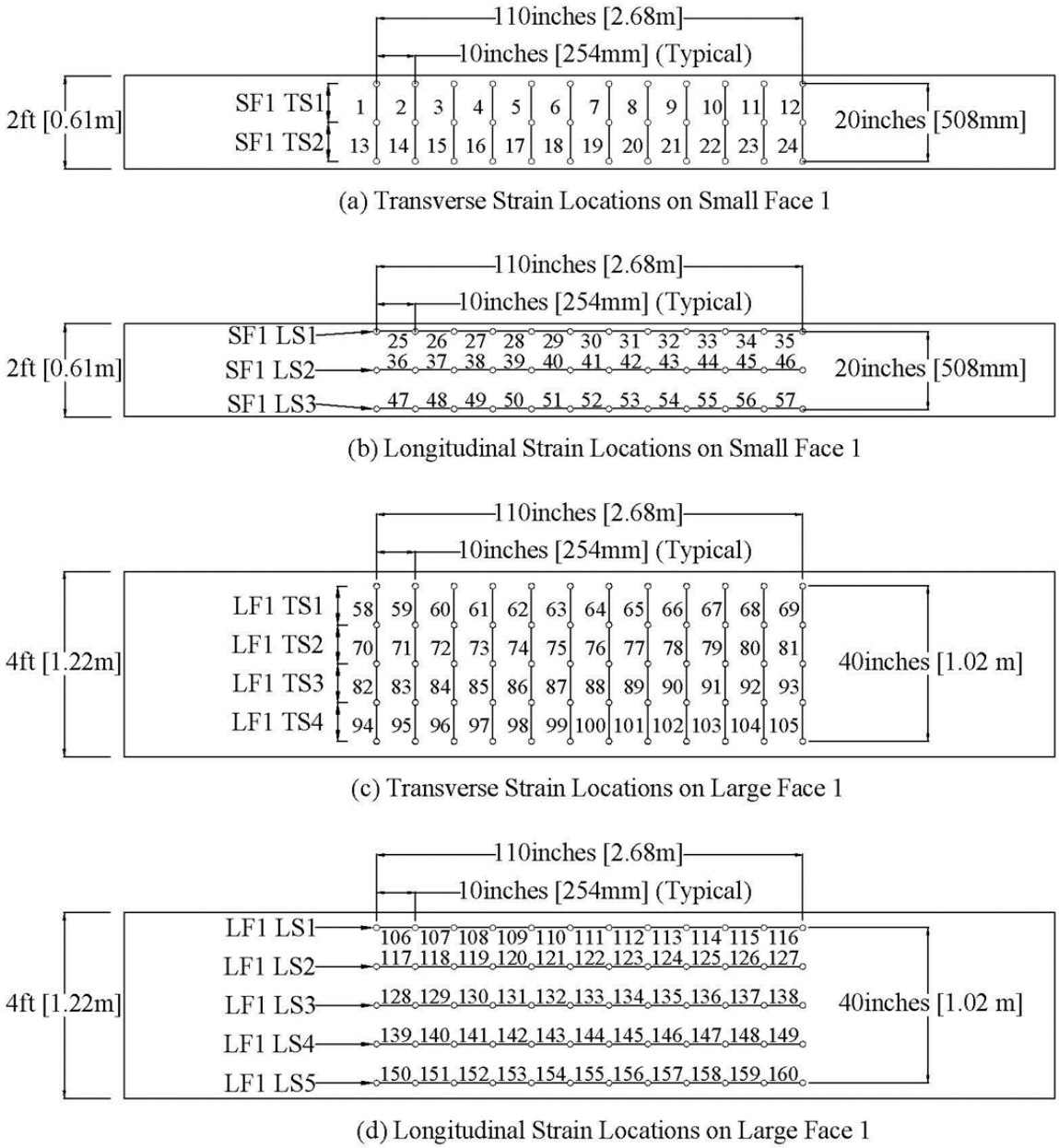

Figure 3-7. Transverse and Longitudinal Strain Locations on the LSC Specimens' Small Face 1 and Large Face 1 during the Initial Orientation.

The averaged strains labeled SF1 TS1, SF1 TS2, LF1 TS1, LF1 TS2, LF1 TS3, and LF1 TS4 from Figure 3-7 were plotted to compare the strains. Figure 3-8 compares the transverse strains on Small Face 1 and Large Face 1. LSC15 and LSC16 were not instrumented with DEMECs since these were the control specimens without ASR/DEF effects. Therefore, no data is shown in the figures for these specimens. The high temperatures during the summer months resulted in an increase in ASR/DEF expansion for most specimens. Therefore, the graphs show a grey region behind the strain plots highlighting the expansion during the summer months. The days with a grey background are May 1 through September 30. The slope of the average transverse surface strain on Small Face 1was calculated to show the effect of the summer months (Table 3-2). The specimens exposed to fewer summer months in 2008 had a larger increase in slope during the summer of 2009. Figure 3-8 shows that the LSC specimens expanded more on Small Face 1 than on the Large Face 1. Also, the strain on the top of Large Face 1 (LF1 TS1) is larger than the strains on the bottom. The top strain on the Large Face, LF1 TS1 reached an about 61% of the average Small Face 1 transverse strain (SF2 TS Avg.), at the last measurement. An average of the other strains on the Large Face, LF1 TS2 through LF1 TS4, only reached an average of 22% of the strain on the Small Face. The direct sunlight and water caused more expansion on the top of the LSC specimens; therefore, the LSC specimens did not expand uniformly. This was the motivation to rotate the specimens providing a more uniform expansion. The last data point in Figure 3-8 is the last measurement before the specimen was rotated for the first time. This rotation inhibited the ability to continue gathering data for Small Face 1 since its position changed to the bottom.

Table 3-2. Strain Rates during Summer and Non-Summer Months.

	Average Slope (Strain/Month) of SF1 TS Avg.		Rate of Increase
	Non-Summer	Summer	
Specimens 1-6	0.00045	0.00074	1.7
Specimens 7-10	0.00046	0.00126	2.7
Specimens 11-14	0.00019	0.00119	6.5

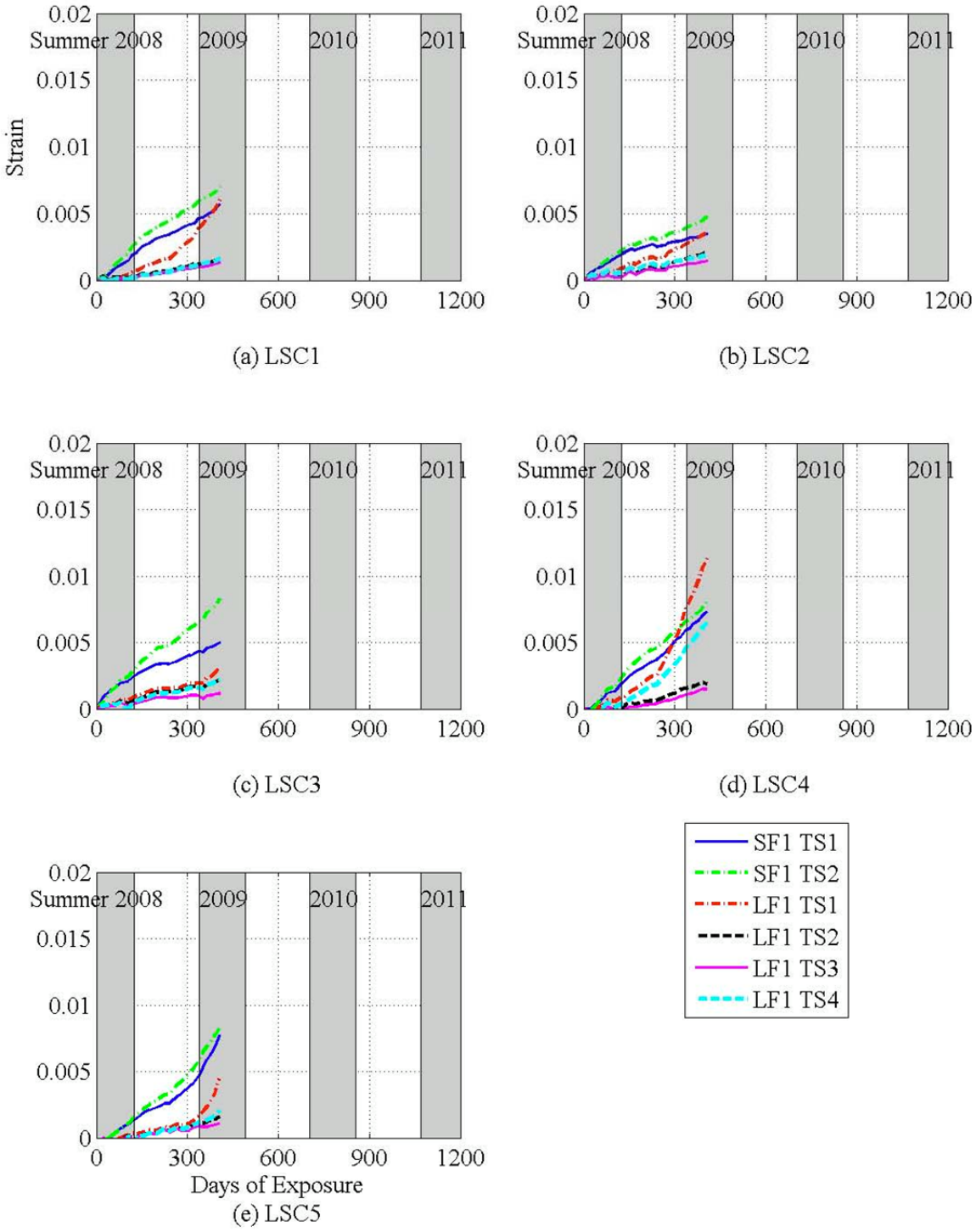

Figure 3-8. Transverse Surface Strains on the LSC Specimens' Small Face 1 and Large Face 1.

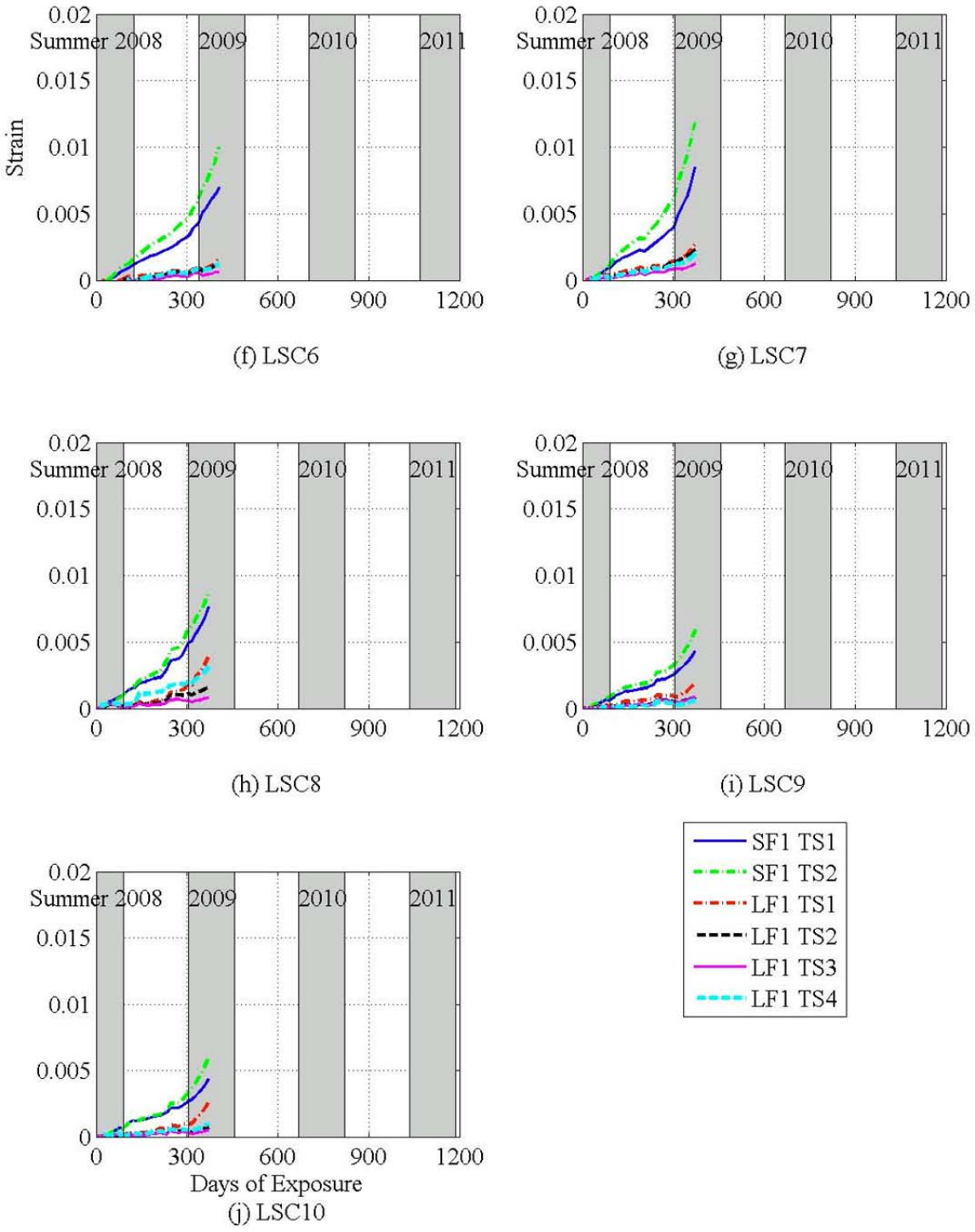

Figure 3-8. (Continued)

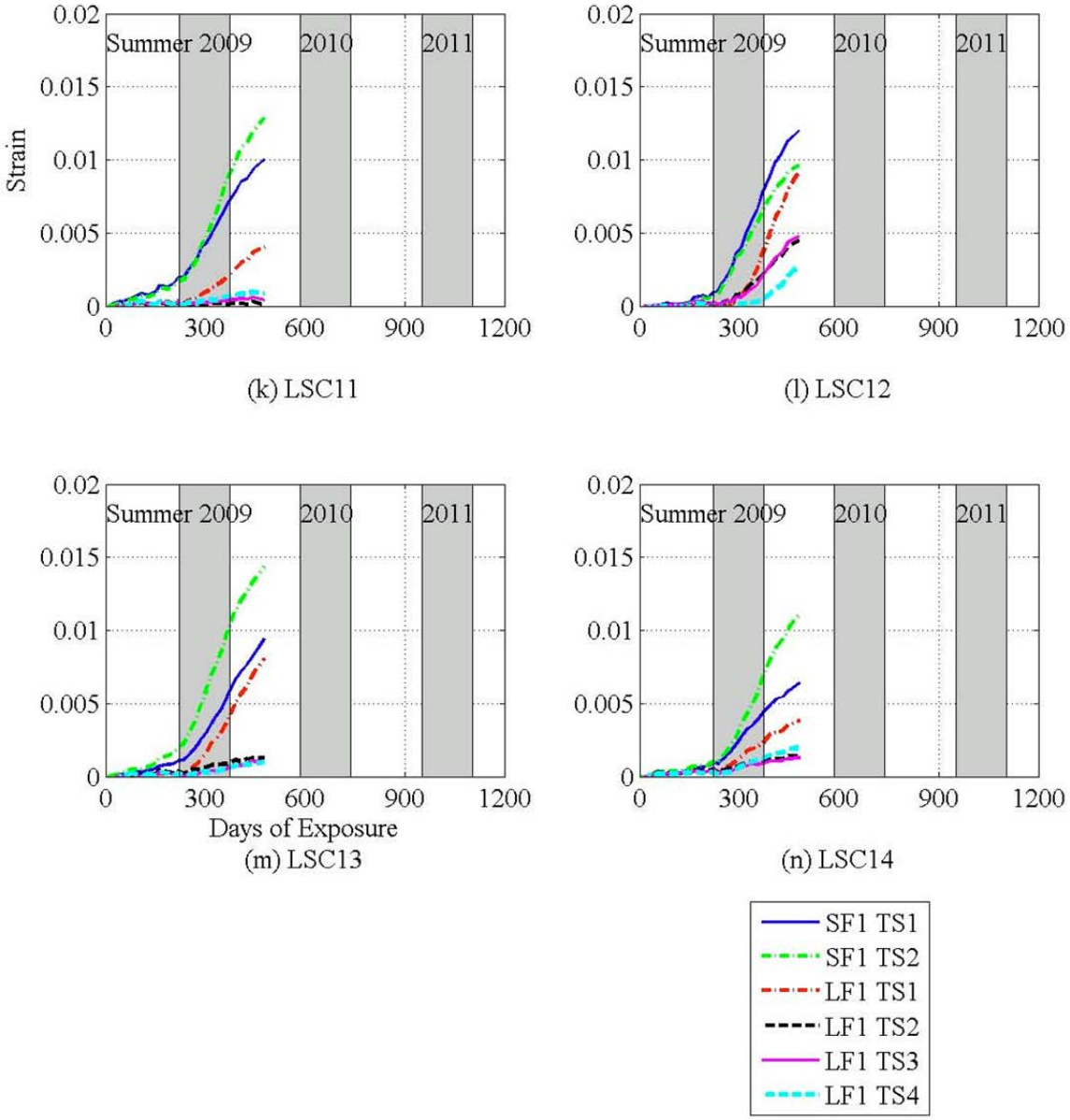

Figure 3-8. (Continued)

After the first rotation, Small Face 2 was now on top available for more surface expansion data. Therefore, additional DEMEC points were mounted on the Small Face 2 to continue the surface strain measurements after the rotation, as discussed in the instrumentation process in section 2. Figure 3-8 shows the two transverse strains on Small Face 1 (SF1 TS1 and SF1 TS2) were similar. Therefore, DEMECs on Small Face 2 were placed in a 2x6 grid instead of a 3x12 grid on Small Face 1 to reduce measurement collection. The DEMECs were spaced at 10 inches (254 mm) on both faces in the transverse and longitudinal directions. Figure 3-9 shows the DEMEC points in the transverse and longitudinal directions on the Small Face 2. The smaller DEMEC grid pattern provided fewer transverse and longitudinal strains used to calculate average strains along the length of the LSC specimens. The fewer DEMECs provided only one transverse strain, SF2 TS1, and two longitudinal strains, SF2 LS1 and SF2 LS2. Small Face 1 had two transverse strains and three longitudinal strains.

On Large Face 1, the transverse and longitudinal strains, LF1 TS1 and LF1 LS1, were on top of the face during the initial LSC specimen orientation. However, after the 180° rotation in the 2nd orientation, these faces were now on bottom as illustrated in Figure 3-9. Again note that the length of the LSC specimens is 25 ft (7.62 m), which is not shown to scale in this figure.

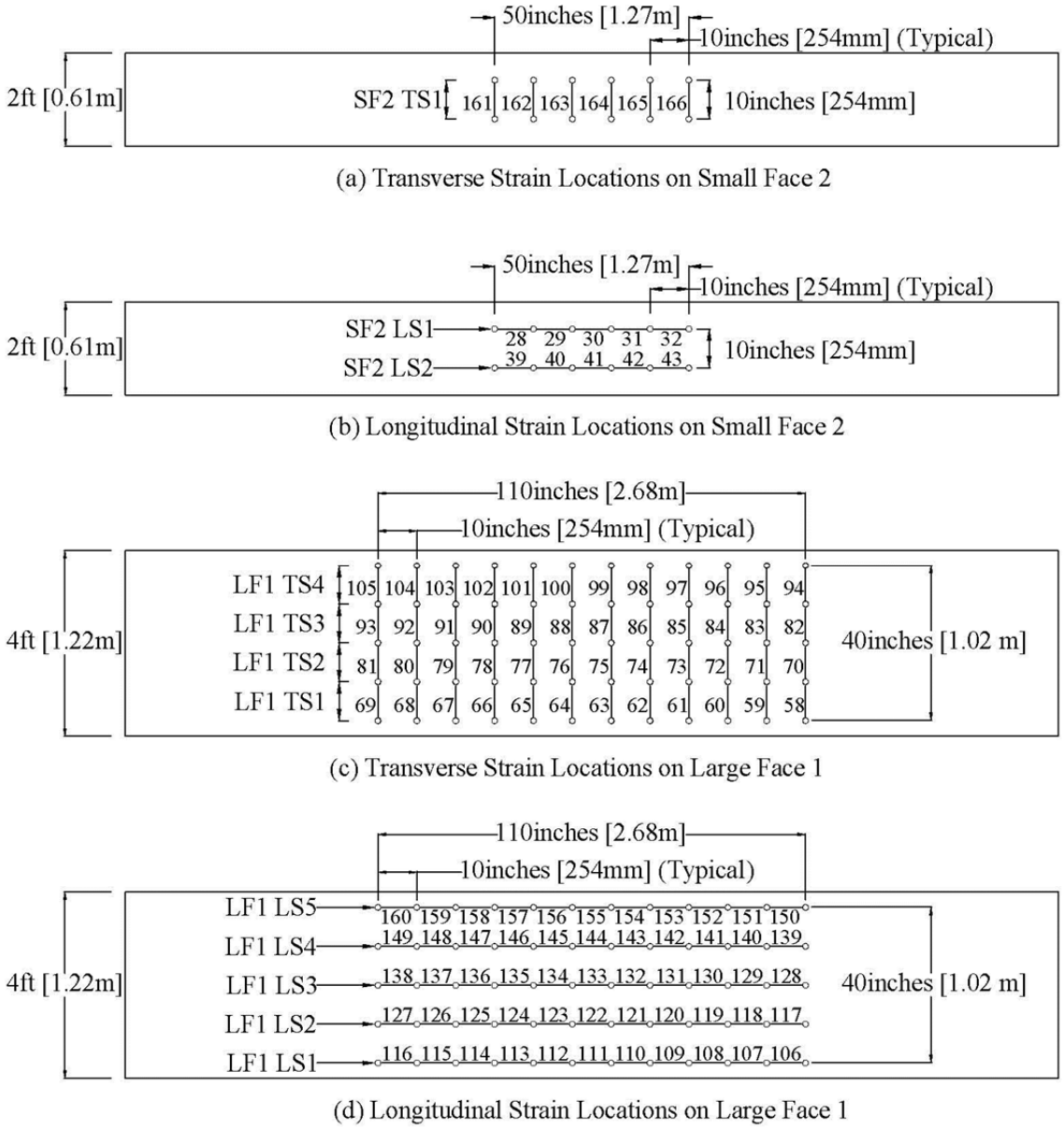

Figure 3-9. Transverse and Longitudinal Strain Locations on the LSC Specimens' Small Face 2 and Large Face 2 during the 2nd Orientation.

After the LSC specimens were rotated 90° for the 3rd orientation, Large Face 1 was placed on the bottom (Figure 3-5). Figure 3-6 shows the LSC specimens during the 3rd orientation with Large Face 2 on top. The distance between each specimen in this

orientation was approximately 1 ft. Since Small Face 1 and Small Face 2 significantly expanded while exposed to direct sunlight and water and now these sides were mostly shaded, no surface data was measured on these faces during the 3rd orientation. New DEMECs were mounted on Large Face 2 following the installation process in 0. Figure 3-10 shows the DEMECs on Large Face 2 in a 5x5 grid compared to the 5x12 grid on Large Face 1. The smaller grid provided fewer transverse and longitudinal strains to average; however there were still 4 transverse and 5 longitudinal averaged strains measured along the splice length of the LSC specimens.

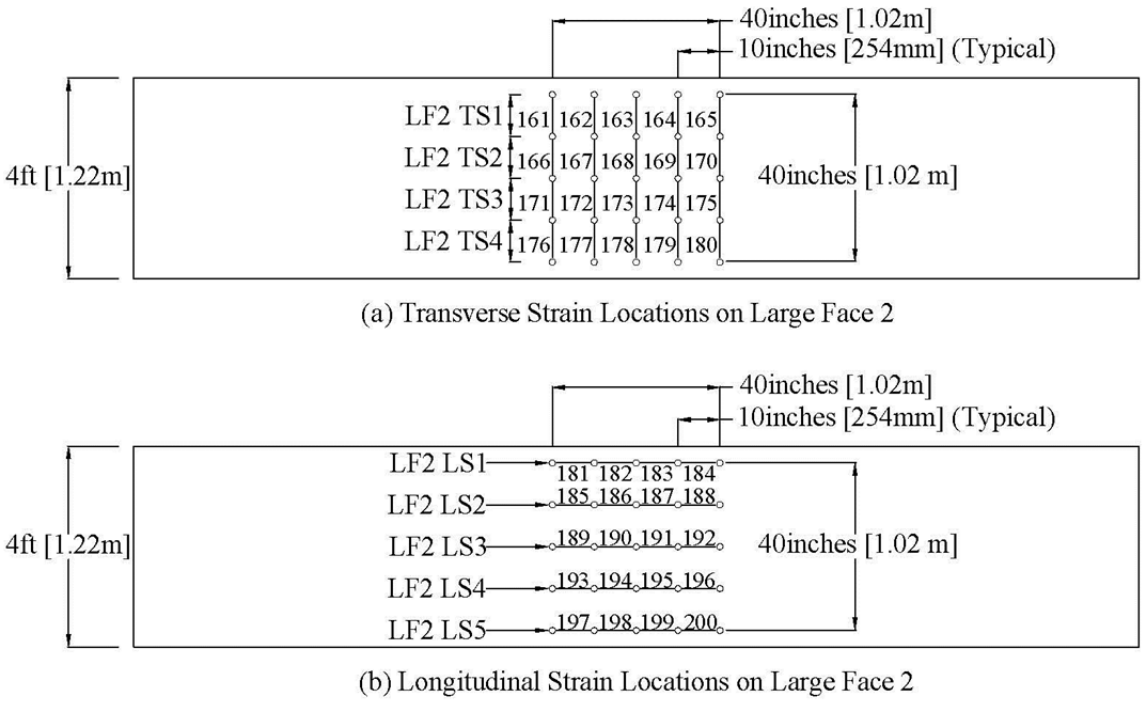

Figure 3-10. Transverse and Longitudinal Strain Locations on the LSC Specimens' Large Face 2 during the 3rd Orientation.

Figure 3-11 and Figure 3-12 show the transverse and longitudinal strains on Small Face 1 and Small Face 2 during the exposure period. The surface strains on Small Face 2 are

shown in Figure 3-11 and Figure 3-12 with an initial value of zero after the first rotation, since this face was on bottom and not exposed to direct sunlight. The surface strain measurements discontinued on Small Face 2 after the 2nd rotation. The strain measurements on Large Face 1 continued after the 180° rotation, however since the top and bottom strains switched, notice the increase of LF1 TS5. After the 90° rotation, surface strain measurements on Large Face 1 discontinued since this face was no longer accessible. The last values of the four transverse strains and five longitudinal strains on Large Face 1 were used as the initial value for the strains on Large Face 2. This was appropriate since both faces were exposed to the same environment.

Figure 3-11 illustrates the small difference between the two transverse strains on Small Face 1. The two transverse strains were both on top exposed to direct sunlight causing similar results. Figure 3-13 and Figure 3-14 show the transverse and longitudinal strains on Large Face 1 and Large Face 2. Since there was a small difference between the two transverse strain on Small Face 1, the average value of the transverse strains on Small Face 1and the transverse strain on Small Face 2 are plotted in Figure 3-13 to compare the strains at different locations.

The "+" symbol depicts the day of 180° rotation of the LSC Specimen. The 90° rotation occurrence is shown on the graph by an "o" symbol. LSC specimens 1, 3, 9, and 10 were tested before the 2nd rotation. These specimens have an "x" on the graph showing when the structural load test occurred. The results from the load tests will be discussed in section 5. The summer months, May through September are once again highlighted by the grey region. The legend lists the strain names corresponding to the labels in Figure 3-7, Figure 3-9, and Figure 3-10.

In the following figures, the transverse surface strains are approximately 10 times as large as the longitudinal surface strains. The axial post tensioning strands along the LSC specimens' length simulating a bridge column axial load discussed in section 2.3 and the column longitudinal reinforcement most likely provided the restraint for the expansion in the longitudinal direction. By day 500, the transverse strains exceeded 0.002. Figure 3-14 shows the longitudinal strains did not reach 0.002. The longitudinal strains were not affected by location as much as the transverse strains since the biggest difference between longitudinal strains at a certain time was 0.0005 whereas the transverse strains had differences of 0.015 on Large Face 1.

The transverse surface strain on Small Face 2 on LSC specimens 1, 3, 9, and 10 did not reach the transverse surface strains on Small Face 1 before the specimens were tested. Table 3-3 shows the transverse strain on Small Face 2 reached around one third the values of the transverse strains on Small Face 1 at the time of the structural load test of LSC specimens 1, 3, 9, and 10. This shows that these specimens did not uniformly expand before the structural load test. However, LSC specimens 5 and 8 did have more uniform expansion before the structural load testing.

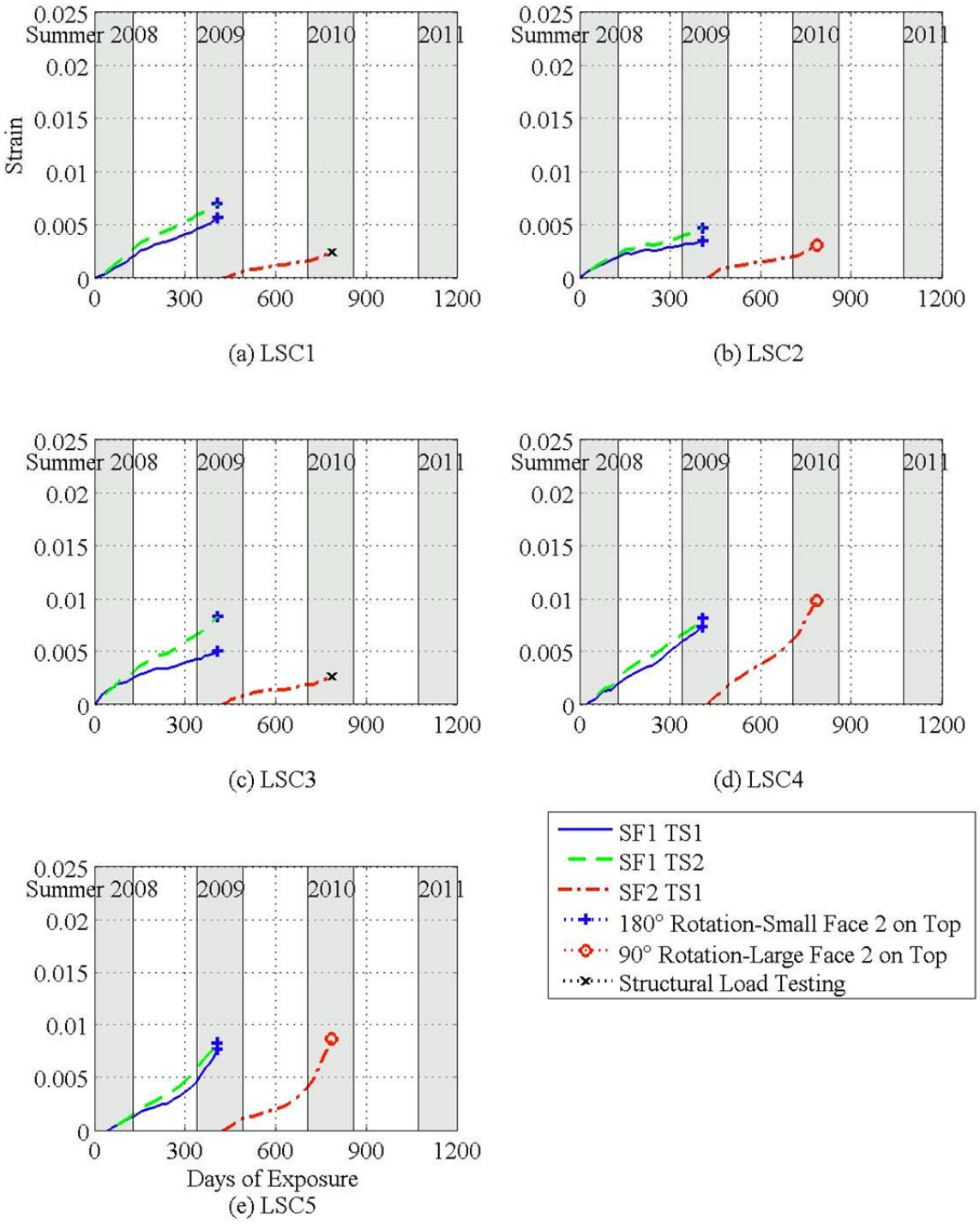

Figure 3-11. Transverse Surface Strains on the LSC Specimens' Small Face 1 and Small Face 2.

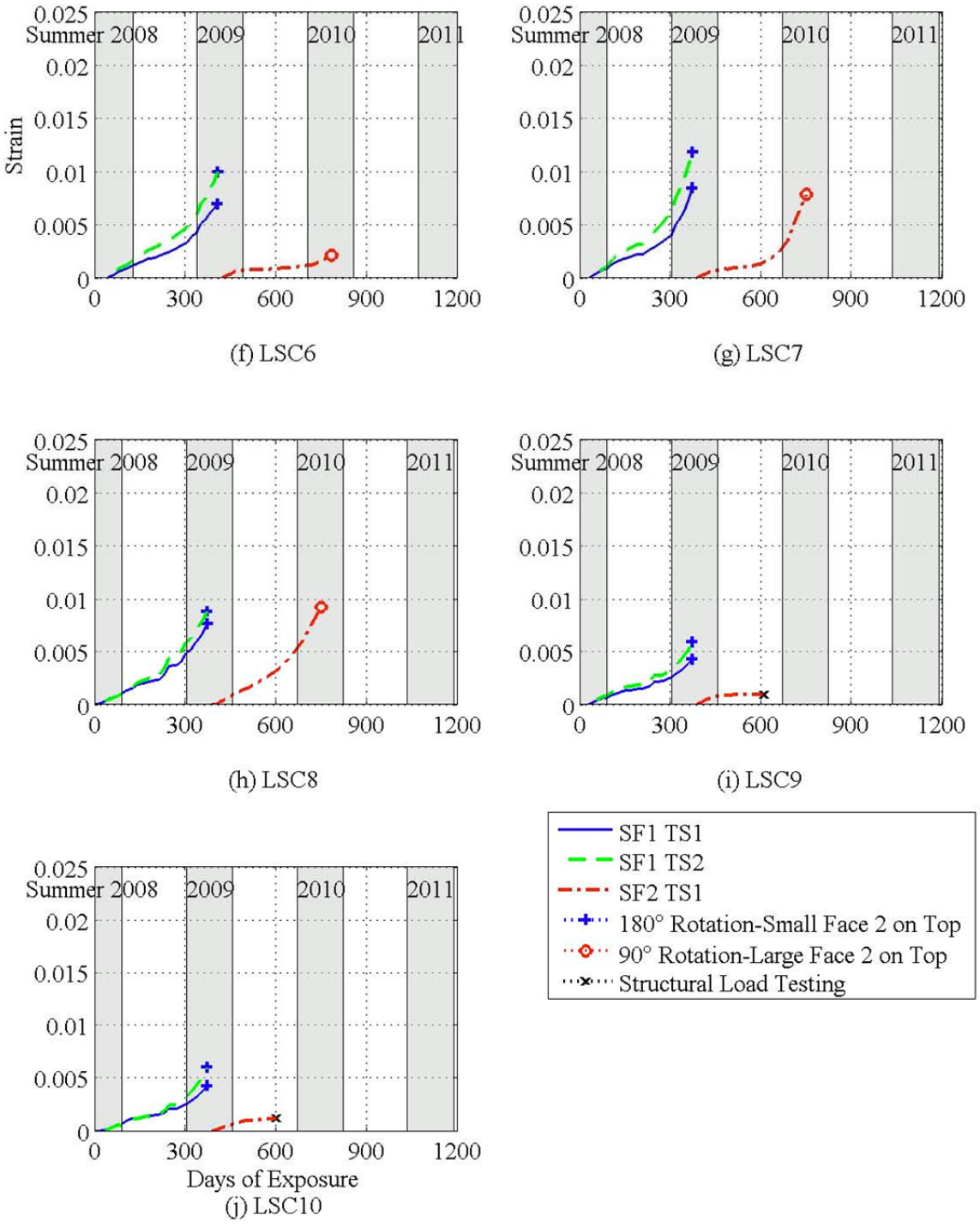

Figure 3-11. (Continued)

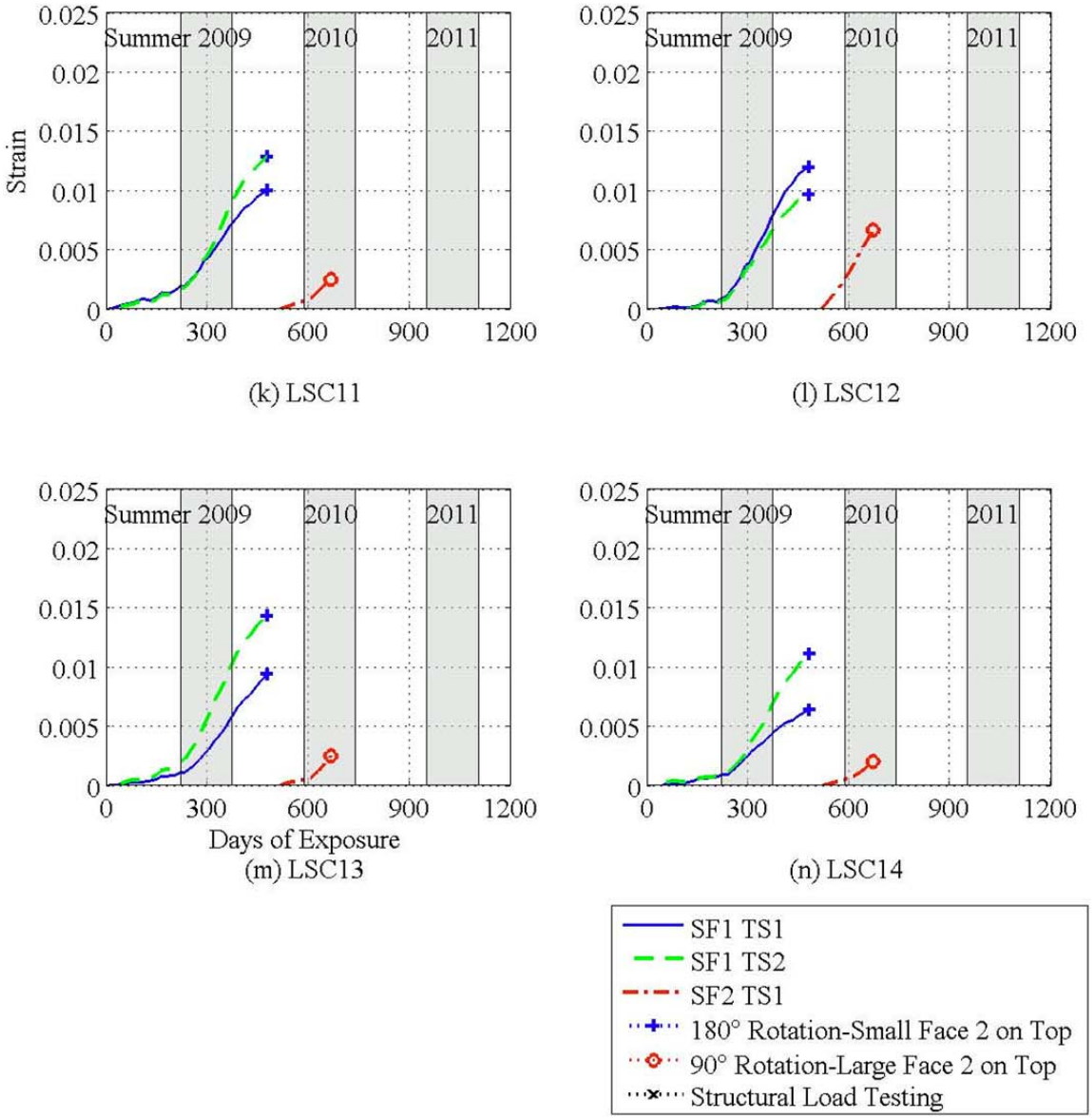

Figure 3-11. (Continued)

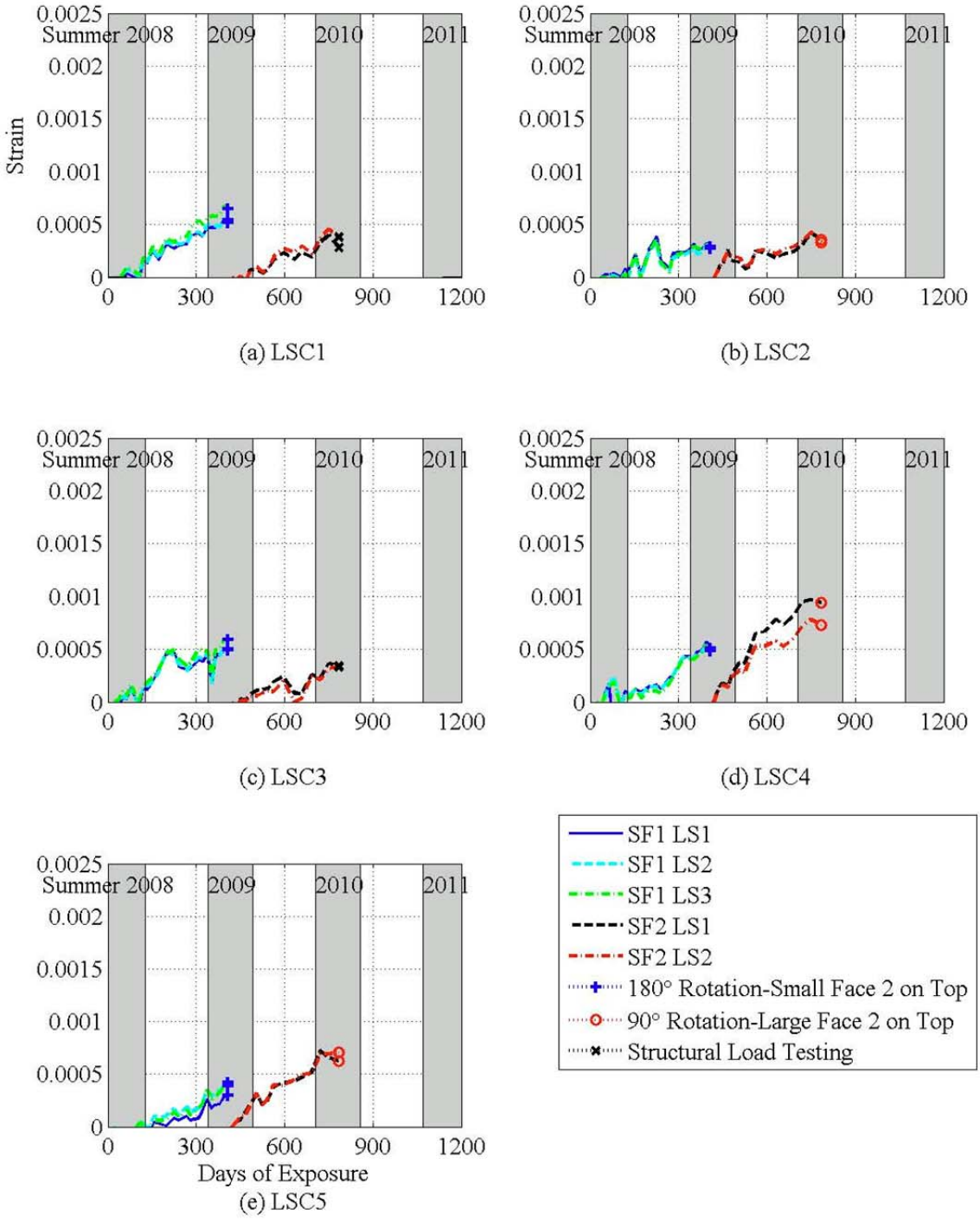

Figure 3-12. Longitudinal Surface Strains on the LSC Specimens' Small Face 1 and Small Face 2.

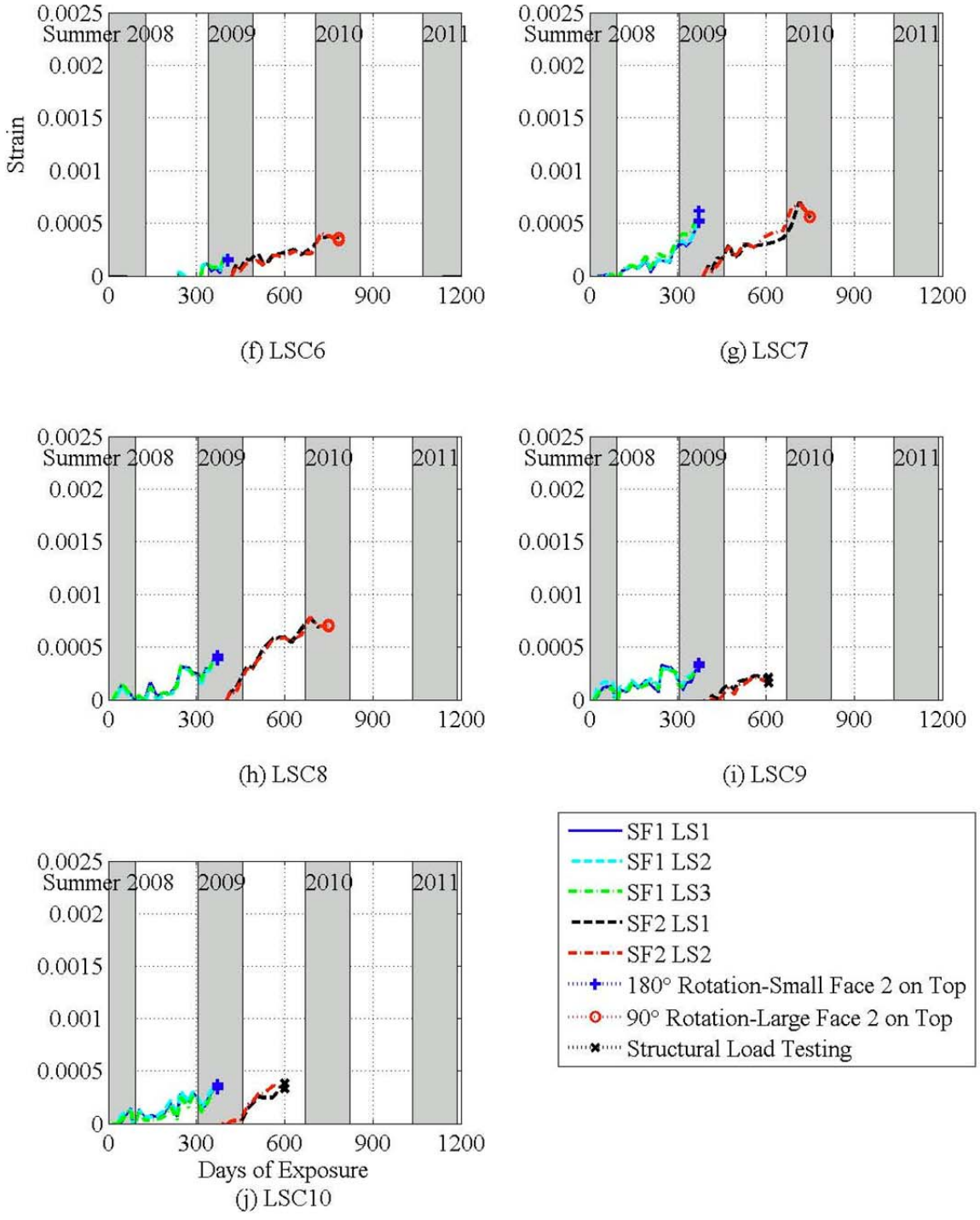

Figure 3-12. (Continued)

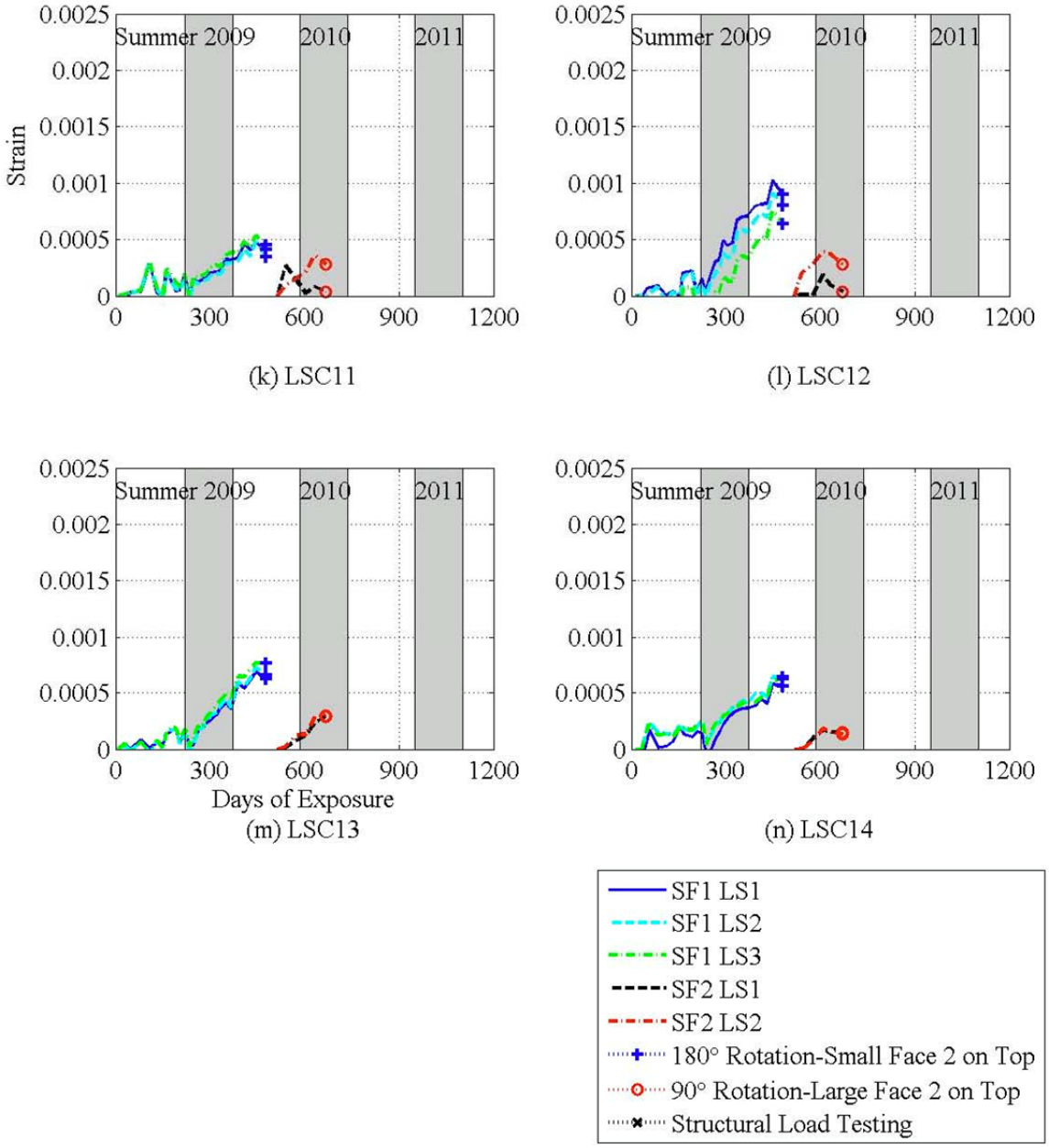

Figure 3-12. (Continued)

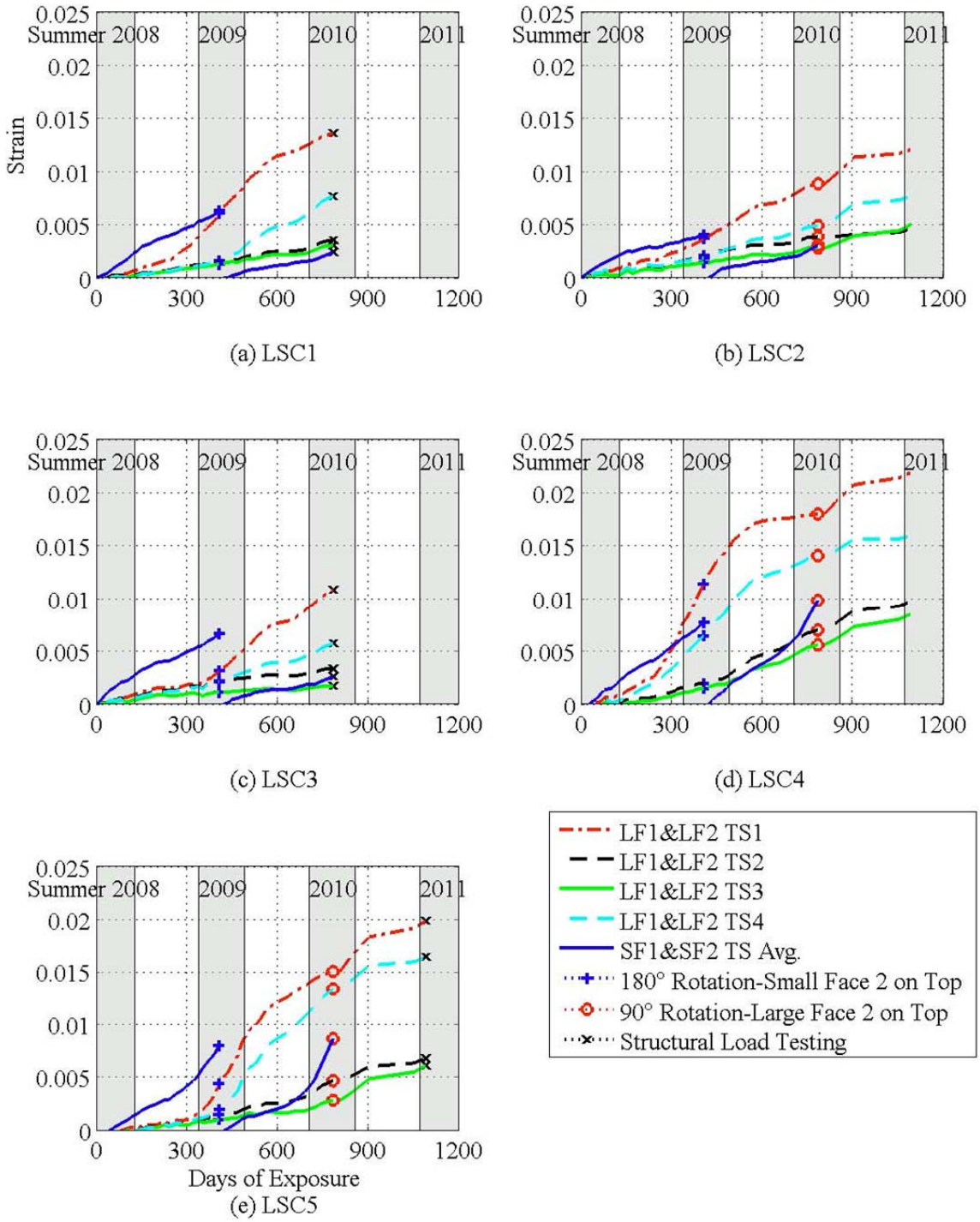

Figure 3-13. Transverse Surface Strains on the LSC Specimens' Large Face 1, Large Face 2, Small Face 1, and Small Face 2.

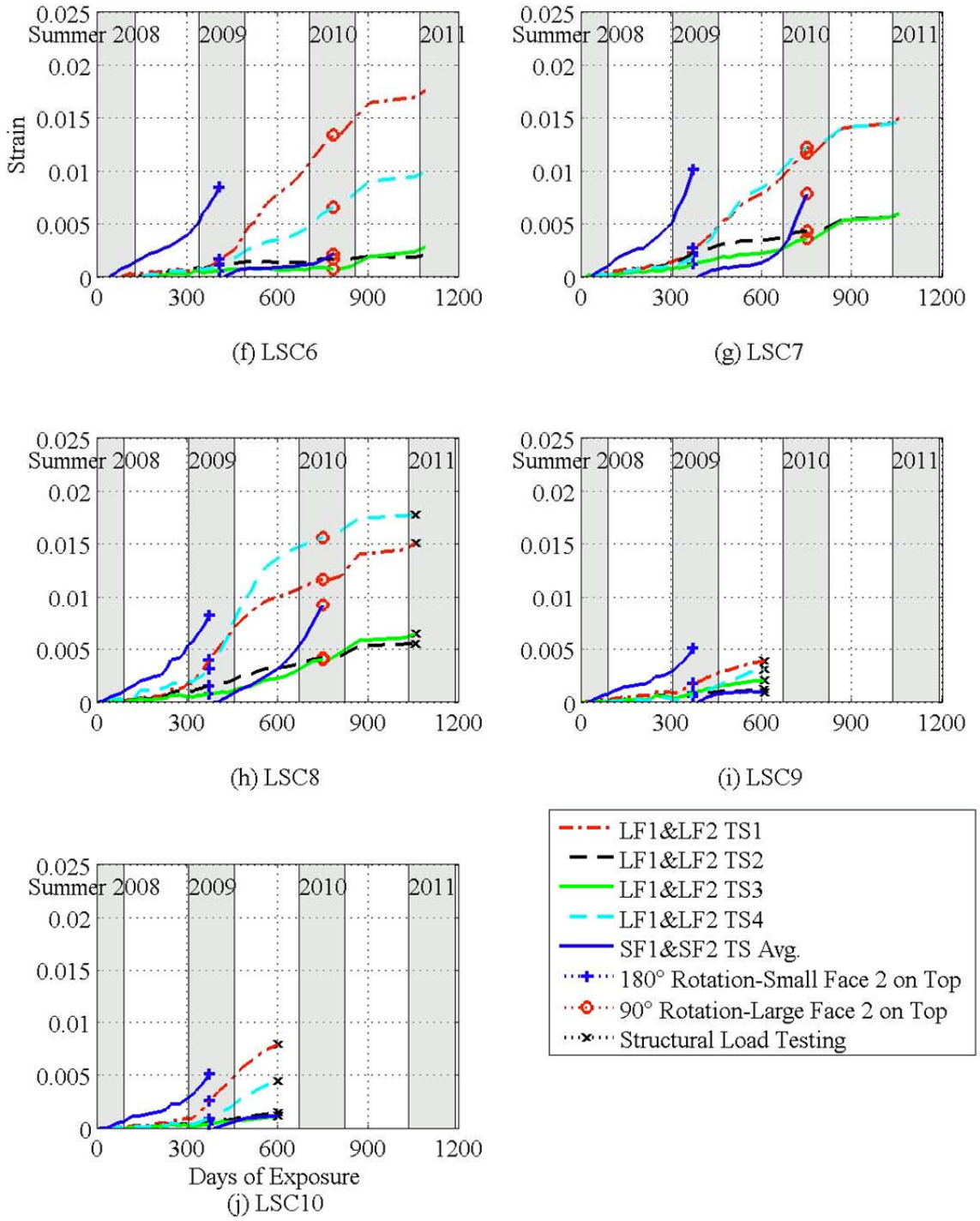

Figure 3-13. (Continued)

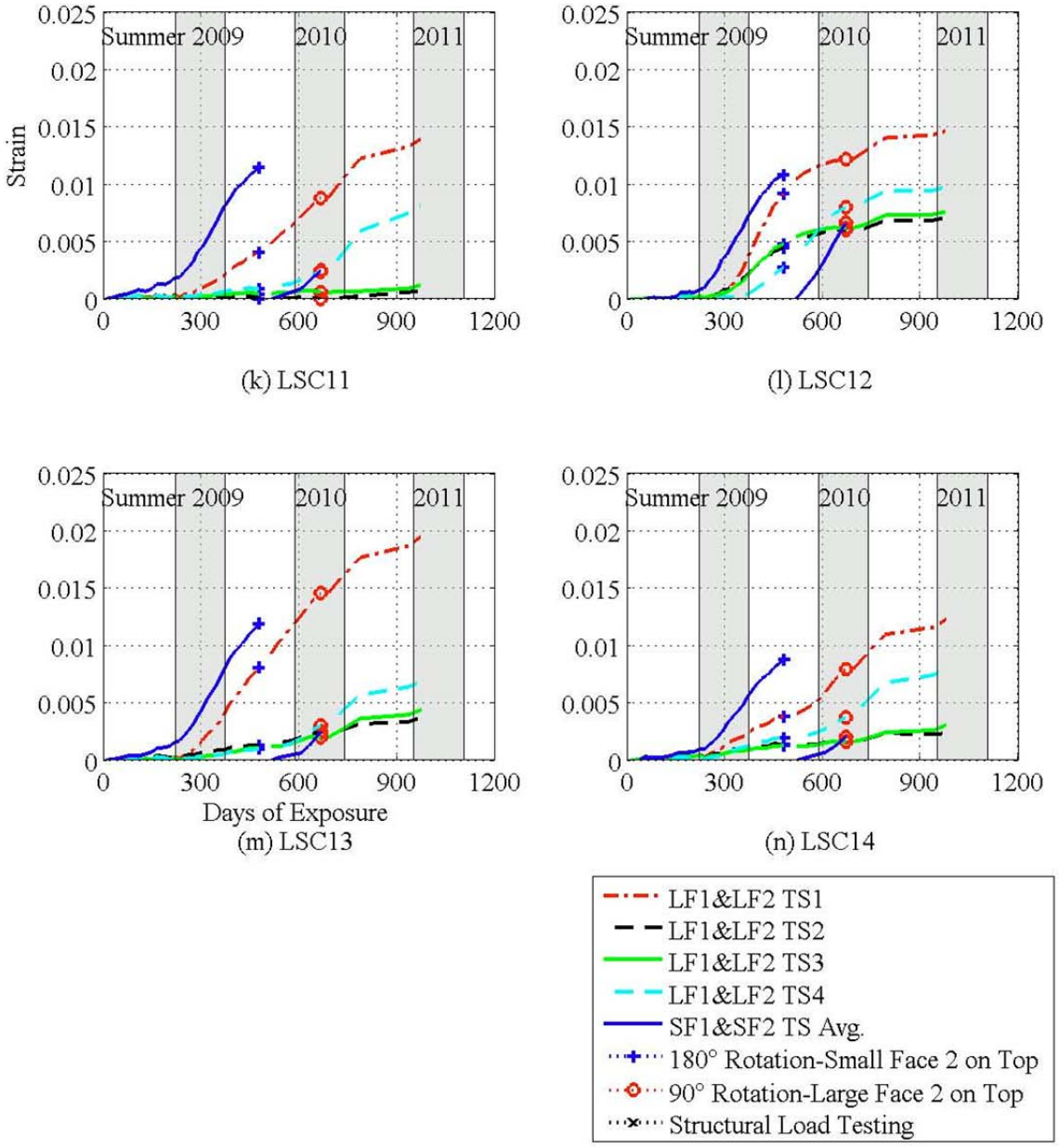

Figure 3-13. (Continued)

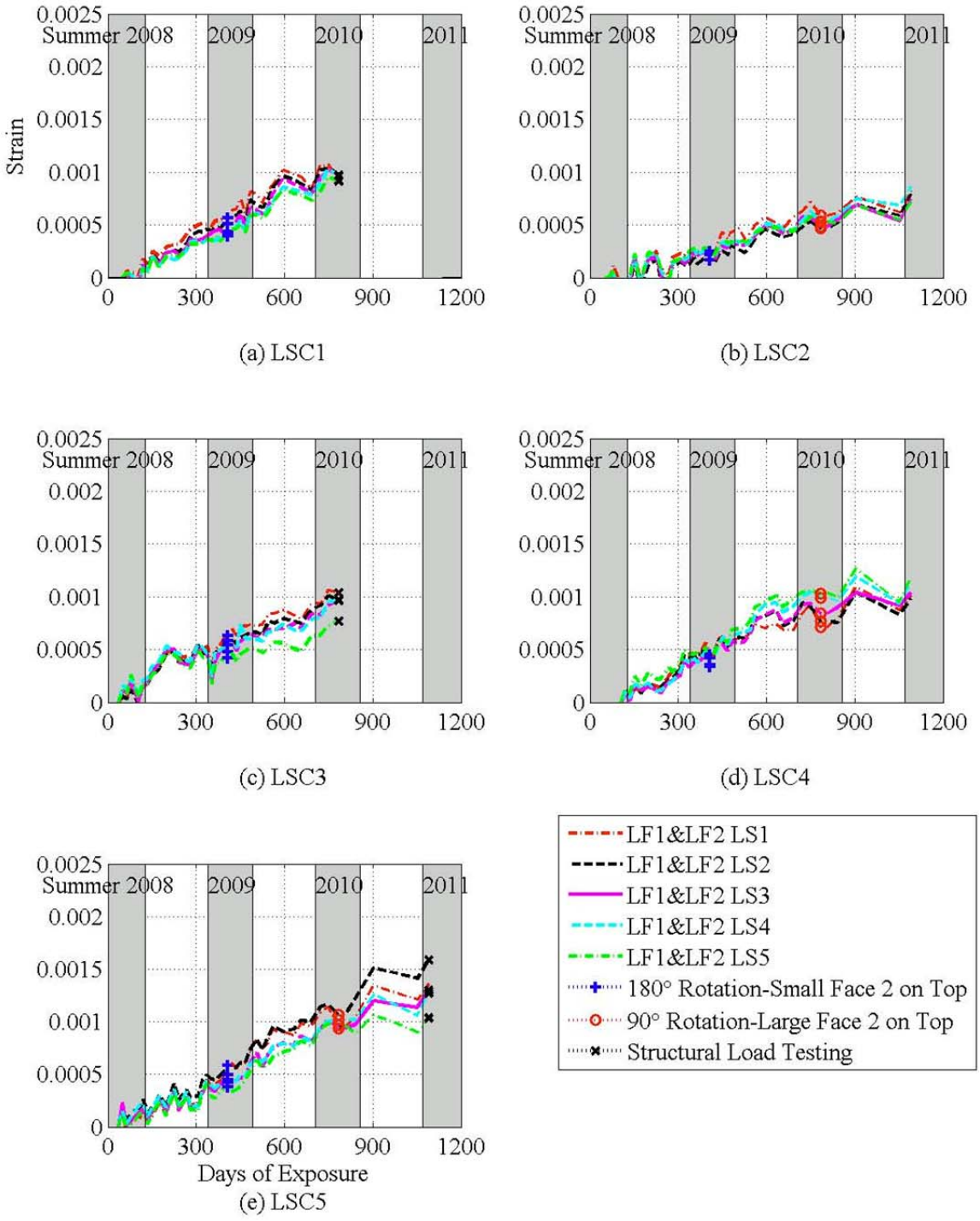

Figure 3-14. Longitudinal Surface Strains on the LSC Specimens' Large Face 1 and Large Face 2.

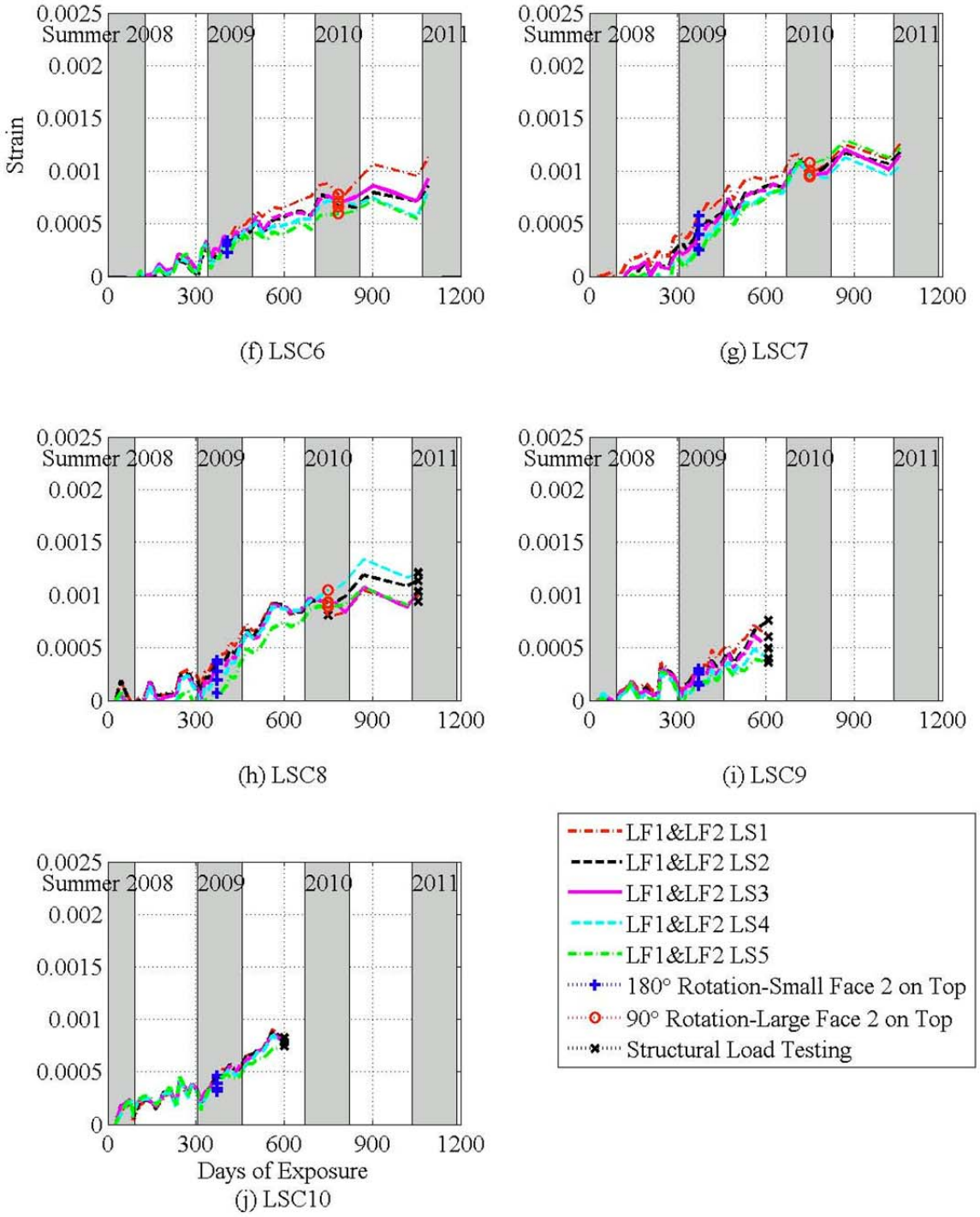

Figure 3-14. (Continued)

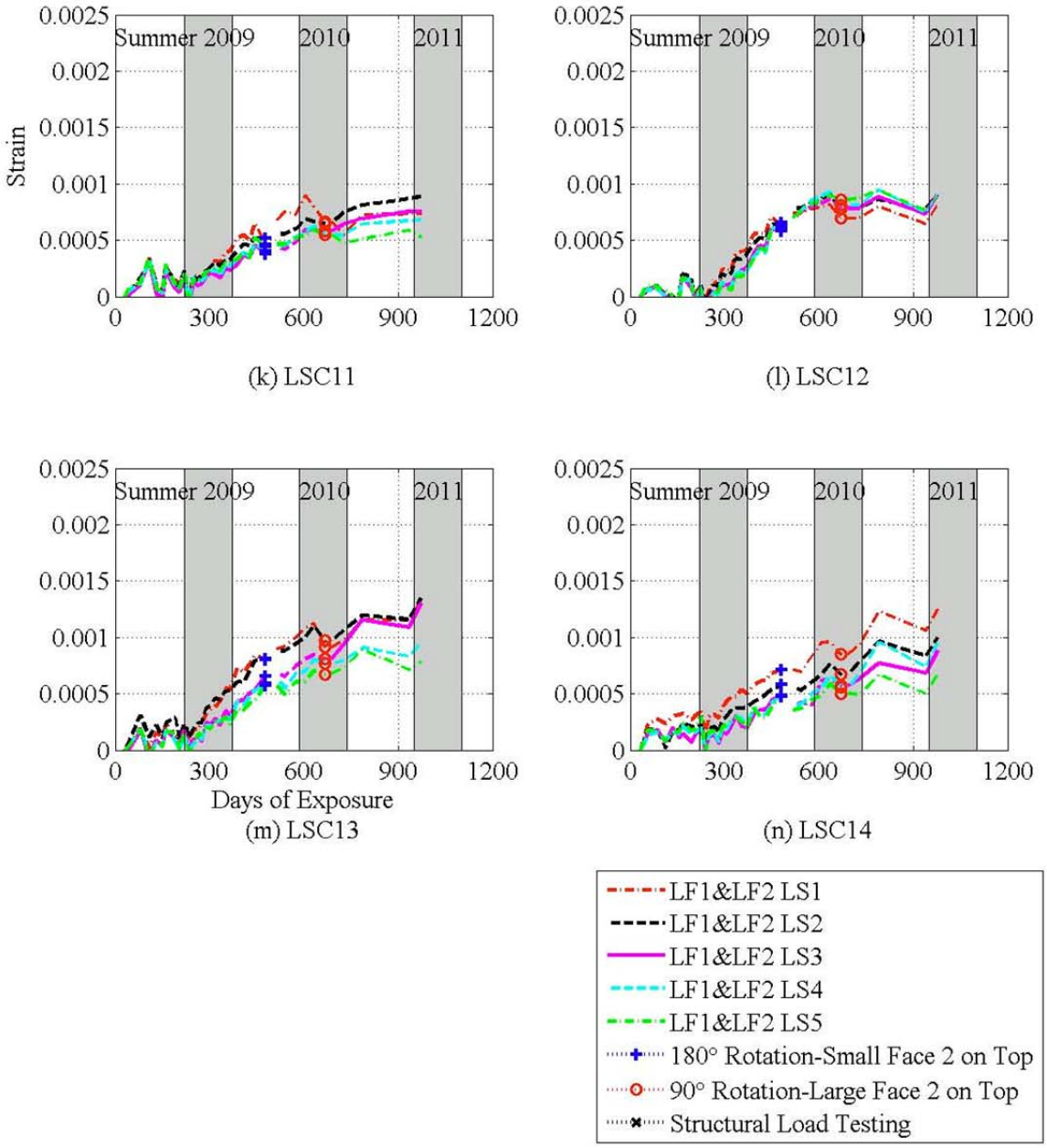

Figure 3-14. (Continued)

Table 3-3. Percent of Transverse Surface Strain on Small Face 2 to Small Face 1 at the Time of the Structural Load Test.

	Last Data Point				
LSC	SF1 TS1	SF1 TS2	SF1 TS Avg.	SF2 TS1	SF2 % of SF1
1	0.0057	0.0070	0.0064	0.0024	38
3	0.0050	0.0083	0.0067	0.0026	39
5	0.0077	0.0083	0.0080	0.0087	109
8	0.0076	0.0088	0.0082	0.0092	112
9	0.0043	0.0059	0.0051	0.0009	18
10	0.0043	0.0061	0.0052	0.0013	25

3.3.2 Crack Width Measurements

In existing bridge columns, cracks can be measured quite easily, while other strain data is more difficult to obtain since instrumentation was not installed prior to bridge construction. However, the surface strains calculated with the DEMECs more accurately represent the total surface expansion since there is micro cracking not visible to the naked eye and also concrete expansion between the cracks due to ASR/DEF. Therefore, the strains from crack width measurements in the large scale specimens were compared to the strain computed using the DEMECs to compare surface strains easily measured in the field to more accurate research data. Figure 3-15 shows the longitudinal cracks on a LSC specimen. To give you an idea of the scale of this figure, the DEMECs are approximately 10 inches (254 mm) apart. There are no visible transverse cracks; therefore only longitudinal cracks were measured with a crack comparator card.

Figure 3-15. Longitudinal Cracks from ASR Expansion.

The crack comparator card measured crack widths as small as 0.005 in (0.13 mm) as shown in Figure 3-16. To estimate the expansive strains, the width of the cracks along the transverse direction between DEMECs were added and then divided by the original distance between DEMECs, $l_d(0)$ to give a strain value shown below.

$$\varepsilon_{crack} = \frac{\sum \text{crack width}}{l_d(0)} \qquad \text{(Eq. 3-3)}$$

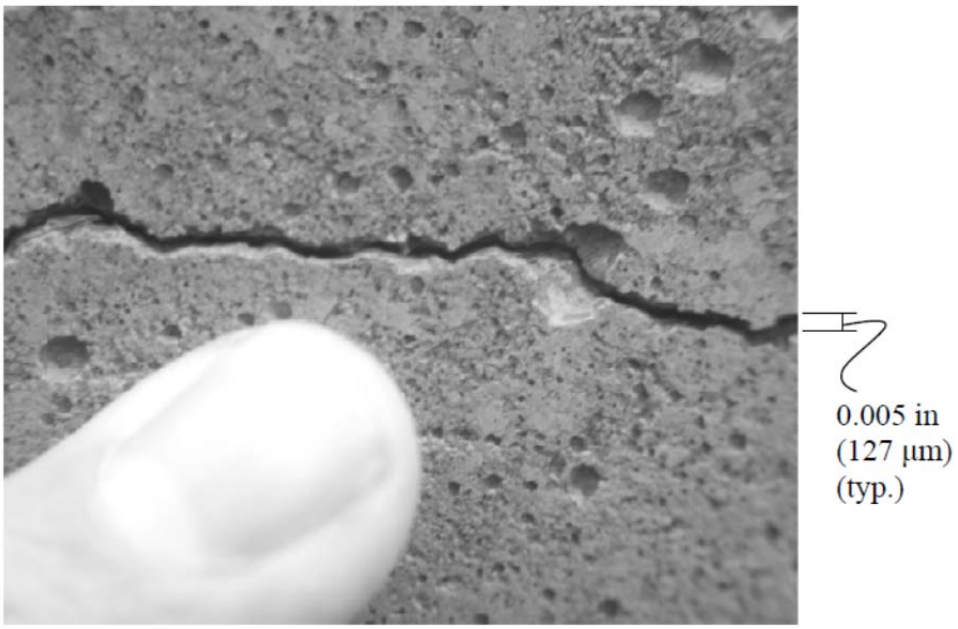

Figure 3-16. Longitudinal Crack Width [taken from Alberson (2009)].

The longitudinal crack widths were measured along the two center DEMEC lines in the transverse direction for all faces. The two lines of DEMECs where the cracks were measured are shown in Figure 3-17. No line is shown between DEMECs on the bottom row of Large Face 1 because the cracks were not measured in this location. After the 180° rotation, the cracks were not measured on the top row between DEMECs so that the crack width measurements would continue in the same location before and after the 180° rotation. The crack widths were measured along all four rows on Large Face 2 after the 90° rotation.

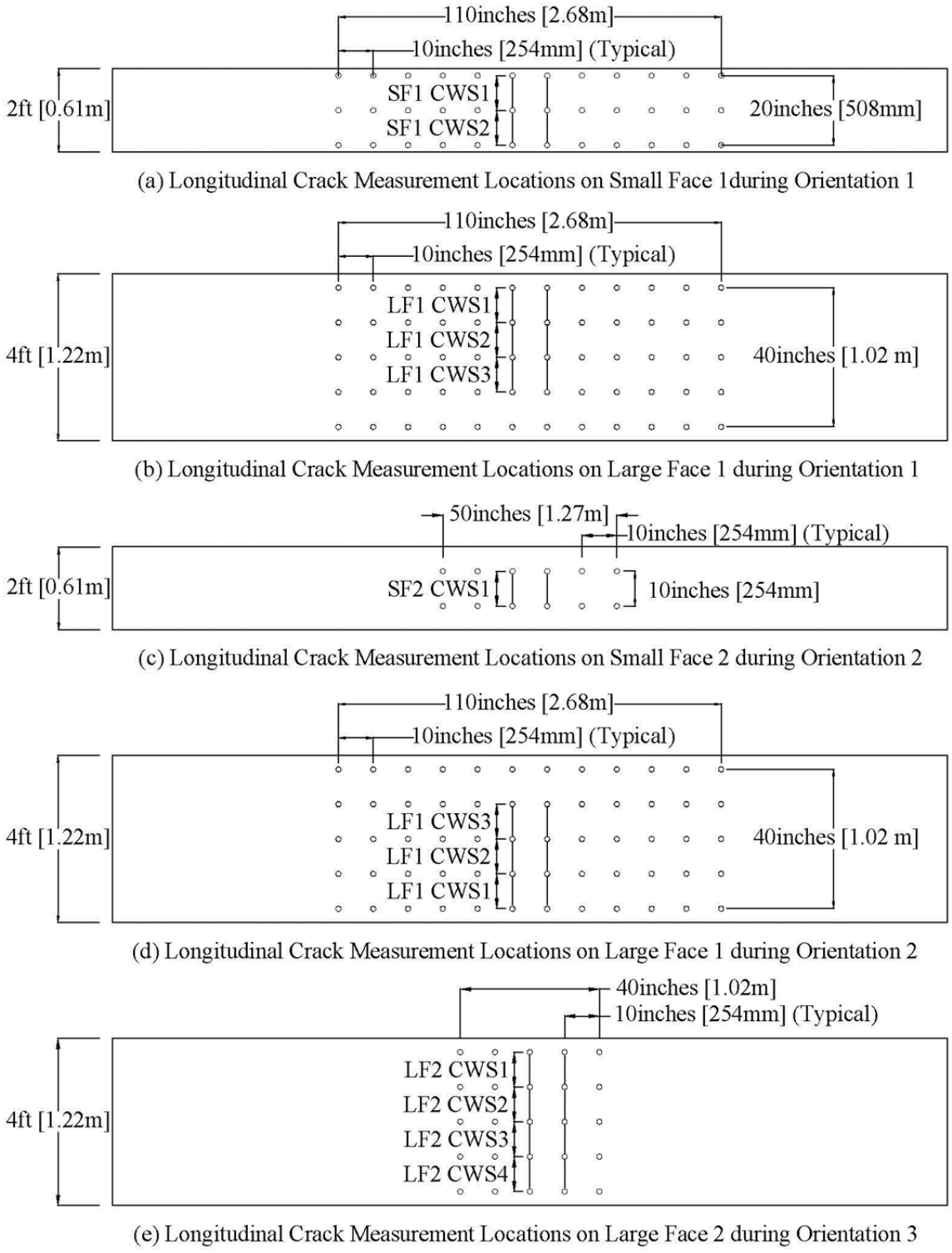

Figure 3-17. Crack Width Measurement Locations and Labels on all Faces in Relation to the DEMEC Grid.

The transverse surface strains calculated from measuring the distance between the DEMECs and from summing the longitudinal crack widths between the DEMECs are compared in Figure 3-18 for Small Face 1, Small Face 2, Large Face 1, and Large Face 2. The crack width strains are abbreviated as CWS. The strains are numbered in the same way as the strains calculated with the DEMEC measurements. The surface strains calculated from measuring the distance between the DEMECs plotted in Figure 3-18 are an average of the two lines of DEMECs where cracks were measured shown in Figure 3-17. These strain values are different from the transverse surface strains in Figure 3-11 and Figure 3-13 which includes more strains in the average as explained in section 3.3.1. No crack width data was taken at the bottom of Large Face 1; however data was taken in this location on Large Face 1. Therefore, there is only data on Figure 3-17 for LF2 CWS4 during the 3rd orientation. Figure 3-19 shows the crack width strain as a percentage of the DEMEC surface strain measurements.

Figure 3-18 shows the sum of the crack width strains are usually smaller than the surface strains which are calculated from the measured distance between DEMECS. The crack width strain percentage is highly scattered, but generally converges to about 50% of the surface strain. This reduced strain from the sum of the crack widths can be explained by the expansion of the concrete between cracks that was not accounted for and other cracks that were too small to measure. When the DEMECs were first installed on Small Face 2 after the first rotation, the distance between the DEMECs was used as a zero baseline, thus showing no strain. However, cracks had already formed and were measured. Therefore the high percentage on some of the LSC specimens after the 180° rotation show there was expansion on that face even though there was no sunlight. The strains from the initial crack widths formed while Small Face 2 was on bottom are less than 0.001 which is very small.

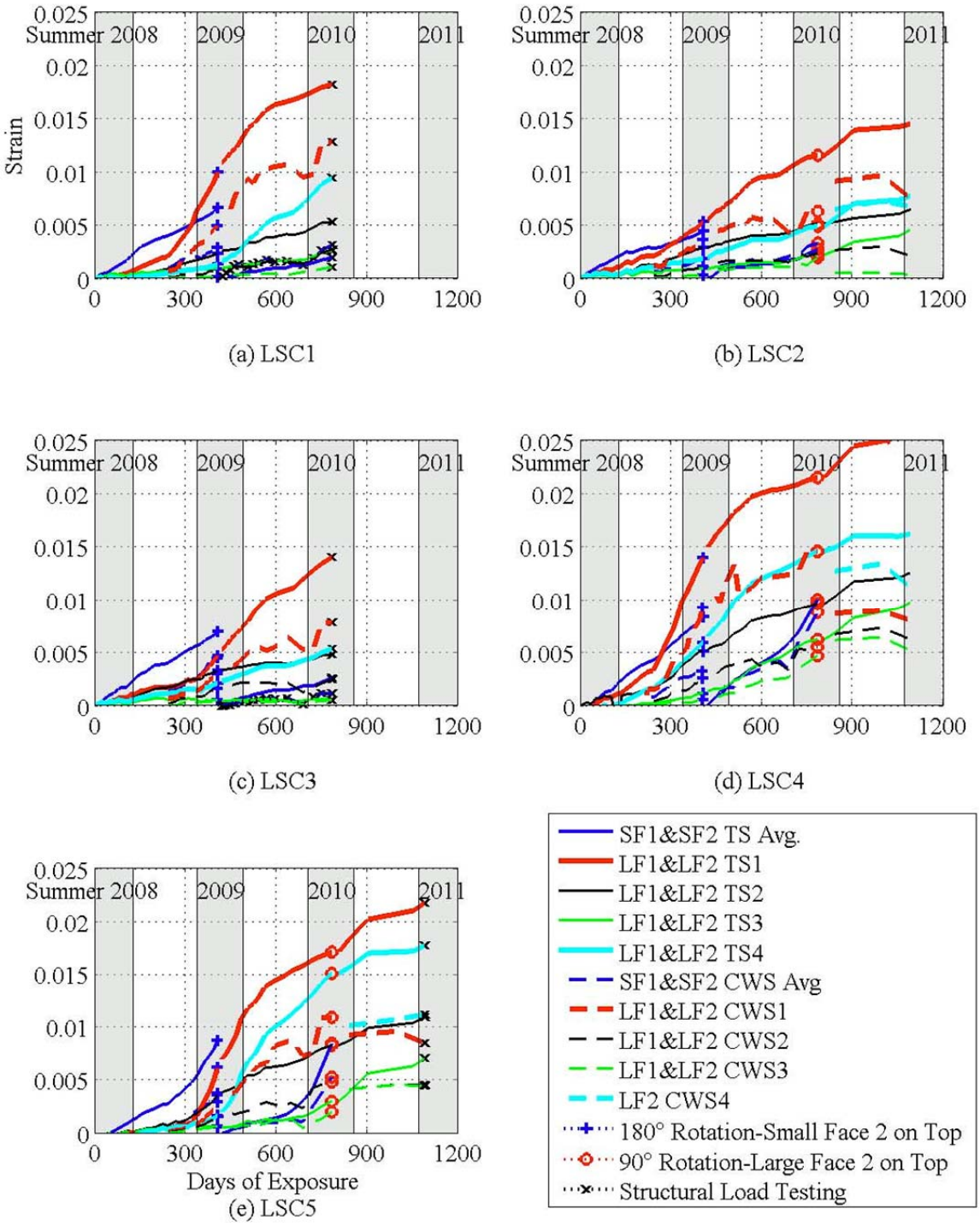

Figure 3-18. Transverse Surface Strains from DEMECs and Crack Width Measurements on All Faces.

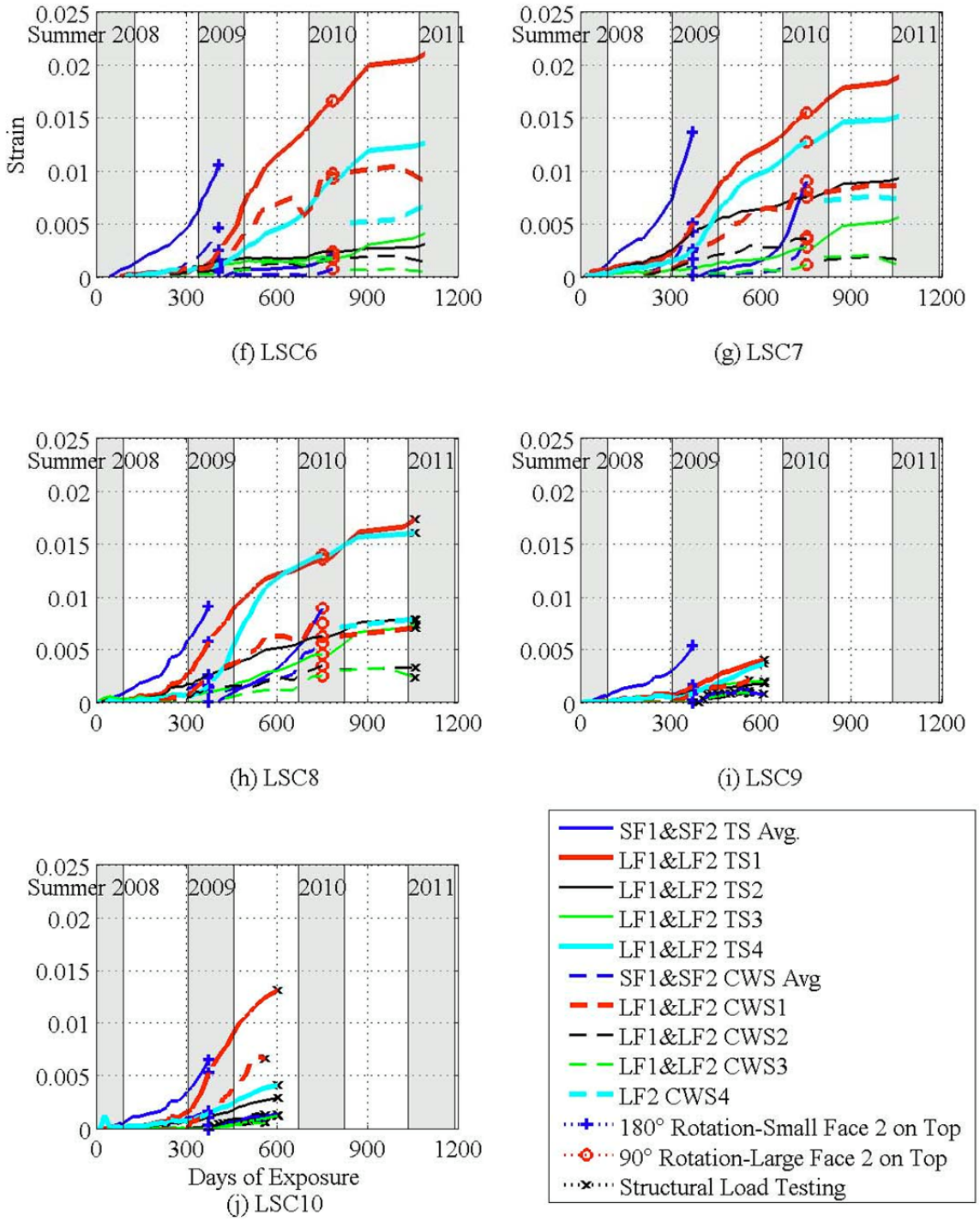

Figure 3-18. (Continued)

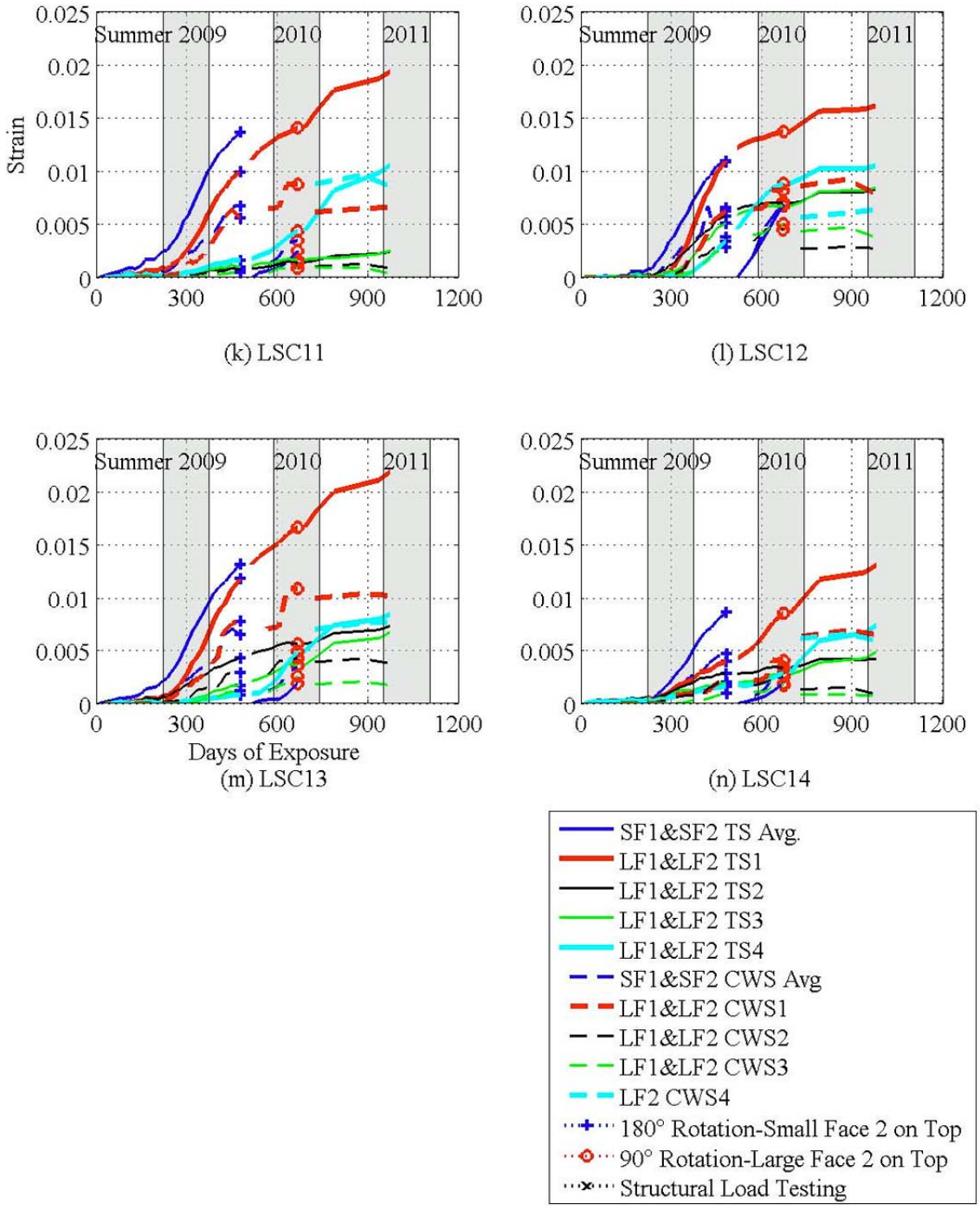

Figure 3-18. (Continued)

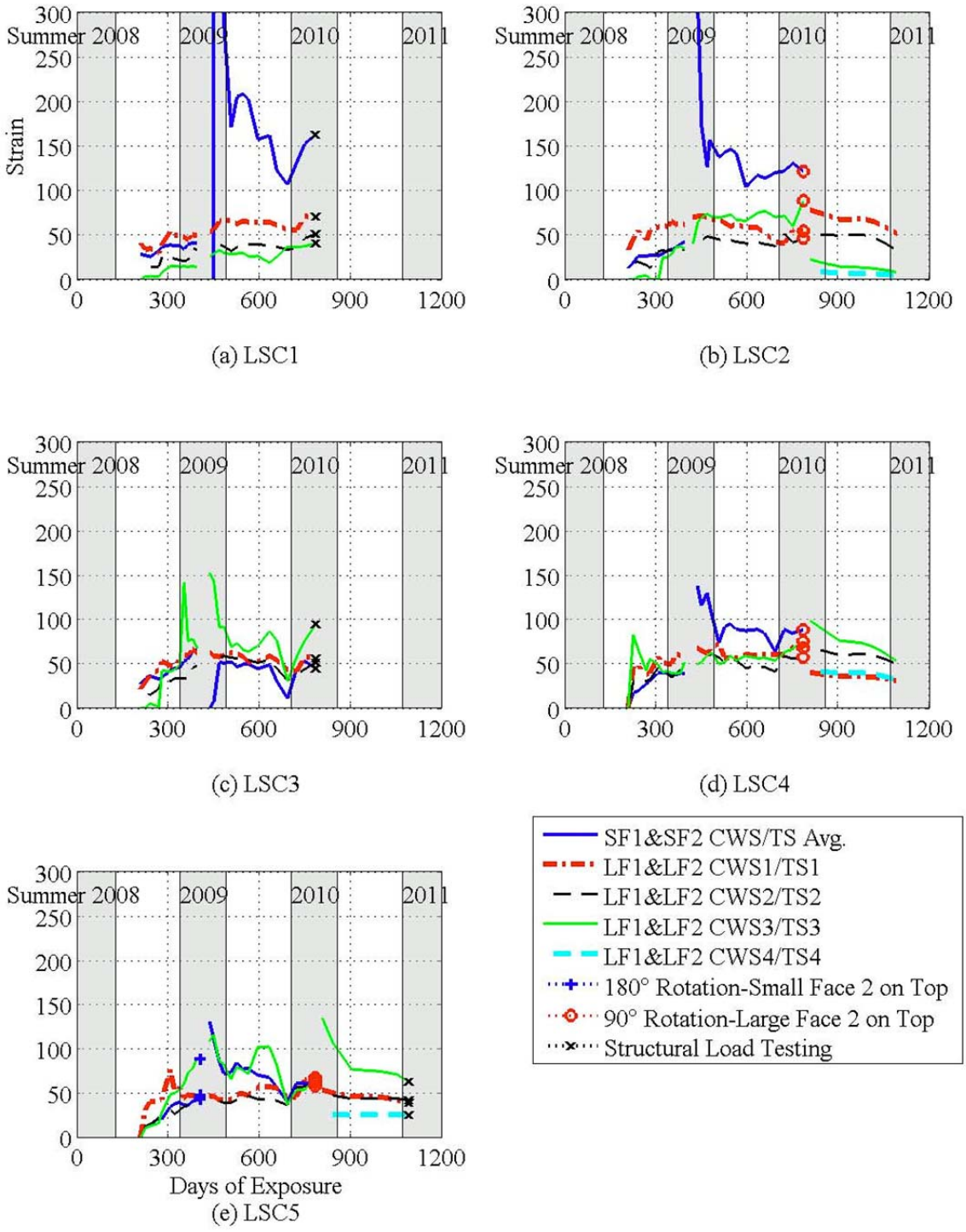

Figure 3-19. Crack Width Strain Percentages of Surface Strains on All Faces.

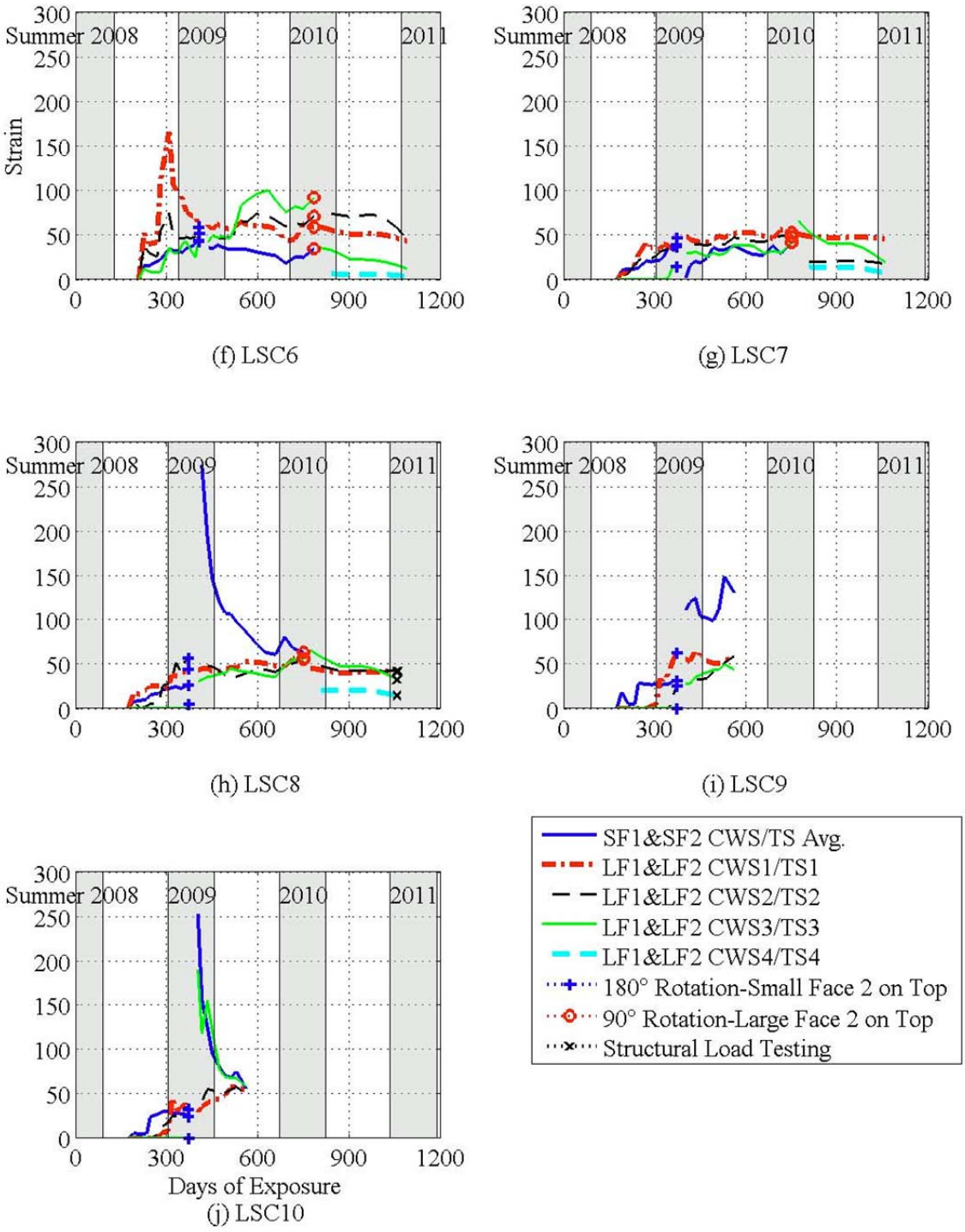

Figure 3-19. (Continued)

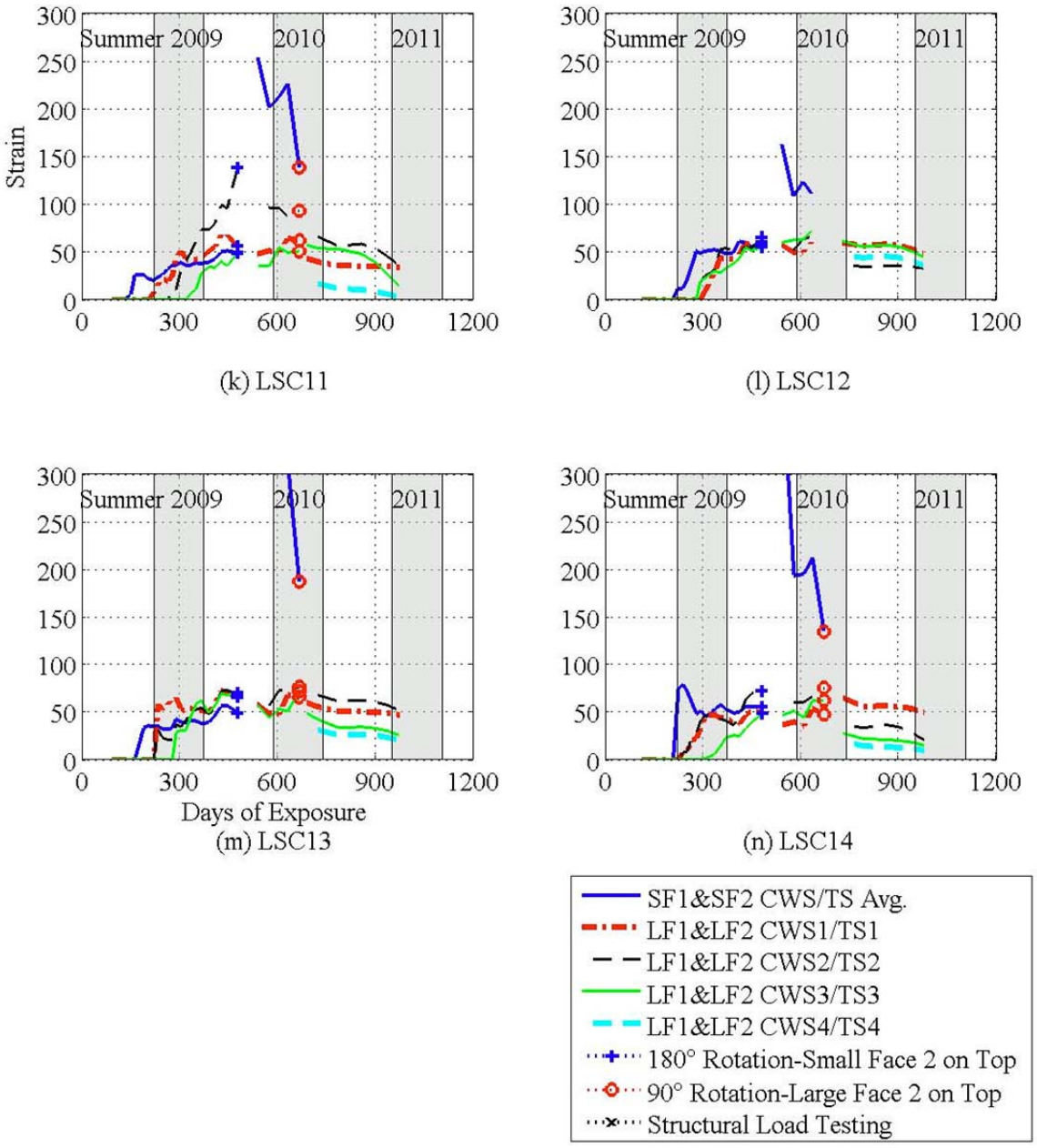

Figure 3-19. (Continued)

3.3.3 Internal Specimen Strains

The strains in the reinforcing steel were measured with 12 strain gages (SG) as shown in section 2. Eight gages (SG1- SG8) were mounted on the tension bars in the splice region; and two gages (SG9 - SG10) were placed on the compression bars (Figure 2-4). The transverse reinforcement was instrumented with SG11 and SG12 (Figure 2-5). The data from the ten gages on the longitudinal reinforcement was primarily used during the experimental testing (section 5); however, the following figures show the strains that occurred during deterioration process before the specimens were tested. Figure 3-20 shows the strains in the edge tension bars with gages: SG1 – SG4. Figure 3-21, shows the strains in the center tension bars with gages: SG5 – SG8. Figure 3-22 shows the strains in the center compression bars with gages: SG9 – SG10. The tension and compression refer to the orientation of the bars during the structural load tests (Figure 2-4).

One strain gage, SG11, was applied to the transverse hoop on the Small Face 1. Another gage, SG12, was placed on the Large Face 1 of the hoop. The internal concrete strains in the LSC specimens were measured using embedded concrete gages (KM). KM1 and KM3 measured the strain in the concrete cover region and were placed in the center of the cover, 1 inch (25.4 mm) from the surface and the steel hoop. Inside the hoop, KM2 and KM4 were placed in the concrete core 1 inch (25.4 mm) from the transverse steel. KM1 and KM2 were installed at the center of Small Face 1. KM3 and KM4 were placed at the center of the Large Face 1. Perpendicular to KM3 and KM4, KM5 was placed to measure the radial strain in the concrete core. The KM gages were placed 6 inches (152 mm) from the instrumented hoop (Figure 2-5).

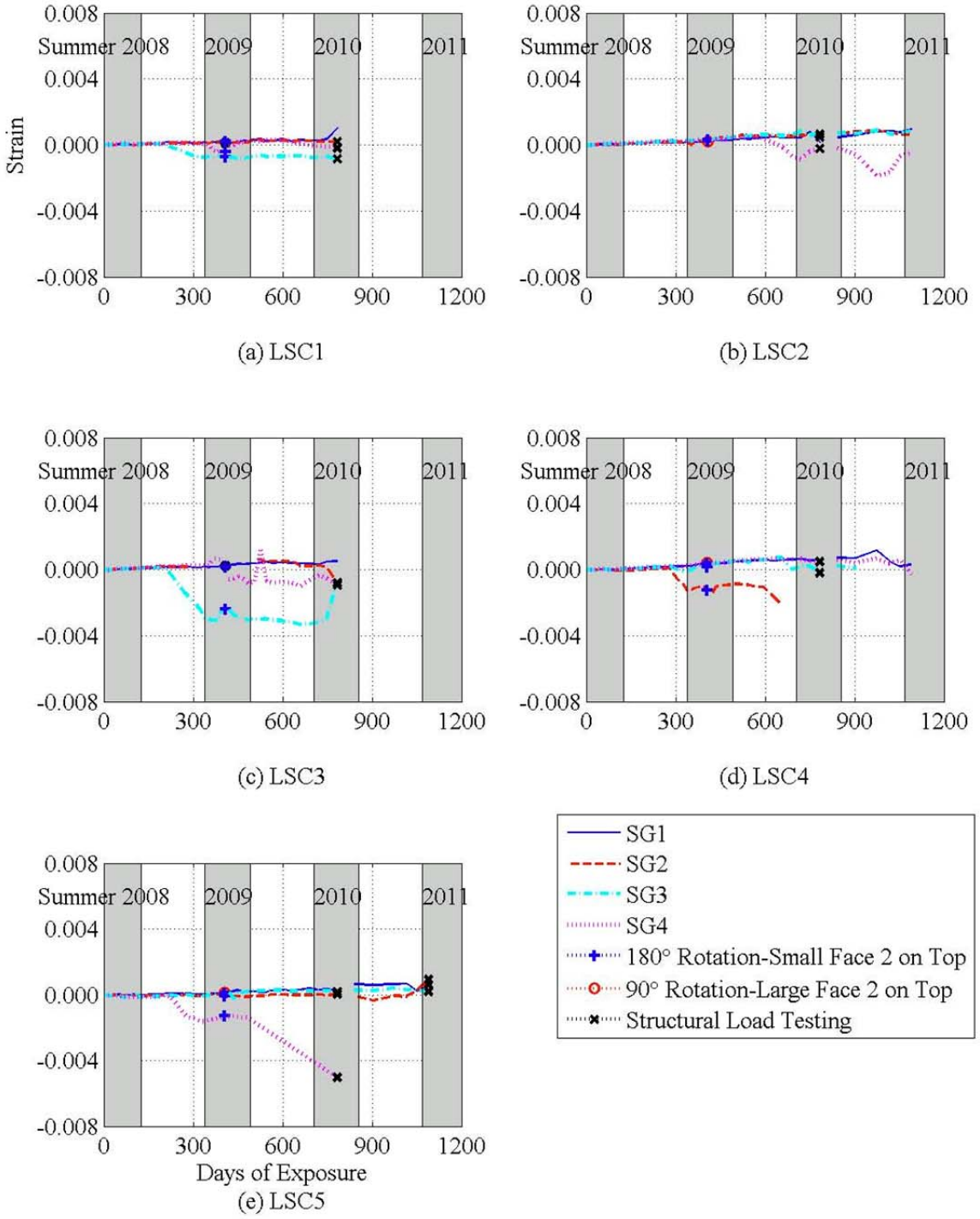

Figure 3-20. Internal Strain Gages (SG1-SG4) along Large Face 1 Tension Steel of the Splice Region.

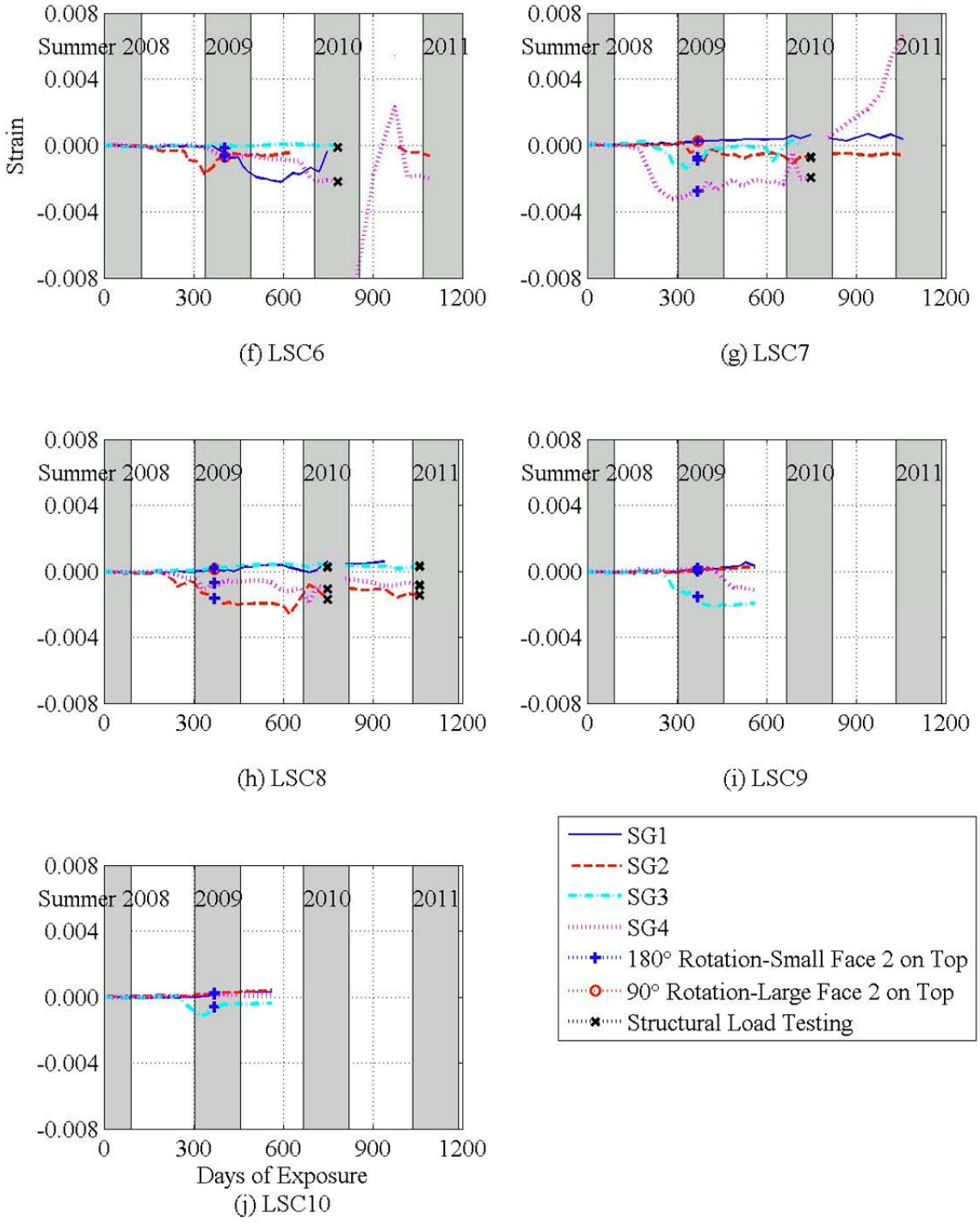

Figure 3-20. (Continued)

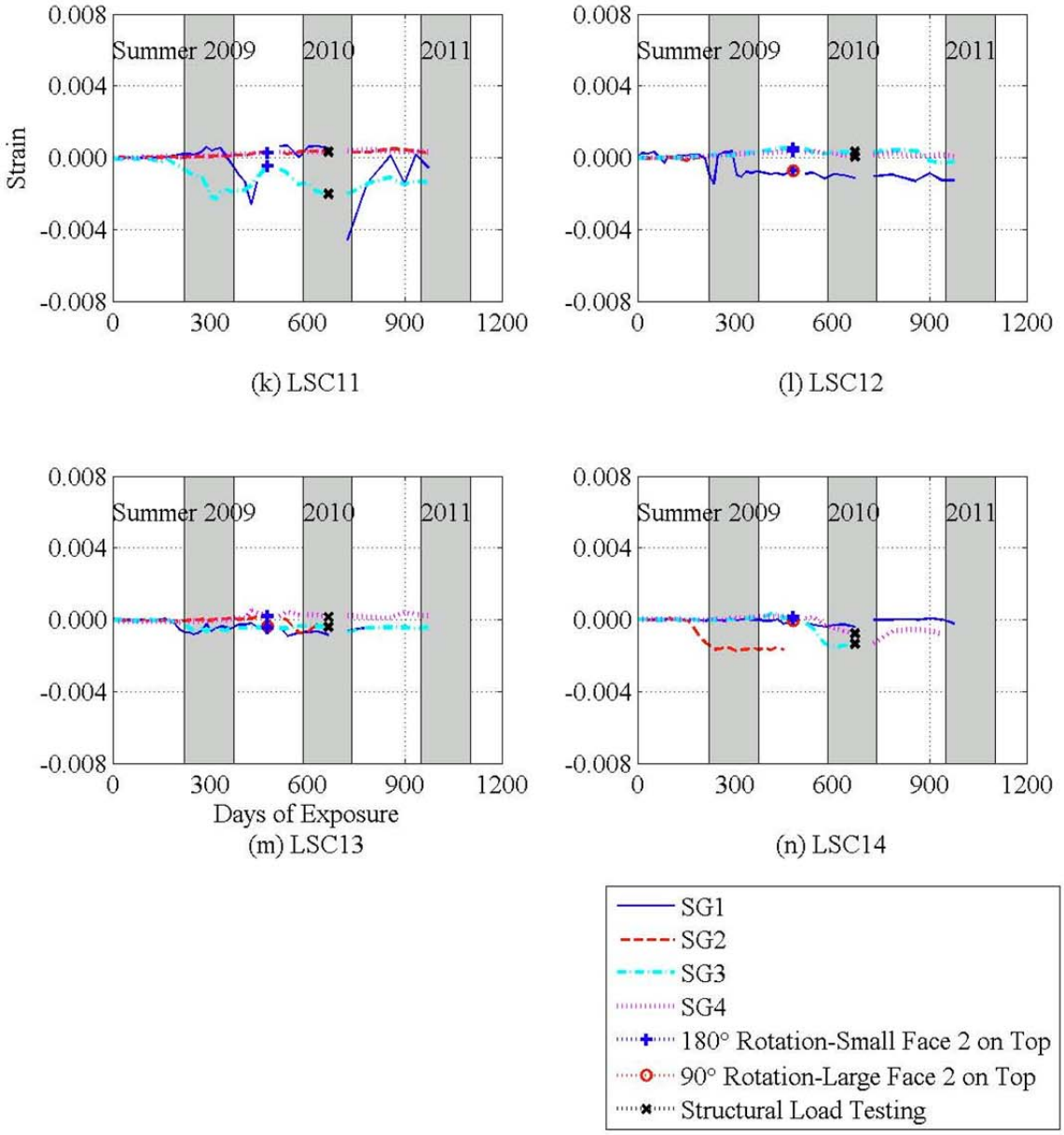

Figure 3-20. (Continued)

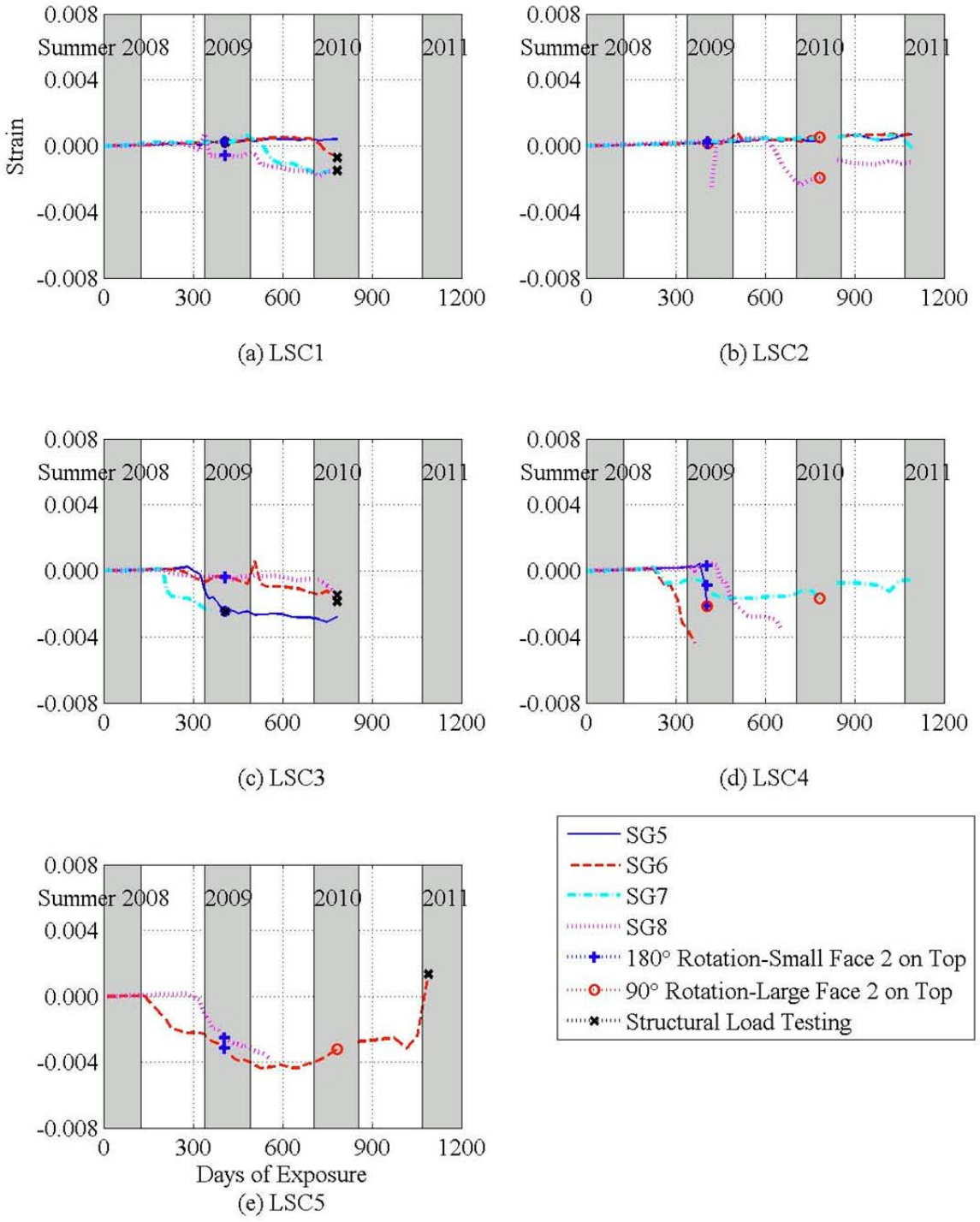

Figure 3-21. Internal Strain Gages (SG5-SG8) along Large Face 1 Tension Steel of the Splice Region.

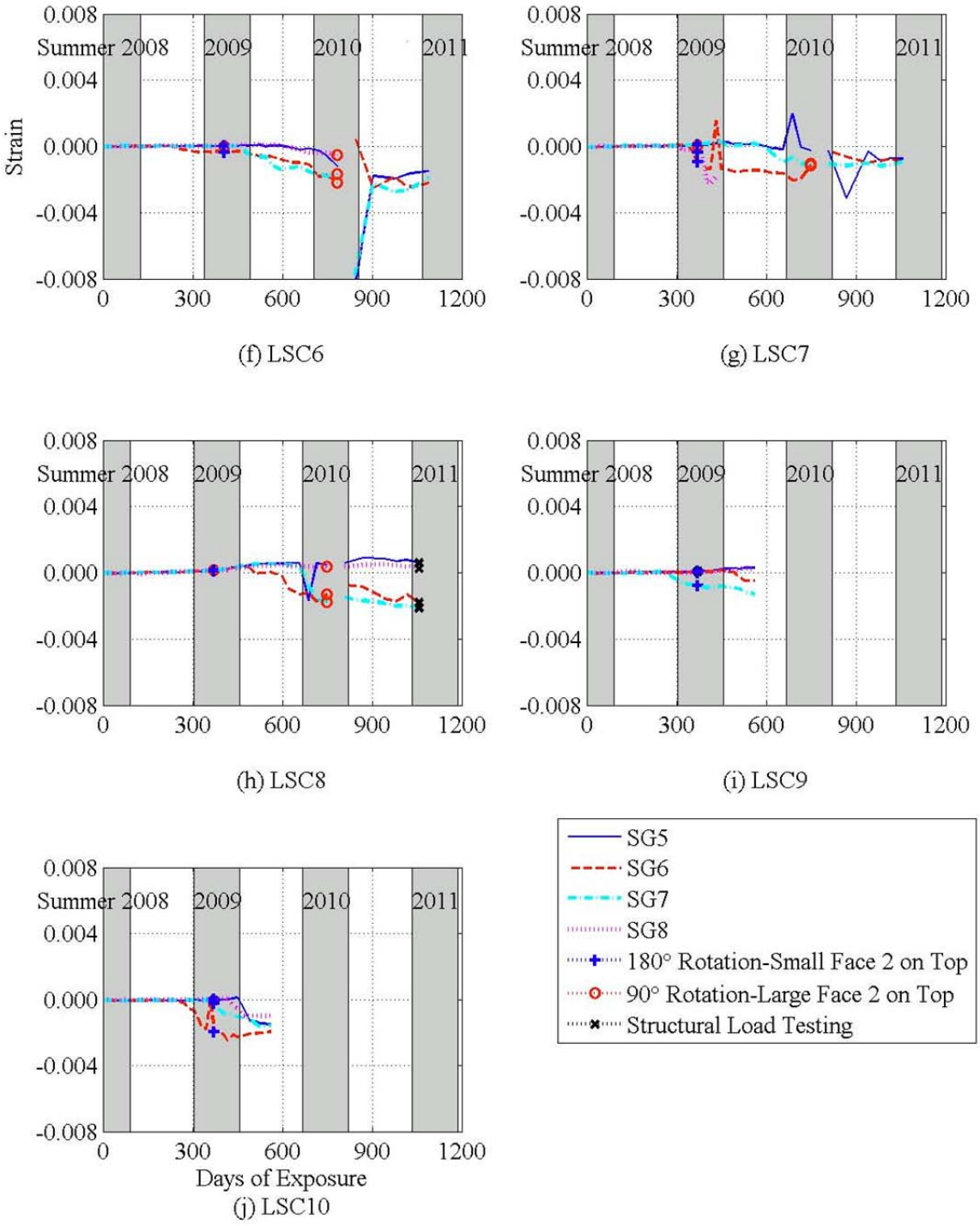

Figure 3-21. (Continued)

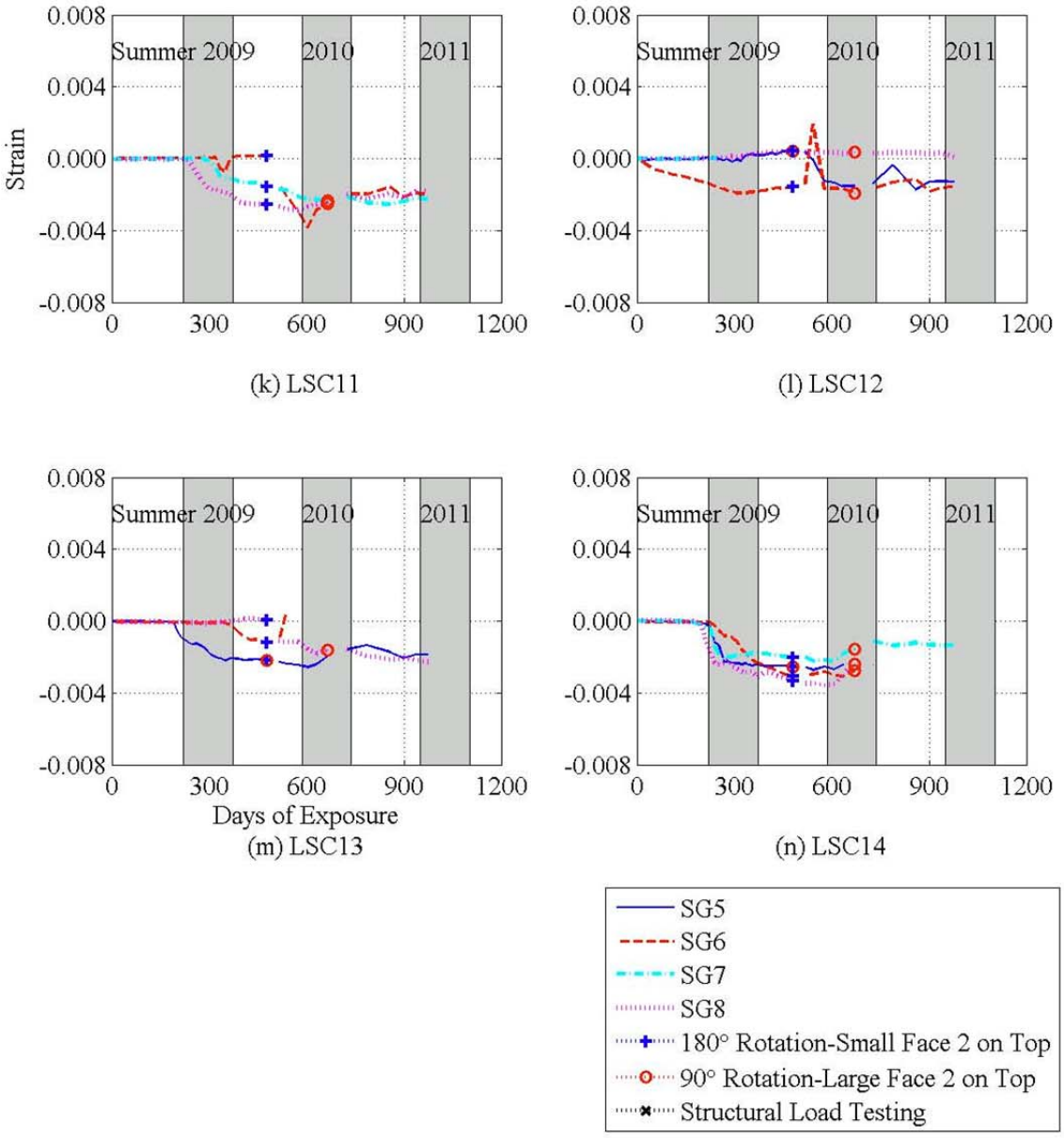

Figure 3-21. (Continued)

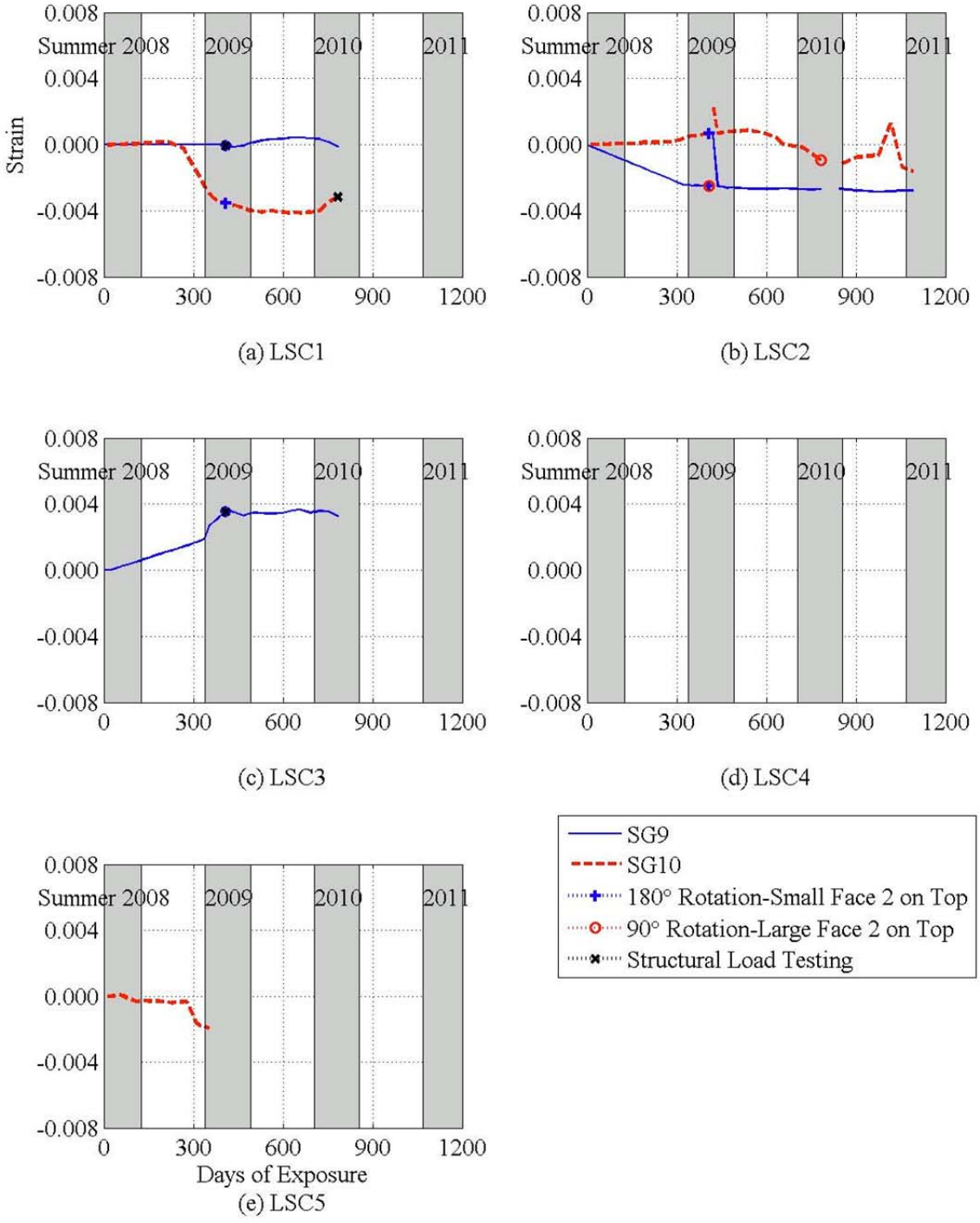

Figure 3-22. Internal Strain Gages (SG9-SG10) along Large Face 2 Compression Steel of the Splice Region.

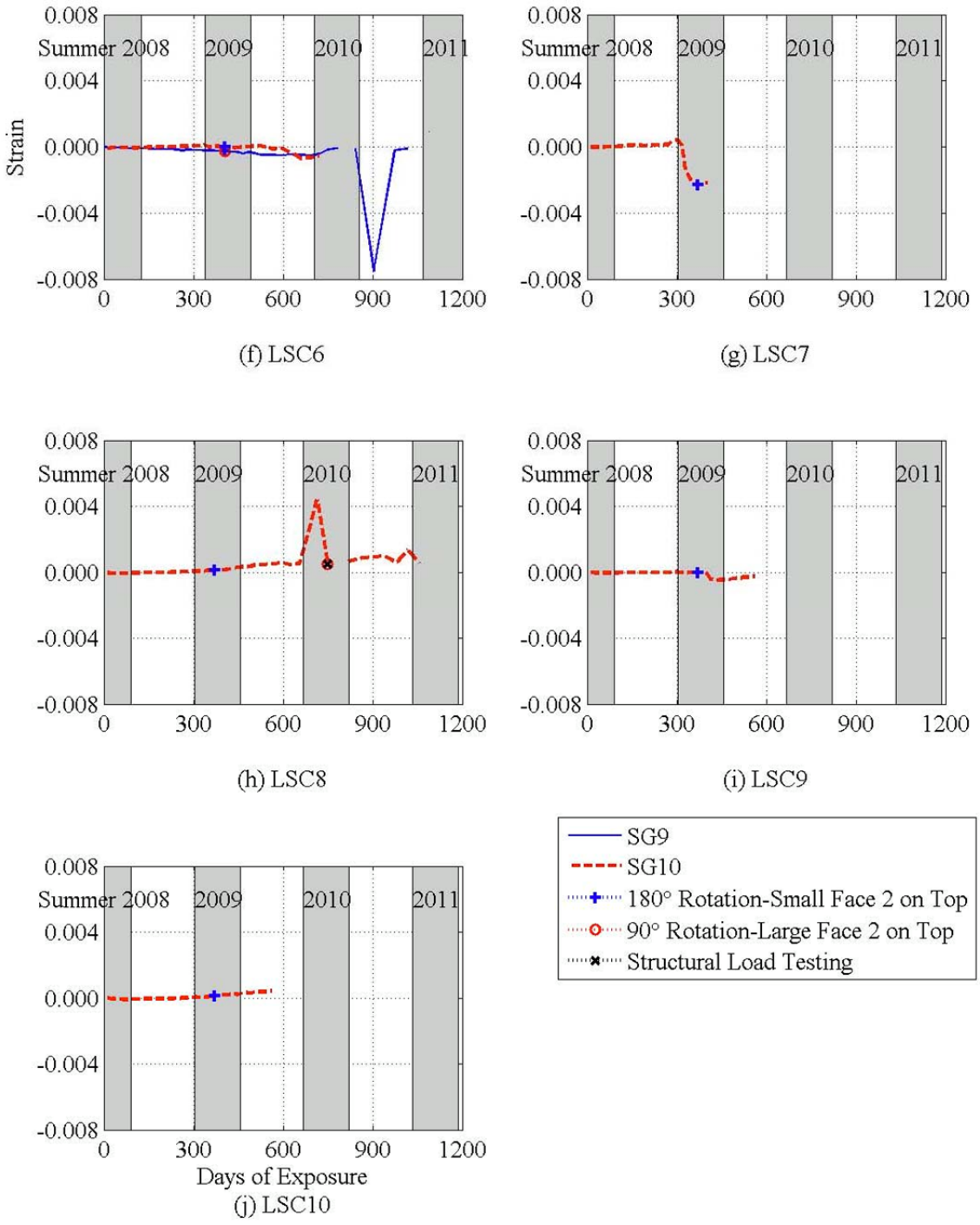

Figure 3-22. (Continued)

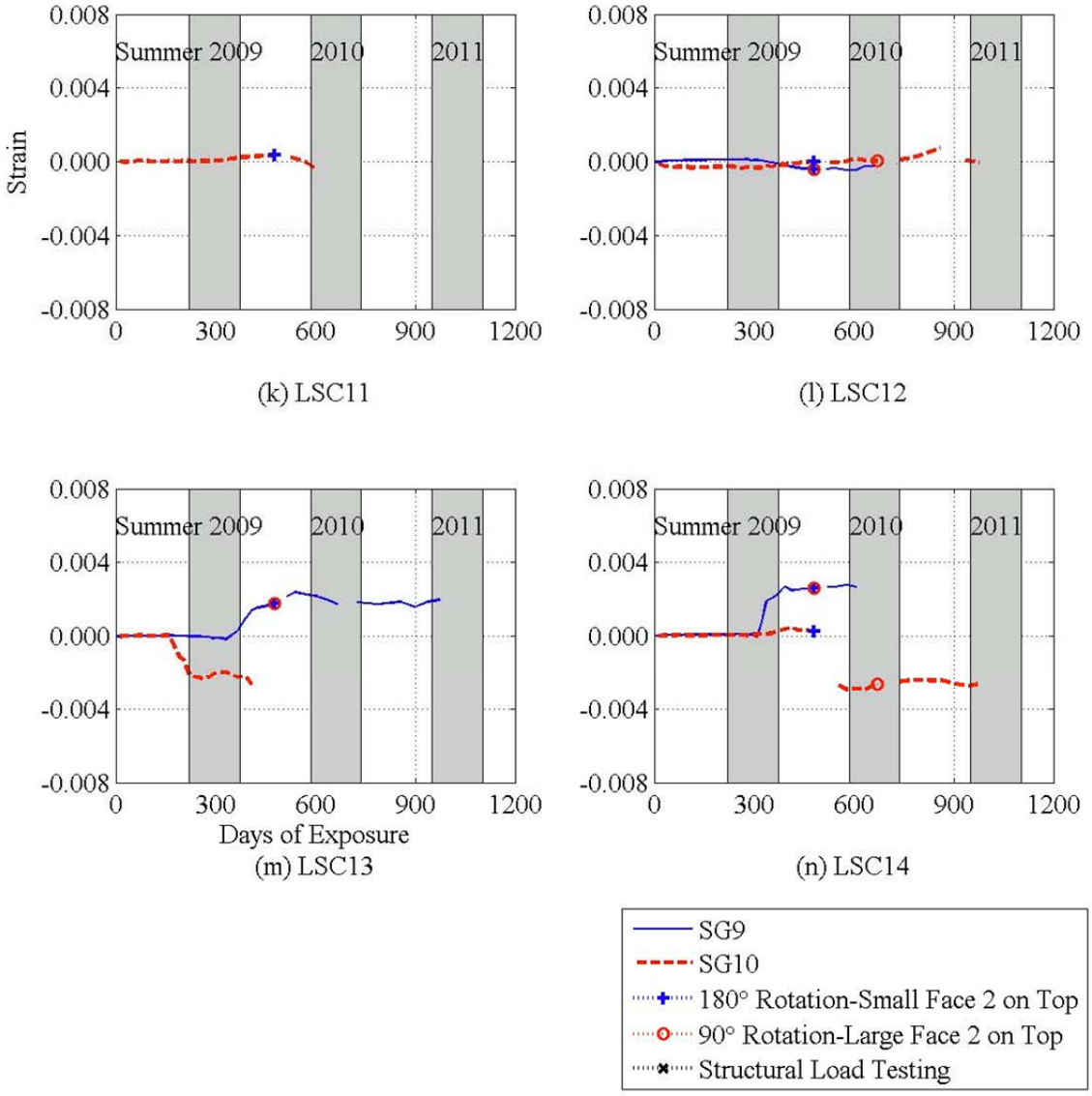

Figure 3-22. (Continued)

3.3.4 Comparison of Surface and Internal Strains

A comparison of the strains on the surface, inside the concrete cover, on the steel hoop, and the core concrete is shown in Figure 3-23 on the small faces. Figure 3-24 shows percentages of the surface strains calculated from the measured distance between DEMECs on the small faces. Figure 3-25 compares the surface and internal stains on the large faces. As expected, the cover concrete expanded more than the core concrete. This is shown in Figure 3-23 with data measured with KM1 and KM2. Since the internal gages were on Small Face 1, the percentages are only calculated for the time than the surface strain was calculation on Small Face 1 which is before the first rotation. At the time of the 180° rotation, the average percentage of the surface strain in the concrete cover, concrete core and steel rebar was 61%, 51%, and 40% on Small Face 1. This shows hoop strains were smaller than the concrete that was on either side of it (both in the concrete cover and core). Similar to the Small Faces, the cover concrete expanded more than the core concrete which is evident through the KM3 and KM4 gages. The average strain in the cover and core concrete at the time of the 180° rotation was 0.0020 and 0.0018. At the time of the 90° rotation, the average strains from the KM3 and KM4 gages were 0.0039 and 0.0036. Figure 3-26 shows the percentages of the surface strain on Large Face 1. The KM3 and KM4 average percentages of the surface strains on Large Face 1 was 63% and 55%, at the time of the 180° rotation. The percentages at the time of 90° rotation were 53% and 48%. The percentages lowered since the surface strain values increased at a faster rate than the cover and core concrete strains. The strain in the steel hoop differed on the Large Face 1 than Small Face 1 in that the strains were larger than the concrete on either side. The SG12 average percentages of the surface strain were 83% and 78% at the first two rotations. The steel on all faces started to yield around day 300 of exposure with strains above 0.002. Some of internal gages gave bad readings for a variety of possible reasons; therefore there are a few gaps in the information on the graphs.

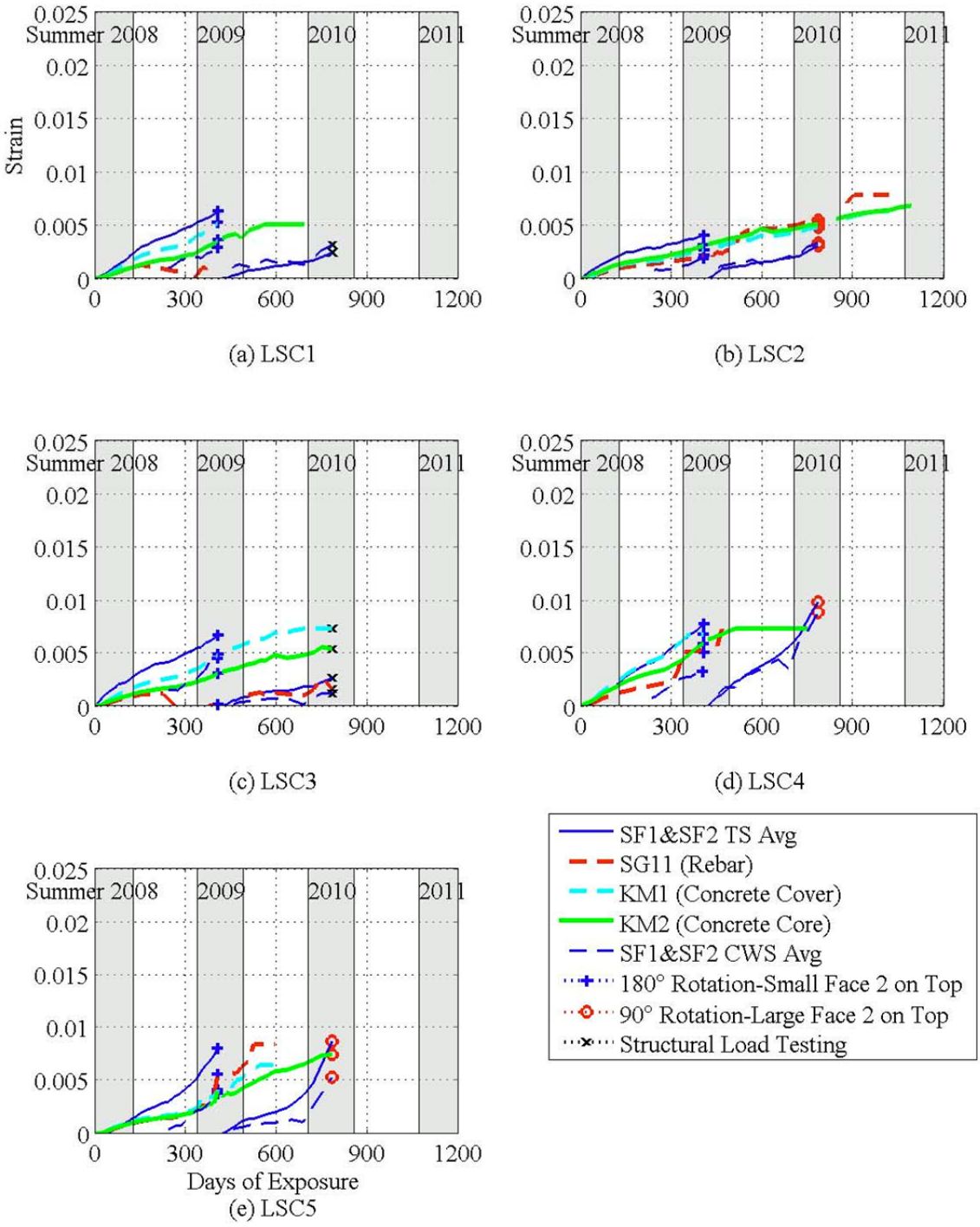

Figure 3-23. Internal and External Strain Measurements on and near the LSC Specimens' Small Face 1 and Small Face 2.

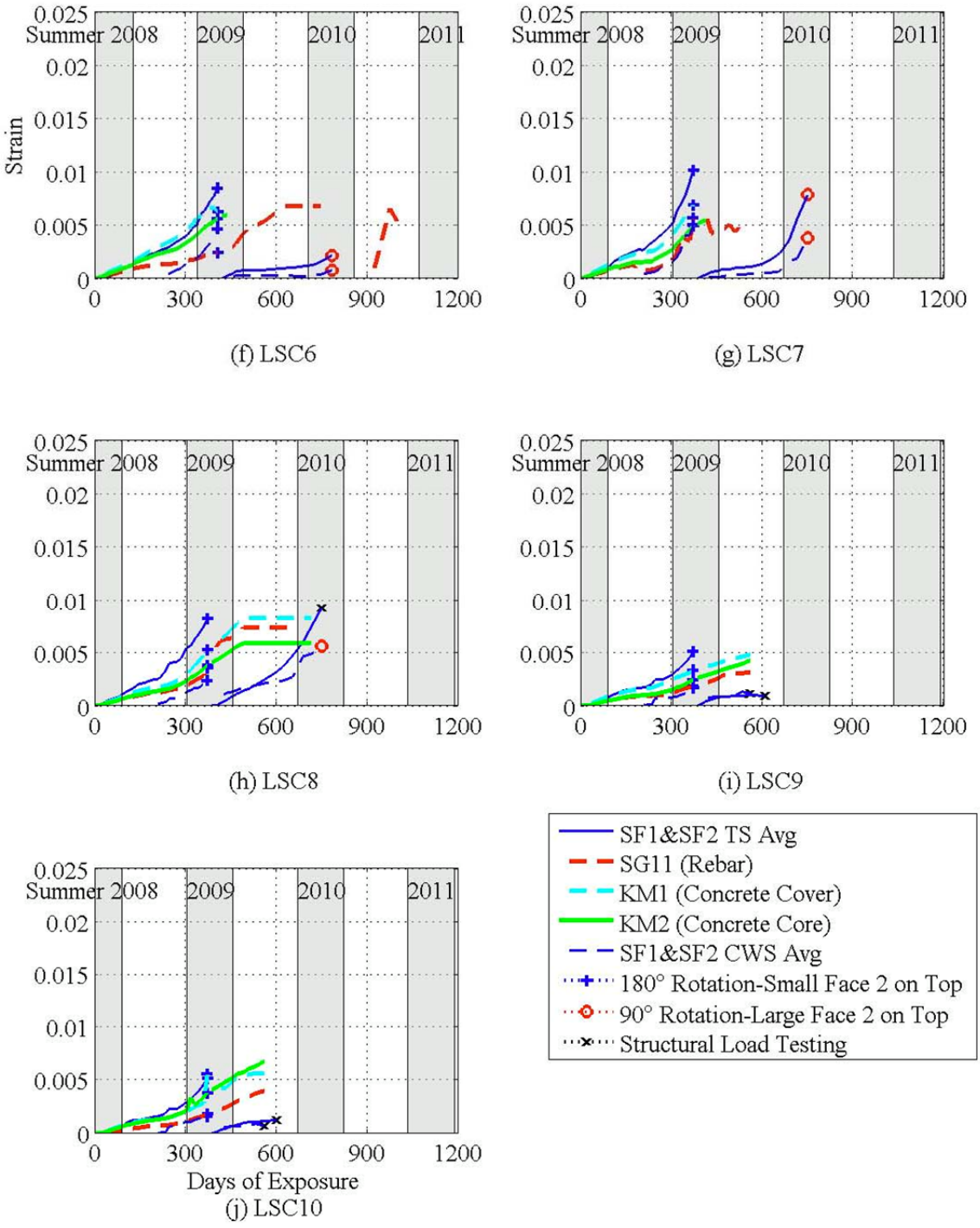

Figure 3-23. (Continued)

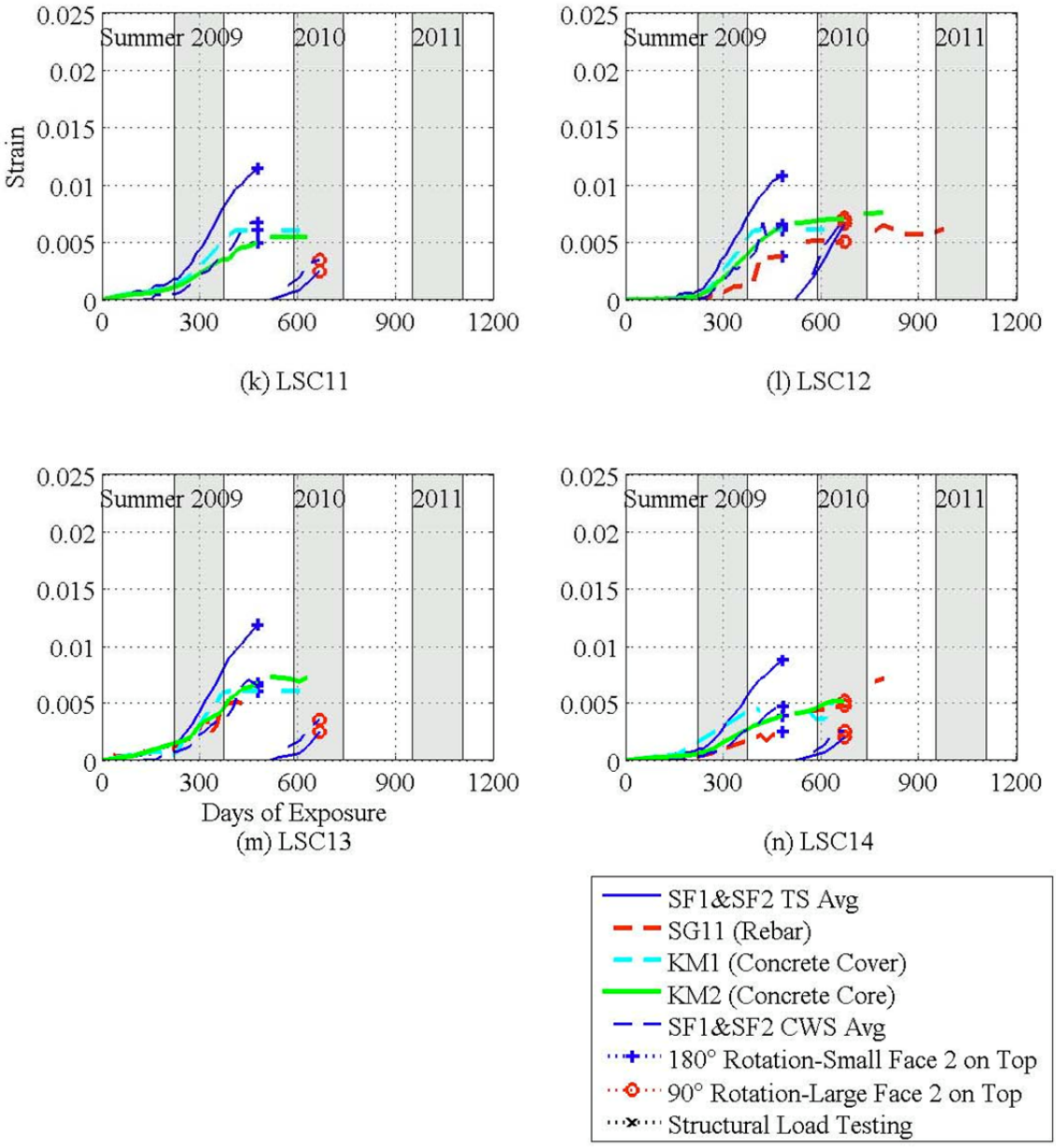

Figure 3-23. (Continued)

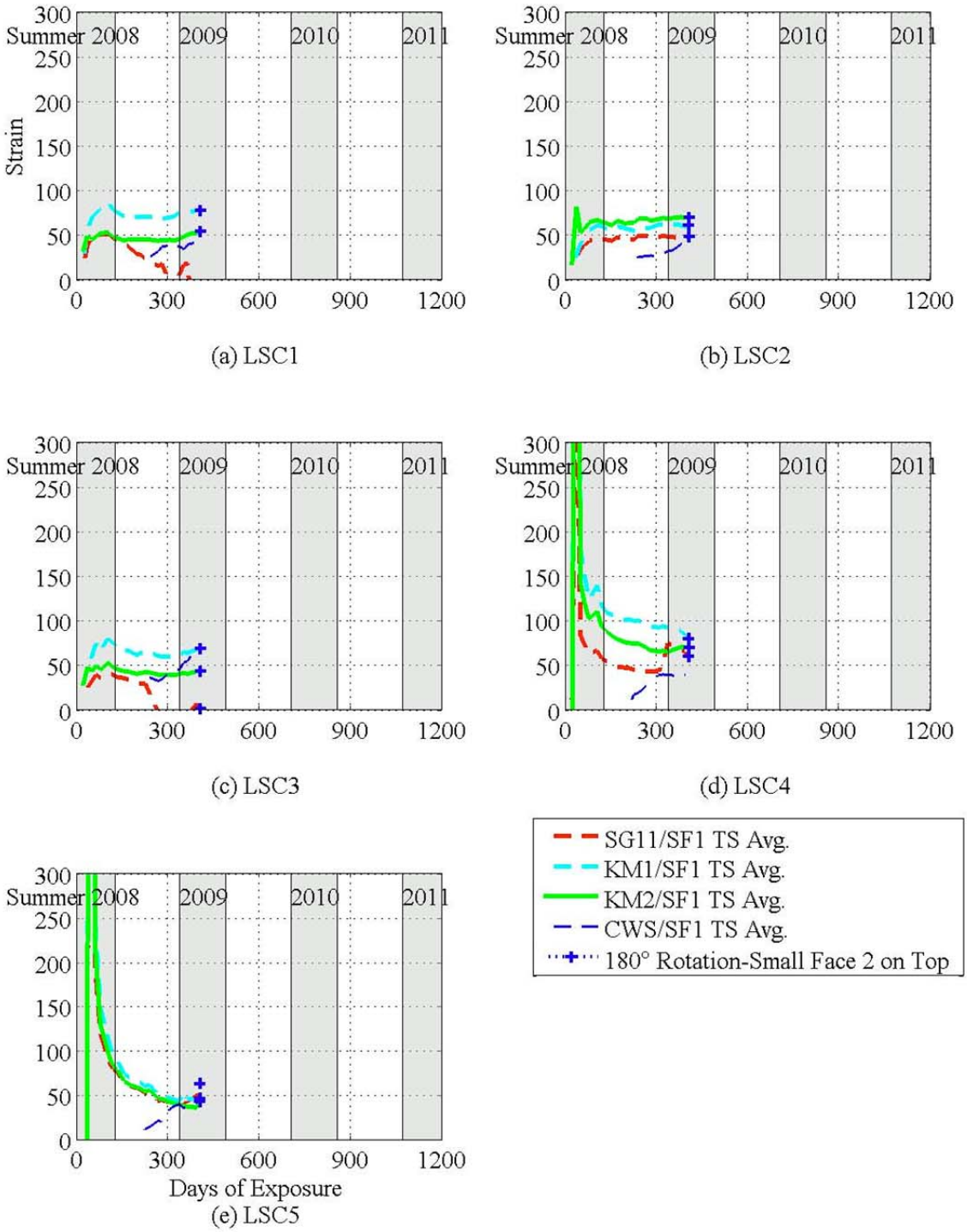

Figure 3-24. Percentages of Surface Strains on LSC Specimens' Small Face 1.

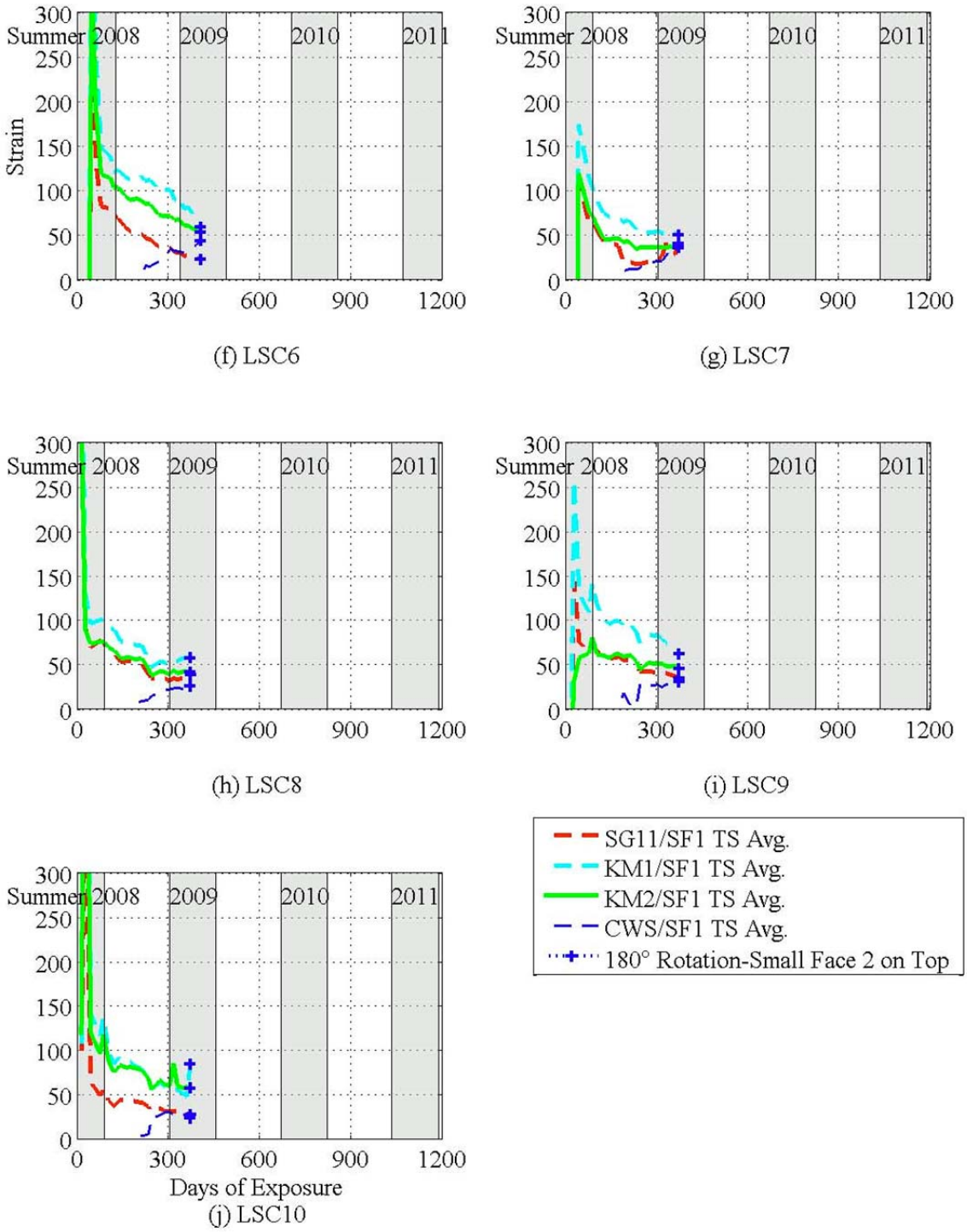

Figure 3-24. (Continued)

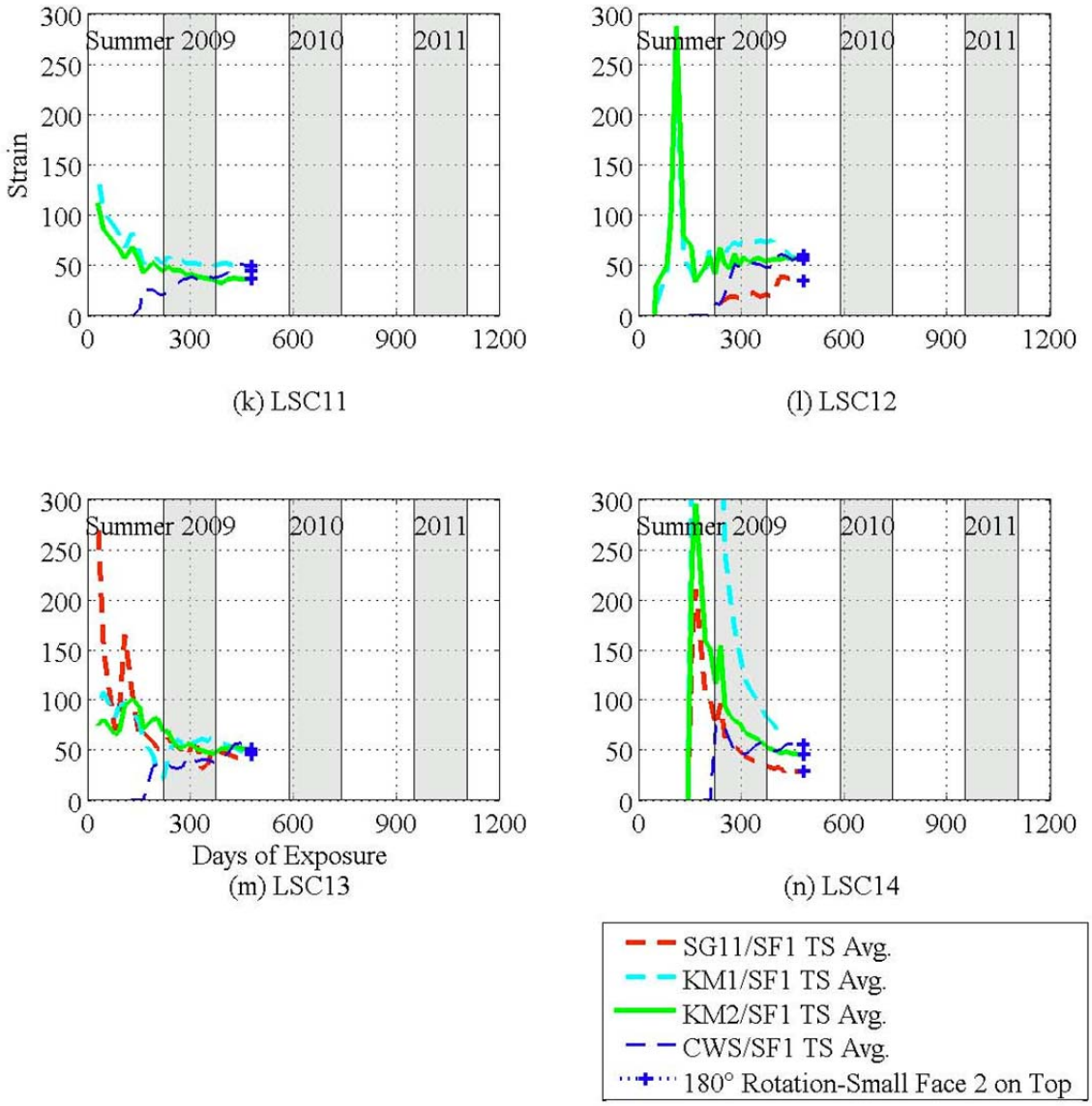

Figure 3-24. (Continued)

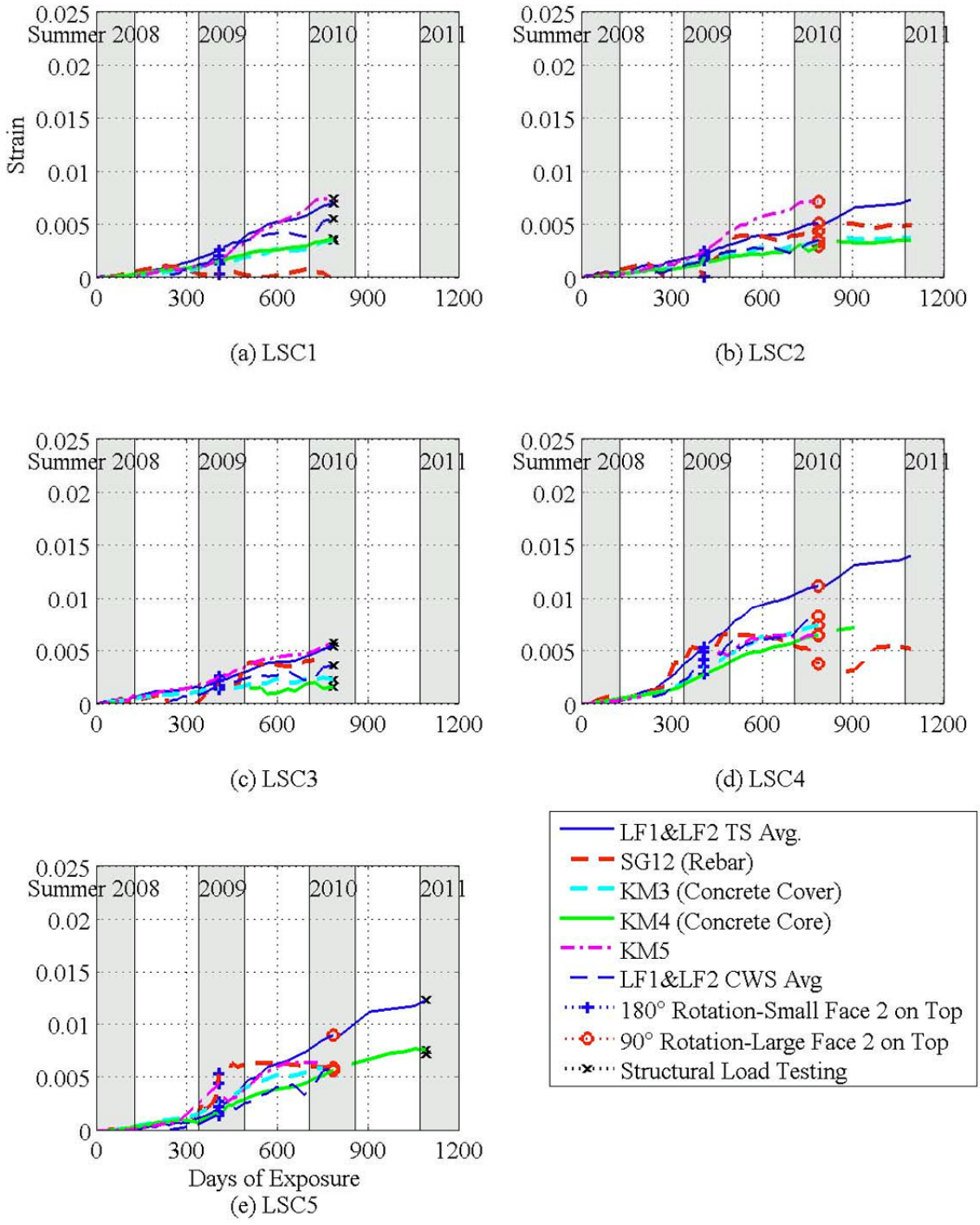

Figure 3-25. Internal and External Strain Measurements on and near the LSC Specimens' Large Face 1 and Large Face 2.

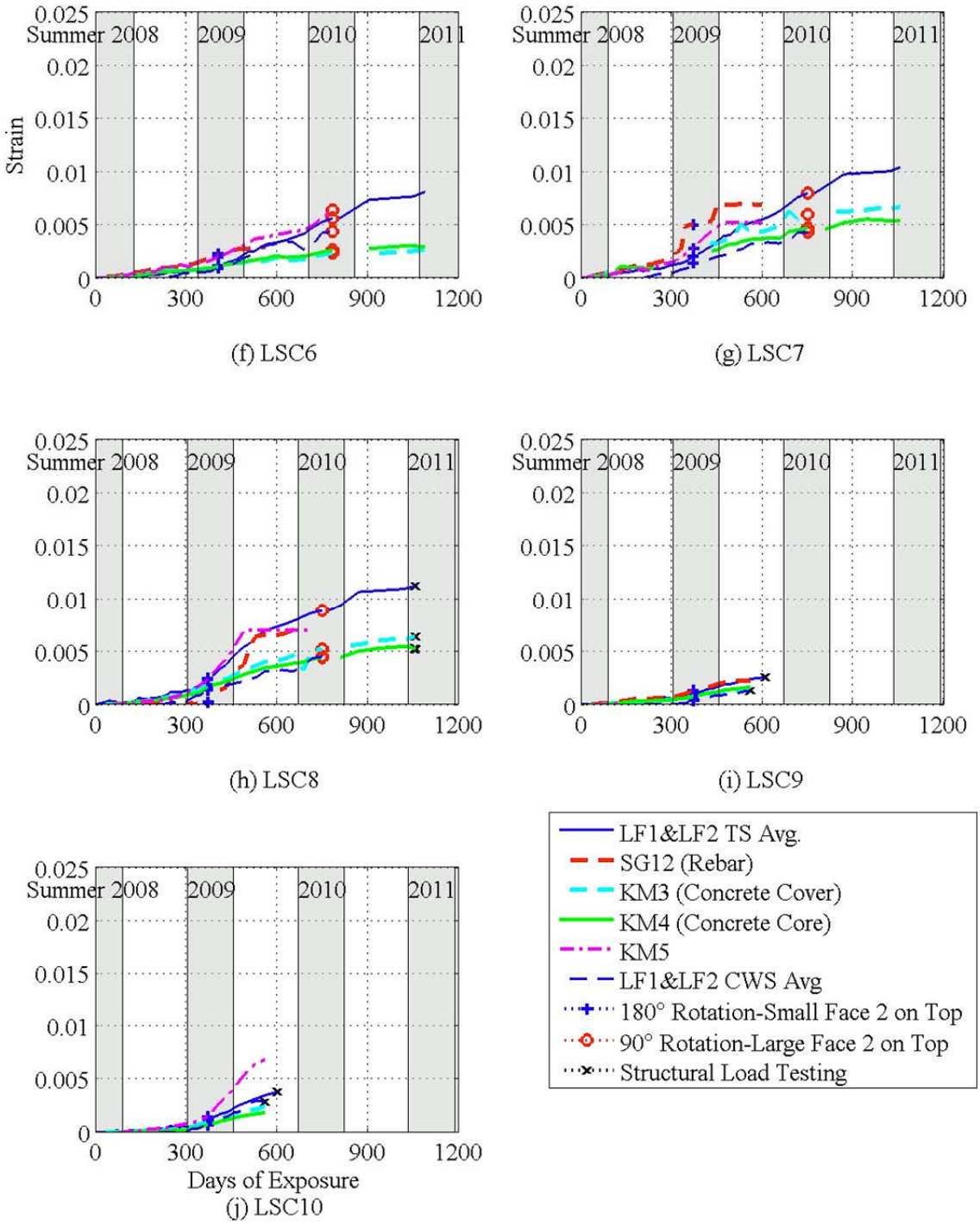

Figure 3-25. (Continued)

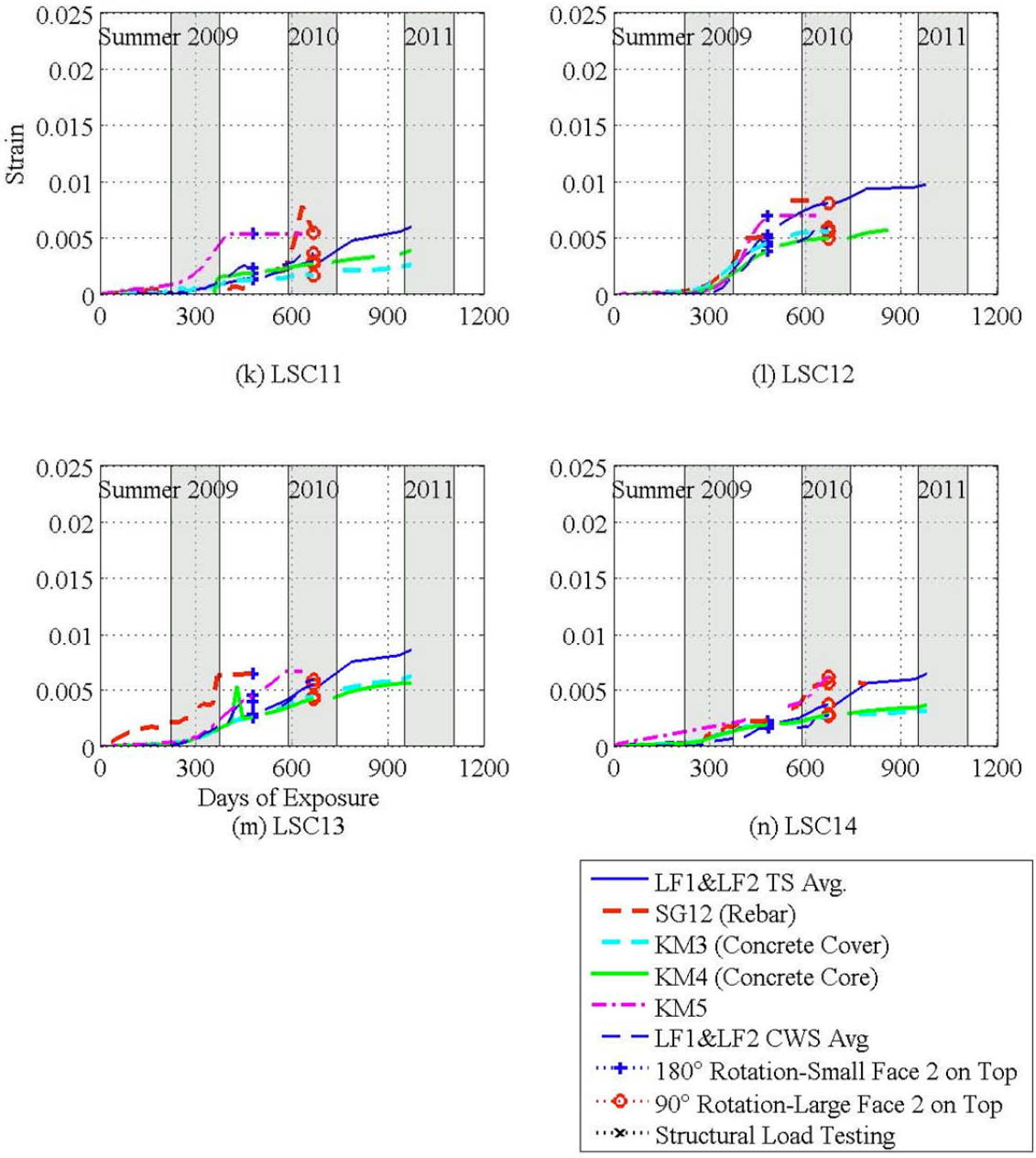

Figure 3-25. (Continued)

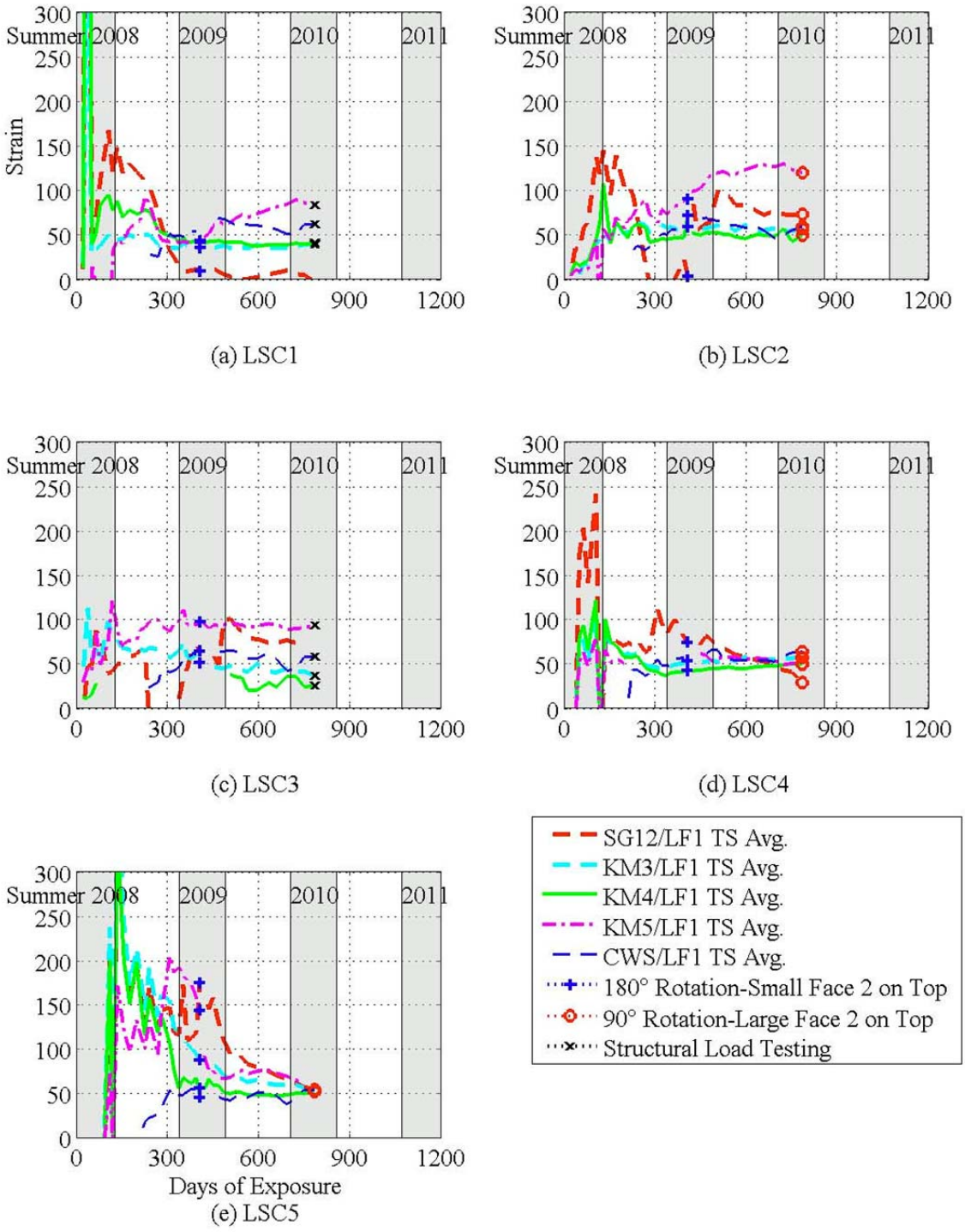

Figure 3-26. Percentages of Surface Strains on LSC Specimens' Large Face 1.

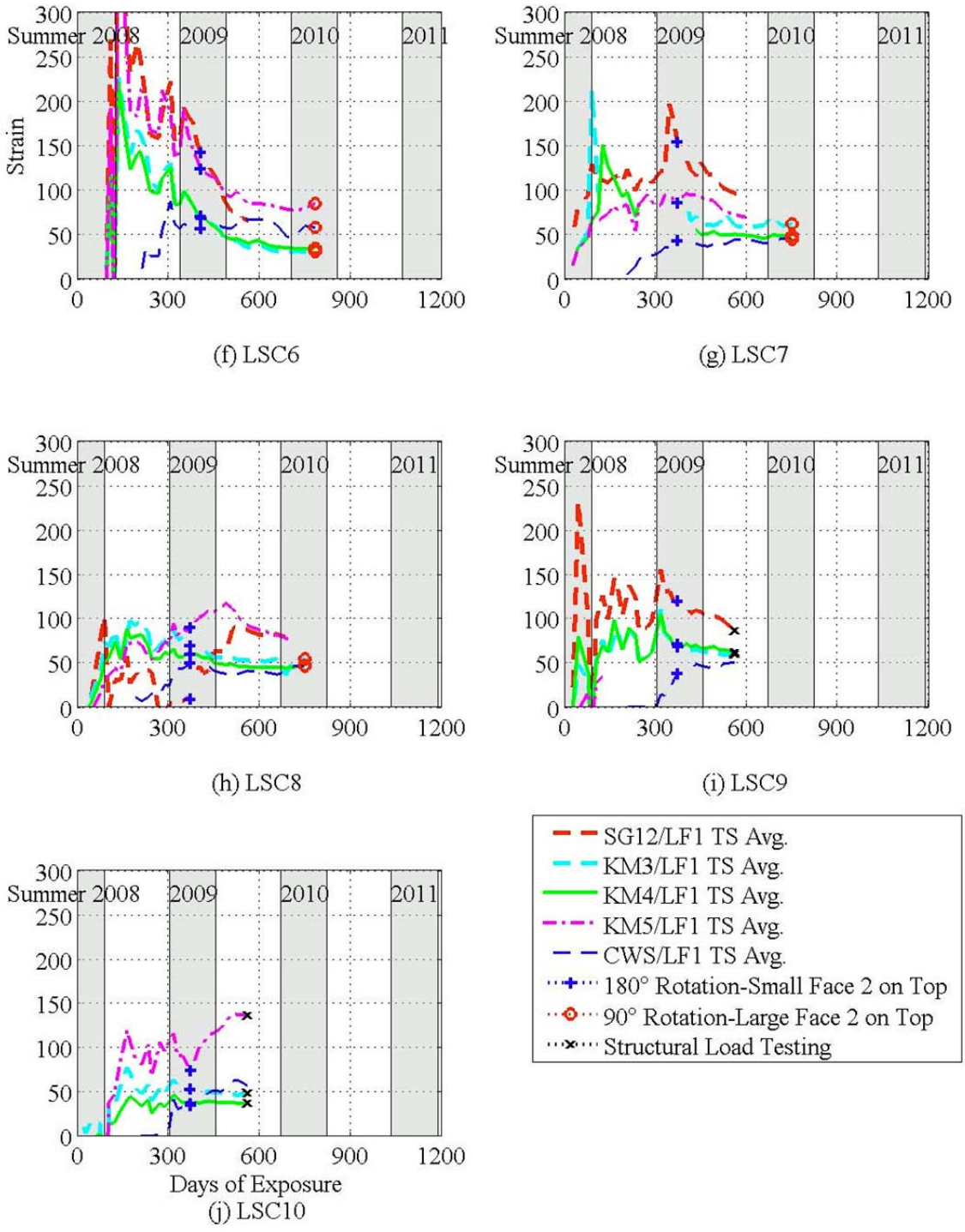

Figure 3-26. (Continued)

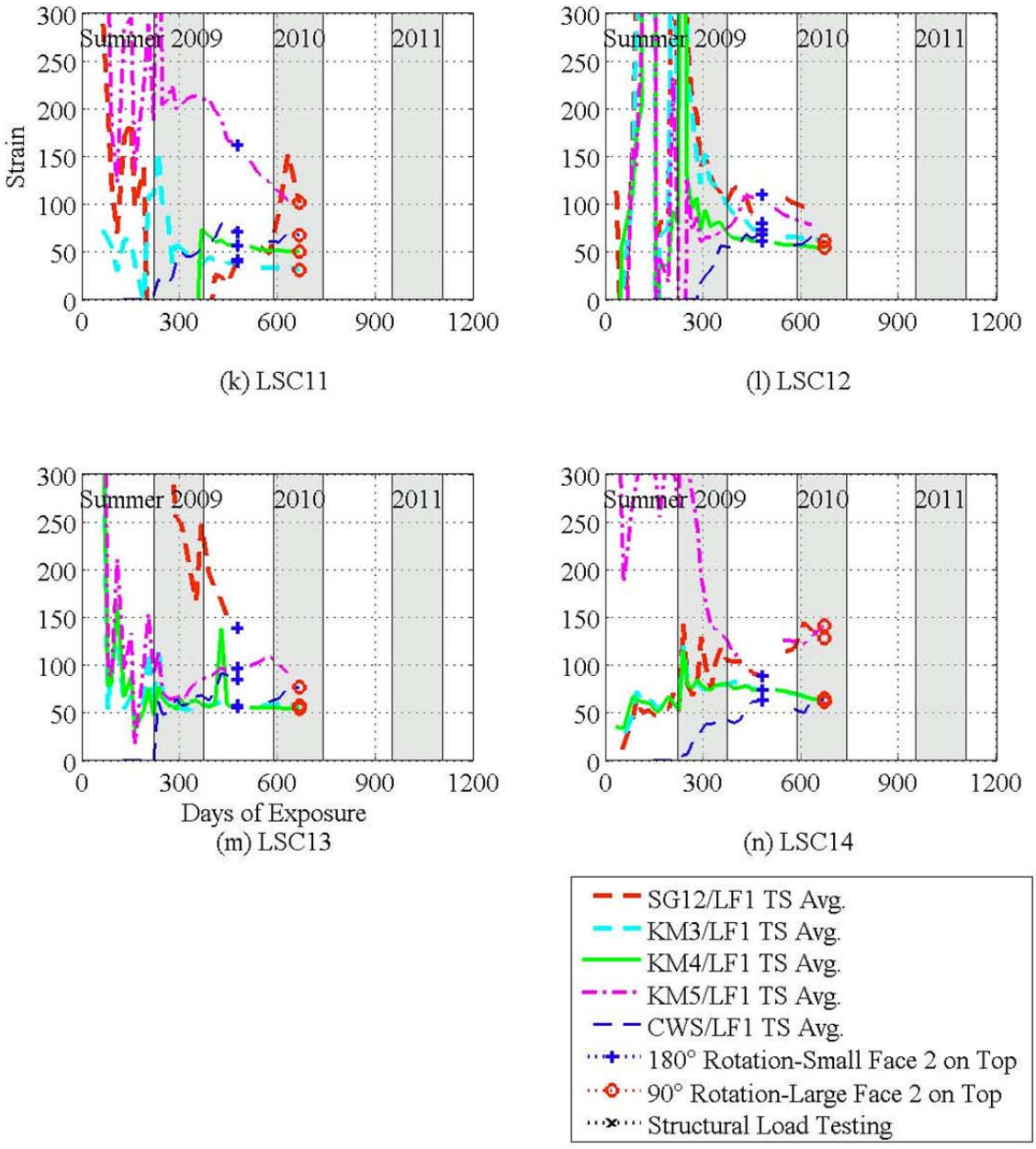

Figure 3-26. (Continued)

3.4 Summary and Conclusions

In summary, 14 large-scale specimens stored at the Riverside Campus were exposed to outdoor weather conditions in Bryan, TX and to wet-dry cycles using supplemental water to accelerate the ASR/DEF deterioration mechanisms. Internal instrumentation and external surface measurements were continually recorded for all specimens throughout the deterioration program. These measurements provided significant information about the expansion mechanism in the LSC specimens due to ASR and minimal DEF. The structural effects of this expansion on the column splice region of the LSC specimens are presented in Section 5.

From the information provided in this Section, it can be concluded that all specimens to date have successfully developed significant premature concrete deterioration due to ASR and minimal DEF in terms of concrete expansion and surface cracking that is representative of observations in in-service bridges. In addition, the deterioration mechanism is continuing. To develop more severe damage states, additional exposure time is required. Therefore, eight untested specimens continue to deteriorate at the Riverside Campus.

The following highlights some of the findings derived from the deterioration program to date:

- The direct sunlight on the specimens made a large impact on the expansion due to ASR and minimal DEF. The surface strain at the top of Large Face 1 (LF1 TS1) only reached 61% of the transverse strain on the top surface (Small Face 1) and an average of the other transverse strains on Large Face 1 (LF1 TS2, LF1 TS3, LF1 TS4, and LF1 TS5) only reached 22% of the transverse strain on Small Face 1 before the first rotation.

- The LSC specimens expanded at a higher strain rate during the summer months (May through September). The increase in the average strain/month on Small Face 1 was calculated to measure this. The rate of increase was different for the three groups of specimens first exposed to the high temperatures and supplemental water at different times, May, July, and September. The strain rate on the first six specimens, which were exposed during all of the summer of 2008, was 1.7 times as large during the summer of 2009 than the non-summer months of 2008 and 2009. The next four LSC specimens were only exposed during half of the 2008 summer. The average strain rate of the transverse strain on the top, Small Face 1, was 2.7 times as large during the summer of 2009 than the non-summer months. The last four specimens were not exposed to the environmental conditions during any of the summer in 2008. The strain rate increase during the first summer months on these LSC specimens was 6.5 of that during the initial strain rate prior to the summer months.

- The transverse surface strains were about 10 times larger than the longitudinal surface strains due to the longitudinal restraint from the axial post-tensioning steel and longitudinal column reinforcement and the transverse tension field induced by Poisson's effect under post-tensioning.

- The average strains calculated from measuring the sum of the crack widths between DEMEC points were about 50% of the surface strains calculated from measuring the distance between DEMEC points.

- The measured strains were larger on the surface than inside the specimen with the strain in the cover reaching about 58% and the strain in the core concrete reaching about 52% of the surface strain. These percentages are an average of the values found on Small Face 1 and Large Face 1. The strain on the steel hoop in the middle of the splice region had very different values on the Small and Large Face with

strains of 0.0036 and 0.0054 on Small Face 1 and Large Face 1, respectively. The hoop strain percentage of the surface strain was 40% on Small Face 1 at the time of the first rotation. The Large Face 1 hoop strain percentages of the surface strain were 83% and 78% at the first two rotations.

- Using measured internal and external concrete expansion data throughout the deterioration program, measured crack widths and lengths throughout the deterioration program, and from petrography analysis of concrete cores taken from the specimens after they were structural tested, the three groups of tested specimens were categorized as having varying levels of primarily ASR deterioration ranging from none to late stage and none/minimal levels of DEF.

4. ANALYSIS OF COLUMN SPLICE REGION

4.1 Introduction

An analytical model was developed to predict the behavior of the specimens during the structural load tests. This prediction was necessary to determine the load used during the load tests. The model will be refined after comparison of the experimental test results from the two undamaged control specimens and the varying degrees of damage from six deteriorated specimens with ASR/DEF deterioration.

4.2 Analytical – Model for Capacity Analysis Using Flexure Theory

4.2.1 Modeling Assumptions

The bending theory assumptions made for compatibility are that plane sections remain plane and the reinforcing steel is bonded to the concrete; therefore, the strains in the reinforcing steel and the surrounding concrete are equal. In accordance with Hooke's Law, the stresses and strains in the concrete and steel were assumed to perform linearly in the elastic region then perfectly plastic. The concrete was assumed to first crack when the largest tensile stress in the concrete reached the modulus of rupture according to ACI 318 (2008). After this first crack, it was assumed the concrete in tension provided no strength. The concrete in compression was assumed to crush when the largest compressive strain reached 0.003 (ε_{cu}) as specified by AASHTO LRFD (2010) and ACI 318 (2008). The spliced reinforcing bars are assumed to increase strength linearly from zero to full strength for a distance determined from development length calculations.

4.2.2 Splice Capacity Model

The capacity of the reinforced concrete column was developed from using flexural bending theory, the assumptions stated in section 4.2.1, and equilibrium of the forces and moments. Figure 4-1 shows the strains, stresses, and resultant forces of structural flexural capacity for the three different limit states as follows:

(1) at first crack in the concrete,
(2) when the tensile reinforcing steel first yields, and
(3) at ultimate when governed by crushing of the concrete in compression.

The height (h) and width (b) of the section are shown in the figure with the depth of the tension (d) compression (d') steel. The depth of the neutral axis is c, and a is the depth of Whitney's stress block. The strains in the concrete (ε_c), tension steel, (ε_s), and compression steel (ε'_s) are shown with the stresses from those strains, concrete (f_c), tension steel (f_s), and compression steel (f'_s) are also shown. The tensile stress in the concrete (f_r) is present until first cracking of the concrete. The resultant forces are found from the stresses from the concrete in compression (C_c), concrete in tension (T_c), tension steel (T_s), and compression steel (C'_s). The axial load from the PT strands representative of in-service loading was accounted for in the flexural capacity, thus shifting the neutral axis down and creating a larger compression region. The scale for the figure is not consistent due to the drastic difference in values. Therefore, the strains and stresses at first cracking are illustrated twice as large as they would with the same scale used with the other two limits. The large stress from the steel is illustrated at 75% the scale of the concrete stress.

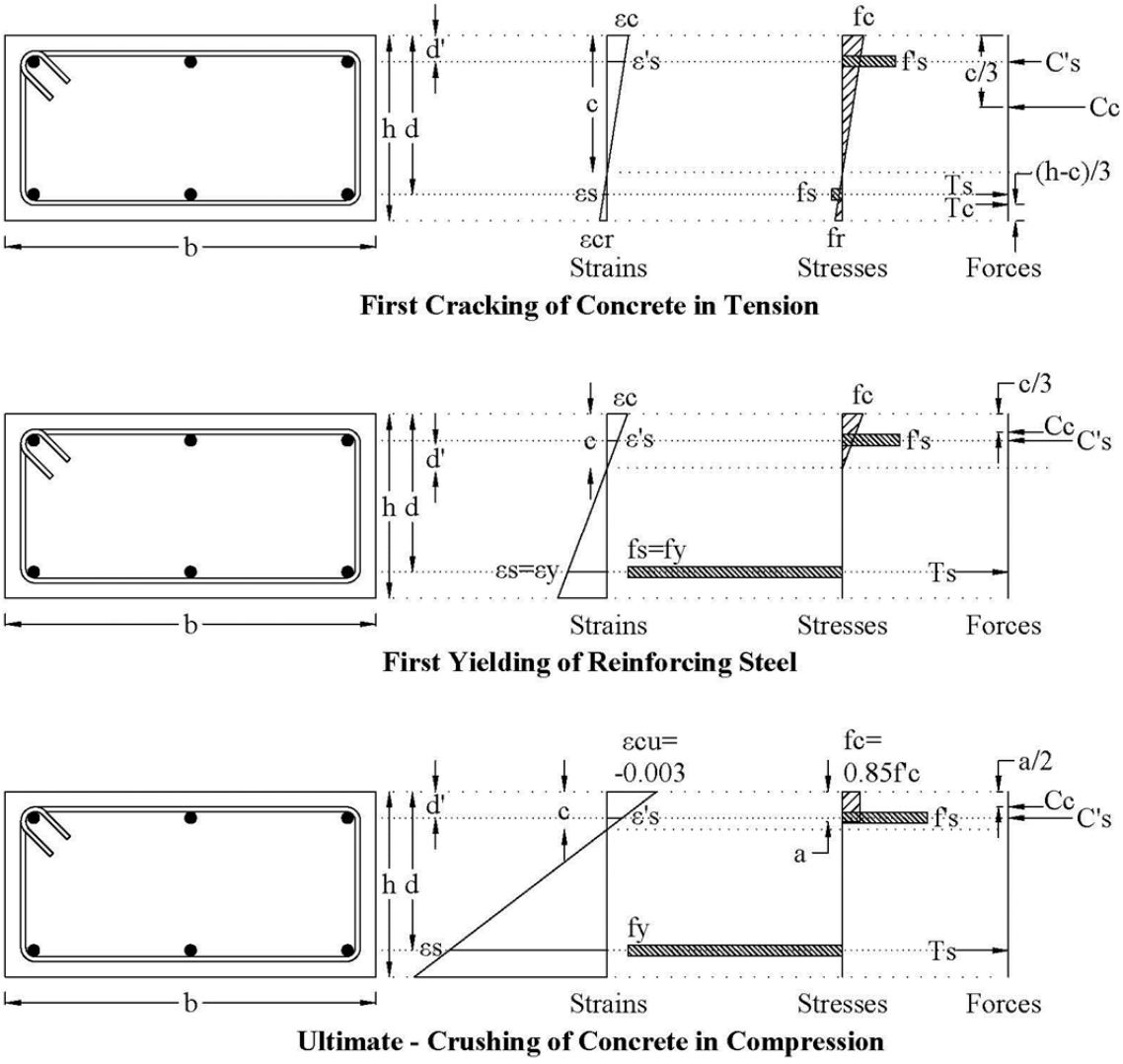

Figure 4-1. Strains, Stresses and Resultant Forces at Three Flexural Limits.

Up to first cracking of the concrete, the entire section contributes to resisting the external load. The limiting criterion is based upon the ability of the concrete to resist tensile loads. The tensile stress in concrete or rupture modulus, f_r, is usually calculated as a function of the 28-day cylinder compressive strength, f'_c. Eq. 4-1 shows the equation for f_r at first cracking according to ACI 318 (2008). AASHTO (2010) lists 0.24 as the coefficient to account for the different units (ksi). For a f'_c of 5000 psi, the ACI 318

gives a value of 530 psi and the ASSHTO gives a value of 537 psi. Note that these equations are only good for the units listed.

$$f_r = 7.5\sqrt{f'_c} \quad \text{(Eq. 4-1)}$$

Eq. 4-2 shows the modulus of elasticity (E_c in psi) for the normal weight concrete (ACI318-08). Once again AASHTO gives a similar value with slight differences in the coefficient from the unit difference.

$$E_c = 57000\sqrt{f'_c} \quad \text{(Eq. 4-2)}$$

Given the concrete tensile stress and the modulus of elasticity, the tensile strain at the bottom of the concrete at first cracking can be calculated as follows:

$$\varepsilon_{cr} = \frac{f_r}{E_c} \quad \text{(Eq. 4-3)}$$

For the second limit state where the tension reinforcement first yields at the stress of f_y, the strain in the reinforcing steel is found from Hooke's Law as:

$$\varepsilon_{sy} = \frac{f_y}{E_s} \quad \text{(Eq. 4-4)}$$

At the ultimate limit state, the concrete crushes in compression when the strain is -0.003 (ε_{cu}) (ACI 318-08 and AASHTO 2010). The compression strains are negative for the sign convention used in this report.

The analytical model is developed so that it can be used at any cross section of the column specimen. First, the area of the steel reinforcement within the splice region is calculated. Since the bars are spliced, the simple multiplication of the number of bars times the area of each bar is not sufficient. The development length for the spliced bar is first calculated and used to find the effective area of the steel at each section. The number and location of the bars is first discussed, then the application of the development length.

Figure 4-2 shows an elevation view of the reinforcement in the LSC specimens. The stirrups are not shown for clarity. Figure 4-3 shows the cross section of the LSC specimens in the splice region. The splice bars, illustrated as solid circles in the cross section views, are located in the splice region and the end region. The straight bars, illustrated as open circles, are only located in the end region (Figure 4-4). Figure 4-5 illustrates where the splice and straight bars begin and end. Note that Figure 4-5 depicts that the splice and straight bars are on top of each other to clearly distinguish between bars. Figure 4-3 and Figure 4-4 properly illustrate these bars are side by side. The longitudinal bars are #11's; these bars are spliced with three more #11 bars both on the top (compression) and bottom (tension) during the four-point load test. The straight bars were placed in the specimen to enhance the specimen strength away from the splice region. However, these bars do not contribute toward the specimen's strength in the splice region. A more thorough description of the reinforcement including the stirrups is provided in section 2 and Bracci et al. (2011).

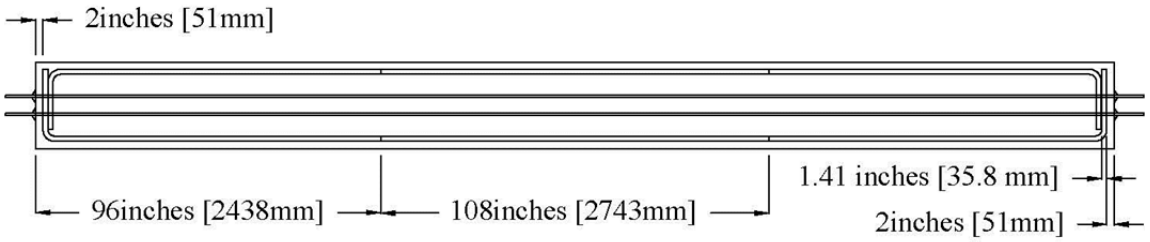

Figure 4-2. Reinforcement Elevation View

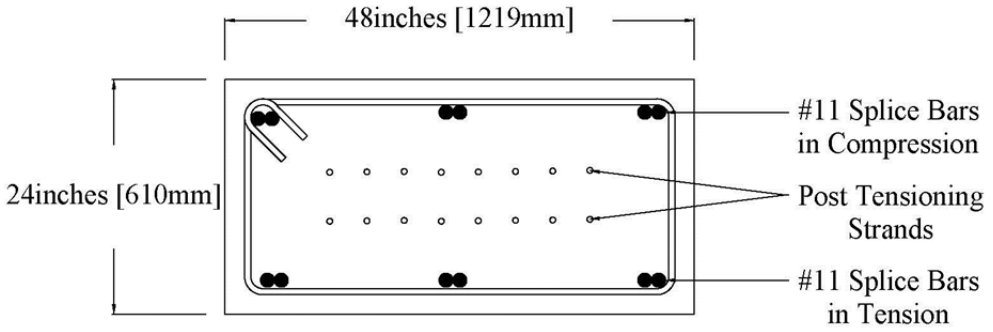

Figure 4-3. Cross Section at Splice Region [taken from Alberson (2009)].

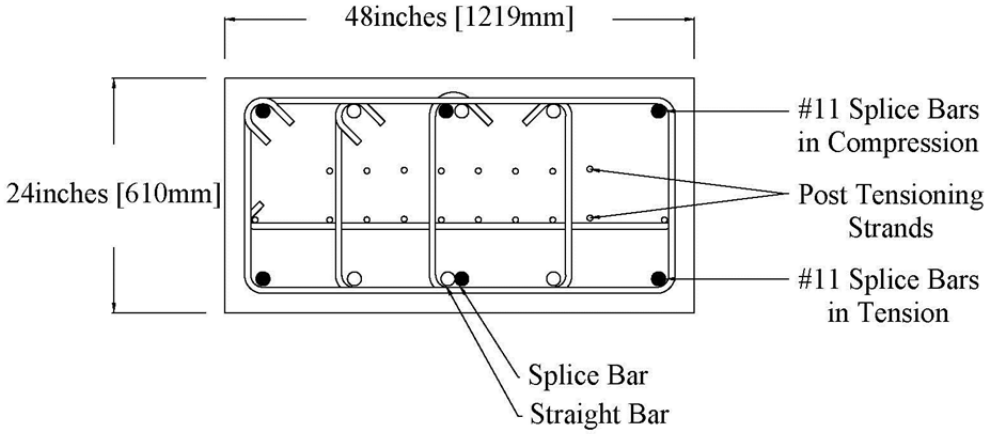

Figure 4-4. Cross Section End Region [taken from Alberson (2009)].

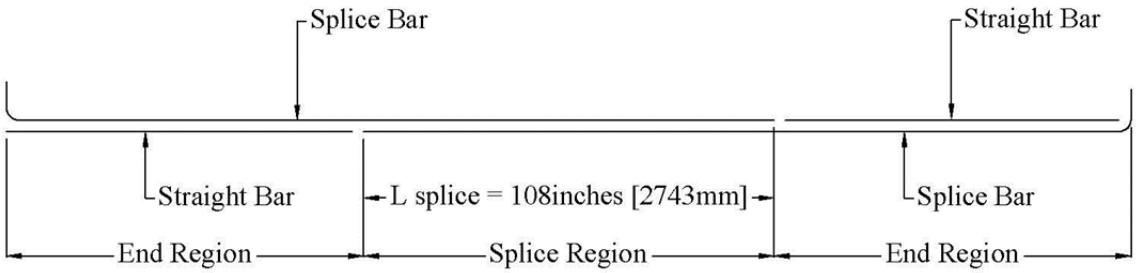

Figure 4-5. Longitudinal Section of Tension Reinforcing Steel [taken from Alberson (2009)].

The development length for reinforcing steel in tension (L_d) is given by AASHTO (2010) as:

$$L_d = \frac{1.25 A_b f_y}{\sqrt{f'_c}} \text{ but not less than } 0.4 d_b f_y \qquad \text{(Eq. 4-5)}$$

where A_b is the area of the steel bar (inches^2) and d_b is the diameter of the steel bar (inches).

The development length for reinforcing steel in compression (L_{dc}) is given below (AASHTO 2010) as:

$$L_{dc} \geq \frac{0.63 d_b f_y}{\sqrt{f'_c}} \text{ or } 0.3 d_b f_y \qquad \text{(Eq. 4-6)}$$

The development length for a hooked bar with a f_y greater than or equal to 60 ksi (414 MPa) is given by AASHTO (2010) as:

$$L_{dh} = \frac{38.0 d_b}{\sqrt{f'_c}} \frac{f_y}{60} \qquad \text{(Eq. 4-7)}$$

These development length calculations were used in conjunction with the reinforcement layout to find the effective steel area at the critical sections, and thus the capacity at those sections. The effective area is found assuming the steel has no contribution at the bar end and linearly increases in contribution up to the development length of the bar, where it then has full contribution (A_b). Figure 4-6 shows the linear increase in the effective bar area at the splice region. The length of the splice, L_{splice} is 108 inches (2743) and x_{splice} the distance from the splice end to the section in question. Figure 4-7 shows the linear increase in the effective bar area at the end region. The length of the straight bar, $L_{straight\ bar}$, is 94 inches (2388 mm) which accounts for the 2 inch (50.8mm) cover and $x_{straight\ bar}$ is the distance from the end of the straight bar to a particular section. The splice bars are hooked at the end not in the splice (Figure 4-5). Therefore, in the splice region, these bars are called Splice Bar 1 and Splice Bar 2 and in the end region, they are referred to as the Hooked Bar.

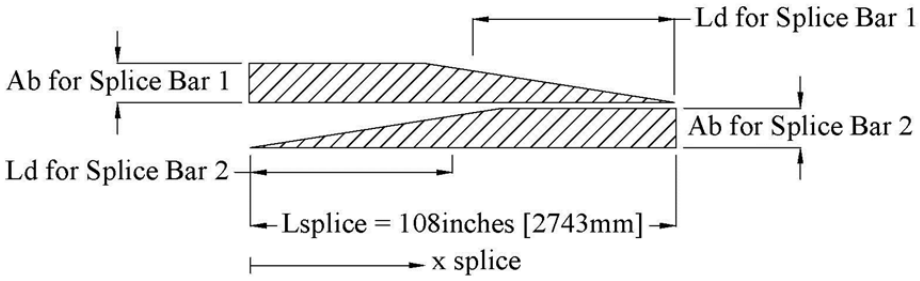

Figure 4-6. Linear Increase in Effective Area at the Splice Region [taken from Alberson (2009)].

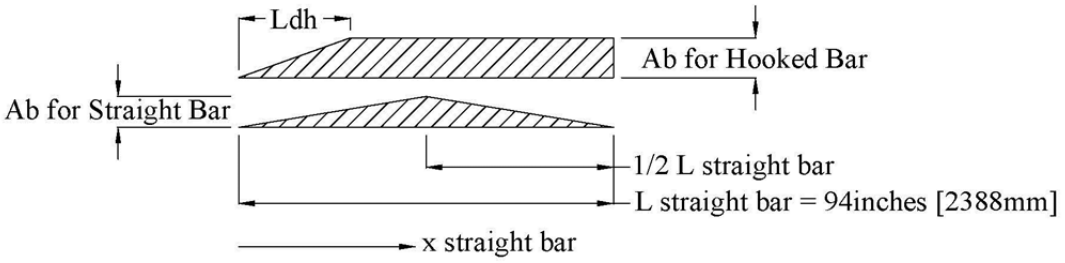

Figure 4-7. Linear Increase in Effective Area at the End Region.

The total effective reinforcement area at each section for the tension steel ($A_{s,eff}$) is then calculated by summing the contributions of each bar. Eqs. 4-8 through 4-10 calculate the effective steel area in tension Splice Bar 1 and Splice Bar 2 (A_{s1} and A_{s2}). The sum of the effective tension steel in the splice region is $A_{s,efff,splice}$. The total effective reinforcement area at the splice ends is calculated with x_{splice} = 0 inches and x_{splice} = 108 inches (2743 mm). Since there are three bars spliced with three others at each steel layer, the total effective reinforcement area is 3 times the area of each bar, A_b, at the splice ends and is more than $3A_b$ at every other section within the splice length.

$$A_{s1} = \begin{cases} 3A_b, & x_{splice} \le L_{splice} - L_d \\ 3A_b\left[1 - \frac{(x_{splice} - (L_{splice} - L_d))}{L_d}\right], & x_{splice} \ge L_{splice} - L_d \end{cases} \quad \text{(Eq. 4-8)}$$

$$A_{s2} = \begin{cases} \frac{3A_b(x_{splice})}{L_d}, & x_{splice} \le L_d \\ 3A_b, & x_{splice} \ge L_d \end{cases} \quad \text{(Eq. 4-9)}$$

$$A_{s,eff,splice} = A_{s1} + A_{s2} \quad \text{(Eq. 4-10)}$$

Eqs. 4-11 through 4-13 calculate the effective steel area in the compression Splice Bar 1 and Splice Bar 2 (A'_{s1} and A'_{s2}) then are summed to give the total effective area in the compression bars at the splice region $A'_{s,eff,splice}$.

$$A'_{s1} = \begin{cases} 3A_b, & x_{splice} \le L_{splice} - L_{dc} \\ 3A_b\left[1 - \frac{(x_{splice} - (L_{splice} - L_{dc}))}{L_{dc}}\right], & x_{splice} \ge L_{splice} - L_{dc} \end{cases} \quad \text{(Eq. 4-11)}$$

$$A'_{s2} = \begin{cases} \frac{3A_b(x_{splice})}{L_{dc}}, & x_{splice} \le L_{dc} \\ 3A_b, & x_{splice} \ge L_{dc} \end{cases} \quad \text{(Eq. 4-12)}$$

$$A'_{s,eff,splice} = A'_{s1} + A'_{s2} \quad \text{(Eq. 4-13)}$$

Eqs. 4-14 through 4-16 calculate the effective areas of the hooked bar ($A_{s,hooked}$) and straight bar ($A_{s,straight\ bar}$) in tension are summed to give the effective tension steel area at the end region, $A_{s,efff,end}$. Since the straight bar has a length of 94 inches (2388 mm), it is shorter than twice the development length for the tension bars. Therefore, $A_{s,straight\ bar}$ is never $3A_b$.

$$A_{s,hooked} = \begin{cases} \frac{3A_b(x_{straight\ bar})}{L_{dh}}, & x_{straight\ bar} \le L_{dh} \\ 3A_b, & x_{straight\ bar} \ge L_{dh} \end{cases} \quad \text{(Eq. 4-14)}$$

$$A_{s,straight\ bar} = \begin{cases} \frac{3A_b(x_{straight\ bar})}{L_d}, & x_{straight\ bar} \le \frac{1}{2} L_{straight\ bar} \\ \frac{3A_b}{L_d}(L_{straight\ bar} - x_{straight\ bar}), & x_{straight\ bar} \ge \frac{1}{2} L_{straight\ bar} \end{cases} \quad \text{(Eq. 4-15)}$$

$$A_{s,eff,end} = A_{s,hooked} + A_{s,straight\ bar} \quad \text{(Eq. 4-16)}$$

Eqs. 4-17 through 4-19 calculate the effective areas of the hooked bar ($A'_{s,hooked}$) and straight bar ($A'_{s,straight\ bar}$) in tension are summed to give the effective tension steel area at the end region, $A'_{s,eff,end}$. Since L_{dc} is shorter than L_d, $A'_{s,straight\ bar}$ does reach $3A_b$.

$$A'_{s,hooked} = \begin{cases} \frac{3A_b(x_{straight\ bar})}{L_{dh}}, & x_{straight\ bar} \le L_{dh} \\ 3A_b, & x_{straight\ bar} \ge L_{dh} \end{cases} \quad \text{(Eq. 4-17)}$$

$$A'_{s,\text{straight bar}} = \begin{cases} \frac{3A_b(x_{\text{straight bar}})}{L_{dc}}, & x_{\text{straight bar}} \le L_{dc} \\ 3A_b, & L_{dc} \le x_{\text{straight bar}} \le L_{\text{straight bar}} \\ 3A_b\left[1 - \frac{(x_{\text{straight bar}} - (L_{\text{straight bar}} - L_{dc}))}{L_{dc}}\right], & x_{\text{straight bar}} \ge L_{\text{straight bar}} - L_{dc} \end{cases} \quad \text{(Eq. 4-18)}$$

$$A'_{s,eff,end} = A'_{s,hooked} + A'_{s,\text{straight bar}} \quad \text{(Eq. 4-19)}$$

Figure 4-8 shows the effective steel areas at every location of the LSC specimens using the equations above. The figure shows the effective steel area is 3 A_b at the splice ends. Since the compression steel has a shorter development length, the linear increase in effective area has a larger slope. There is a change in slope at the end region where the hooked bar is fully developed and the straight bar continues to develop.

4.2.3 Iterative Analytical Model for Flexural Capacity with Constant Axial Loading

The equations used for concrete flexural capacity are discussed in this section. The depth of the neutral axis, c, is found such that the sum of the forces in the section equal the axial load from the post-tensioning representing a column service load.

The strain at the top section of concrete, ε_c, is found from similar triangles for the cracking and yield limit states and is given as ε_{cu} for the ultimate limit state (Figure 4-1). Eq. 4-20 is used when the concrete first cracks, where ε_{cr} is given in Eq. 4-3

$$\varepsilon_c = \frac{-\varepsilon_{cr}}{h-c} c \quad \text{(Eq. 4-20)}$$

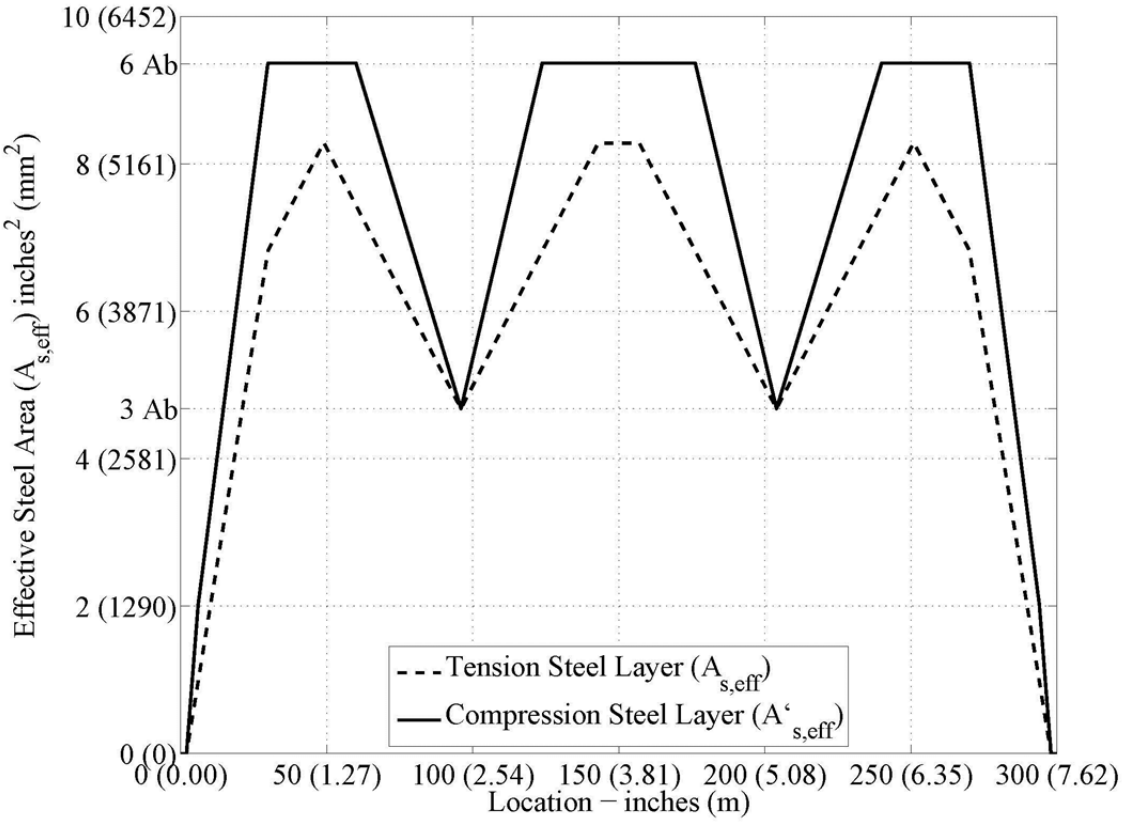

Figure 4-8. Effective Steel Areas along the Length of the LSC Specimens.

At first yielding of the longitudinal tension reinforcement, ε_c is found as function of the yield strain of the tension reinforcement, ε_{sy}, from Eq. 4-4

$$\varepsilon_c = \frac{-\varepsilon_{sy}}{d-c} c \qquad \text{(Eq. 4-21)}$$

The concrete stress in the compression region at the first and second limit states, first cracking of concrete and first yielding of steel, is calculated below according to Hooke's Law:

$$f_c = \varepsilon_c E_c \quad \text{(Eq. 4-22)}$$

When the concrete compression strain reaches ε_{cu}, the effective concrete stress is found using the Whitney's Stress Block approximation shown below, noting that the stress is negative in compressive.

$$f_c = -0.85\, f'_c \quad \text{(Eq. 4-23)}$$

The force from the concrete, C_c, when the stress is linearly proportional to the strain (triangular), which occurs before ε_c reaches ε_{cu}, is found below.

$$C_c = \frac{1}{2}(f_c\ c)b \quad \text{(Eq. 4-24)}$$

At ultimate, when the Whitney's Stress Block assumption is used (MacGregor and Wight 2009), the concrete compression force is found as follows:

$$C_c = 0.85 f'_c\ a\ b \quad \text{(Eq. 4-25)}$$

$$\text{where } a = \beta_1 \mathbf{c} \quad \text{(Eq. 4-26)}$$

where coefficient, β_1 is found as (ACI318-08)

$$\beta_1 = 0.85 - 0.05\left(\frac{f'_c - 4000}{1000}\right) \quad \text{for } 4000 < f'_c < 8000 \text{ psi} \quad \text{(Eq. 4-27)}$$

Note that β_1 has a minimum value of 0.65 and a maximum value of 0.85; therefore, β_1 is 0.65 for f'_c values greater than or equal to 8000 psi and 0.85 for f'_c values less than or equal to 4000 psi. Eq. 4-27 only works with f'_c in psi.

Prior to cracking of the concrete in tension, the concrete tension force is determined using Hooke's Law. Eq. 4-28 shows the expression for the concrete tension force at first cracking

$$T_c = \frac{1}{2}[f_r(h - c)]b \quad \text{(Eq. 4-28)}$$

The strains in the tension reinforcing steel, ε_s, and compression reinforcing steel, ε'_s, at first cracking are given in Eq. 4-29 and Eq. 4-30, respectively, from similar triangles using the assumption that plane sections remain plane.

$$\varepsilon_s = \frac{-\varepsilon_c}{c}(d - c) \quad \text{(Eq. 4-29)}$$

$$\varepsilon'_s = \frac{\varepsilon_c}{c}(c - d') \quad \text{(Eq. 4-30)}$$

Note that the negative sign in Eq. 4-29 results in a positive tensile strain.

The stresses in the tension reinforcing steel, f_s, and compression reinforcing steel, f'_s, at first cracking are found from Hooke's Law and given in Eqs. 4-31 and 4-32, respectively. For the other limit states, the reinforcing steel is modeled as elastic-perfectly plastic and the strength is limited to f_y.

$$f_s = \varepsilon_s E_s \leq f_y \quad \text{(Eq. 4-31)}$$

$$f'_s = \varepsilon'_s E_s \leq f_y \text{ and } \geq -f_y \quad \text{(Eq. 4-32)}$$

The force from the tension reinforcing steel is found from Eq. 4-33 multiplied by $A_{s,eff}$ as shown below. Since this steel is in the tension region, there is no adjustment necessary for the concrete compression force beyond cracking. The first equation in Eq. 4-33 was used for the first limit state when there is a tensile concrete force below the neutral axis. The steel force subtracts out the force in the concrete calculated at the location of the steel. The second equation was used right after cracking when the tensile concrete force equals zero. The general variable, $A_{s,efff}$, is used for both $A_{s,efff,splice}$ and $A_{s,efff,splice}$. This generalization is also used for the compression steel.

$$T_s = \begin{cases} (f_s - \varepsilon_s E_c)A_{s,eff}, & T_c < 0 \\ f_s A_{s,eff}, & T_c = 0 \end{cases} \quad \text{(Eq. 4-33)}$$

Similarly, the force from the compression reinforcing steel is found using the stress calculated in Eq. 4-32 multiplied by $A'_{s,eff}$ as shown below in Eq. 4-34. The equation subtracts the force from the concrete at the location of the steel already accounted for in the concrete force. The first part of the equation was used when the stress is linearly proportional to the strain. The second part was used when the Whitney's Stress Block assumption was applied. When the top layer of steel is below a, the concrete force does not include the steel area and can be neglected in these equations.

$$C'_s = \begin{cases} (f'_s - \varepsilon_s E_c)A'_{s,eff}, & d' < a, \varepsilon_c < 0.003 \\ (f'_s - .85f'_c)A'_{s,eff}, & d' < a, \varepsilon_c \geq 0.003 \\ f'_s A'_{s,eff}, & d' \geq a \end{cases} \quad \text{(Eq. 4-34)}$$

The axial load at a given section is a sum of the compression and tension forces at that section. Eq. 4-35 is a summation of the forces in the section where the compression forces are negative and the tension forces are positive. Since the axial load is constant from the post-tensioning of the strands, the model is iterated with different values of c

until P_{axial} reaches the desired value of post-tensioning force for equilibrium. The LSC specimens were initially post-tensioned to 580.5 kips (2582 kN) in compression, therefore the model was iterated until P_{axial} = -580.5 kips.

$$P_{axial} = C_c + T_c + C_s' + T_s \quad \text{(Eq. 4-35)}$$

The total moment capacity of the column section can next be calculated by summing the section forces about the centroidal axis of the section as shown below in Eqs. 4-36 through 4-38 for first cracking ($M_{total\ cap_{cr}}$), first yield ($M_{total\ cap_{y}}$), and ultimate limit states ($M_{total\ cap_{ult}}$). The moments from the compression forces and tension forces are counter-clockwise about the centroid; therefore the negative sign is used in front of the compression forces counter the negative force value from equations listed above.

$$M_{total\ cap_{cr}} = -C_c\left(\frac{h}{2} - \frac{c}{3}\right) + T_c\left(\frac{h}{2} - \frac{h-c}{3}\right) - C_s'\left(\frac{h}{2} - d'\right) + T_s\left(d - \frac{h}{2}\right) \quad \text{(Eq. 4-36)}$$

$$M_{total\ cap_{y}} = -C_c\left(\frac{h}{2} - \frac{c}{3}\right) - C_s'\left(\frac{h}{2} - d'\right) + T_s\left(d - \frac{h}{2}\right) \quad \text{(Eq. 4-37)}$$

$$M_{total\ cap_{ult}} = -C_c\left(\frac{h}{2} - \frac{\beta_1 c}{3}\right) - C_s'\left(\frac{h}{2} - d'\right) + T_s\left(d - \frac{h}{2}\right) \quad \text{(Eq. 4-38)}$$

The section curvature, ϕ, (or slope of the strain diagram) at each limit state is calculated from similar triangles as follows:

$$\phi = \frac{\varepsilon_c}{c} \quad \text{(Eq. 4-39)}$$

Figure 4-9 shows the calculated moment vs. curvature response of the LSS specimen section directly under actuator (or at the splice end) where the effective reinforcing steel area is $3A_b$ or 4.68 square inches (3019 mm^2), P_{axial} is -580.5 kips (-2582 kN), the design concrete compressive strength, f'_c, is 5.0 ksi (34 MPa), and the yield strength of the reinforcement, f_y, is taken as 70 ksi (483 Mpa) to account for over strength in Grade 60 steel. The three points are for the three limit states as discussed above: first cracking of the concrete, first yielding of the tension steel, and concrete crushing.

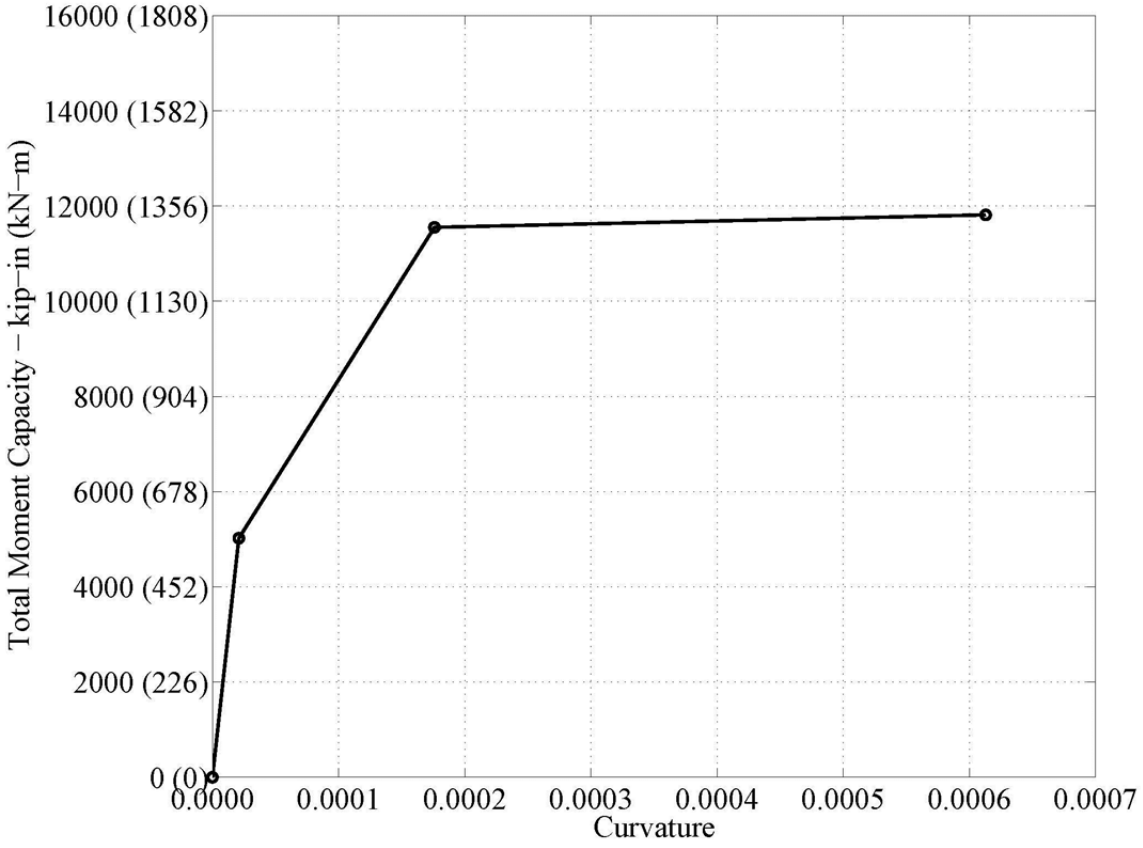

Figure 4-9. Moment vs. Curvature at the Section under the Actuator

4.3 Analytical Predictions

4.3.1 Four-Point Test Predictions

The moment calculated from the iterative procedure listed above gives a total moment capacity for any given section. To compare the analytical capacity for the LSS specimens in the four-point load setup to the experimental demands from the actuator loading, the moment demands from the self-weight of the specimens must be considered, even though the self-weight moment is much smaller than the moment demand from actuators. Figure 4-10 shows the shear and moment diagram for the self-weight of the LSC specimens in the four-point test setup. The total length of the LSC specimen, L, is 300 inches (7620 mm). The distance from the support to the desired cross section is x_{supp} and x is the distance from the end to the cross section. These variables will be used in the deflection equations.

The moment from self-weight when the specimen is in the four-point setup ($M_{SW,4pt}$) is calculated as follows.

$$M_{SW,4pt} = \frac{w}{2}(L * x_{supp} - x^2) \qquad \text{(Eq. 4-40)}$$

The values for the variables L, x_{supp}, and x are illustrated in Figure 4-10. The cross sectional weight per inch of the specimen, w, is calculated using the actual dimensions for the specimens in this research (24 inches by 48 inches) below:

$$w = \left(0.15\,\frac{kips}{ft^3}\right)(24 \cdot 48\ in^2)\left(\frac{ft^3}{12^3 inches^3}\right) = 0.1\,\frac{kips}{inch}\ \ \left(0.018\,\frac{kN}{mm}\right) \qquad \text{(Eq. 4-41)}$$

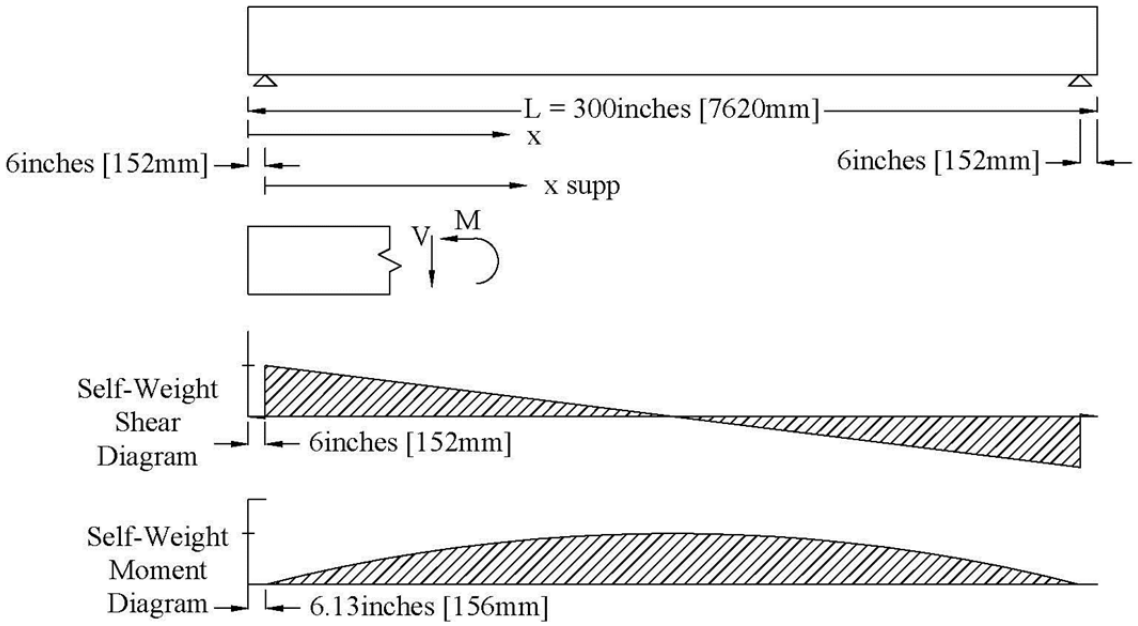

Figure 4-10. Shear and Moment Diagram for Self-Weight in the Four-Point Setup [taken from Alberson (2009)].

Figure 4-11 shows the shear and moment diagrams from the actuator loading in the four-point test setup. In this test setup, the moment is constant along the splice length and is actuator load times L_{supp}, where L_{supp} is the distance between the support and actuator. The distance between each support is L_s.

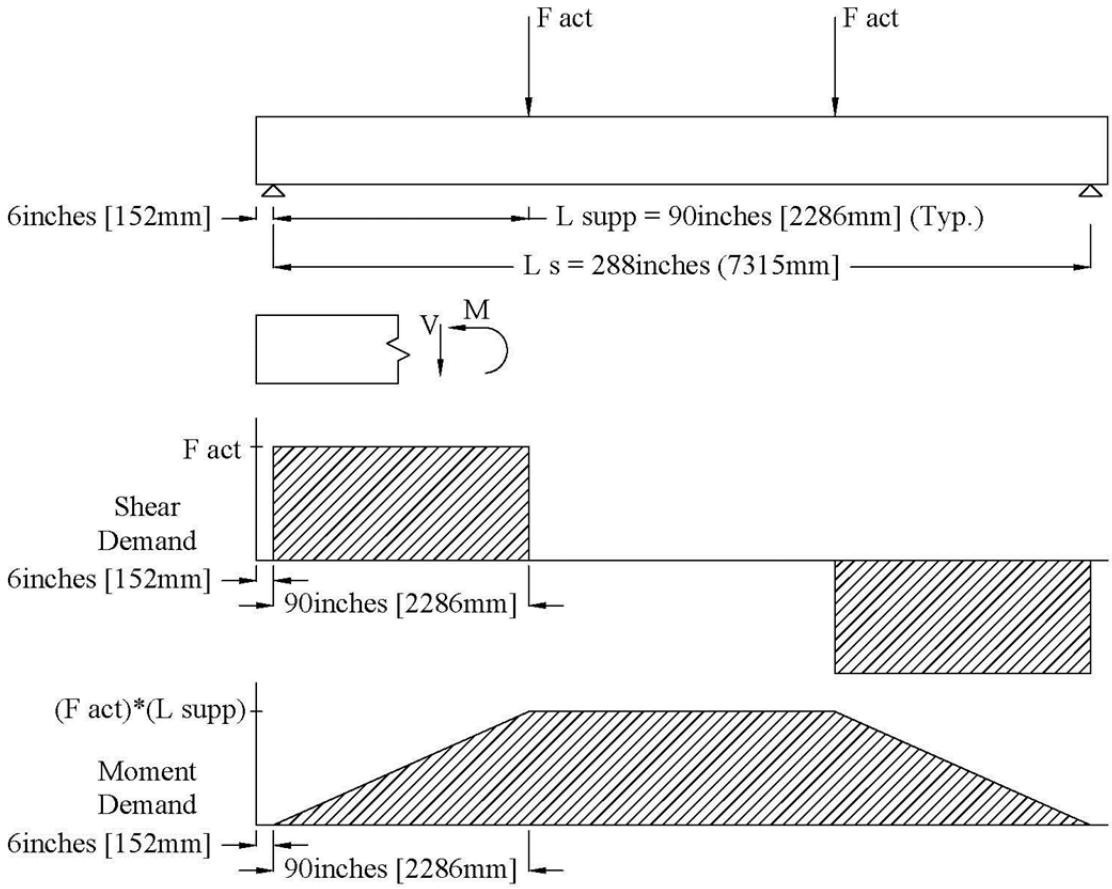

Figure 4-11. Four-Point Test Shear and Moment Diagram [taken from Alberson (2009)].

Eq. 4 -42 calculates the individual actuator loads for the four-point setup, $F_{act,4pt}$, located at the critical splice end sections, are found from the total moment capacity of the section, the moment due to self-weight at that location, and the distance between the support and actuator. $M_{total\ cap}$ is used as a general variable for the total moment capacity at each limit state or between limit states.

$$F_{act,4pt} = \frac{M_{total\ cap} - M_{SW,4pt}}{L_{supp}} \qquad \text{(Eq. 4-42)}$$

Figure 4-12 shows the ultimate moment capacity and demand from the actuator at each section of the LSC specimen. The moment capacity shown is the difference between the total moment capacity and the moment the specimen resists from the self-weight. The highest moment demand the specimen can resist until failure (concrete crushing) is located at the splice end (section under actuator) and is 10926 kip-inches (1234 kN-m). The load from each actuator equals the moment divided by the moment arm. For the four-point setup, the moment arm equals the distance between the support and the actuator which is 90 inches (2286 mm). Therefore, expected actuator load at failure is 121 kips (538 kN).

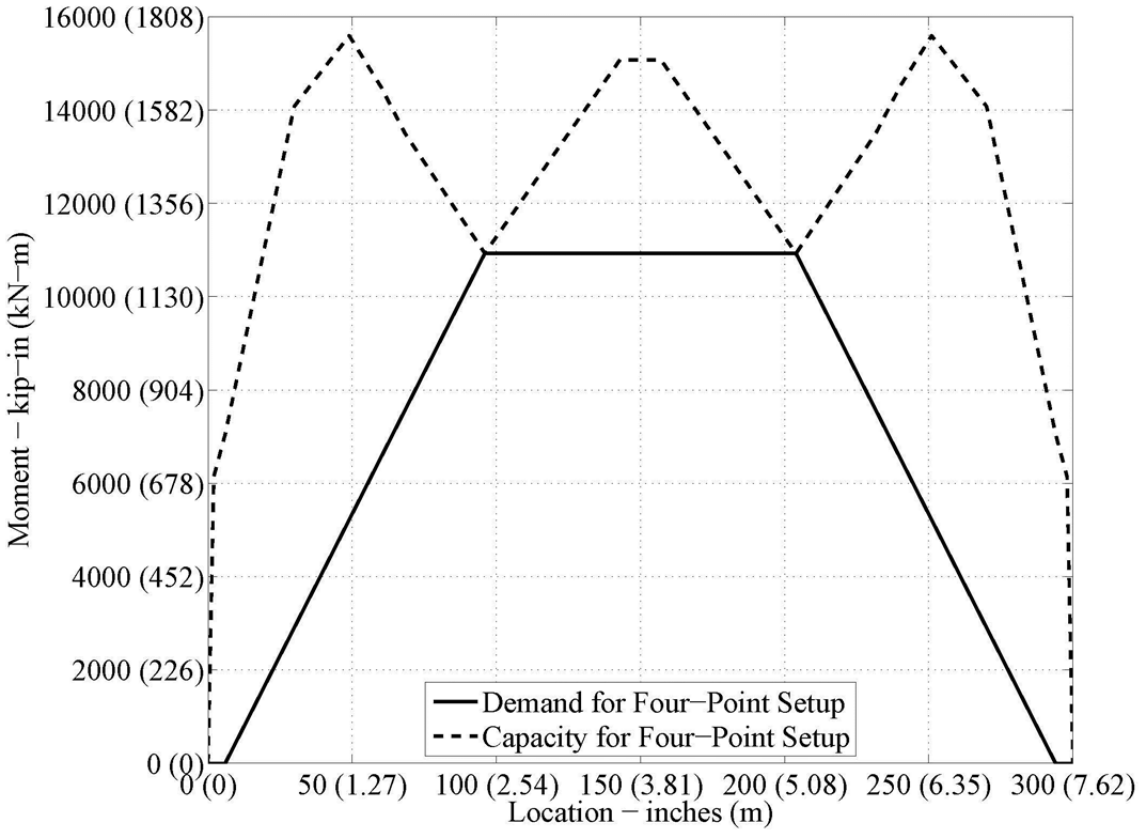

Figure 4-12. Ultimate Moment Capacity vs. Demand for Four-Point Setup.

Next the deformations in the specimens at first cracking, first yield and ultimate limit states are discussed below. Eq. 4-43 is used to find the elastic deflection of the specimen at any point between the actuator loads (Δ_{4pt}).

$$\Delta_{4pt} = \frac{F_{act,4pt}\, L_{supp}}{6\, E_c\, I}\left(3L_s x_{supp} - 3L_s x_{supp}^2 - {L_{supp}}^2\right) \qquad \text{(Eq. 4-43)}$$

The values for the variables used in Eq. 4-43 are shown in Figure 4-10 and Figure 4-11. The value of the second moment of area, I, depends on the limit state; these equations are listed next. Note that this deflection equation is only used to calculate the elastic deformations. Plastic deformations can also occur when the specimens yields and another equation is used to determine the approximated plastic deformations, which will be listed later. These plastic deformations can be added to the elastic deformations to find total deformations at any cross section.

Figure 4-13 shows the specimen cross section dimensions and depths of each steel layer needed for the second moment of area calculation.

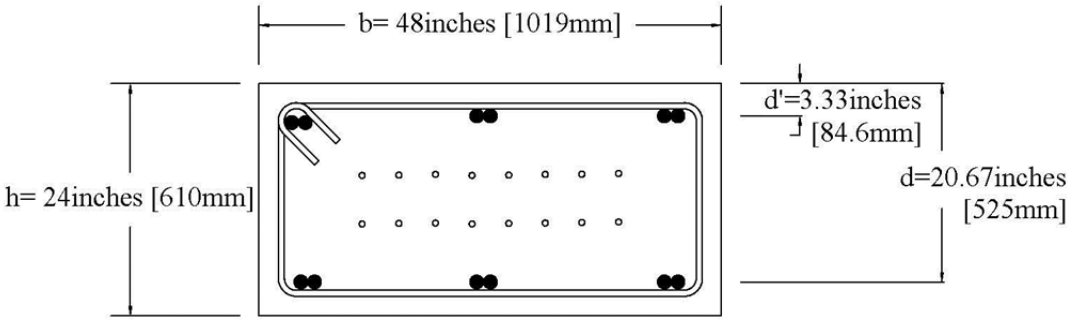

Figure 4-13. Cross Section at Splice Region with Steel Depths.

Neglecting the steel reinforcement, the second moment of area, I_g., can be found directly from the column dimensions as follows: for the equations below,

$$I_g = \frac{1}{12} bh^3 \quad \text{(Eq. 4-44)}$$

Considering the contribution of the steel reinforcement, the transformed second moment of area can be calculated as follows:

$$I_{gt} = \frac{1}{12} bh^3 + bh\left(\frac{h}{2} - y_t\right)^2 + A_{s,eff,tr}(d - y_t)^2 + A'_{s,eff,tr}(d' - y_t)^2 \quad \text{(Eq. 4-45)}$$

where y_t is calculated from the equation below.

$$y_t = \frac{\frac{bh^2}{2} + A_{s,eff,tr}(h-d) + A'_{s,eff,tr}(h-d)}{bh + A_{s,eff,tr} + A'_{s,eff,tr}} \quad \text{(Eq. 4-46)}$$

The effective steel areas (Eqs. 4-8 through 4-19) are transformed to account for difference the modulus of elasticity between the steel and concrete and calculated below:

$$A_{s,eff,tr} = (n-1)A_{s,eff} = \left(\frac{E_s}{E_c} - 1\right)A_{s,eff} \quad \text{(Eq. 4-47)}$$

$$A'_{s,eff,tr} = (n-1)A'_{s,eff} = \left(\frac{E_s}{E_c} - 1\right)A'_{s,eff} \quad \text{(Eq. 4-48)}$$

where n is the ratio of the modulus of elasticity of steel to concrete.

After first cracking of the concrete, the second moment of area at a critical section should not include any concrete area in tension or c, which is different than at the

uncracked state. So the cracked second moment of area, I_{cr}, is calculated about c, for the cracked section instead of the centroid in Eq. 4-45.

$$I_{cr} = \frac{1}{12}bc^3 + bc\left(\frac{c}{2} - c\right)^2 + A_{s,eff,tr}(d - c)^2 + A'_{s,eff,tr}(c - d')^2 \qquad \text{(Eq. 4-49)}$$

For loading beyond yielding of the reinforcing steel, linear deformations up to yielding and plastic deformations beyond yielding must be considered in determining the ultimate deflections for the specimens. For the plastic deformations, the plastic hinge rotation of a critical section is first calculated using Eq. 4-50.

$$\theta_p = (\phi_u - \phi_y)l_d \qquad \text{(Eq. 4-50)}$$

The curvatures at ultimate and first yielding limit states, ϕ_u and ϕ_y, are calculated using Eq. 4-39 with the corresponding values are each limit state. The plastic hinge length, l_d, is calculated using Eq. 4-51 (Mattock 1967).

$$l_d = (.5d + .05(z)) \qquad \text{(Eq. 4-51)}$$

where z is the distance between the maximum moment and zero moment. For the four-point setup, z equals L_{supp} and 90 inches (2286mm).

Assuming that the entirety of plastic deformations occur at the critical splice ends within the specimens (having the least effective steel area), the plastic deformations can be found from the plastic hinge rotations and the geometry of the test setup illustrated in Figure 4-14. The elastic deflection and first yield of the steel, $\Delta_{4pt,y}$, was added to the plastic deflection to calculate the total deflection at the ultimate limit, $\Delta_{4pt,u}$, in Eq. 4-47.

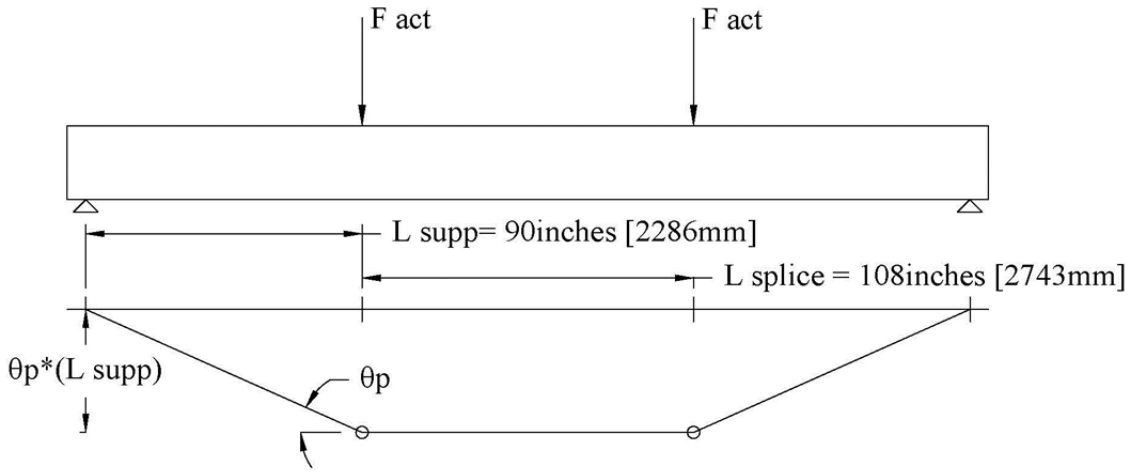

Figure 4-14. Plastic Hinge Rotation for Four-Point Setup.

$$\Delta_{4pt,u} = \theta_p L_{supp} + \Delta_{4pt,y} \quad \text{(Eq. 4-52)}$$

In order to calculate a complete moment vs. deformation response, different methods for computing the second moment of area beyond cracking were reviewed in the literature for computing deflections as listed above. The PCI Design Handbook which is further explained by Naaman (PCI 2004, Naaman 2004) recommends the use of I_g for the deflections up to the cracking moment. For deformations beyond cracking, up to when the tension steel yields, the cracked second moment of area, I_{cr}, is used. Figure 4-15 illustrates that difference between the load at cracking (L1) and the load beyond cracking is the load (L2) used with I_{cr} to compute the deflection between cracking and beyond cracking ($\Delta 2$). The total deflection ($\Delta 1 + \Delta 2$) is found by adding the deflection at cracking ($\Delta 1$) to the additional deflection ($\Delta 2$).

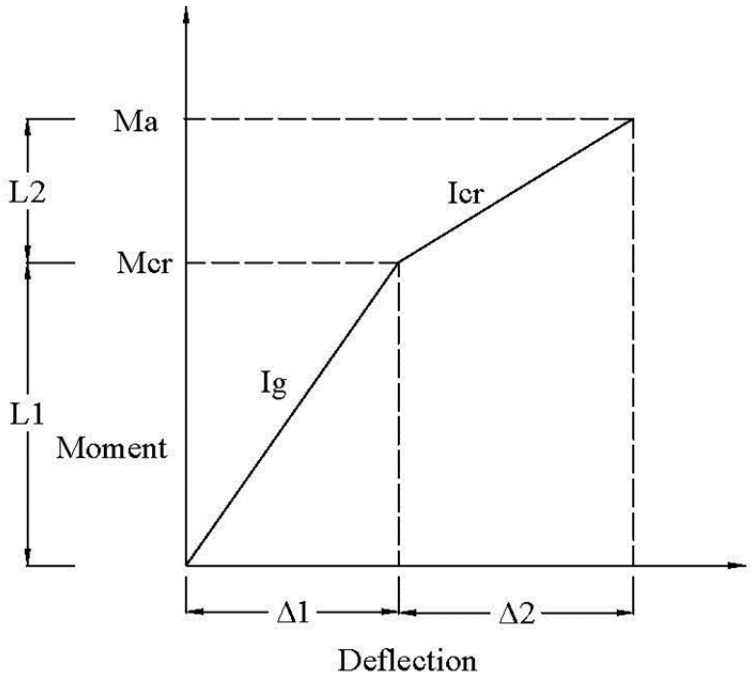

Figure 4-15. Bilinear Moment vs. Deflection Relation (Naaman 2004).

The bilinear method described from PCI and Naaman is used in conjunction with plastic analysis for the deflection at ultimate and is referred to as the Tri-Linear method for the three slopes used in the method. The linear deflection equation for the four-point test set up, Eq. 4-43, can be modified for Tri-Linear method. Eqs. 4-53 and Eq. 4-54 calculate the deflection at cracking using I_g ($\Delta_{4pt,cr,Ig}$) and at the yield limit ($\Delta_{4pt,y,Tri-Linear}$) for the Tri-Linear method. The load from the actuator when the concrete begins to crack and when the steel yields is $F_{act,4pt_{cr}}$ and $F_{act,4pt_y}$ respectively. $F_{act,4pt_{cr}}$ and $F_{act,4pt_y}$ are calculated using Eq. 4-42 with $M_{total\ cap_{cr}}$ and $M_{total\ cap_y}$ respectively. When the steel begins to yield, the load at cracking is subtracted from the load at yielding and the deflection at cracking is added to the yield deflection to account for the deflection found in Eq. 4-53. The other variables are illustrated in Figure 4-10 and Figure 4-11.

$$\Delta_{4pt,cr,Ig} = \frac{F_{act,4pt_{cr}} L_{supp}}{6\, E_c\, I_g}\left(3L_s x_{supp} - 3L_s x_{supp}^2 - {L_{supp}}^2\right)$$

(Eq. 4-53)

$$\Delta_{4pt,y,Tri-Linear} = \frac{\left(F_{act,4pt_y} - F_{act,4pt_{cr}}\right) L_{supp}}{6\, E_c\, I_{cr}}\left(3L_s x_{supp} - 3L_s x_{supp}^2 - {L_{supp}}^2\right) + \Delta_{cr,4pt,Ig}$$

(Eq. 4-54)

For finding beam deflections beyond cracking of the concrete, ACI-318 (2008) proposes an effective section moment of area, I_e, for reinforced concrete beams and states it is suitable for Class C (cracked) and Class T (transition) members as follows:

$$I_e = \left(\frac{M_{cr}}{M_a}\right)^3 I_g + \left[1 - \left(\frac{M_{cr}}{M_a}\right)^3\right] I_{cr} \qquad \text{(Eq. 4-55)}$$

where M_{cr} is the total bending moment at cracking. M_{cr} is referred to as $M_{total\ cap_{cr}}$ in this report. M_a is the critical section bending moment at the step the deflection is computed which is referred to as the general $M_{total\ cap}$ in this report. Eq. 4-55 approximates the second moment of area of the section between I_g and I_{cr}. At and prior to first cracking, I_g can be used for the deflection calculation. Therefore the deflection at cracking using the I_e method from ACI 318 is the same as the Tri-Linear method described above (Eq. 4-53). However, after cracking according to ACI, the specimen deflection can be calculated as shown below:

$$\Delta_{4pt,y,Ie} = \frac{F_{act,4pt_y} L_{supp}}{6\, E_c\, I_e}\left(3L_s x_{supp} - 3L_s x_{supp}^2 - {L_{supp}}^2\right) \qquad \text{(Eq. 4-56)}$$

Note that the load in Eq. 4-51 is simply $F_{act,4pt_y}$ and the load at first cracking, $F_{act.4pt_{cr}}$, does not need to be subtracted. This is a characteristic of the I_e formula. To calculate the

ultimate deflection when there is plasticity in the critical section, the plastic deformations are calculated with Eq. 4-52 in the same way as explained previously.

Further calculations were done by the author to find that beams with no axial force have a constant neutral axis depth immediately after first cracking to first yielding of the tension reinforcement. This was found by computing the calculations presented in section 4.2.3 with a desired P_{axial} = 0 kips (0 kN) instead of 580.5 kips (2582 kN) in compression. In the case of no axial force, the Tri-Linear method and the I_e method provide the similar deflection approximations. The two methods have the same results at each data point for the Tri-Linear method; however for the I_e method, the points between first cracking and first yielding form a curve. Figure 4-16 compares the two methods with no axial load using the dimensions and reinforcement from the specimens in this research. Two arbitrary points between first cracking and first yielding were chosen for this illustration.

However, in columns and beams with an axial force, the neutral axis is constantly changing between first cracking of the concrete and first yielding of the tension reinforcement. Therefore, I_{cr} is constantly changing from first cracking to first yielding of the tension reinforcement. To account for this varying stiffness between first cracking and yield in members with axial loading, the Step-by-Step I_{cr} method is proposed where I_{cr} is calculated at several different stages between first cracking and yielding. In this work, I_{cr} is calculated at three intermediate points between first cracking and yield based on the varying neutral axis depth, c, which can be calculated at each point based on bending theory and the required constant level of axial loading that was presented previously in section 4.2.3. Additional intermediate calculation points can be used; however, three points provided sufficient simplicity and accuracy for this research.

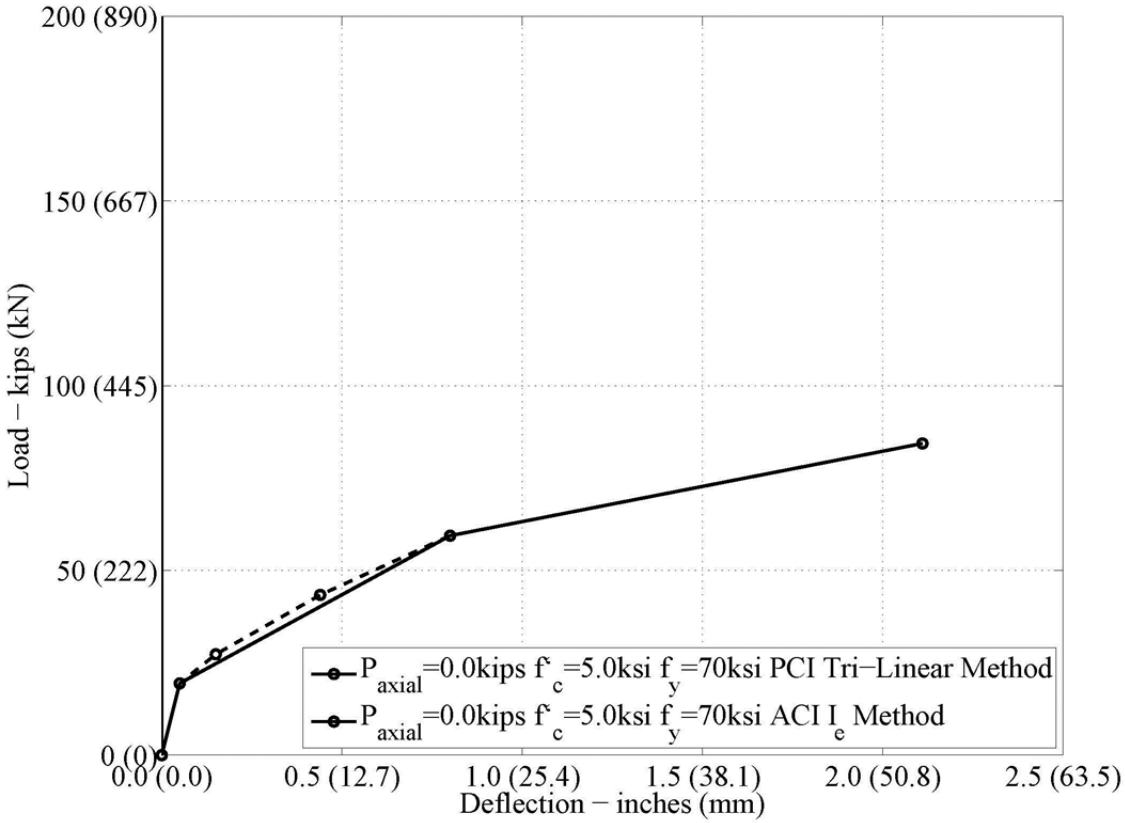

Figure 4-16. Load vs. Deflection for Tri-Linear and I_e Methods with No Axial Load.

In this research, the developed analytical program first calculates the section curvatures at cracking and yielding using Eq. 4-39 and the appropriate c and strain values at each limit state. Then the three intermediate curvatures ($\phi_{cr,y,i}$) are calculated using Eq. 4-57 where i equals the intermediate step and n equals the total number of intermediate steps desired. In our case, n=3 and there are three curvature equations for value of i: 1, 2, and 3.

$$\phi_{cr,y,i} = (\phi_y - \phi_{cr})\frac{i}{(n+1)} \qquad \text{(Eq. 4-57)}$$

Since the strain at the top of the concrete section, ε_c, is not dependent on strain limits for the intermediate steps, a different equation, Eq. 4-53, was used for the three intermediate ε_c values ($\varepsilon_{c,i}$). The neutral axis depths at the intermediate steps, c_i, are iterated until the P_{axial} equaled the desired force.

$$\varepsilon_{c,i} = c_i \phi_{cr,y,i} \quad \text{(Eq. 4-58)}$$

Eq. 4-59 calculates the deflection at cracking in the Step-by-Step I_{cr} method ($\Delta_{4pt,cr,Step-by-Step\ Icr}$) using I_{gt} instead of I_g.

$$\Delta_{4pt,cr,Step-by-Step\ Icr} = \frac{F_{act,4pt_{cr}}\, L_{supp}}{6\, E_c\, I_{gt}} \left(3L_s x_{supp} - 3L_s x_{supp}^2 - {L_{supp}}^2\right) \quad \text{(Eq. 4-59)}$$

The deflection for the intermediate values was calculated using Eq. 4-60 where $F_{act,4pt_i}$ and I_{cr_i} are the load and second moment of area calculated at each step using Eq. 4-42 and Eq. 4-49. For the calculation of $\Delta_{cr,y,1}$, $F_{act,4pt_{cr}}$ must be used for $F_{act,4pt_{i-1}}$ since the force at cracking is the preceding force.

$$\Delta_{4pt,cr,y,i} = \frac{(F_{act,4pt_i} - F_{act,4pt_{i-1}})\, L_{supp}}{6\, E_c\, I_{cr_i}} \left(3L_s x_{supp} - 3L_s x_{supp}^2 - {L_{supp}}^2\right) \quad \text{(Eq. 4-60)}$$

The deflection at yielding is calculated using Eq. 4-61 where the preceding force that is subtracted from the load when steel yields is $F_{act,4pt_n}$ which is the last intermediate force. The second moment of area using the neutral axis at yielding, I_{cr_y}, is also used.

$$\Delta_{4pt,y,Step-by\ Step\ Icr} = \frac{(F_{act,4pt_y} - F_{act,4pt_n})\, L_{supp}}{6\, E_c\, I_{cr_y}} \left(3L_s x_{supp} - 3L_s x_{supp}^2 - {L_{supp}}^2\right) \quad \text{(Eq. 4-61)}$$

The deflection at ultimate for the Step-by-Step I_{cr} method was found using Eq. 4-47 which accounts for the plastic behavior in the critical hinge regions at the splice ends, as previously described.

Figure 4-17 shows the three methods described for calculating the force vs. deflection response for a sample specimen with constant axial loading in the four-point test configuration: Tri-Linear, I_e, and Step-by-Step I_{cr}. Since the ACI 318 I_e method can be used to find equivalent second moment of areas beyond first cracking and up to yielding of the reinforcing steel, three intermediate calculations between first cracking and yield were also computed similar to the Step-by-Step I_{cr} method and the resulting force-deflection calculations were joined linearly. In the Step-by-Step I_{cr} method, the deflection at each intermediate point and yield point depends on the force and deflection at the prior step. Therefore, the deflection at yield changes when the number of intermediate steps changes. However, with the I_e method, the deflection at yield is the same regardless of the number of intermediate steps since Eqs. 5-50 and 5-51 do not depend on the prior step, only the moment at cracking. The figure shows none of the methods calculate the same deflection at first yielding.

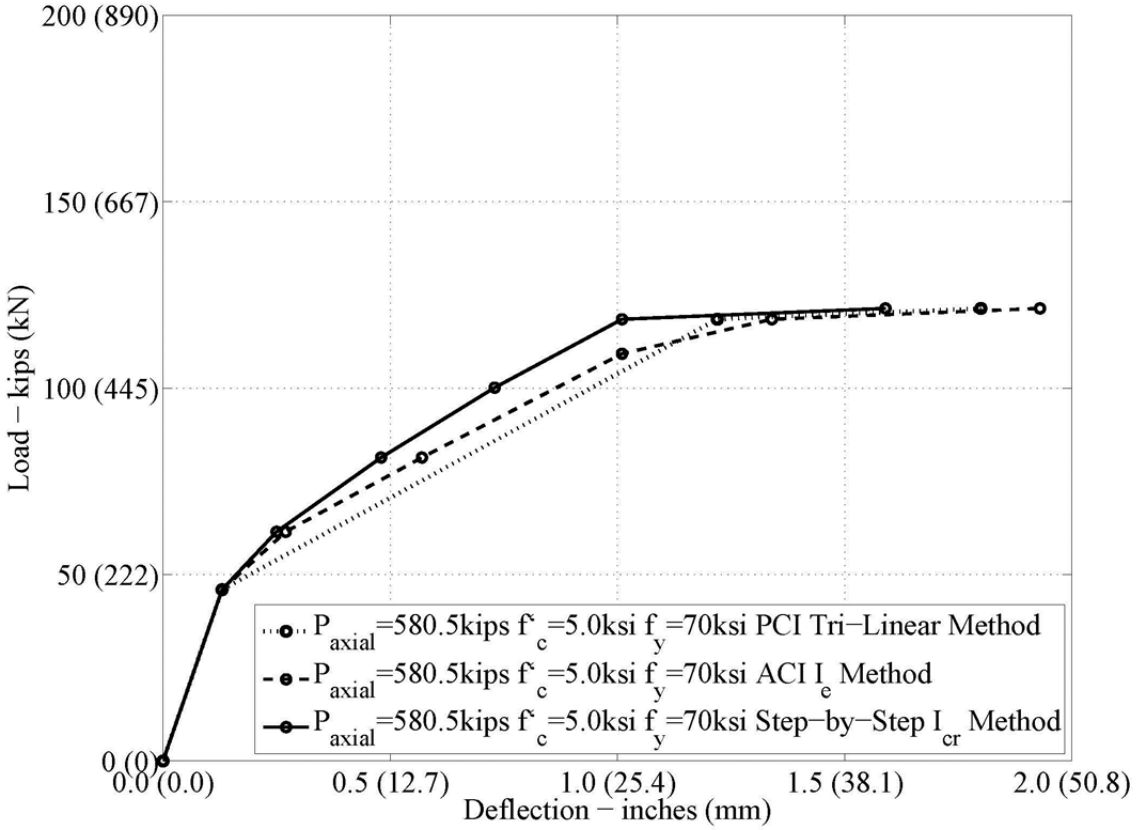

Figure 4-17. Load vs. Deflection for Tri-Linear, I_e, and Step-by Step I_{cr} Methods for Four-Point Test Setup.

4.3.2 Three-Point Test Predictions

Experimentally, the three-point test was executed after the four-point test. For three-point test setup, the actuators were adjusted to their new positions, 15 ft (180 inches, 4.57 m) (L_{act}) apart. Before the test, the LSC specimen was rotated so that the tension face from the four-point test was the tension face for the three-point test and then balanced on a pin connection at the specimen's center. Figure 4-18 illustrates the three-point test setup and the shear and moment diagrams for this test. The figure shows that the shear force is constant between the actuators (ie, constant along the splice length), whereas there was no shear force present in the splice region for the four-point test. The

moment varies along the splice length in the three-point test, instead of a constant moment as in the four-point test. The maximum moment occurs at the center of the specimen which is also at the pinned support.

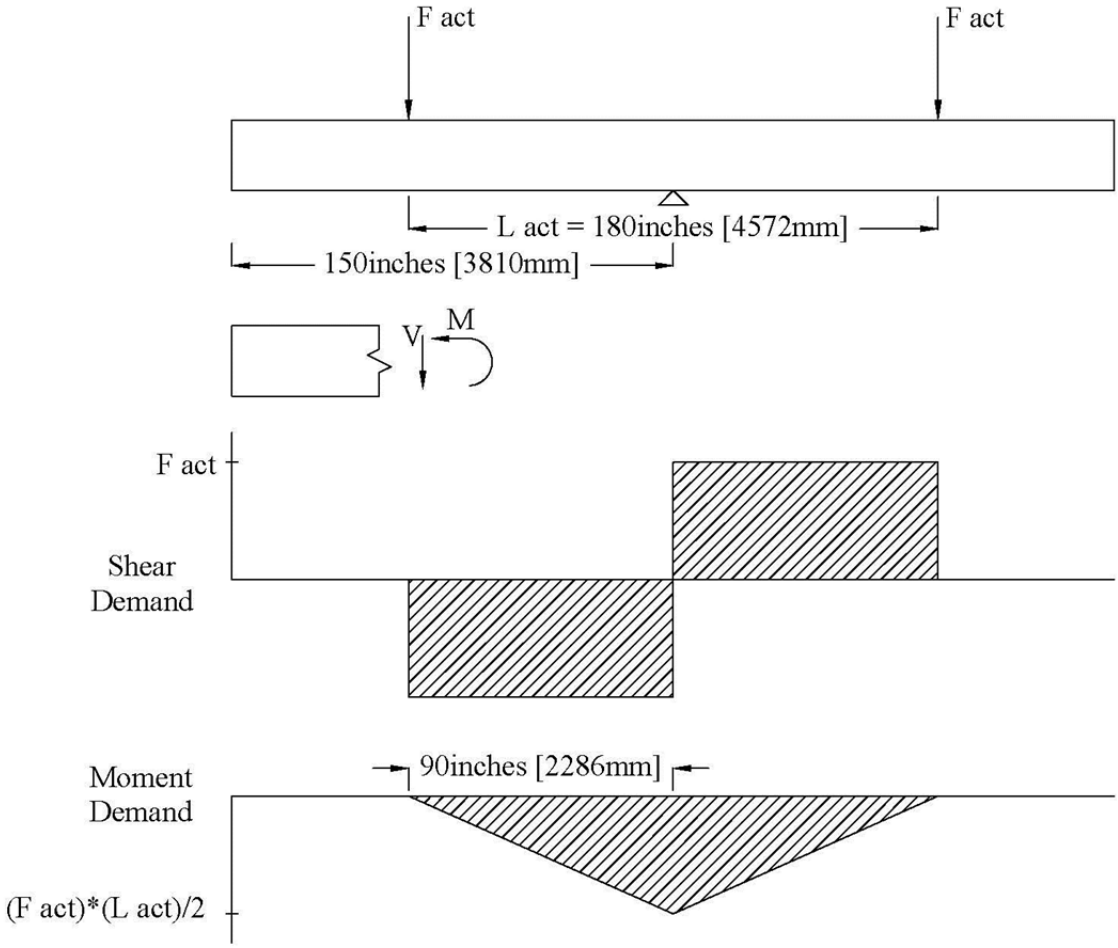

Figure 4-18. Three-Point Test Shear and Moment Diagram [taken from Alberson (2009)].

As in the four-point test, the self-weight moment was accounted for by subtracting it from the total moment capacity. Figure 4-19 shows the shear and moment diagrams from self-weight in the three-point setup. The moment from self-weight for the three-point setup ($M_{SW,3pt}$) is calculated using Eq. 4-56 for points between the end and the midpoint.

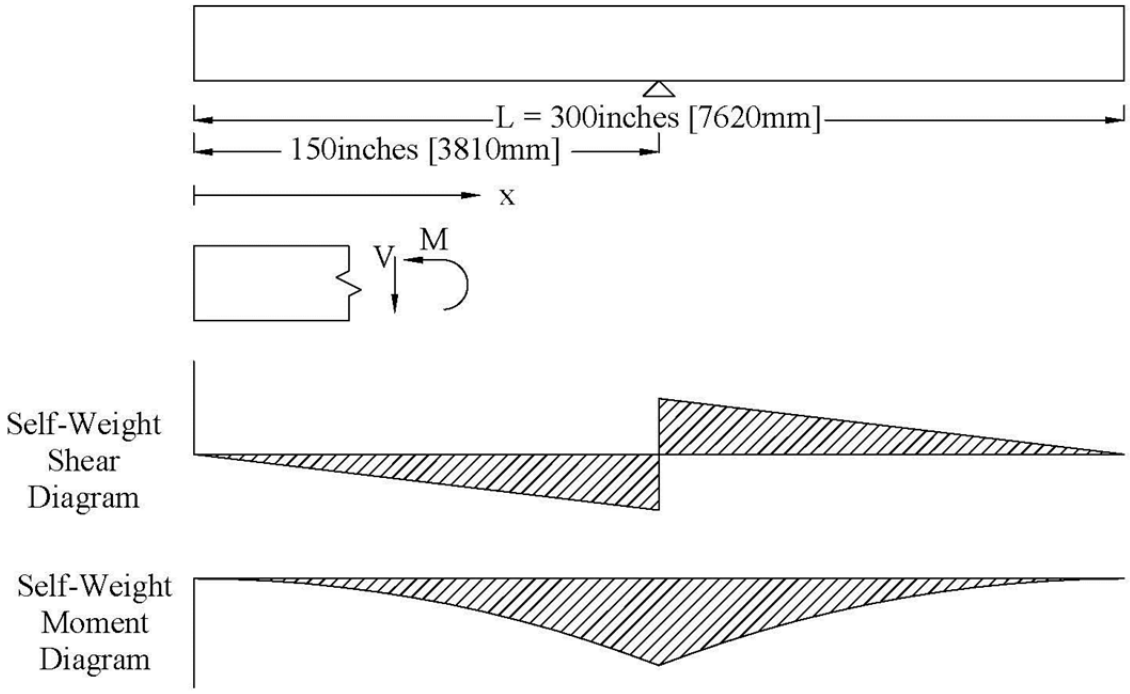

Figure 4-19. Shear and Moment Diagram for Self-Weight in the Three-Point Setup.

$$M_{SW,3pt} = \frac{w\,x^2}{2} \qquad \text{(Eq. 4-62)}$$

The distance between the end and the section the self-weight moment is being calculated is x, as illustrated in Figure 4-19. The weight of the specimen was calculated in Eq. 4-41.

The force from each actuator in the three-point setup ($F_{act,3pt}$)is found with the following equation.

$$F_{act,3pt} = (M_{total\ cap} - M_{SW,3pt})\frac{2}{L_{act}} \quad \text{(Eq. 4-63)}$$

Figure 4-20 compares the ultimate moment capacity of the LSC specimens to the moment demand from the three-point test setup. The moment capacity shown is the difference between the total moment capacity and the self-weight. The figure shows that the LSC specimens should fail from bending when the load from each actuator reaches 167 kips (743 kN). The three-point moment capacity is the same as the four-point except for the self-weight subtracted from the total capacity. The cracks formed from the four-point test were neglected since they formed under the actuators (splice end) and the bending cracks from the three-point form at the center. Bond slip can reduced the specimen strength if the reinforcing steel is not able to yield. However, in the structural tests on the specimens performed to date, bond slip didn't occur.

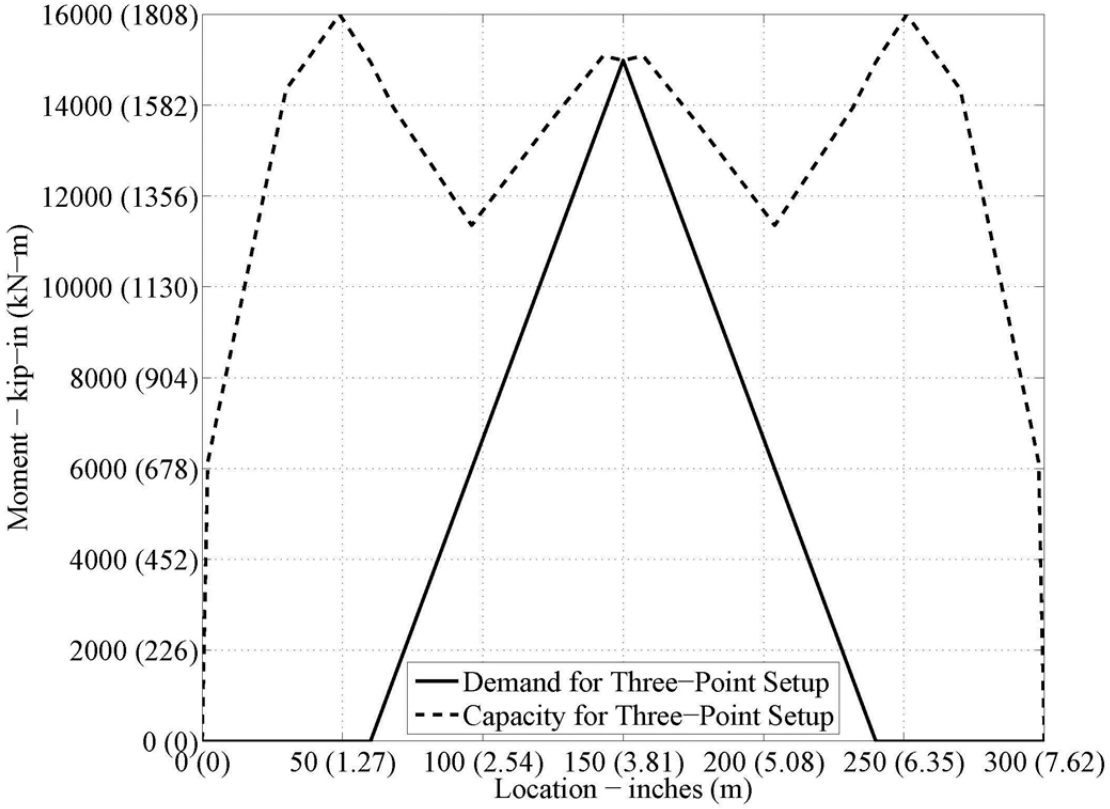

Figure 4-20. Ultimate Moment Capacity vs. Demand for Three-Point Setup.

Shear failure has also been considered since the three-point setup provides a shear demand in the splice region. Several methods to compute the shear capacity were explored and two are presented in the following equations. The first procedure is the AASHTO Method 1, simplified procedure for nonpresstressed sections. The following equations calculate the shear resistance, V_n comprised of the resistance from the concrete and transverse shear reinforcement, V_c and V_s, respectively reusing the AASHTO Method 1 (AASHTO 2010) as follows:

$$V_c = 0.0316\beta\sqrt{f'_c}b_v d_v \qquad \text{(Eq. 4-64)}$$

$$V_s = \frac{A_v f_y d_v (\cot\theta)}{s} \quad \text{(Eq. 4-65)}$$

$$V_n = \text{lesser of} \begin{cases} V_c + V_s \\ 25 f'_c b_v d_v \end{cases} \quad \text{(Eq. 4-66)}$$

where β equals 2.0 and θ equals 45°. The other variables are defined as: A_v is the area of shear reinforcement within spacing, s; the width of the section is b_v; and the shear depth is d_v. The units for the variables mentioned are square inches, inches and kips per square inch. This method is technically not applicable for the specimens in the research program since the specimens have axial load from post-tensioning, similar to service load conditions. However, this common procedure was included to show the difference between methods.

The second method is the AASHTO Method 3 which is the simplified procedure for prestressed and nonprestressed sections. The equations for V_s and V_n are the same as listed previously, Eq. 4-59 and Eq. 4-61, respectively. However, the shear resistance from the concrete is the larger of the resistance when shear and moment cause cracking, V_{ci}, and the resistance when tension in the web cause cracking, $V_{cw,}$ which is given below.

$$V_c = \begin{cases} V_{ci} = 0.02\sqrt{f'_c} b_v d_v + V_d + \frac{V_i M_{cre}}{M_{max}} \geq 0.06\sqrt{f'_c} b_v d_v \\ V_{cw} = \left(0.06\sqrt{f'_c} + 0.30 f_{pc}\right) b_v d_v + V_p \end{cases} \quad \text{(Eq. 4-67)}$$

The shear force from dead load and external loads is V_d and V_i, respectively. The maximum moment from the external loads is M_{max} and the moment causing cracking is M_{cre}. An equation is listed in the AASHTO code for M_{cre}. However, the flexural capacity when the concrete begins to crack was previously calculated based on bending theory and was documented earlier in this section. M_{cre} is calculated below from the flexural capacity results at any location along the specimen.

$$M_{cre} = M_{\text{total cap}_{cr}} - M_{SW,3pt} \quad \text{(Eq. 4-68)}$$

The stress from the post-tensioning is accounted for in the variable, f_{pc}, given below.

$$f_{pc} = \frac{P_{axial}}{bh} \quad \text{(Eq. 4-69)}$$

Section 2 describes the design of the specimens; however the important information for calculating the shear resistance is described below. The area of transverse shear reinforcement and the spacing of this reinforcement is different in the end region and splice region. Figure 4-21 and Figure 4-22 show the transverse reinforcement in the splice region and the end region. Table 4-1 summarizes the area of the transverse shear reinforcement and the center-to-center spacing, s, between each stirrup.

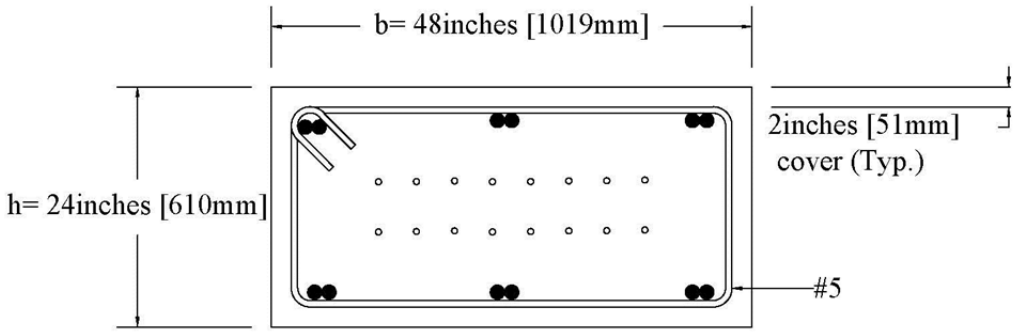

Figure 4-21. Cross Section at Splice Region with Transverse Reinforcement [taken from Alberson (2009)].

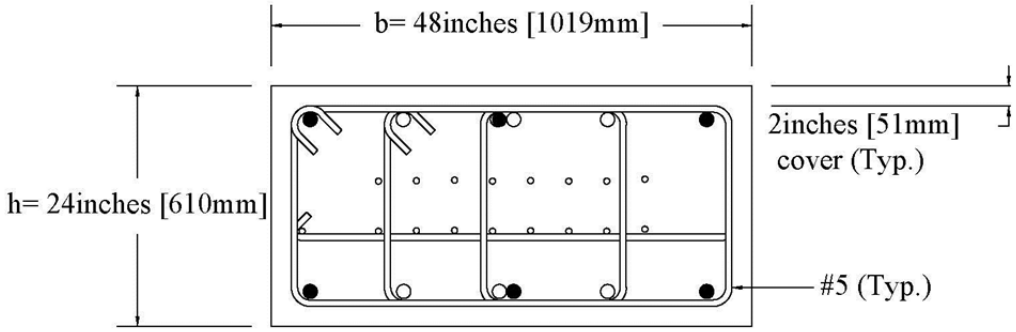

Figure 4-22. Cross Section at End Region with Transverse Reinforcement [taken from Alberson (2009)].

Table 4-1. Area and Spacing of Transverse Shear Reinforcement.

Region	A_v (inches^2)	s (inches)
Splice	0.62	12
End	1.55	6

Figure 4-23 shows the calculated shear capacity from the varying methods and the shear demand from the 3 point test setup along the LSC specimen. The shear values shown are in absolute values. The methods are constant for the given A_v and s except for at the splice end for AASHTO Method 3. At all locations, V_{ci} governed over V_{cw}. The second part of the V_{ci} equation governs for the all locations except at the splice ends where a larger value was computed for the first part. A closer look at this formula shows that in the end region, no maximum moment is present except between under the actuator and the splice end. Therefore the fraction with M_{max} is omitted at those locations. Also, the ratio between M_{cre} and M_{max} is over twice as much at the splice end than the other locations which gives reason for the second part of the equation to govern when the ratio is small. From the AASHTO Method 3, the specimen should fail from shear at the splice region from 201 kips (894 kN) at each actuator.

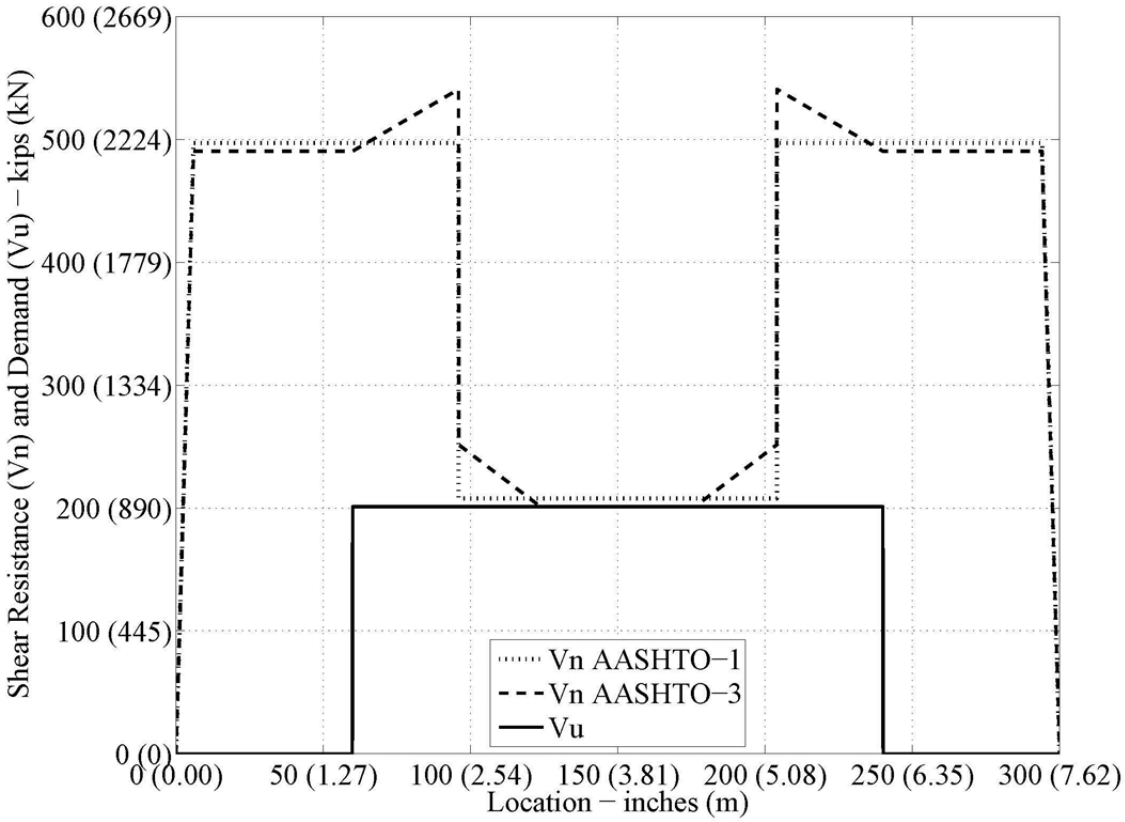

Figure 4-23. Three-Point Load Test Shear Demand and Capacity (Absolute Values)

The LSC specimens were first tested in the four-point setup, then in the three-point setup. The tension side was the same for both tests. Therefore, cracks were present prior to the three point test. The significant cracking from the four-point test occurred under the actuators (at splice end). Since the critical section for the three-point test is at the specimen center, the previous cracking was ignored for the analysis of the three-point test and the same I_{gt} and I_{cr} values were used. The only deflection method described for the three-point setup is the Step-by-Step I_{cr} method since the differences between the methods are the same for both test setups and the Step-by-Step I_{cr} was the best one for the four-point setup.

The deflection at first concrete cracking for the three-point setup ($\Delta_{3pt,cr,Step-by-Step\ Icr}$) is calculated below:

$$\Delta_{3pt,cr,Step-by-Step\ Icr} = \frac{F_{act,3pt_{cr}}}{6\ E_c\ I_{gt}}\left(4x - 3L_{act}x^2 - {L_{act}}^2\right) \quad \text{(Eq. 4-70)}$$

The deflection at the intermediate values between first cracking and first yielding are calculated using the Step-by-Step I_{cr} method described for the four-point setup. The deflection at intermediate steps for the three-point test $\Delta_{3pt,cr,y,i}$is calculated as follows:

$$\Delta_{3pt,cr,y,i} = \frac{(F_{act,3pt_i} - F_{act,3pt_{i-1}})}{24\ E_c\ I_{cr_i}}\left(4x - 3L_{act}x^2 - {L_{act}}^2\right) \quad \text{(Eq. 4-71)}$$

where $F_{act,3pt_i}$, and I_{cr_i} are the load and second moment of area calculated at each step using Eq. 4-63 and Eq. 4-49. For the calculation of $\Delta_{cr,3pt,y,1}$, $F_{act,3pt_{cr}}$ must be used for $F_{act,3pt_{i-1}}$ since the force at cracking is the preceding force.

The deflection at first yielding is calculated as follows where the preceding force that is subtracted from the load when steel yields is F_{act_n} which is the last intermediate force. The second moment of area using the neutral axis at yielding, I_{cr_y}, is also used.

$$\Delta_{3pt,y,Step-by\ Step\ Icr} = \frac{(F_{act_y} - F_{act_n})\ L_{supp}}{6\ E_c\ I_{cr_y}}\left(3L_s x_{supp} - 3L_s x_{supp}^2 - {L_{supp}}^2\right) \quad \text{(Eq. 4-72)}$$

The deflection at ultimate must consider the plastic deformations which occur after the reinforcing steel yields similarly to the four-point setup. The plastic hinge rotation is the

same for each test setup. The plastic hinge length is also the same. This is caused by the same depth of the bottom layer of the reinforcing steel, 20.67 inches (525 mm), and the same distance between the maximum moment and no moment, 90 inches (2286 mm).

Assuming that the entirety of plastic deformations occur at the center support, the plastic deformations can be found from the plastic hinge rotations and the geometry of the test setup illustrated in Figure 4-24. The elastic deflection at first yielding for the three-point setup, $\Delta_{3pt,y}$, was added to the plastic deflection to calculate the total deflection at the ultimate limit, $\Delta_{3pt,u}$, in Eq. 4-73.

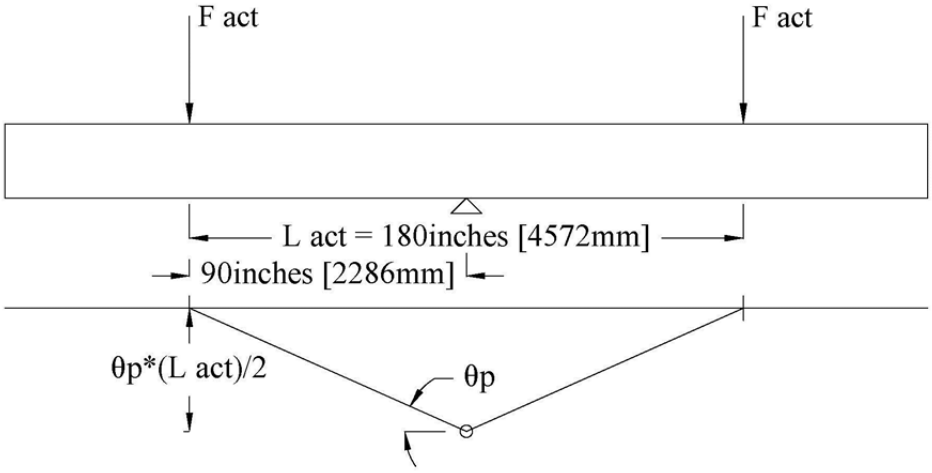

Figure 4-24. Plastic Hinge Rotation for Three-Point Setup.

$$\Delta_{3pt,u} = \theta_p \frac{L_{act}}{2} + \Delta_{3pt,y} \qquad \text{(Eq. 4-73)}$$

Figure 4-25 shows the calculated load vs. deflection for the three-point setup. The deflection calculated for the three-point setup is under the actuator which is 60 inches (1524mm) from the end of the specimen. Shear deflection was neglected in the

deflection calculations for simplicity and a check on whether the response is governed by bending. The deflections from the three-point setup were smaller than the four-point setup. At the same load from each actuator in both setups, the deflection for the four-point test under the actuator (90 inches (2286 mm) from end) is 2.8 times the deflection for the three point test under the actuator (60 inches (1524mm) from end). The specimen can resist the calculated shear failure until each actuator is loaded with 201 kips (894 kN). However, the specimen will fail from flexural bending at 167 kips (743 kN). Therefore, the moment capacity and demand controls the failure for both the three-point and four-point test setups.

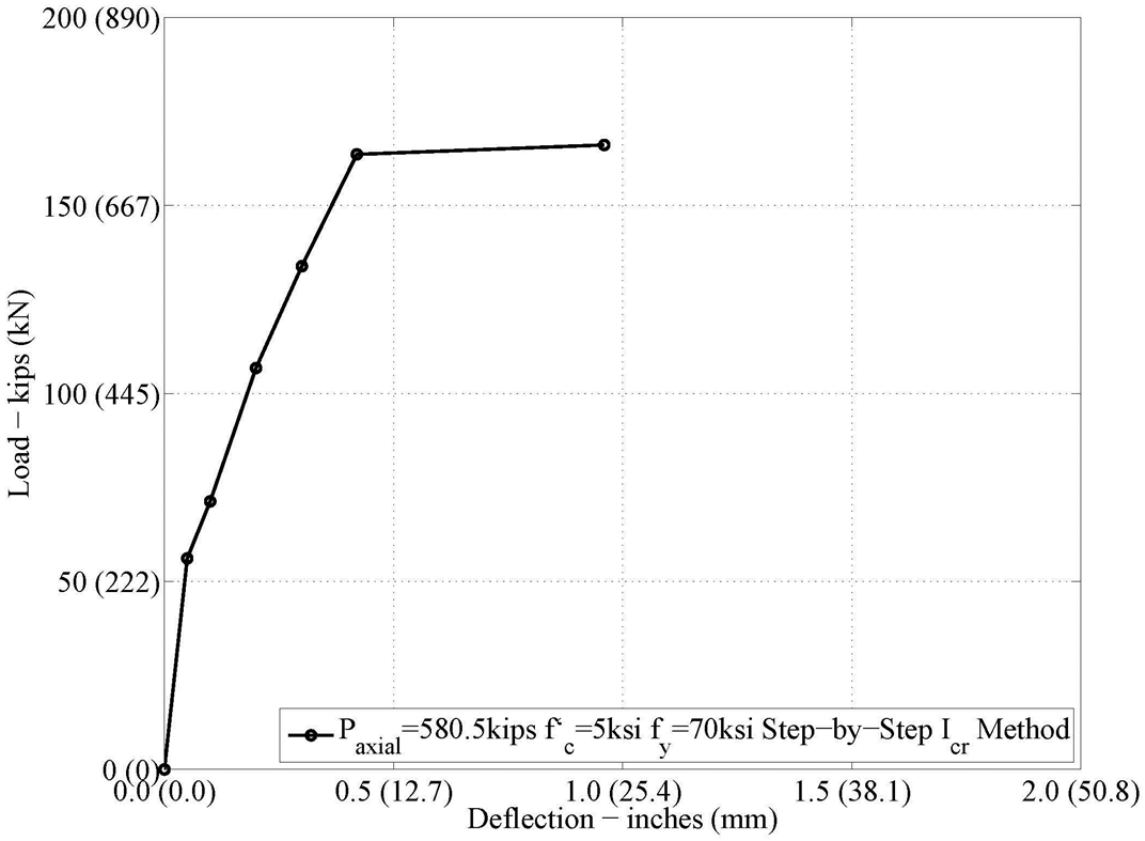

Figure 4-25. Load vs. Deflection for Step-by-Step I_{cr} Method under Actuator for Three-Point Test Setup.

4.4 Summary

An analytical model was developed to predict the behavior of the specimens during the four-point and three-point tests. The flexural capacity in the splice region and end region was calculated by assuming the longitudinal reinforcement develops anchorage linearly from zero at the end to the full strength at the L_d, L_{dh}, or L_{dc} from the end. In addition, the shear capacity was calculated since a shear force is present during the three-point test.

5. EXPERIMENTAL TESTING PROGRAM

5.1 Introduction

This section discusses the experimental test setups, specimen instrumentation, and specimen behavior during structural load testing. LSC specimens 1, 3, 5, 8, 9, 10, 15, and 16 were tested with varying degrees of ASR/DEF deterioration at the time of testing. The LSC specimens are numbered chronologically with the casting date. The concrete compression strength results from cylinders stored in a curing room and in the field conditions at the Riverside Campus are also reported in this section. The control specimens, LSC15 and LSC16, were stored inside the Structure and Materials Testing Laboratory with no exposure to the environmental weather conditions or supplemental water, thus eliminating ASR and DEF from forming. In a similar project with the same concrete composition, a TxDOT petrography report confirmed from cores taken from specimens kept in the lab that no ASR or DEF distress had formed. The test procedures and instrumentation are summarized in this section, for more details see Bracci et al. (2011).

Table 5-1 shows the dates of the specimen casting, initial environmental exposure, structural load testing, and the degree of deterioration from ASR and DEF. The degree of ASR and DEF deterioration was established from knowledge gained from the internal and external strains measured (section 3) and the petrography analysis report summarized in section 3. Table 5-2 shows the last average transverse surface strains of all faces before the LSC specimen was tested and the maximum crack width measured on each face. LSC1, LSC3, LSC9, and LSC10 were tested before the 90° rotation are described in 3; therefore data readings on Large Face 2 had not begun. Of the specimens exposed to the ASR and minimal DEF deterioration conditions, LSC9 and LSC10 had the smallest amount of surface expansion and least amount of surface cracking on all sides prior to testing. A moderate amount of surface expansion and cracking occurred in

LSC 1 and LSC3. LSC5 and LSC8 had the most expansion and surface cracking prior to structural testing of all specimens tested to date. These surface expansions and maximum crack width amounts are summarized in the tables as one way of trying to characterize the degree of deterioration.

Table 5-1. Specimen Age and Degree of Deterioration.

LSC Specimen #	Date of Casting	Date of Initial Exposure	Date of Structural Load Test	Degree ASR	Degree DEF
1	1/2008	5/2008	8/2010	M/L	N/E
3	2/2008	5/2008	8/2010	M/L	N/E
5	4/2008	5/2008	7/2011	M/L	N/E
8	5/2008	7/2008	7/2011	M/L	N/E
9	6/2008	7/2008	2/2010	M/L	N/E
10	6/2008	7/2008	2/2010	M/L	N/E
15	8/2008	N/A	2/2009	N	N
16	8/2008	N/A	2/2009	N	N

N/A – specimen was not exposed to the environmental deterioration conditions.
N – None; E – Early stage; M – Middle stage; L-Late stage. Note that these stages were established based on the petrography analysis of concrete cores taken from specimens after structural testing and also from the surface and internal expansion measurements and cracking throughout the specimen prior to testing.

Table 5-2. Specimen Surface Expansions.

LSC #	Average Transverse Surface Strain at Time of Load Test				Maximum Crack Width at Time of Load Test (inches)			
	Small Face 1	Small Face 2	Large Face 1	Large Face 2	Small Face 1	Small Face 2	Large Face 1	Large Face 2
1	0.0064	0.0024	0.0070	N/A	0.03	0.04	0.04	N/A
3	0.0067	0.0026	0.0054	N/A	0.04	0.03	0.03	N/A
5	0.0080	0.0087	0.0090	0.0123	0.03	0.03	0.03	0.04
8	0.0082	0.0092	0.0088	0.0112	0.01	0.03	0.03	0.03
9	0.0051	0.0009	0.0026	N/A	0.01	0.01	0.01	N/A
10	0.0052	0.0013	0.0038	N/A	0.01	0.02	0.02	N/A
15	N/A	N/A	N/A	N/A	N/A	N/A	N/A	N/A
16	N/A	N/A	N/A	N/A	N/A	N/A	N/A	N/A

N/A – data not taken, but presumed to be minimal.

The LSC specimens were structurally tested in two different test setup arrangements to evaluate the performance of the column lap splice region under varying levels of premature concrete deterioration due to ASR and minimal amounts of DEF. The test setups, structural performance and comparison of results will be reported in the remainder of the section.

5.2 Four-Point Flexural Load Setup

The specimens' were first tested in the four-point setup which causes a constant moment and no shear force across the splice length. The experimental testing procedure and instrumentation locations are summarized and illustrated in this section, but for more details see Bracci et al. (2011).

5.2.1 Experimental Design and Specimen Layout

Figure 5-1 shows LSC specimen in the four-point test. The pinned supports were located 6 inches (152.4 mm) from either end of the specimen. This distance was chosen to prevent the concrete cover from crushing. Neoprene pads were placed between the support and the concrete to prevent stress concentrations intensified by material imperfections (Figure 5-2). The neoprene pads were also placed between the fixed support for the actuator load and the top of the specimen (Figure 5-3).

Figure 5-1 shows the shear and moment demand from the four-point load setup. The max shear force is the force from each actuator, F_{act}, which is constant between the support and the load. There is no shear force in the splice region which is between the two actuator loads. The maximum moment is the F_{act} times the distance between the supports, L_{supp}.

Two 220 kips (979 kN) actuators attached to an overhead steel frame were used to load the specimen in displacement control loading. The steel frame was anchored to the strong floor in the Structure and Materials Testing Laboratory. Figure 5-4 shows the actuators positioned over one of the LSC specimens.

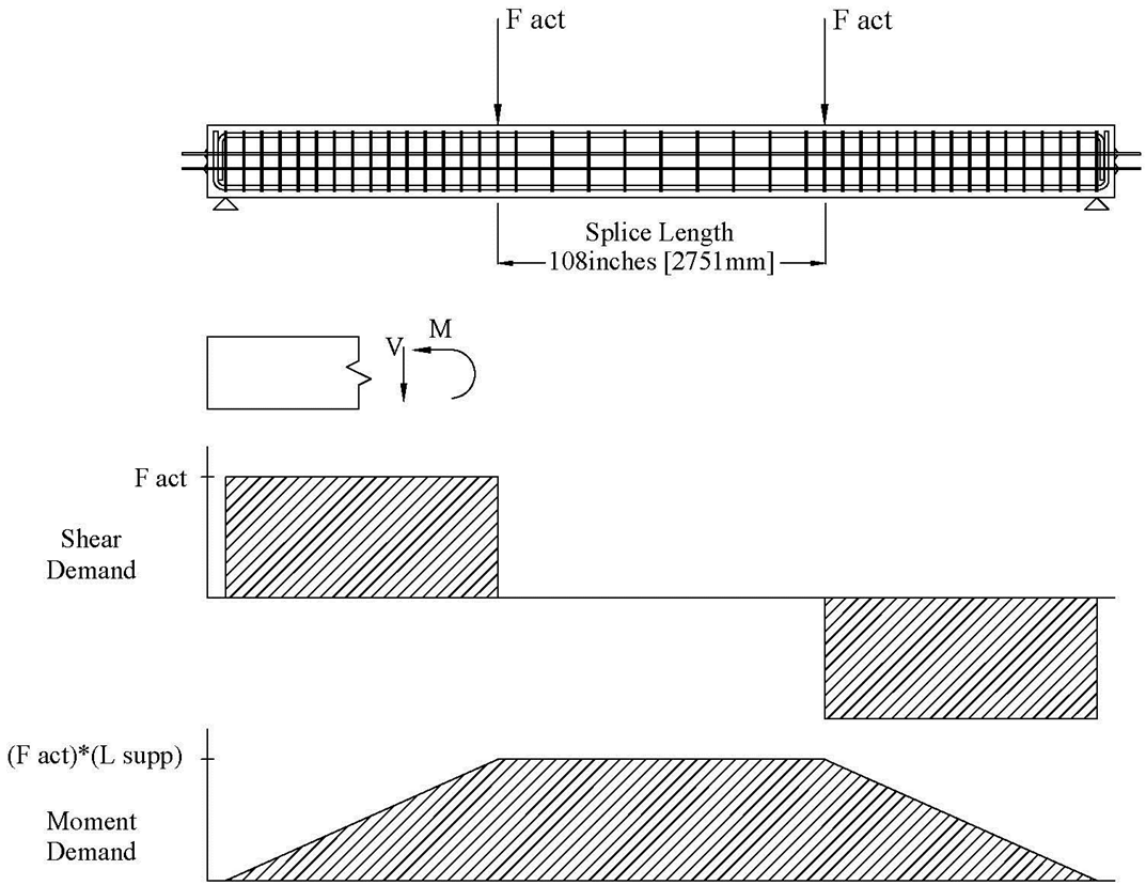

Figure 5-1. Four-Point Load Test Setup and Demand Loading [taken from Alberson (2009)].

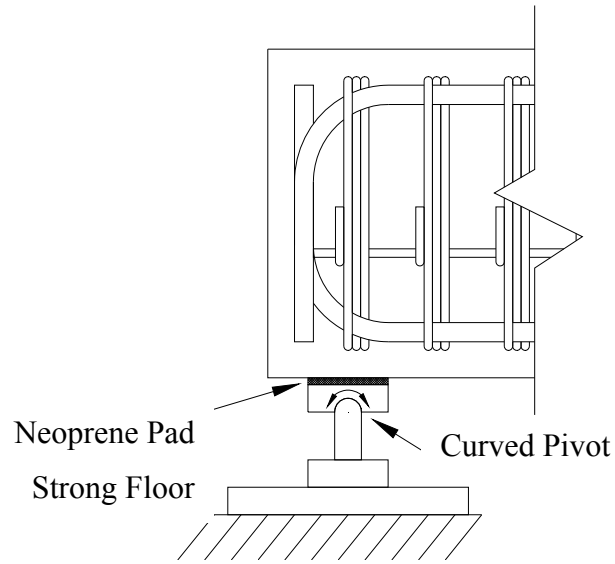

Figure 5-2. Pinned Support Setup [taken from Alberson (2009)].

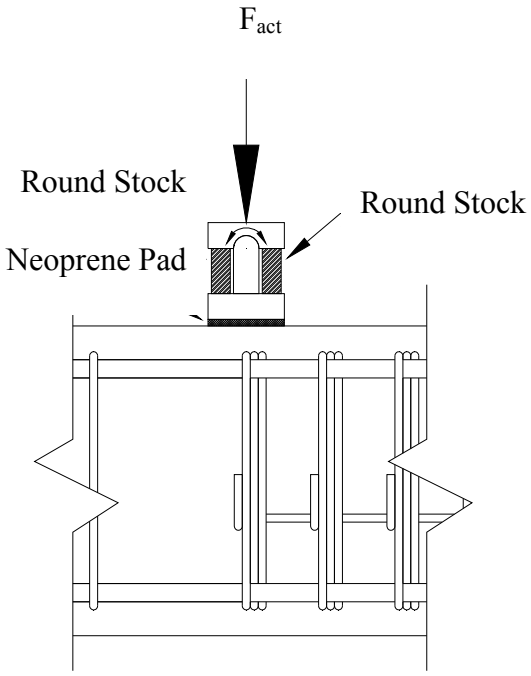

Figure 5-3. Fixed Support Setup [taken from Alberson (2009)].

Figure 5-4. Specimen in the Four-Point Test Setup [taken from Alberson (2009)].

5.2.2 Instrumentation

In addition to the internal instrumentation installed during construction (see section 2.2), external instrumentation was attached to the LSC specimens to measure the deflections and external surface strains during the structural load testing. String potentiometers (STR) with a 4 inch (102 mm) stroke, were used measured the specimen deflections at various points. Figure 5-5 shows a typical STR connected to the bottom of the LSC specimen to measure vertical deformations. Figure 5-6 shows the position of the STRs on the LSC specimen to measure critical deformations during testing.

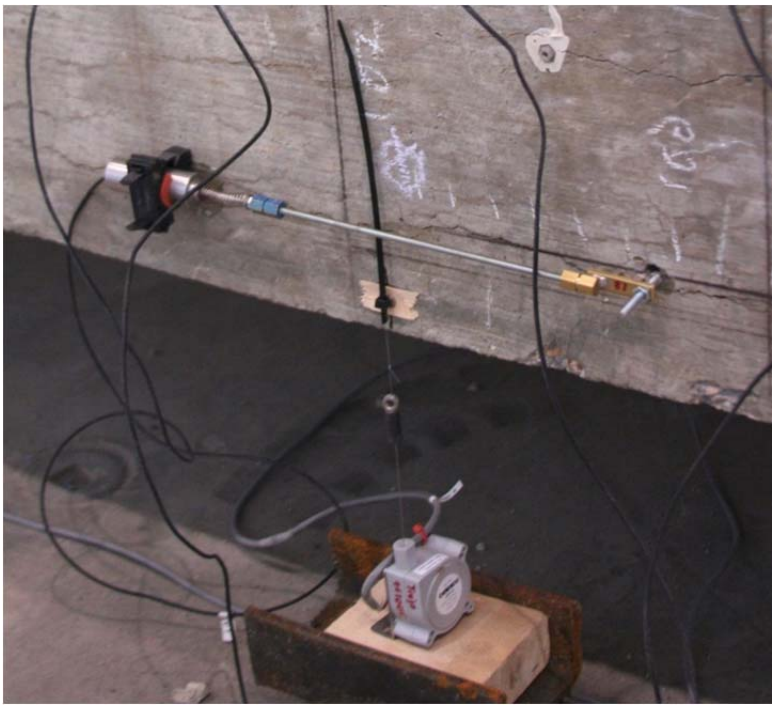

Figure 5-5. STR Installation Prior to Testing.

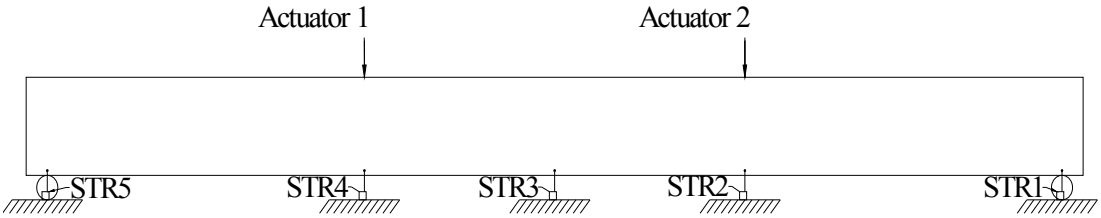

Figure 5-6. STR Locations for the Four-Point Test [taken from Alberson (2009)].

The relative specimen deflections under Actuator 1 and Actuator 2 were calculated using STR readings. The initial readings from the STRs were zeroed to account for the flexibility in the test setup and neoprene support conditions. The deflection under Actuator 1 and Actuator 2 ($\Delta_{\text{act 1,4pt}}$ and $\Delta_{\text{act 2,4pt}}$) was calculated by subtracting the deflection at the ends (Δ_{STR5} and Δ_{STR1}) which accounted for the flexibility in the test

setup and neoprene support conditions from the original deflection under the actuators (Δ_{STR4} and Δ_{STR2}).

$$\Delta_{act\ 1,4pt} = \Delta_{STR4} - \Delta_{STR5} \quad \text{(Eq. 5-1)}$$

$$\Delta_{act\ 2,4pt} = \Delta_{STR2} - \Delta_{STR1} \quad \text{(Eq. 5-2)}$$

Linear variable differential transformers (LVDT or LV) and concrete embedment gages (KM) were also used to measure the tension and compression strains of the specimen in various locations during the load testing. LVDTs were securely attached to the concrete specimen separated by a gage length of 4 inches (102mm) or 12 inches (305 mm). Holes (1/4”) were drilled into the specimen face and 1/4" stainless steel threaded couplers were hammered into the holes and secured using adhesive epoxy. These couplers provided an anchor to screw the threaded rod into the specimen. The threaded rods were attached to the LVDT using metal and plastic brackets. Figure 5-5 and Figure 5-7 show sample LVDTs on the LSC specimens. The final positioning of the LVDTs on the specimens and the LVDT gage lengths are discussed in the forthcoming paragraphs.

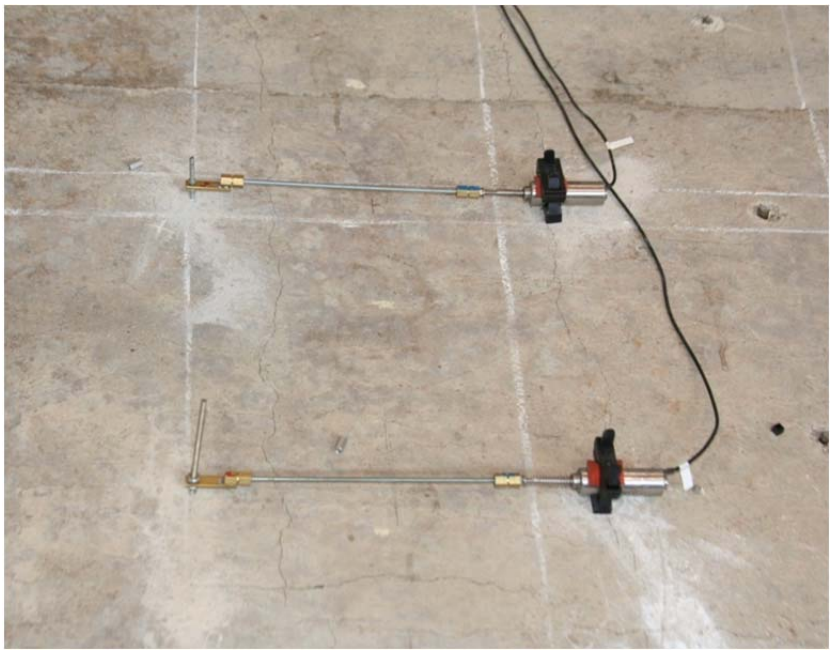

Figure 5-7. LVDT Installation Prior to Testing.

KM gages were attached to the surface of the LSC specimens using adhesive epoxy. First, the surface was smoothed by sanding across the entire footprint of the KM base plates. A spacing bar was placed between the KM base plates to keep the base plates a proper distance apart (4 inches (100 mm) gage length). Before testing, the base plates were epoxied to the concrete surface, the spacing bars were then removed, and the KM gages were attached to the base plates. Figure 5-8 shows a KM gage attached to the LSC specimen.

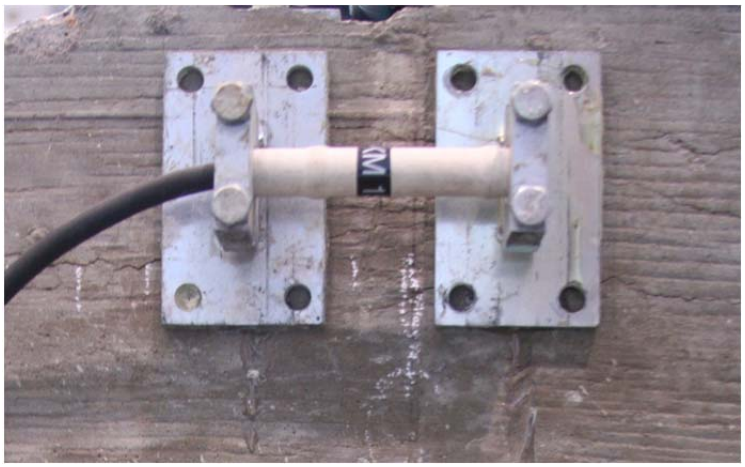

Figure 5-8. KM Gage Installation Prior to Testing.

The first tested specimen was LSC16. The four-point test for LSC16 was used to determine the external strain locations for the other tests. The KMs and SGs were in the same locations on different sides of the specimen to compare the accuracy between these two gages in the tension and compression region. Figure 5-9 shows the locations of the SGs, KMs, and STR external instrumentation on each face of the LSC specimens.

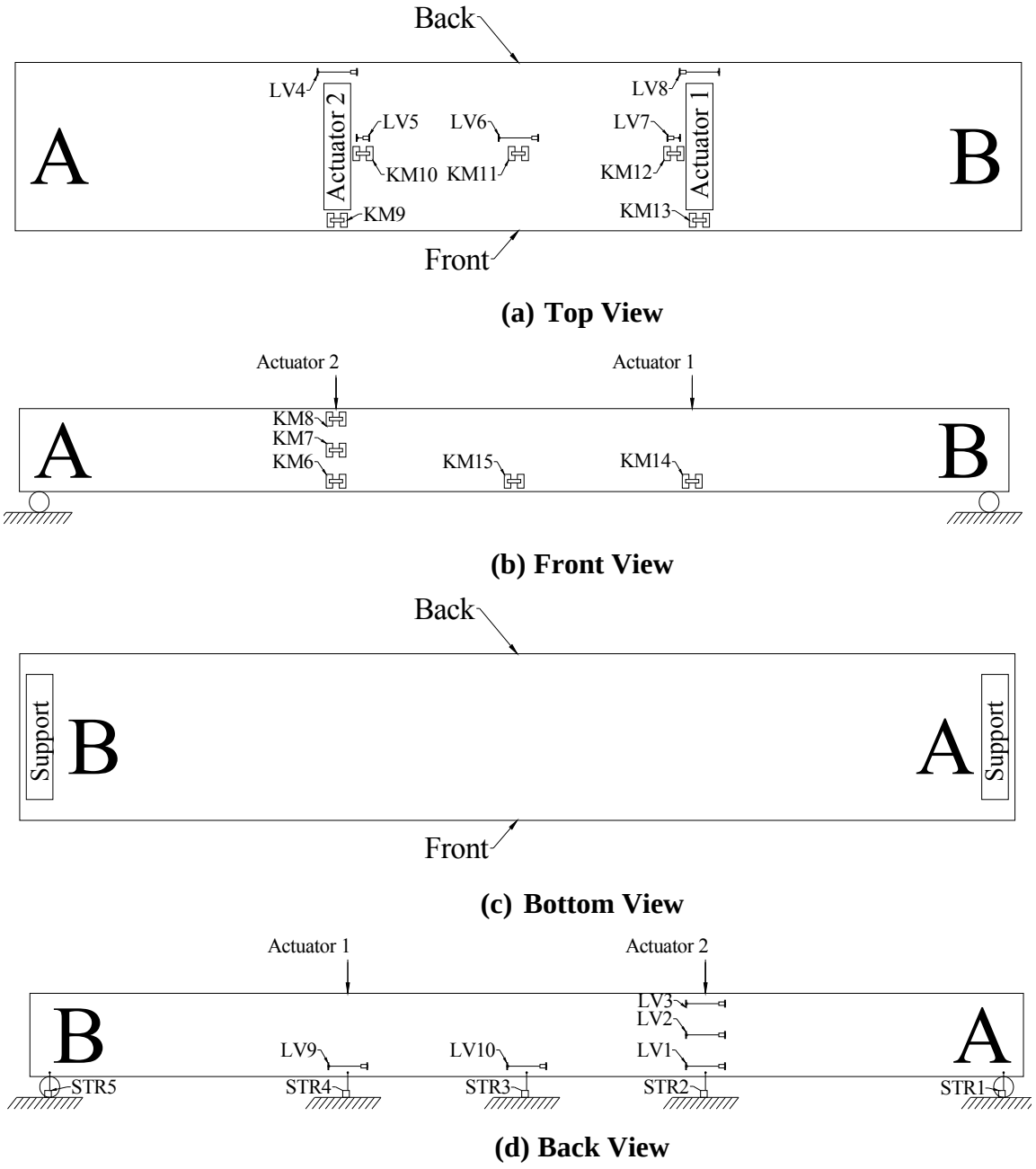

Figure 5-9. External Instrumentation Layout for the Four-point Test of LSC16 (taken from Alberson [2009]).

On the tension side, the cracks did not always from in the small 4 inch (102 mm) gages length of the KM gages (Figure 5-10). Therefore, only LVDTs were used in the tension region for the remaining tests.

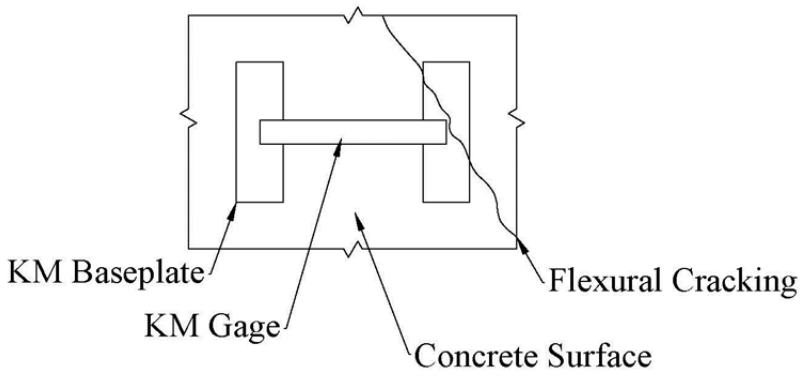

Figure 5-10. KM Gage Detail [taken from Alberson (2009)].

Figure 5-11 shows the external instrumentation for the four-point tests following LSC16. Additional LVDTs were added in the tension region to compare the strains along the splice length.

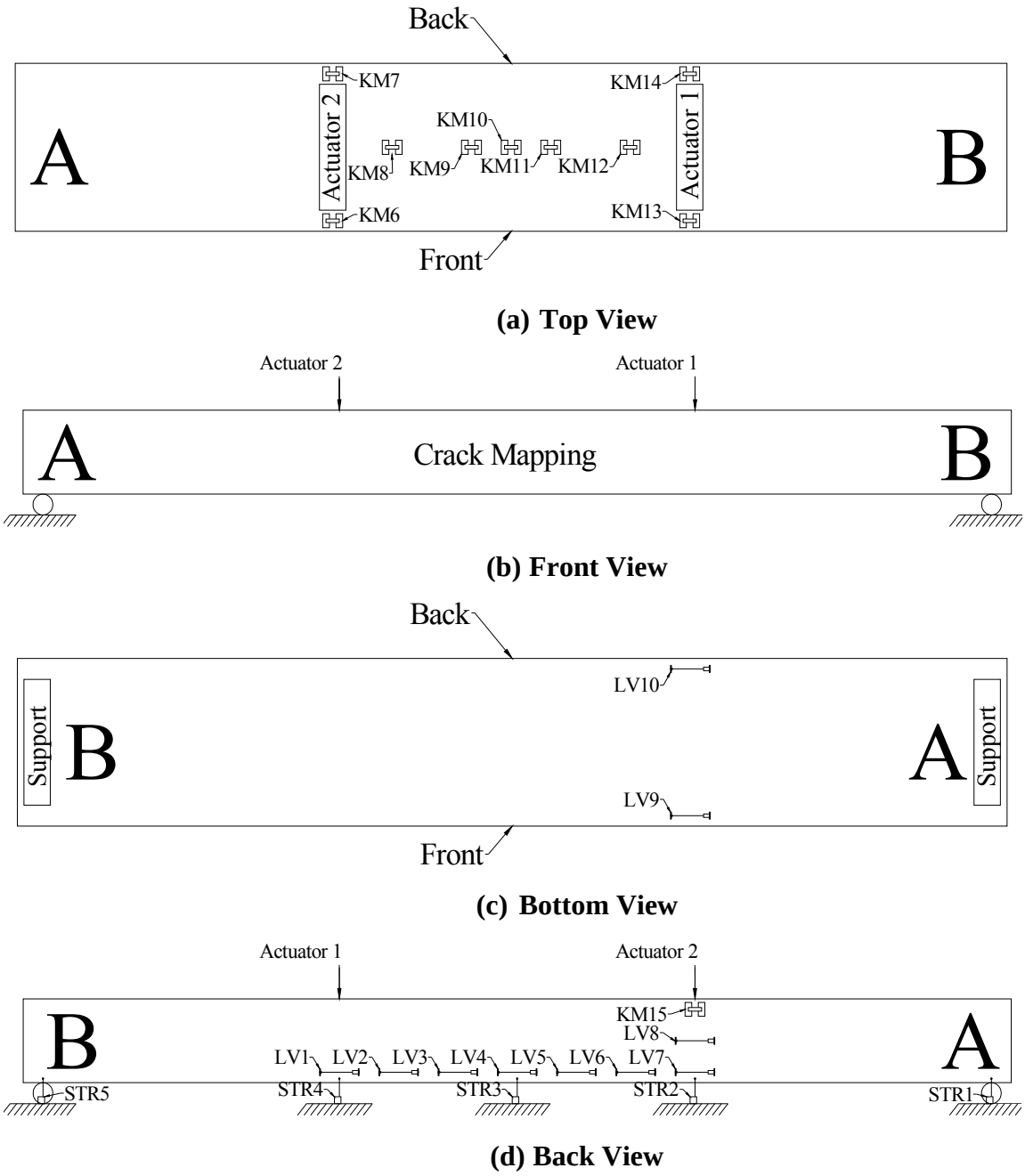

Figure 5-11. External Instrumentation Layout for the Four-Point Tests except for LSC16 [taken from Alberson (2009)].

5.2.3 Test Procedures

A data acquisition system (DAQ) recorded the data once every second. The actuators exerted a load on the specimen in a displacement controlled rate of 0.001 inch/second (25 μm/second). Once the first cracks occurred, the load rate increased to 0.002 inches/second (50 μm/second) until near failure of the specimen. A few times during the test, the loading was stopped to view the cracks and take pictures.

5.3 Three-Point Flexural Load Setup

After the specimens were tested in the four-point setup, the three-point test took place. Figure 5-12 shows the three-point test setup, shear demand, and moment demand. The specimen was balanced on a pin support at center before the loading began. This setup provides a shear demand equal to the load from each actuator between the load points. The actuators were moved to 180 inches (4572 mm) apart which produced a linearly varying moment demand. The maximum moment which occurs at the support is equal to the constant moment during the four-point test when the same actuator load is applied. However, since the specimen does not need to be preserved for a future test, the maximum load during the three-point test will be larger than the four-point test.

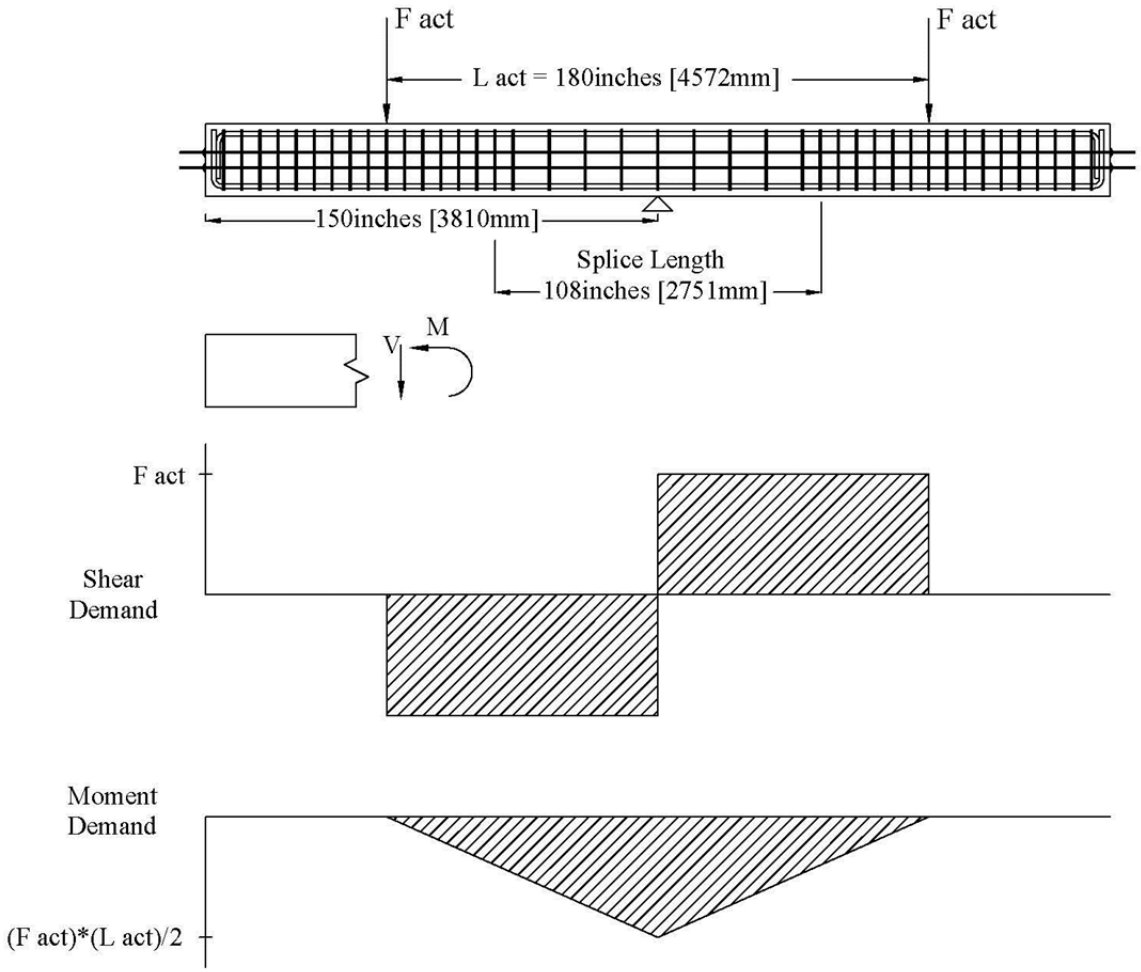

Figure 5-12. Three-Point Load Test Setup and Demand Loading [taken from Alberson (2009)].

5.3.1 Experimental Design and Specimen Layout

Figure 5-12 shows that the tension side is on top. The specimens were rolled 180° about the longitudinal axis so that the tension side during the four-point test is also the tension side during the three-point test.

5.3.2 Instrumentation

Figure 5-13 shows the external instrument layout during the three-point test. Strain gages (KM and LV) are attached to the specimen in a similar layout as four-point test. However, since the maximum moment occurs at the support, the majority of the instruments are attached in the center section.

Three string potentiometers measured the specimen deflections at the support and under each actuator during the three-point test. The following equations were used to calculate the relative specimen deflection at each actuator loading point. The deflections under the support, Actuator 1, and Actuator 2 are Δ_{STR1}, Δ_{STR3}, and Δ_{STR2}. The relative deflection under Actuator 1 and Actuator 2 are $\Delta_{act\ 1,3pt}$ and $\Delta_{act\ 2,3pt}$. The locations of the actuators and string potentiometers (STR) are pictured in Figure 5-13.

$$\Delta_{act\ 1,3pt} = \Delta_{STR3} - \Delta_{STR1} \quad \text{(Eq. 5-3)}$$

$$\Delta_{act\ 2,3pt} = \Delta_{STR2} - \Delta_{STR1} \quad \text{(Eq. 5-4)}$$

5.3.3 Test Procedures

The specimens were loaded at a constant, displacement controlled rate of 0.002 inches/sec (50.8 μm/sec) during the three-point test. A few times during the test, the loading was stopped to view the cracks and take pictures.

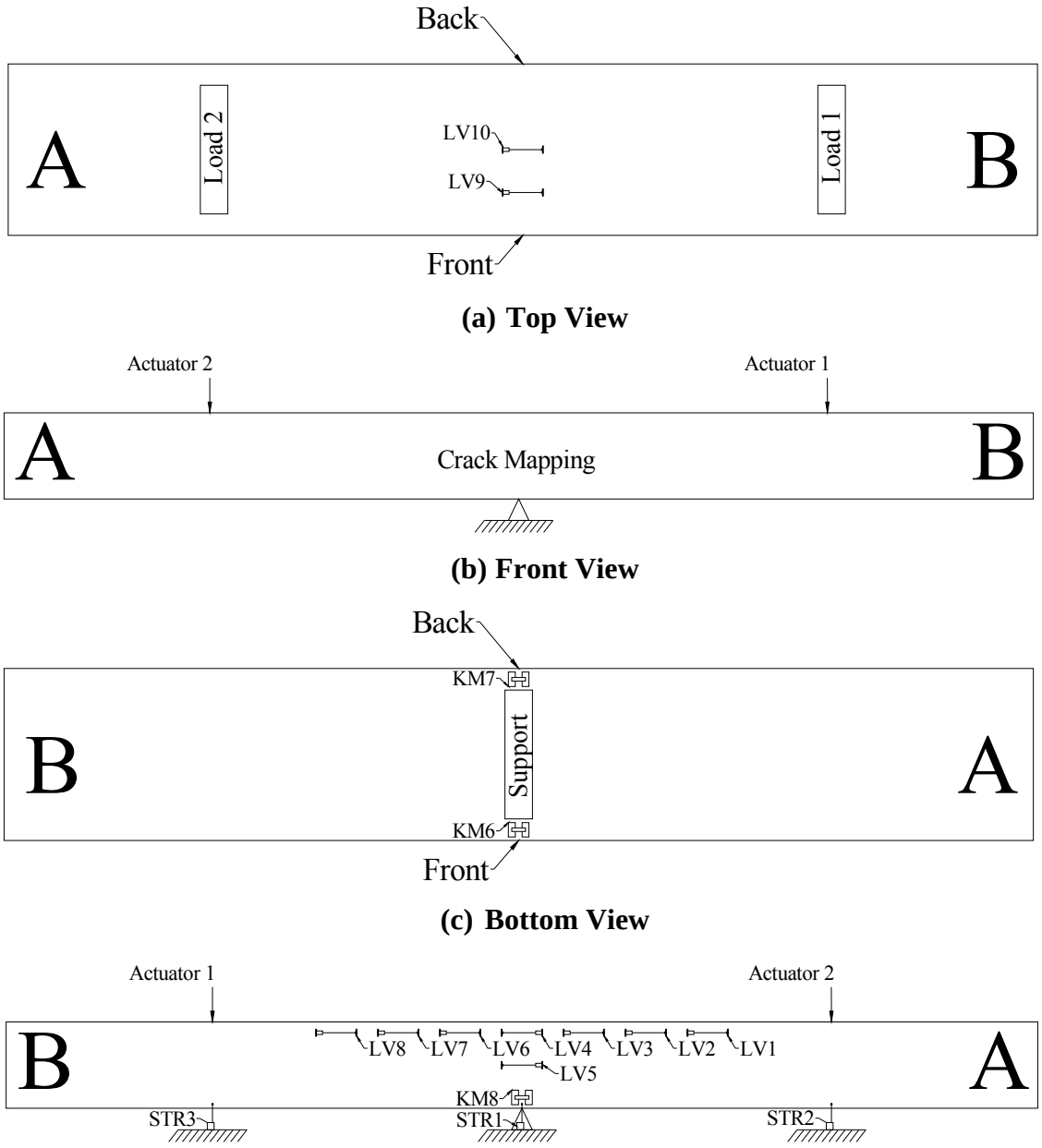

(a) Top View

(b) Front View

(c) Bottom View

(d) Back View

Figure 5-13. External Instrument Layout for the Three-Point Tests [taken from Alberson (2009)].

5.4 Experimental Response

5.4.1 Material Strength Test Results

At the time of casting the large scale specimens, 4 in x 8 in (101 mm x 203 mm) cylinders were also cast according to ASTM C39-01. Half of the cylinders were stored at the Texas A&M University Riverside Campus with the LSC specimens exposed to accelerated deterioration; the other half were stored in a curing room. Three cylinders from both the field as well as curing room were tested for 28 day strength as specified by ASTM C39-01 (2001). In addition, cylinders were tested at the time of LSC specimen testing. Table 5-3 displays the individual and average compressive strength of 3 cylinders for all cases as well as the cylinder test date. Note that the field cylinders for LSC15 and LSC16 were not exposed to the same environmental conditions as the others since they were the control specimens. The specimens were all cast separately, therefore with different mixes, even though the same mix design was used throughout. The concrete mix was designed for a compressive strength of 5.0 ksi (34 MPa); however, few cylinder tests resulted with this strength. Only 2% of the cylinders had a compressive strength above the 5.0 ksi (34 MPa) design at 28 days and 56% of cylinders reached this strength at the time of the structural load test. The control specimens compressive strength averaged 1.0 ksi (7 MPa) lower than the non-control specimen which is probably due to excess water during batching from aggregate moisture. The non-control specimens increased an average of 0.9 ksi (6 MPa) from the 28 day strength test and the time of the structural load test which shows the concrete continued to gain strength after 28 days as usual. The strength at the time of the structural load test for control specimens was 0.2 ksi (1 MPa) lower than at the 28 day strength which may be due to the small sample size.

Table 5-3. Concrete Cylinder Compressive Strengths [taken from Bracci et al. (2011)].

LSC #	28 Day Strength ksi (Mpa)					Strength at Time of Structural Testing ksi (Mpa)				
	Test Date	Cured		Field		Test Date	Cured		Field	
		Sample	Avg.	Sample	Avg.		Sample	Avg.	Sample	Avg.
1	2/08	4.6	4.6 (31)	4.5	4.5 (31)	9/10	4.3	5.5 (38)	5.3	5.3 (37)
		4.5		4.7			6.1		5.0	
		4.6		4.4			6.2		5.6	
3	3/08	4.7	4.8 (33)	4.6	4.4 (31)	9/10	6.2	5.7 (39)	5.1	5.2 (36)
		4.9		4.3			5.4		6.6	
		4.8		4.4			5.5		3.9	
5	4/08	4.7	4.6 (32)	4.3	4.3 (30)	8/11	5.9	5.6 (39)	6.1	6.0 (42)
		4.6		4.3			5.4		6.2	
		4.6		4.3			5.6		5.8	
8	6/08	4.0	3.9 (27)	4.0	3.9 (27)	8/11	5.3	5.3 (37)	5.3	5.2 (36)
		3.8		3.8			5.3		5.4	
		4.0		3.9			5.4		5.0	
9	7/08	4.7	4.9 (34)	3.8	4.1 (28)	3/10	4.6	4.2 (29)	5.4	5.0 (34)
		5.0		4.2			4.4		4.1	
		4.9		4.3			3.7		5.4	
10	7/08	4.6	4.6 (32)	4.5	4.4 (30)	3/10	4.6	4.9 (34)	5.1	5.0 (35)
		4.6		4.4			4.7		5.7	
		4.7		4.3			5.3		4.3	
15	9/08	3.8	3.9 (27)	3.8	3.9 (27)	2/09	3.4	3.5 (24)	4.0	3.9 (27)
		4.0		3.8			3.8		3.7	
		3.9		4.0			3.3		4.1	
16	9/08	4.0	4.0 (27)	3.9	3.7 (26)	2/09	3.7	3.9 (27)	3.2	3.5 (24)
		3.9		3.5			3.9		3.5	
		4.0		3.8			4.0		3.7	

Figure 5-14 and Figure 5-15 shows the typical cracking from cylinders stored in the curing room and in the field respectively. There is significantly more cracking from the cylinder stored in the field similar to the LSC specimens. However, the tests results (Table 5-3) show this cracking did not negatively affect the compressive strength. Figure 5-16 shows the cylinders stored with the LSC specimens at the Riverside Campus. More information about the cylinder tests is available in Bracci et al. (2011).

Figure 5-14. Cracking of a Cylinder Stored in the Curing Room [taken from Bracci et al. (2011)].

Figure 5-15. Cracking of a Cylinder Stored at the Riverside Campus [taken from Bracci et al. (2011)].

Figure 5-16. Cylinders at the Riverside Campus [taken from Bracci et al. (2011)].

To estimate the stress-strain behavior of the concrete, an analytical model using Todeschini's concrete stress function (Todeschini et al. 1964) was used as follows:

$$f_c' = 0.9f_c' \quad \text{(Eq. 5-5)}$$

$$\varepsilon_0 = 1.71\frac{f_c'}{E_c} \quad \text{(Eq. 5-6)}$$

$$f_c = \frac{2f_c'\frac{\varepsilon}{\varepsilon_0}}{1+\left(\frac{\varepsilon}{\varepsilon_0}\right)^2} \quad \text{(Eq. 5-7)}$$

where f_c and ε are the varying stress and strain, respectively. The specified concrete strength, f'_c , is shown in Table 5-3 for the different specimens and E_c was calculated from the f'_c per ACI. An additional computation for E_c can be found in Gardoni et al. (2007). The cylinders for LSC15 and LSC16 were instrumented with two LVDT's, one on each side of the cylinder. These LVDT's were used to measure the axial strain during

the compression tests. The average displacements from each LVDT were divided by the gage length of the LVDTs to calculate the strain as follows.

$$\varepsilon_{LVDT} = \frac{(\Delta_{LVDT\,1}+\Delta_{LVDT\,2})/2}{L_{LVDT}} \quad \text{(Eq. 5-8)}$$

The concrete stress was calculated by dividing the applied force by the cross sectional area of the cylinder. Figure 5-17 shows the stress vs. strain from the cylinder compression tests on LSC15 and LSC16 cylinders. The cylinders stored in the field are about 75% less stiff than the cylinders stored in the curing room. The analytical model with an f'c of 4 ksi (28 MPa) is a good match for average cylinder.

In addition to the cylinder compression tests, one 4 in. diameter core was taken from LSC1 and LSC3 after they were structurally tested. The cores were tested and instrumented in the same manner as the cylinders from LSC15 and LSC16. Figure 5-18 shows the compressive stress-strain plots for the two cores. The strength of the core from LSC1 was about 1 ksi (7 MPa) lower than both the cured and field cylinder strengths for LSC1 at time of structural testing. The LSC3 core had about the same strength as the field cylinder and was around 0.5 ksi (3 MPa) lower than the cured cylinder average at time of structural testing. The loss in strength could be due to material deterioration, but is most likely due to imperfections in the cores as a result of the coring process. In addition, it seems that the analytical axial stress-strain stiffness is somewhat larger than the experimentally measured stiffness, possibly due to the effects of premature concrete deterioration.

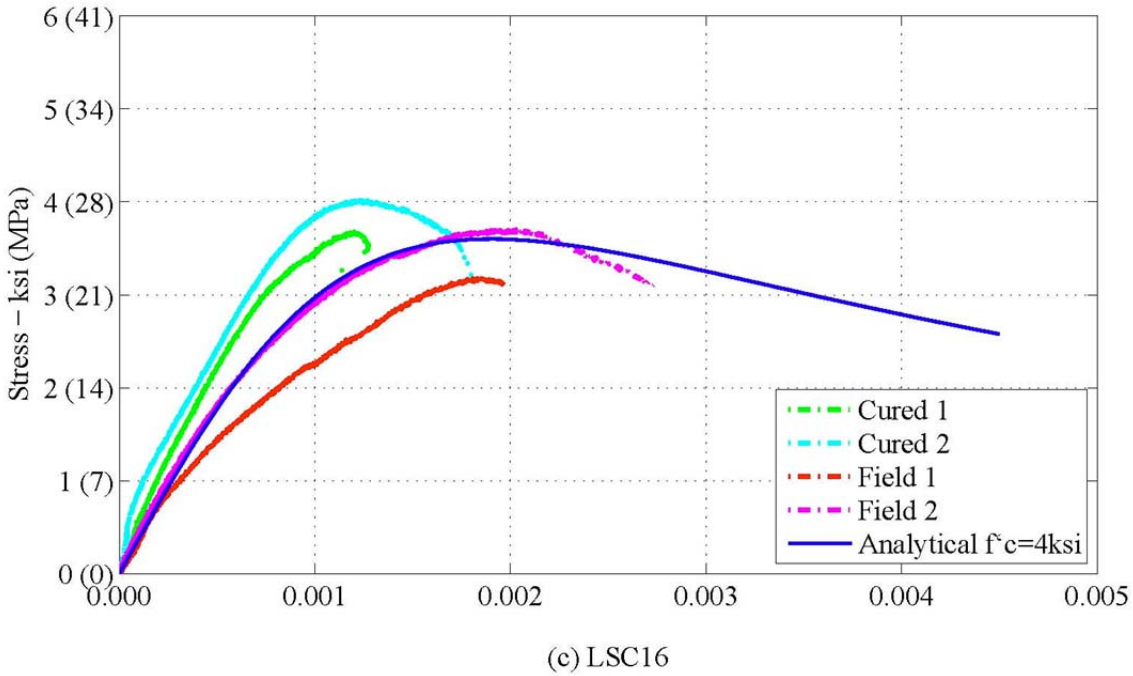

(c) LSC16

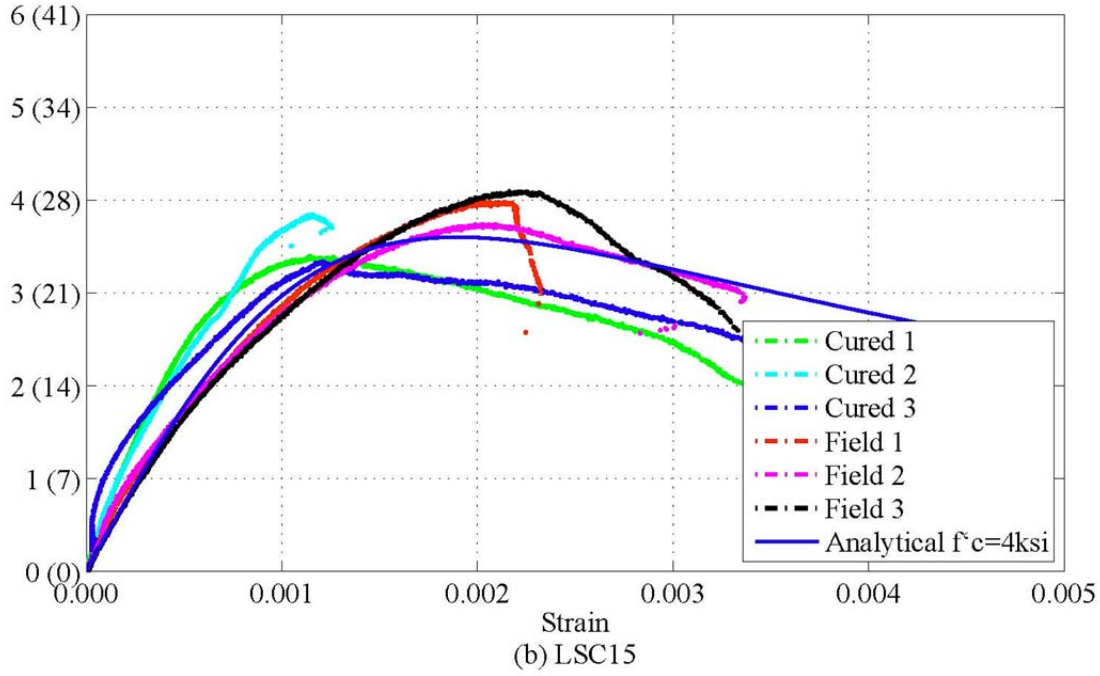

(b) LSC15

Figure 5-17. Compression Stress vs. Strain for LSC15 and LSC16 Cylinders (taken from Alberson [2009]).

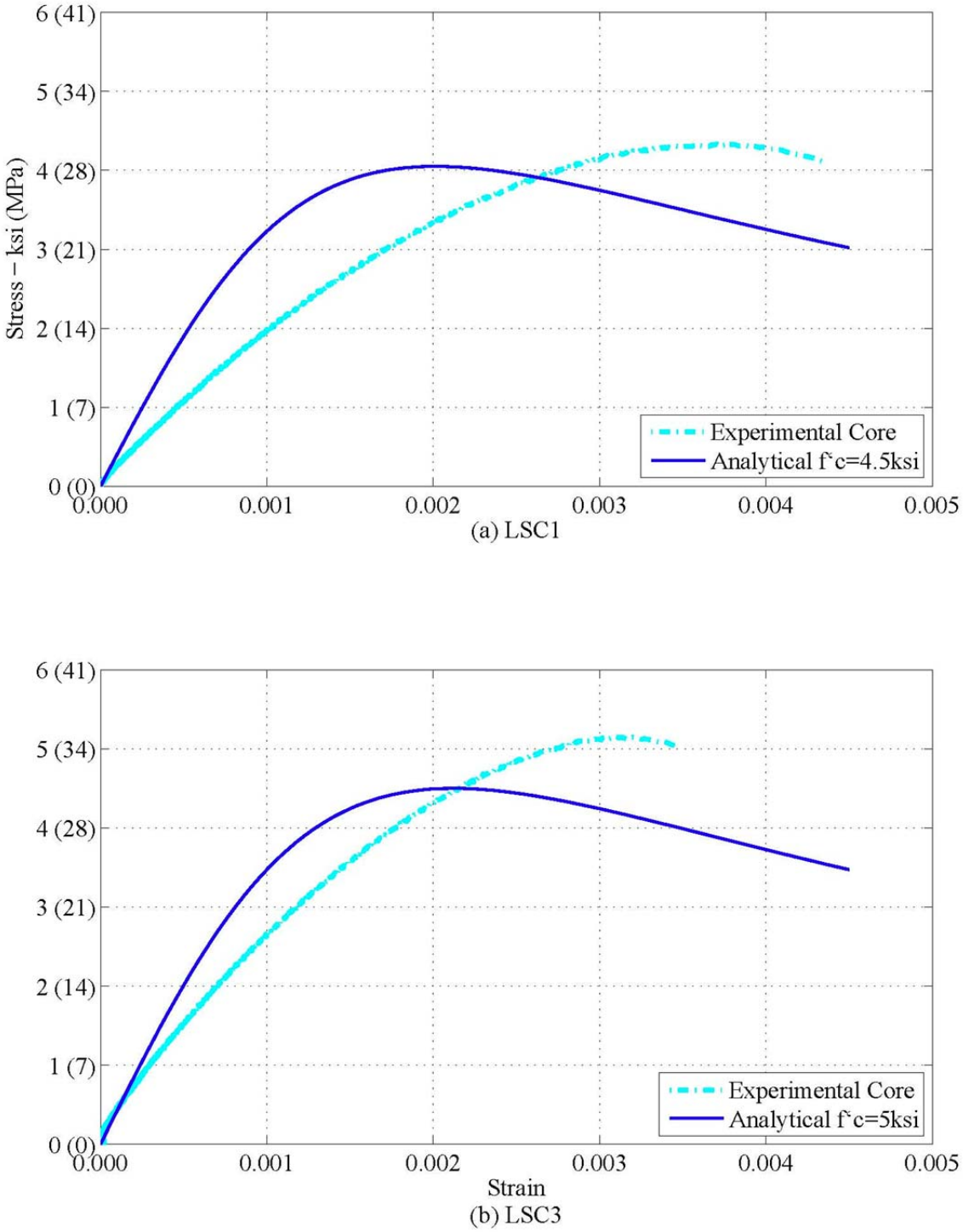

Figure 5-18. Compression Stress-Strain Response for LSC1 and LSC3 Cores.

5.4.2 Four-Point Flexural Test Results and Comparison with Analytical Model

The four-point test results from LSC specimens 1, 3, 5, 8, 9, 10, 15, and 16 are presented in this section. Some things to note prior to further discussion is that LSC15 and LSC16 were the control specimens and were kept in the climate controlled Structure and Materials Testing Laboratory for 6 months before testing without supplemental water and no developed premature concrete deterioration. Figure 5-19 compares the experimentally measured force-deformation response from all specimens tested to date. There are two lines for each specimen, one for each actuator. The actuator load is plotted vs. the deflection measured under the respective actuator using the string pot data and Eqs. 5-1 and 5-2. For specimens LSC15 and LSC16, the hydraulic valve in one of the actuators caused minor oscillations in the structural response during testing. The loading was stopped a few times during the tests to view the cracking and assess the condition of the specimen. Therefore, the results show a slight drop in load at a view strains when the loaded halted for a short time. All of the specimens had about the same stiffness (force-deflection slope) until first cracking. The deteriorated specimens were about 25-35% stiffer and had a slight (5-15%) increase in yield strength than the two control specimens (LSC15 and LSC16) between first cracking and first yielding of the reinforcing steel. The results from each specimen will be shown separately in figures later in this section.

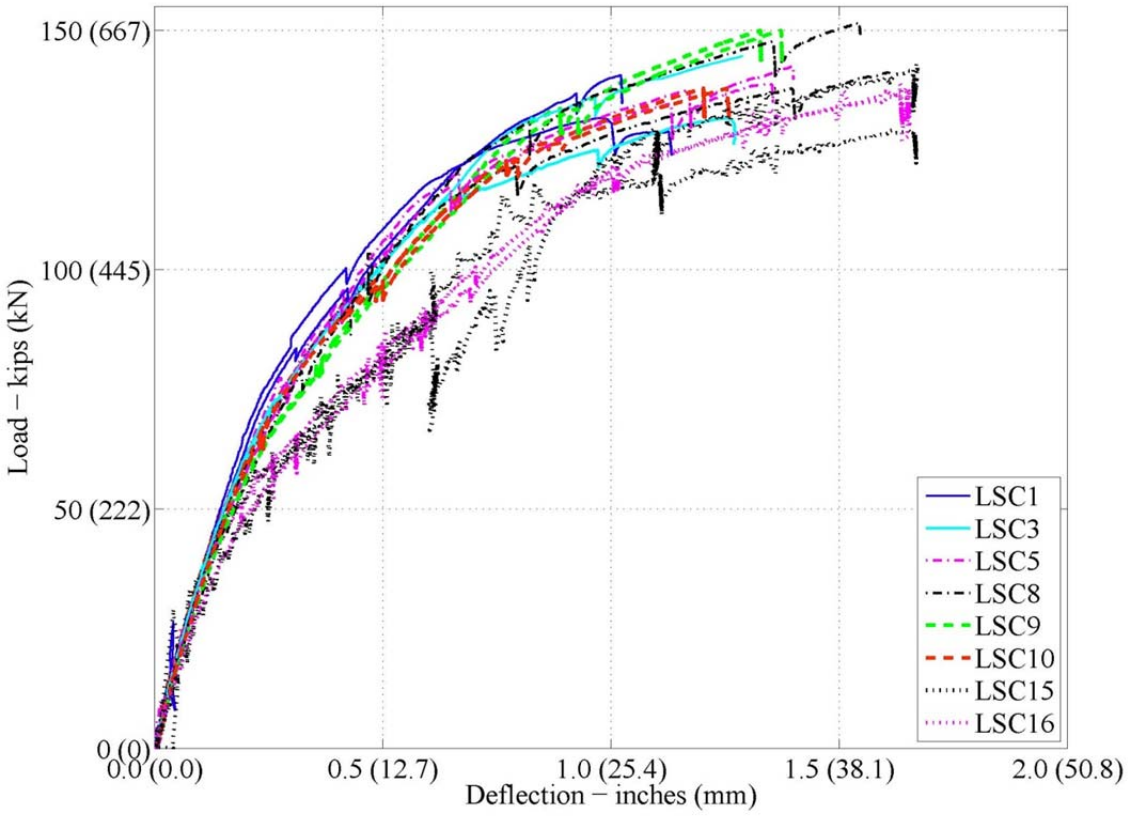

Figure 5-19. Experimental Load vs. Deflection during Four-Point Test: All Tested Specimens at the Actuator Load Point (Splice End).

Figure 5-20 compares the experimental data from LSC15 and LSC16 with the three analytical models described in section 4. The figure clearly shows that the analytical Step-by-Step I_{cr} method best correlated with the experimental test behavior up to the yield point. Beyond the yield point, the results from all analytical models did not fit the post-yield stiffness of the experimental data well since confinement of the concrete and strain hardening of the reinforcement were intentionally not accounted for. In addition, the four-point structural load tests were not meant to find the ultimate specimen strength and deformation, and were not done so experimentally in the four-point test setup. Because of this, the LSC specimens were able to be further tested in the three-point test setup.

The analytical models described in assumed f_y, was 70 ksi (483 MPa) and f'_c, was 5 ksi (34 Mpa). For the forthcoming comparison of the analytical model with the experimental behavior, the yield strength of the reinforcement, ASTM Grade 60 steel, was also taken to be 70 ksi (483 MPa) for all specimens since it seemed to give the best fit for the data and probably is on the higher-end of actual material yield strength produced. Although the degree of concrete deterioration of the test cylinders differed significantly from that of the LSC specimens, the concrete compression strength of the cylinders were mostly unaffected by the deterioration due to ASR/DEF and was consistent for all LSC specimens as reported in Table 5-3. Therefore, the concrete compression strength used in the analytical model was taken as an average of the data from cylinders that were stored at the Riverside Campus and tested at the time of the specimen's structural load test. The data from the cylinder tests of LSC specimens: 1, 3, 5, 8, 9, and 10 were averaged to obtain the analytical f'_c value of 5.3 ksi (37 MPa) that was used for all non-control LSC specimens. The two control specimens, LSC15 and LSC16, had lower f'_c values from the cylinders tested at the time of the load test (see Table 5-3). Therefore, the f'_c used in the analytical model for the control specimens was 3.9 ksi (26MPa).

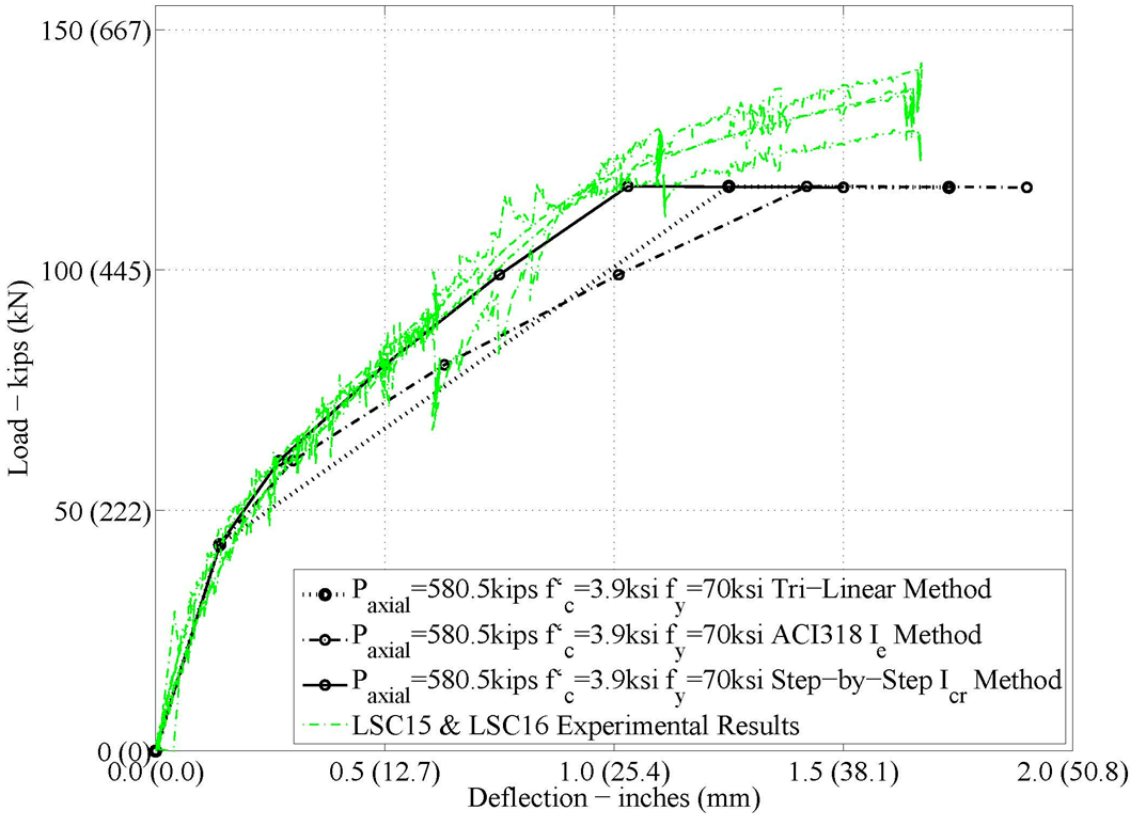

Figure 5-20. Experimental and Analytical Load vs. Deflection of Control Specimens for the Four-Point Test at the Actuator Load Point (Splice End).

Since the column specimens had a presumed constant axial loading from post-tensioning strands of 580.5 kips (2582 kN), the analytical model used this value for computing the first predicted analytical response for the control specimens. Since the other specimens in the deterioration program expanded longitudinally due to ASR and minimal DEF effects (measured from surface mounted instrumentation and internal instrumentation as shown in 3), the axial loading on the specimen from the strands and column longitudinal reinforcement presumably increased. Although the post-tensioning strands were not strain gaged to measure the actual strain at testing, Table 5-4 shows the average longitudinal surface strain expansions on all four faces for the deteriorated specimens at

the time of structural testing. These measurements show that the specimens expanded in the longitudinal direction and thus indicating the potential for higher levels of axial loading from the post-tensioning strands and longitudinal reinforcement.

Table 5-4. Longitudinal Strains in Tested LSC Specimens.

LSC #	Date of Casting	Date of Initial Exposure	Date of Structural Load Test	Average Longitudinal Surface Strain at Time of Load Test (strain)			
				Small Face 1	Small Face 2	Large Face 1	Large Face 2
1	1/2008	5/2008	8/2010	0.0006	0.0003	0.0010	N/A
3	2/2008	5/2008	8/2010	0.0005	0.0003	0.0010	N/A
5	4/2008	5/2008	7/2011	0.0004	0.0007	0.0010	0.0014
8	5/2008	7/2008	7/2011	0.0004	0.0007	0.0009	0.0011
9	6/2008	7/2008	2/2010	0.0003	0.0002	0.0006	N/A
10	6/2008	7/2008	2/2010	0.0004	0.0004	0.0008	N/A
15	8/2008	N/A	2/2009	N/A	N/A	N/A	N/A
16	8/2008	N/A	2/2009	N/A	N/A	N/A	N/A

Since the Step-by-Step method best fits the test data for controls specimens, it is the only method used for comparing the analytical model to the experimental test data for the remainder of the specimens. The deteriorated specimens have aged and have induced longitudinal expansions; therefore, Figure 5-21 compares the Step-by-Step I_{cr} analytical model using different values of the column axial loading, F_{act} , and the concrete compression strength, f'_c , to the test results from LSC specimens: 1, 3, 5, 8, 9, and 10. Comparing the black dashed lines with the dotted lines, the change in concrete compression strength did not significantly influence the analytical model behavior. However, the increase in the column axial loading (determined based on a best fit of the experimental data) significantly affected the post-cracking stiffness and the yield strength of the analytical response and is shown to fit the experimental response data very well. Therefore in the analytical model for the non-control specimens, an increased

axial force on the specimen was determined to best fit the measured structural response. Table 5-5 shows the final values used for the analytical model, where the LSC specimens were grouped by control and non-control specimens.

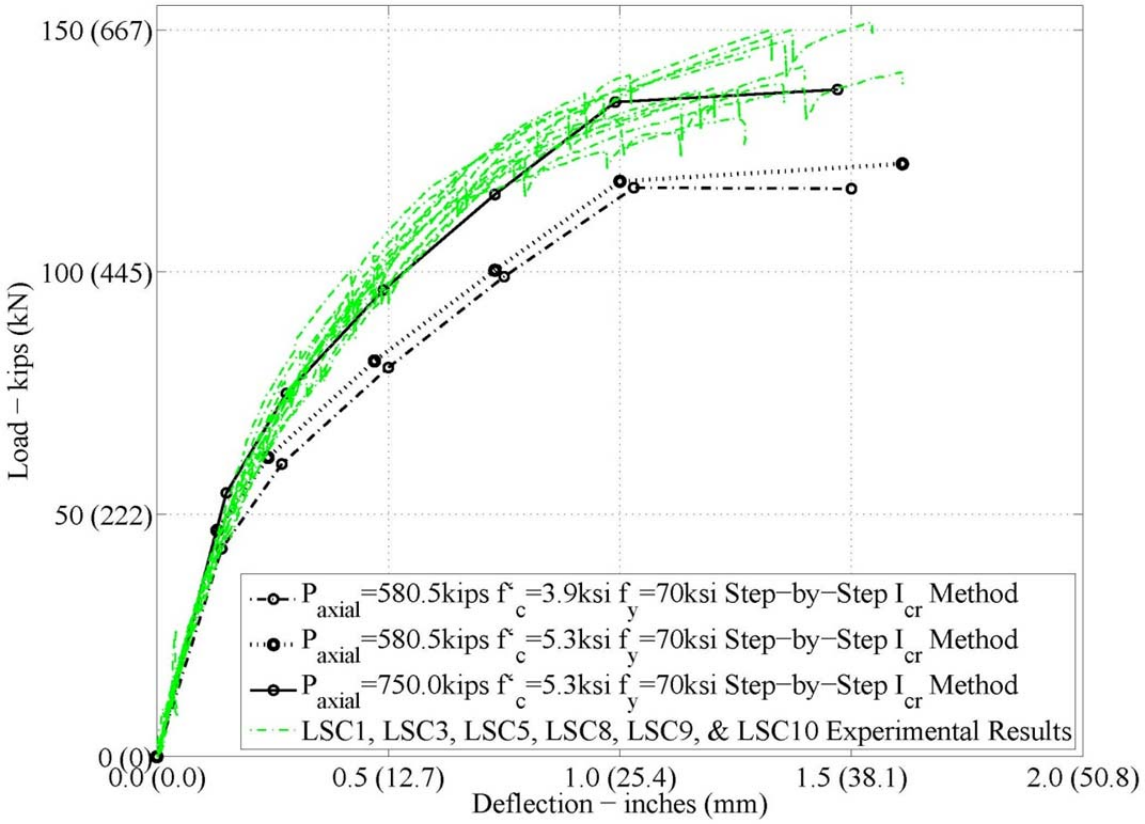

Figure 5-21. Experimental and Analytical Load vs. Deflection of Non-Control Specimens for the Four-Point Test at the Actuator Load Point (Splice End).

Table 5-5. Variables Used for Analytical Model.

	f'_c		f_y		P_{axial}	
	ksi	(Mpa)	ksi	(Mpa)	kips	(kN)
Non-Control LSC Specimens: 1, 3, 5, 8, 9, and 10	5.3	37	70	483	750	3336
Control LSC Specimens: 15 and 16	3.9	27	70	483	580.5	2582

Figure 5-22 compares the experimental and analytical actuator load vs. deflection results for the control specimens and non-control specimens. Note that the figure shows the results for each group of two specimens that were tested at various stages of ASR and minimal DEF deterioration. LSC16 and LSC15 are shown first since they were the control specimens with no ASR/DEF deterioration and tested first. The results from LSC 9 and 10, LSC 1 and 3, and then LSC 5 and 8 are subsequently shown according to their increasing exposure time and deterioration. The variables from Table 5-5 used for the Step-by-Step I_{cr} analytical model almost accurately predict the structural response up to the yield point for all specimens. However, beyond yielding, the analytical model does not fit the post-yield stiffness of the experimental behavior well because the model does not account for concrete core confinement and strain hardening of the reinforcing steel, which was not the focus of the research. The figure also highlights the difference in the load vs. deflection response at the sections under each actuator near the yielding point of the specimen response. Experimentally, the actuators were placed in displacement control loading with the exact same displacement targets and displacement rates (implying that they displace the same amount at any given time). However, the measured actuator loading shows slightly different values starting near yielding, most likely due to the uneven accumulation of damage in the specimen at the critical section under each actuator during testing. However, this slight difference in actuator loadings had no impact on the overall findings of the experimental structural behavior.

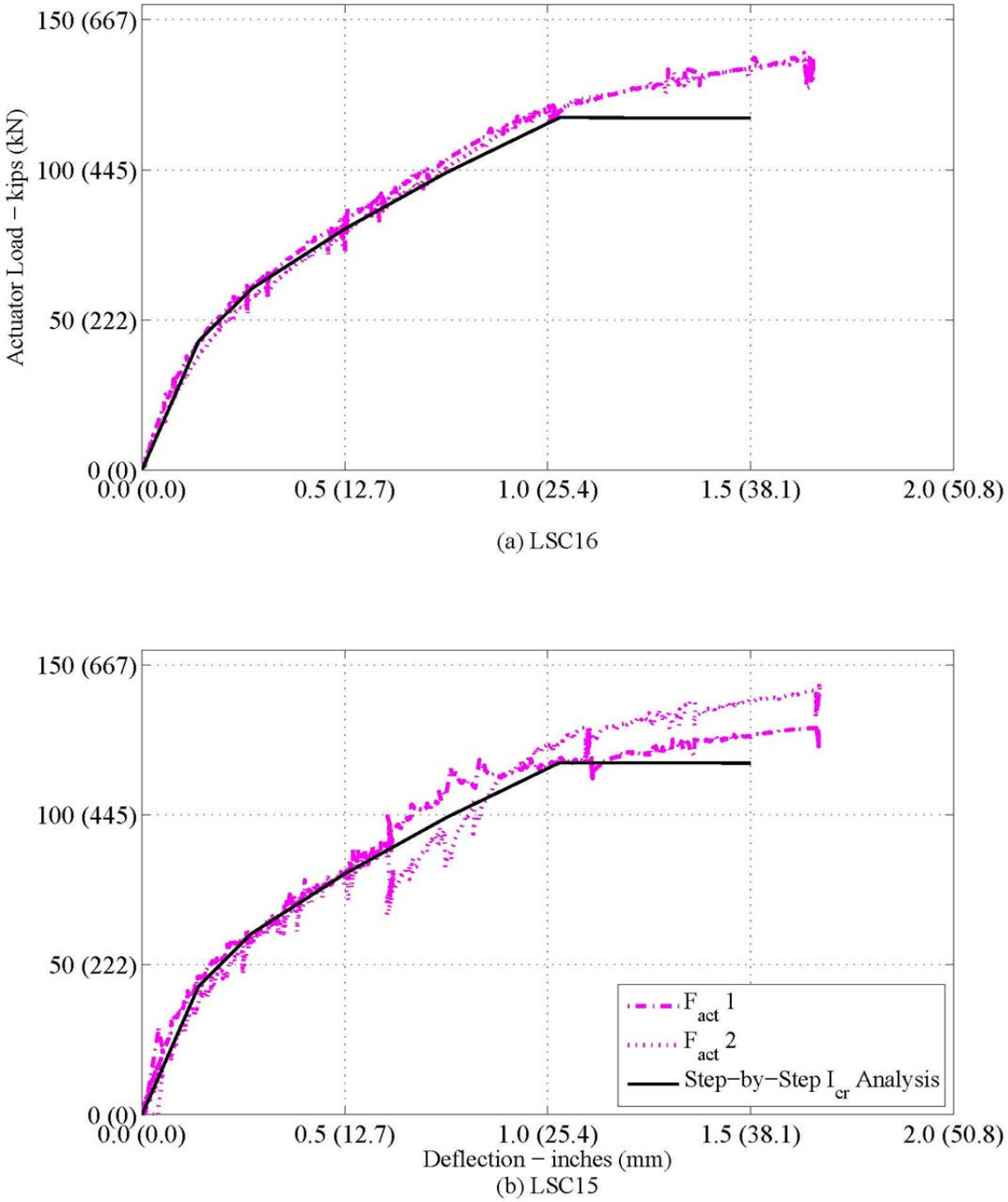

Figure 5-22. Experimental and Analytical Load vs. Deflection during the Four-Point Test:
At the Actuator Load Point (Splice End).

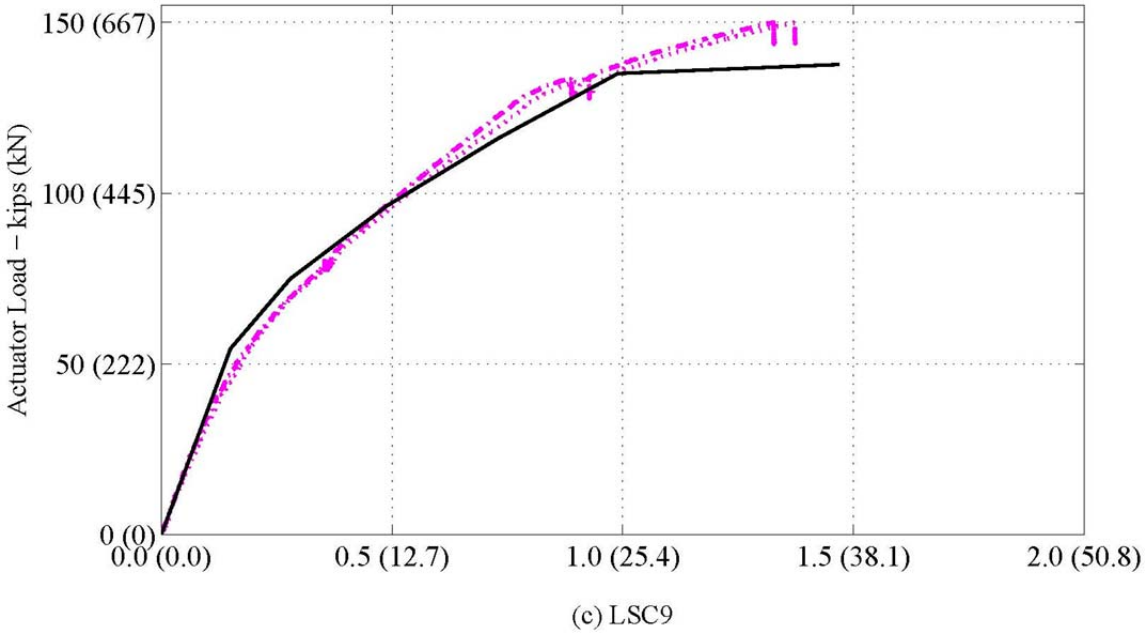

(c) LSC9

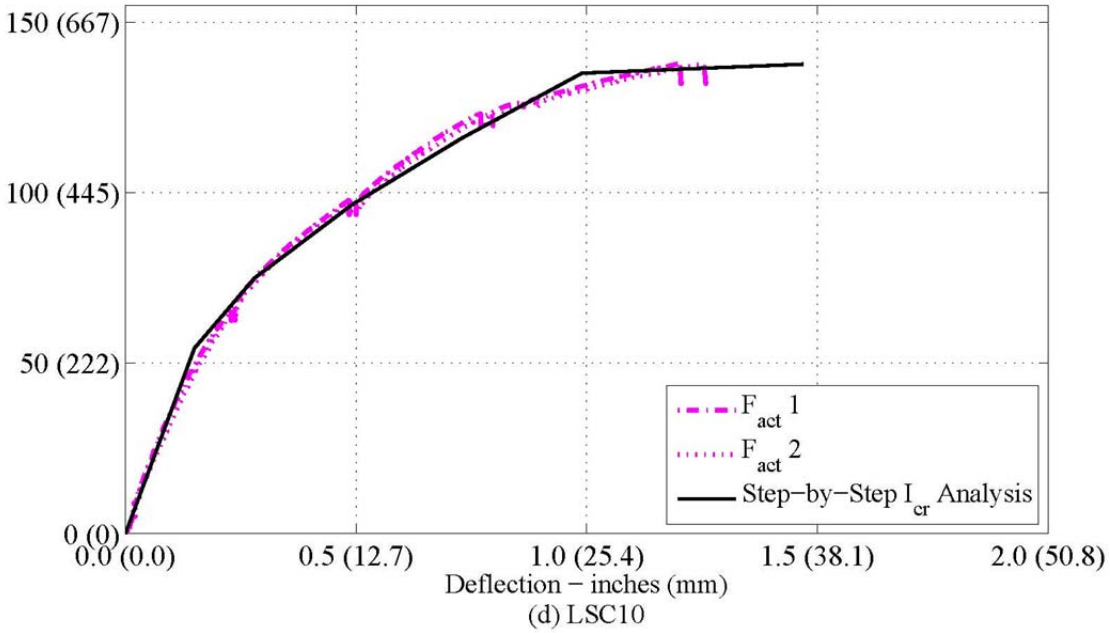

(d) LSC10

Figure 5-22. (Continued)

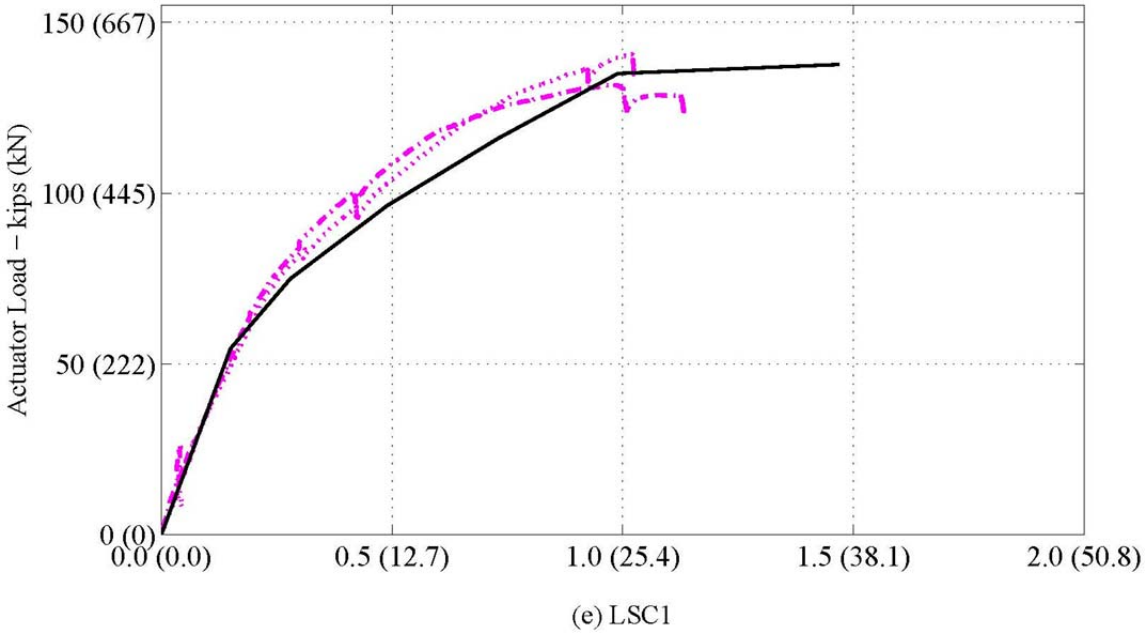

(e) LSC1

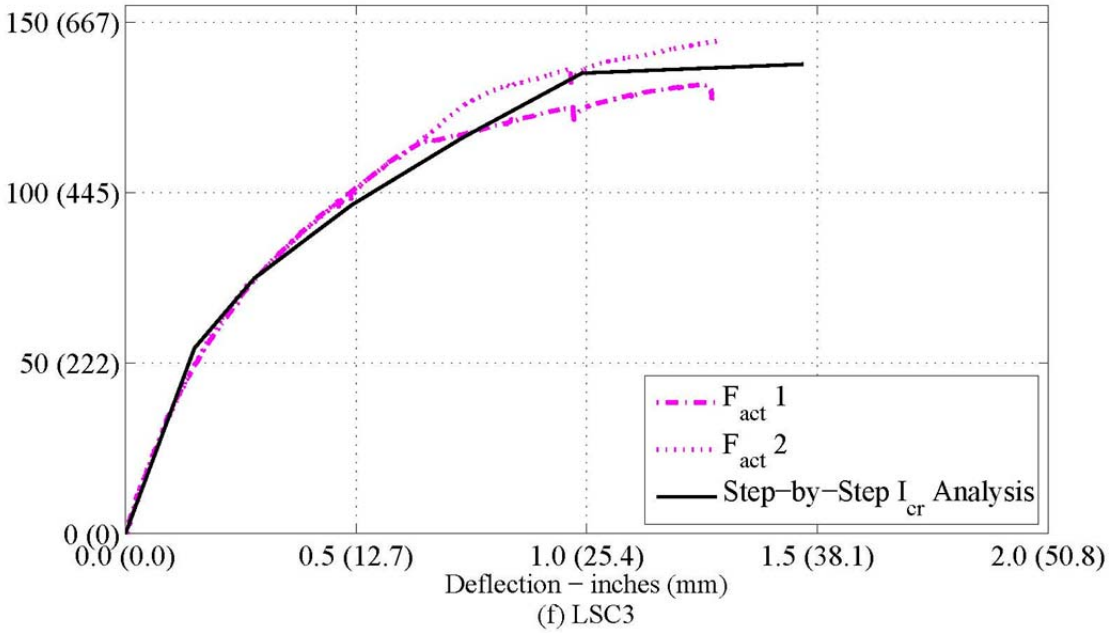

(f) LSC3

Figure 5-22. (Continued)

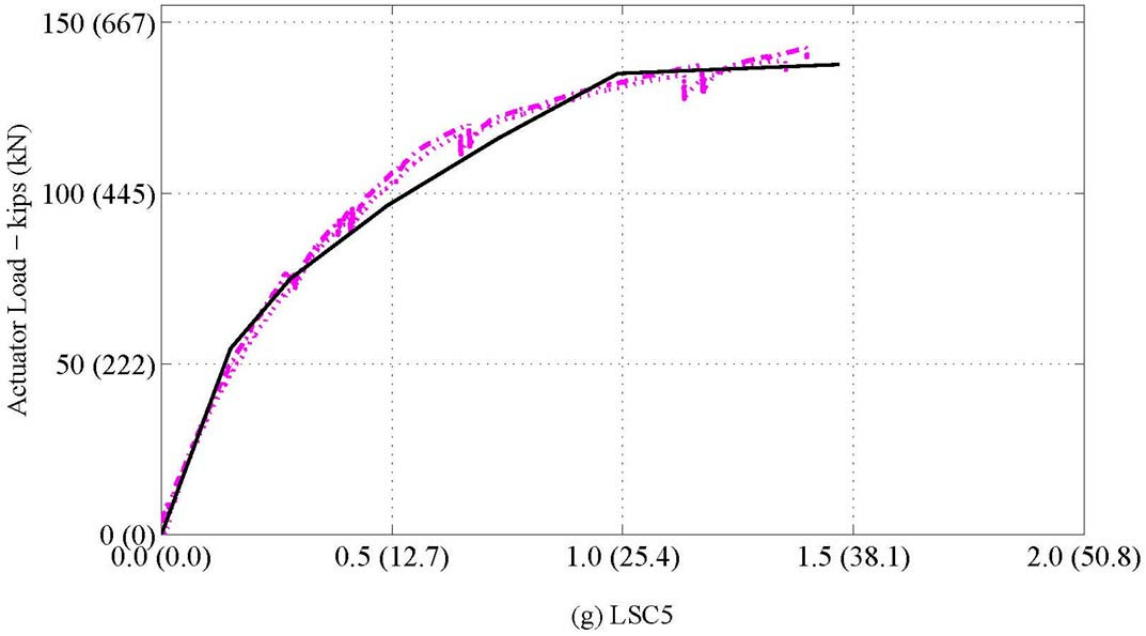

(g) LSC5

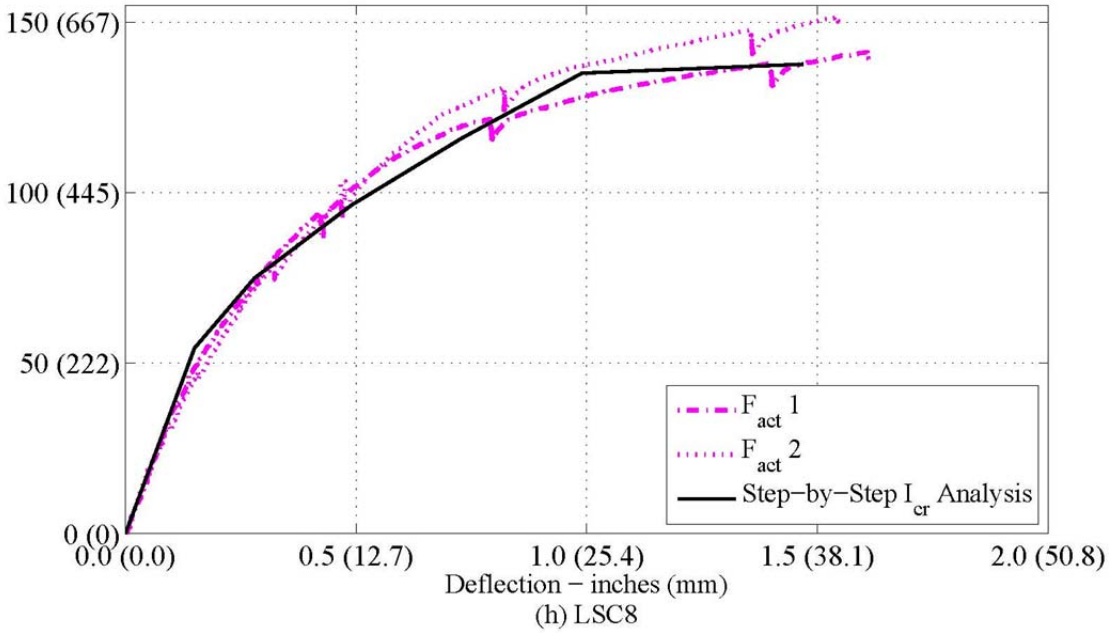

(h) LSC8

Figure 5-22. (Continued)

The internal and external strains were measured with the instrumentation presented in section 2 (internal) and section 5.2.2 (external). The results from these measurements are presented to show the behavior of the specimen in the compression and tension regions during structural load testing. If the capacity of the lap splice was not adequate, an assessment of the strains can show the location of the lap splice failure and also the load at which it occurred. The reinforcing steel within the splice region was instrumented internally with strain gages (SGs) as discussed in section 3. Four gages (SG1 – SG4) were located on the bottom (tension side during loading) edge reinforcing steel; four gages (SG5 – SG8) were located on the bottom center steel; and two gages (SG9 – SG10) were located on the top (compression side during loading) center splice bars. Figure 5-23 shows a cross section in the splice region with the locations of the strain gages identified. Figure 5-24 illustrates the longitudinal location of the strain gages. Note that the three groups of strain gages were located on the same splice bar and SG4 and SG8 were located near the end of the bar with little available anchorage.

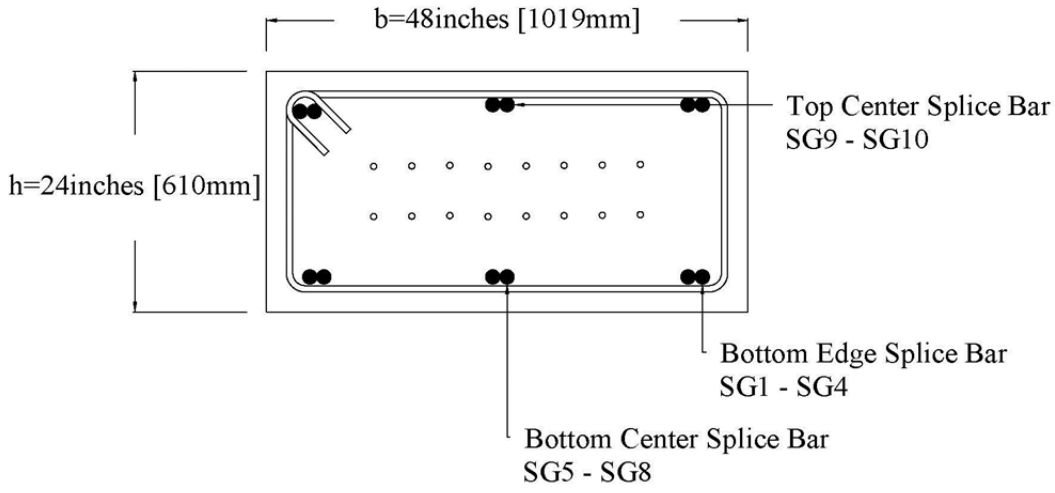

Figure 5-23. Cross Section at Splice Region with SG Locations.

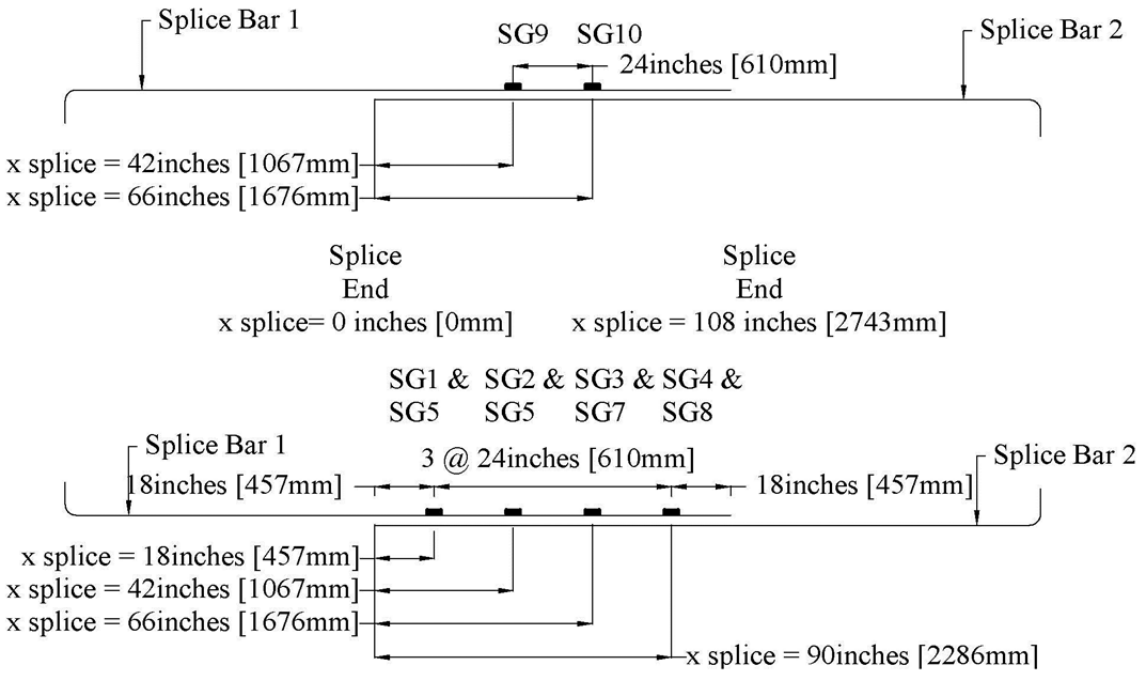

Figure 5-24. SG Locations on Steel in Compression and in Tension.

Figure 5-25 shows the average actuator force plotted versus the internal strains measured by the SG1 – SG4. The values from the gages were set to zero at the beginning of the test; therefore the strains from deterioration are not shown. Figure 3-20, Figure 3-21, and Figure 3-22 showed the strains in SG1-SG10 during the deterioration process and also showed that some of these SG readings had significantly scattered behavior. However, as shown in Figure 5-26, it seems these gages were still able to work during the experimental load testing. In general, Figure 5-26 shows the strain measured with SG1 is usually the largest, and SG4, the smallest. This is the result of the locations of the SGs with respect to the splice bar development. In section 4 the effective area of the reinforcing steel is calculated based on a linear increase up to full participation at the development length of the bar. Since SG4 is located near the bar end and has very little anchorage, the contributing area is very small compared to the full area contributing on the bar where SG1 is located. The analytical model used the sum of the effective areas

from Splice Bar 1 and Splice Bar 2 to calculate the strain at the tension steel. In order to compare the experimental strain gage readings on Splice Bar 1 to the analytical model, a SG factor was proposed to modify the calculated strain values at a given section so that individual bars strains could be approximated as shown below:

$$\text{SG Factor} = \frac{A_{s1}}{A_{s,eff,splice}} \quad \text{(Eq. 5-9)}$$

A_{s1} is the area from Splice Bar 1 and $A_{s,eff,splice}$ is the area from both splice bars depending on the location with respect to the development length of each bar. The formulas for these variables are in section 4. The SG distances from the bar ends are shown in Figure 5-24.

Figure 5-26 shows the strains on the bottom reinforcing steel measured with SG5 – SG8. These strains are assumed to be the same as SG1-SG4 since the only difference is SG1-SG4 are located on an edge bar and SG5 – SG8 are located on a center bar. Therefore, the analytical predictions for SG5 - SG8 are the same as SG1 – SG4.

The four SG analytical values in Figure 5-25 and Figure 5-26 are different since the distance from the end of Splice Bar 1 (development of splice bar) is different for each gage. The analysis assumed the steel and concrete remained bonded (plane sections remain plane). However, when the SGs were mounted to the steel bars, a sleeve was placed around the SG to protect the gage. This consequentially did not allow for perfect bond between the concrete and the steel at the location of the SGs. The figure shows the steel within the splice region is within the yield strain of the reinforcement (around 0.002) with very few exceptions (SG1 in LSC15, SF5 in LSC8, and SG8 in LSC10); therefore, the sections between the spliced ends have not yielded. Comparing the analytical and experimental response, differences are clearly evident; however general trends of the response are similar. The SG application that removed the bond between

the reinforcing steel and concrete at the location of the gage possibly caused the experimental results to be 5 times larger than the analytical model at the first cracking limit state.

Figure 5-27 shows the strains in the top reinforcing steel measured with SG9 and SG10. These strains are compressive strains therefore, have negative strains. A SG Factor was used on the top steel in the same manner as the bottom steel previously described. The development length for compression steel is smaller than tension steel and smaller than the distance from the splice end to SG10. Therefore, at the location of SG9 and SG10, both Splice Bar 1 and Splice Bar 2 were fully developed. This gave a SG Factor of 0.5 for both gages, predicting the same strain measured in each gage. LSC10, LSC3, LSC5, and LSC8 have one or two gages which measured no variation in strains during the test. Therefore, these gages were considered as not reliable. The figure shows the experimental compression strains are about 80% of the analytical model at first cracking and have similar differences after first cracking. This is a much closer match than the analytical and experimental comparison for the tension splice bar strains.

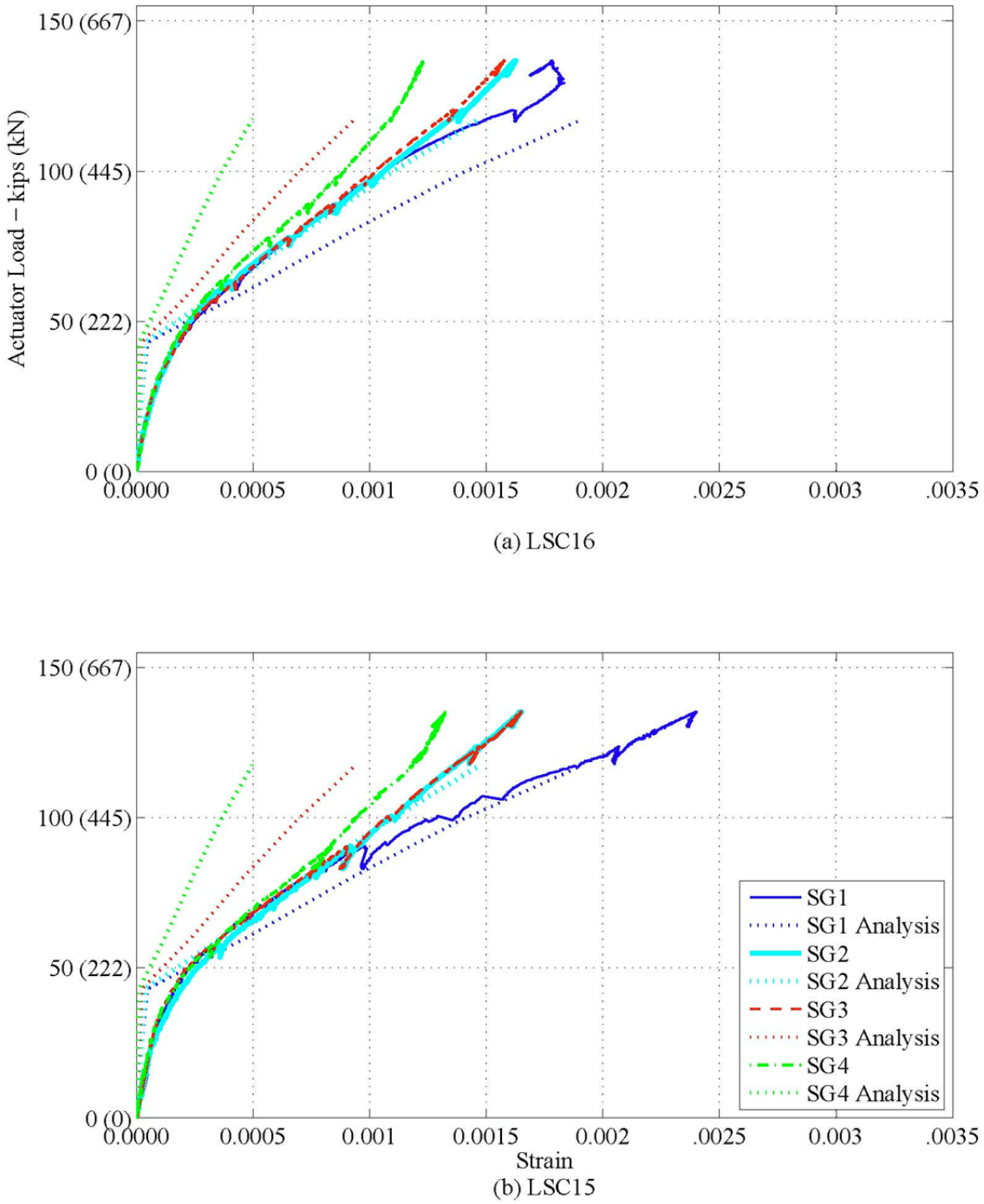

Figure 5-25. Experimental and Analytical Load vs. Strain during the Four-Point Test: Internal Strain Gages (SG1–SG4) along the Tension Steel of the Splice Region.

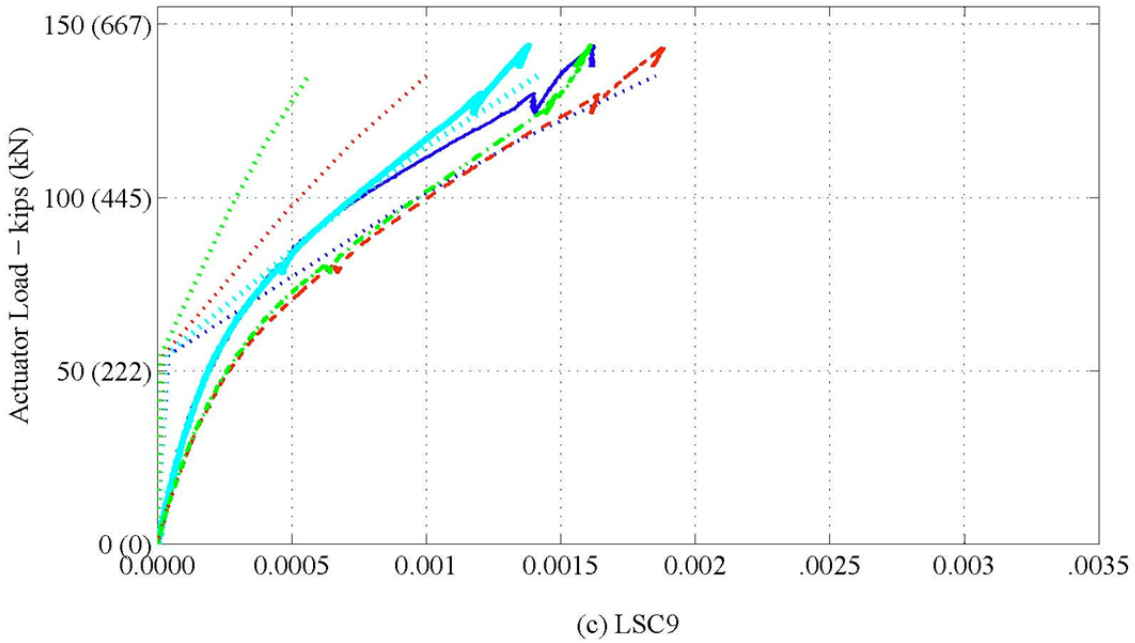

(c) LSC9

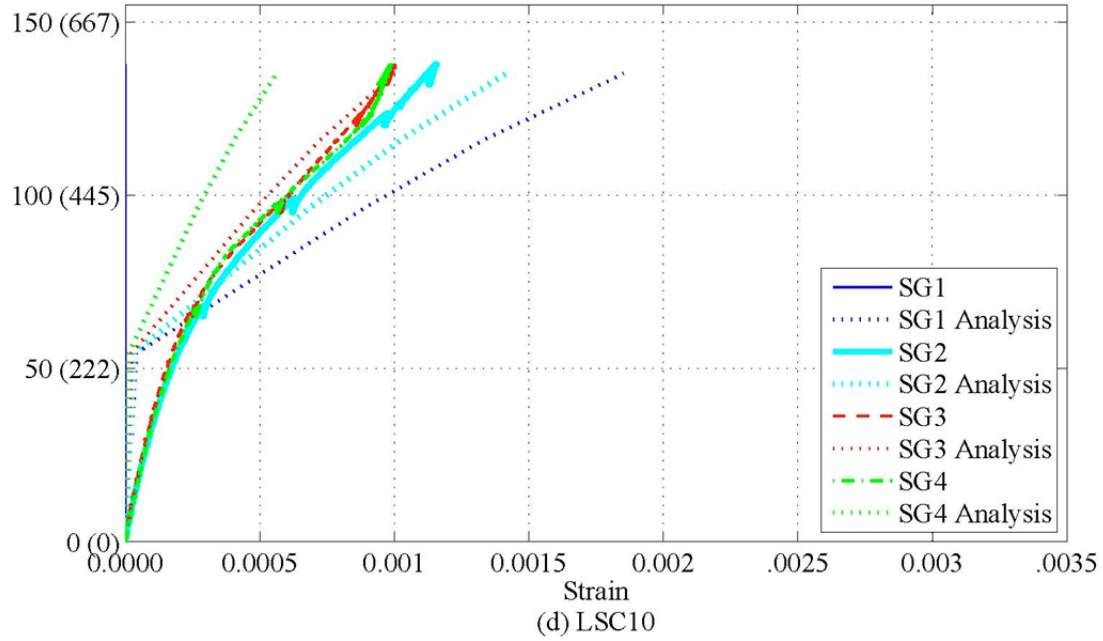

(d) LSC10

Figure 5-25. (Continued)

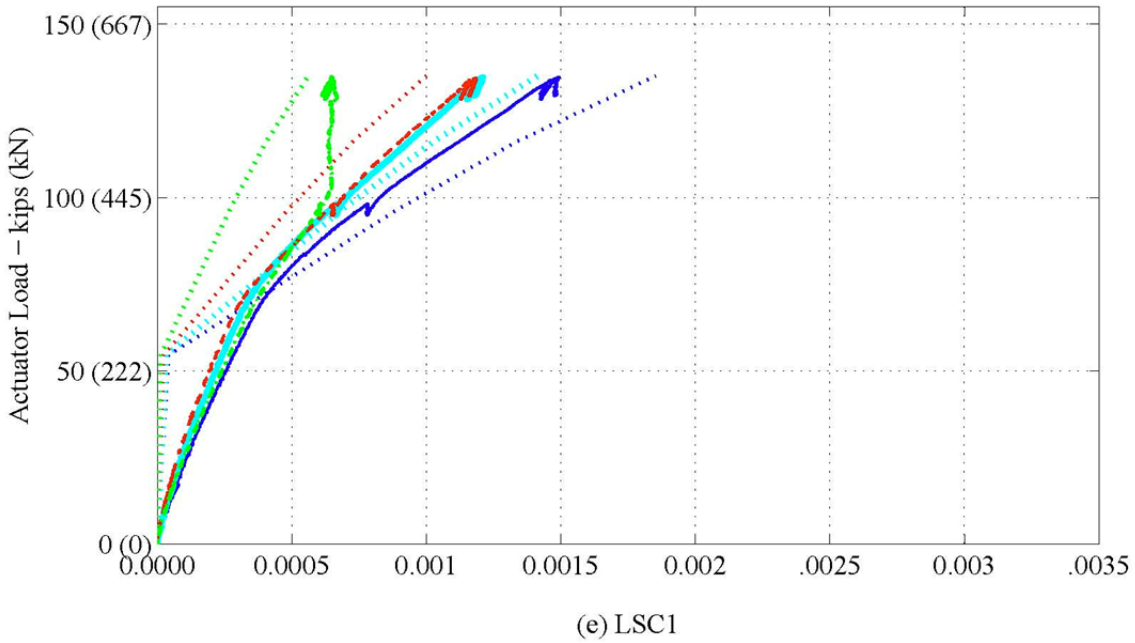

(e) LSC1

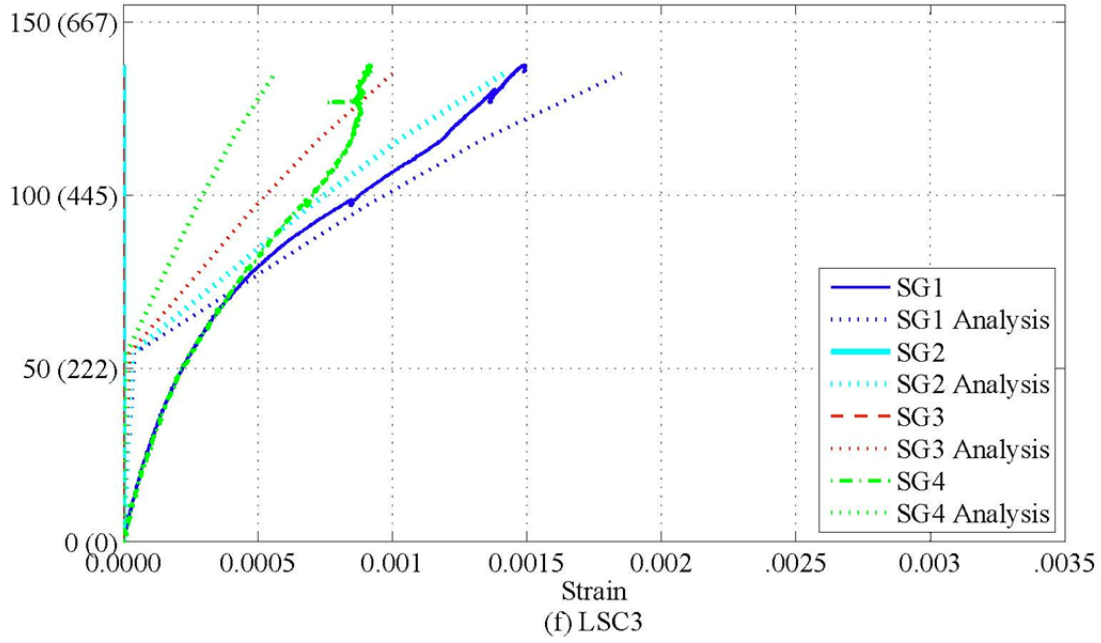

(f) LSC3

Figure 5-25. (Continued)

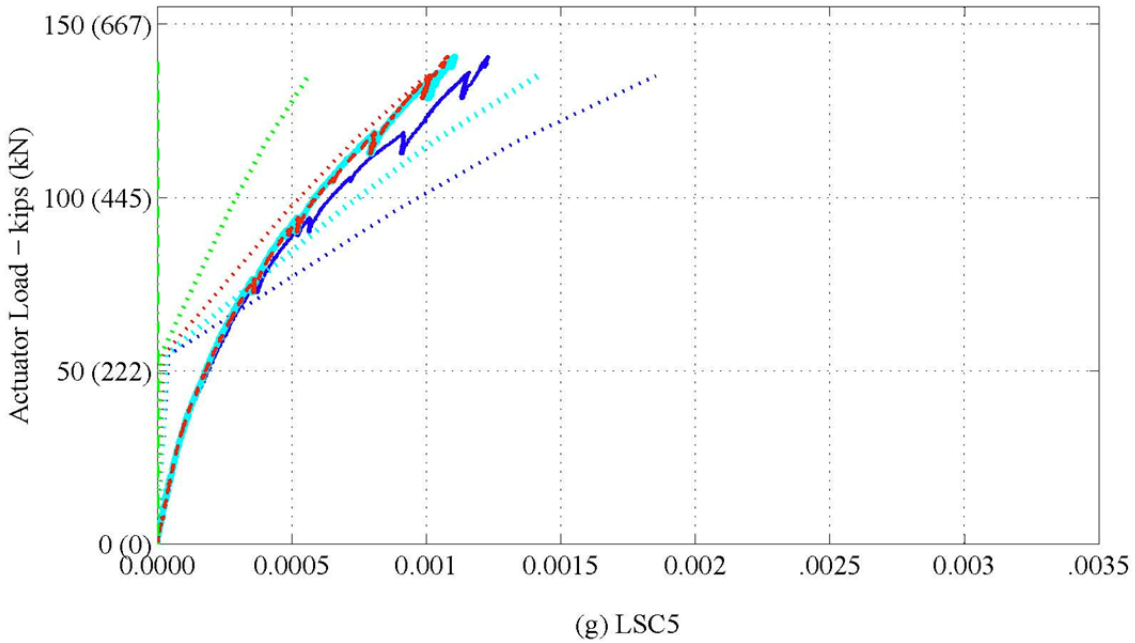

(g) LSC5

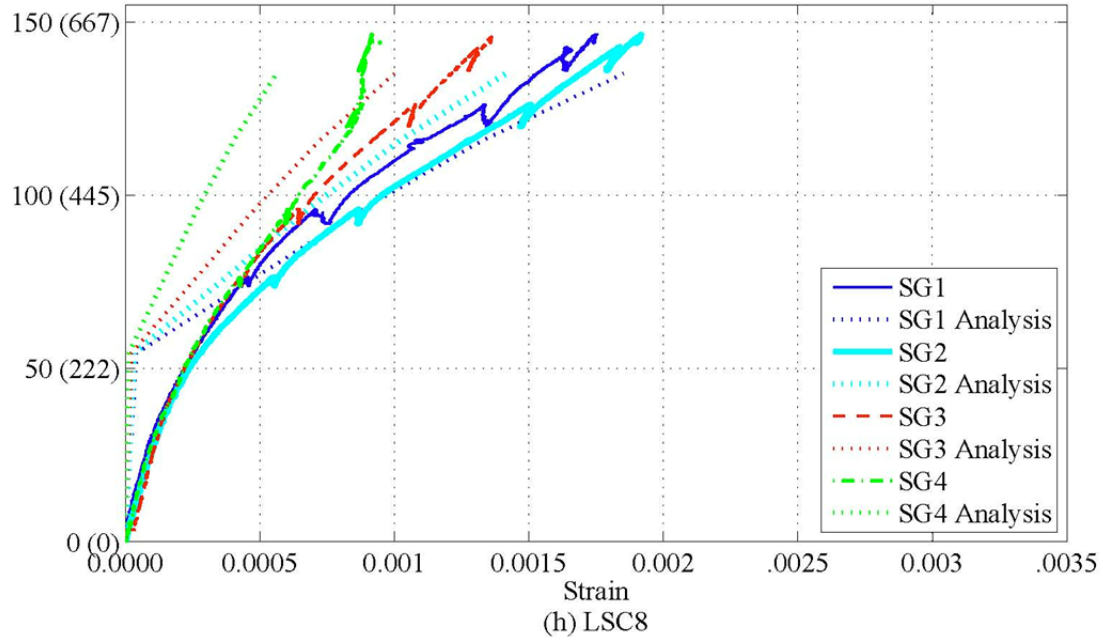

(h) LSC8

Figure 5-25. (Continued)

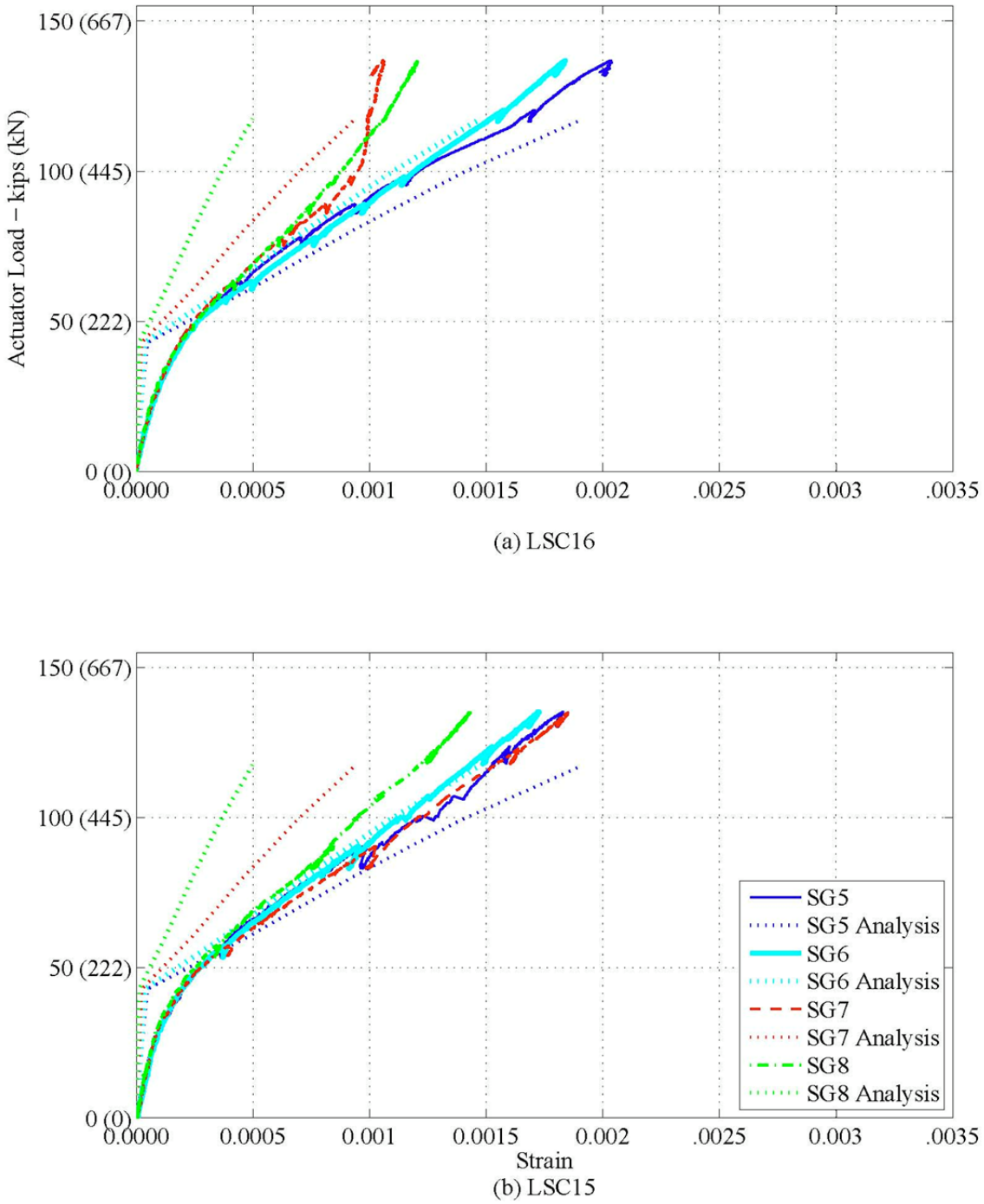

Figure 5-26. Experimental and Analytical Load vs. Strain during the Four-Point Test: Internal Strain Gages (SG5-SG8) along Tension Steel of the Splice Region.

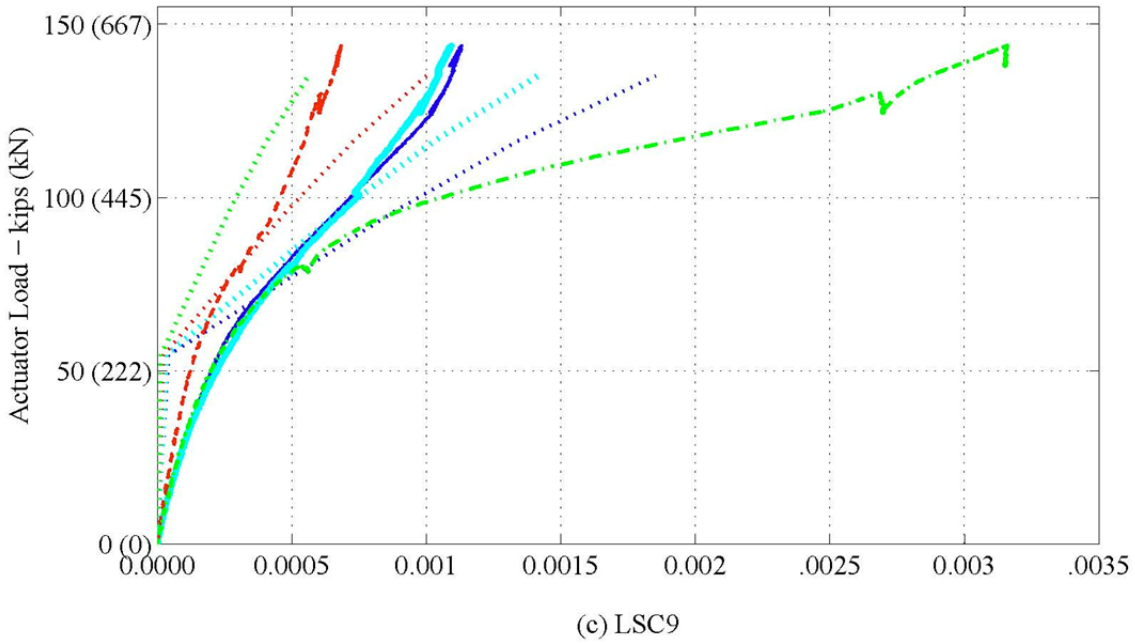

(c) LSC9

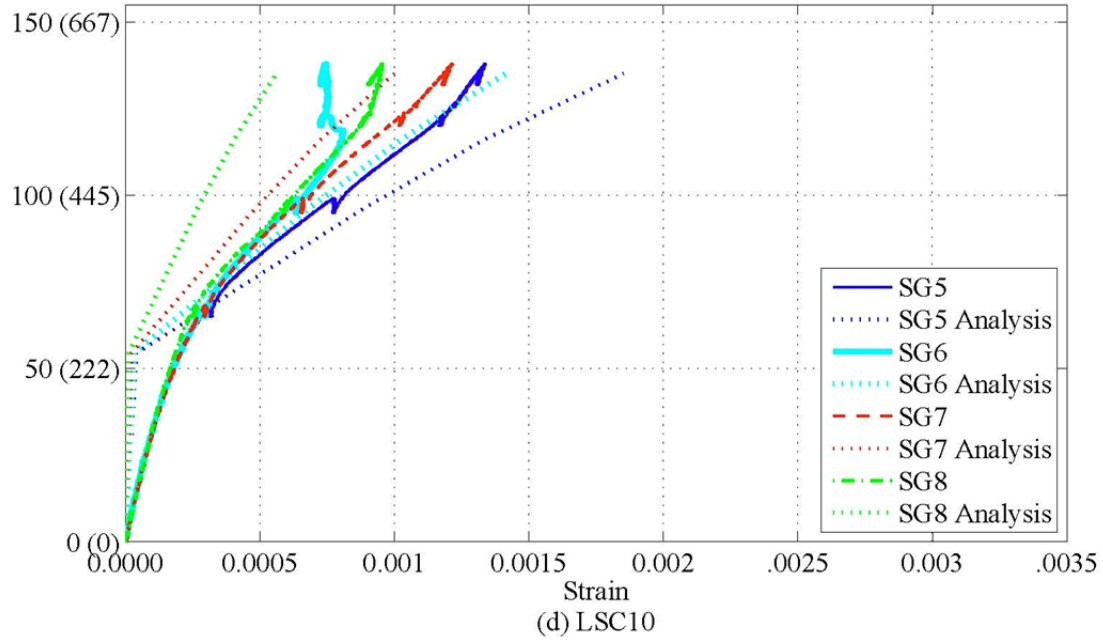

(d) LSC10

Figure 5-26. (Continued)

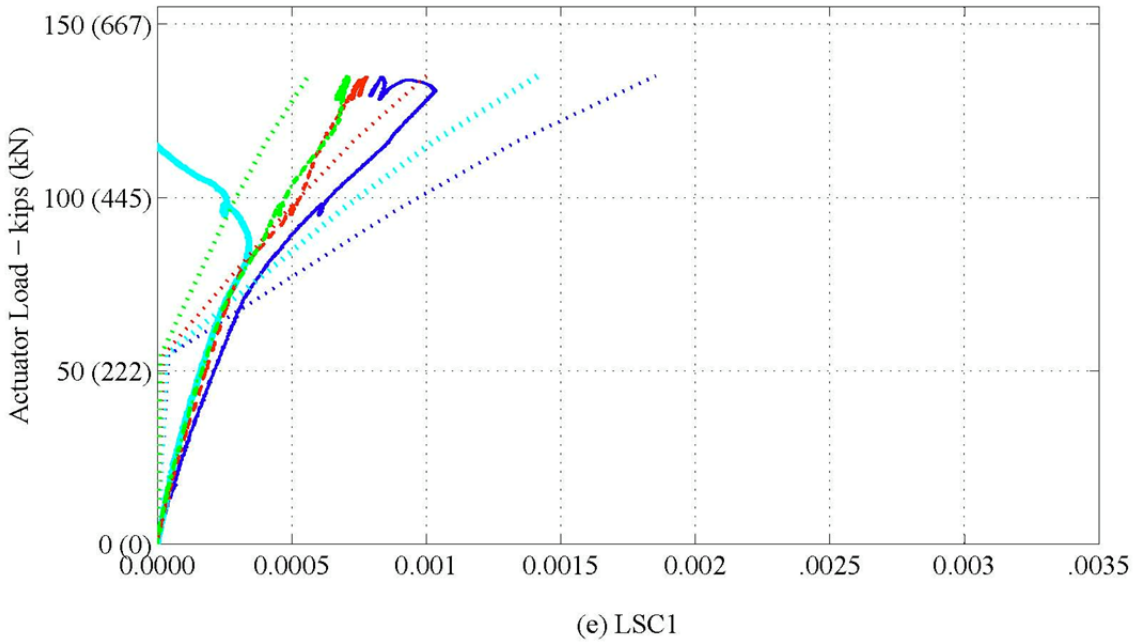

(e) LSC1

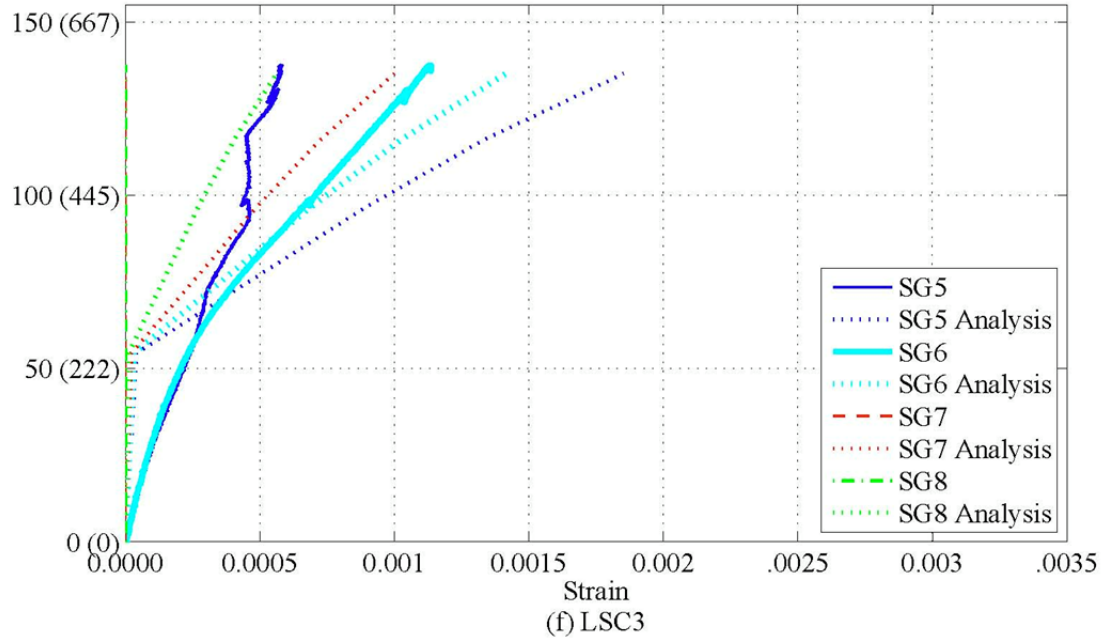

(f) LSC3

Figure 5-26. (Continued)

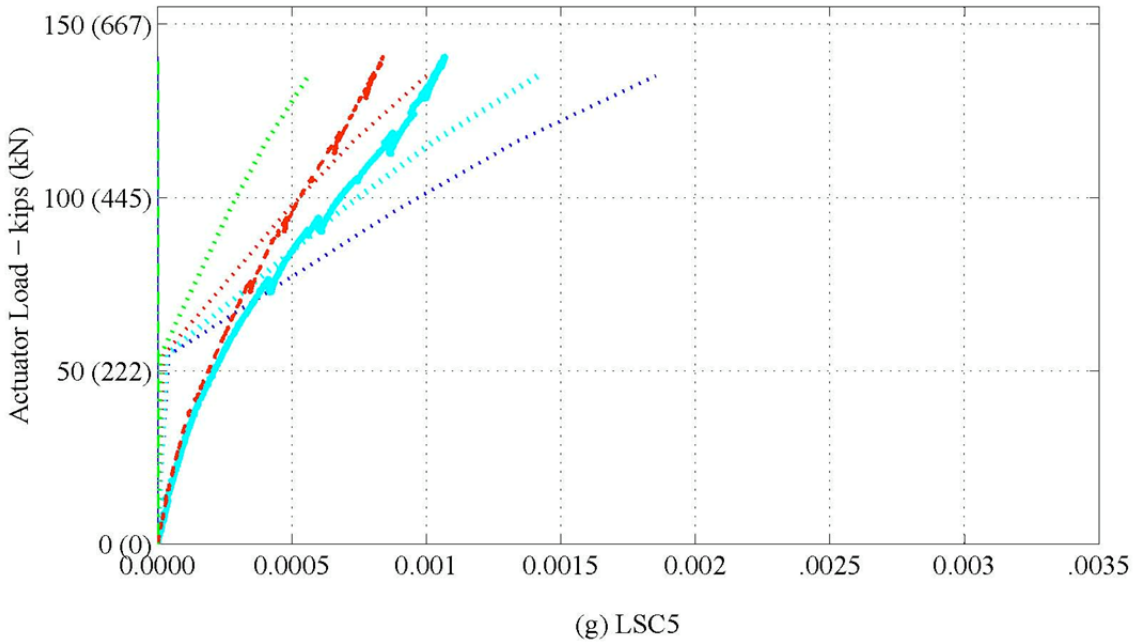

(g) LSC5

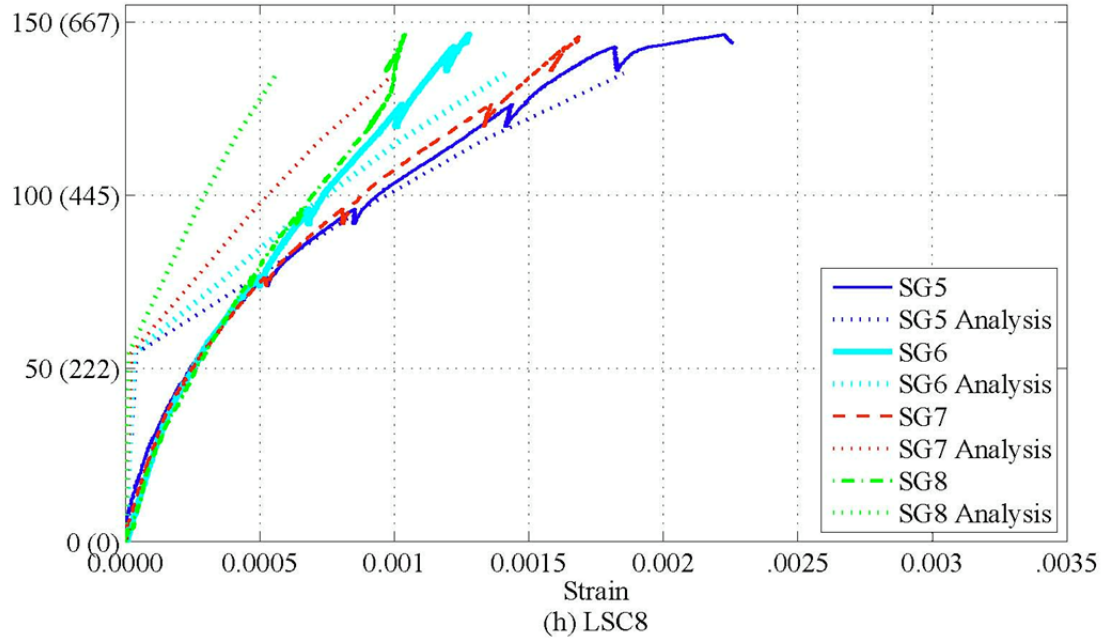

(h) LSC8

Figure 5-26. (Continued)

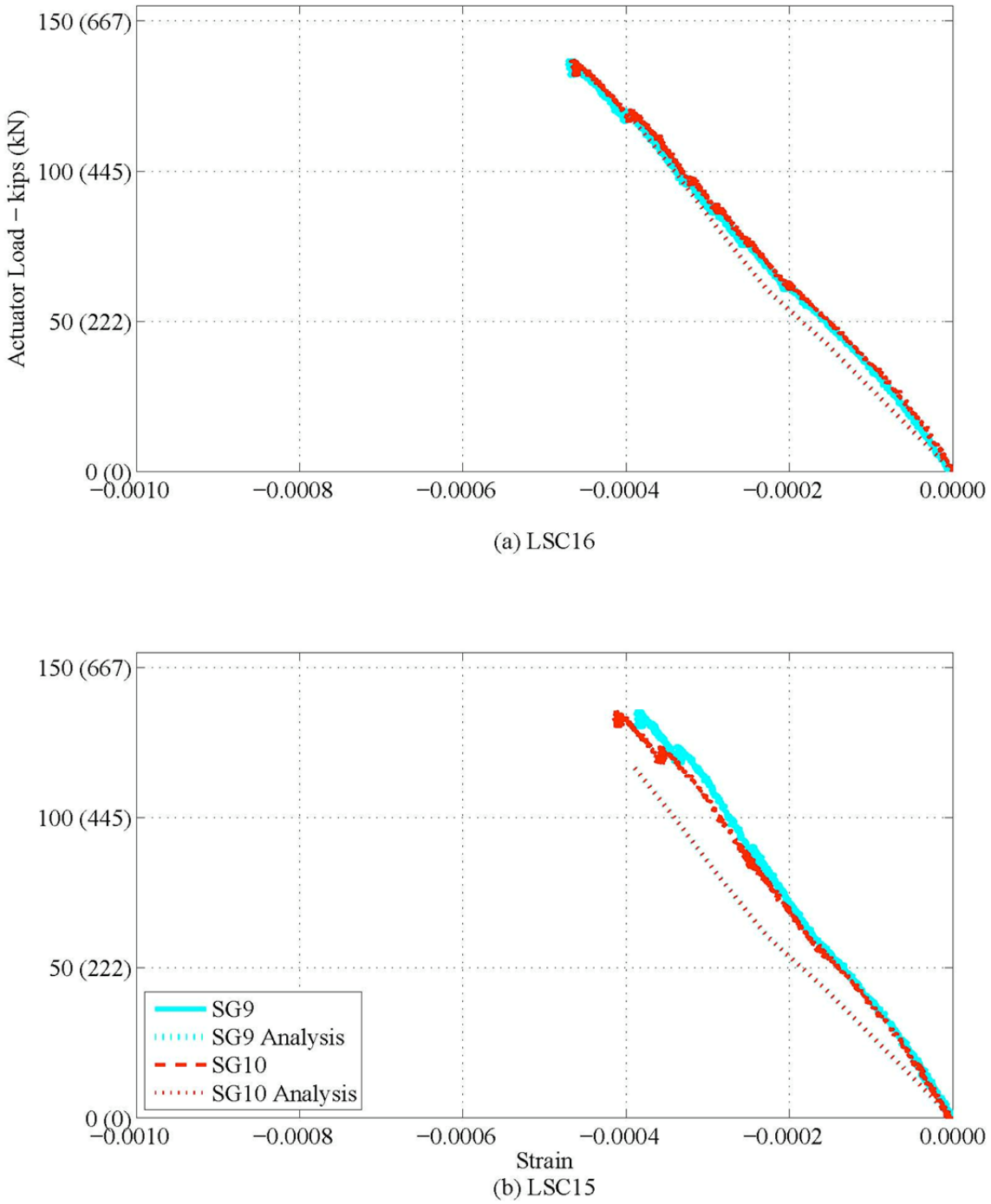

Figure 5-27. Experimental and Analytical Load vs. Strain during the Four-Point Test: Internal Strain Gages (SG9-SG10) along the Compression Steel of the Splice Region.

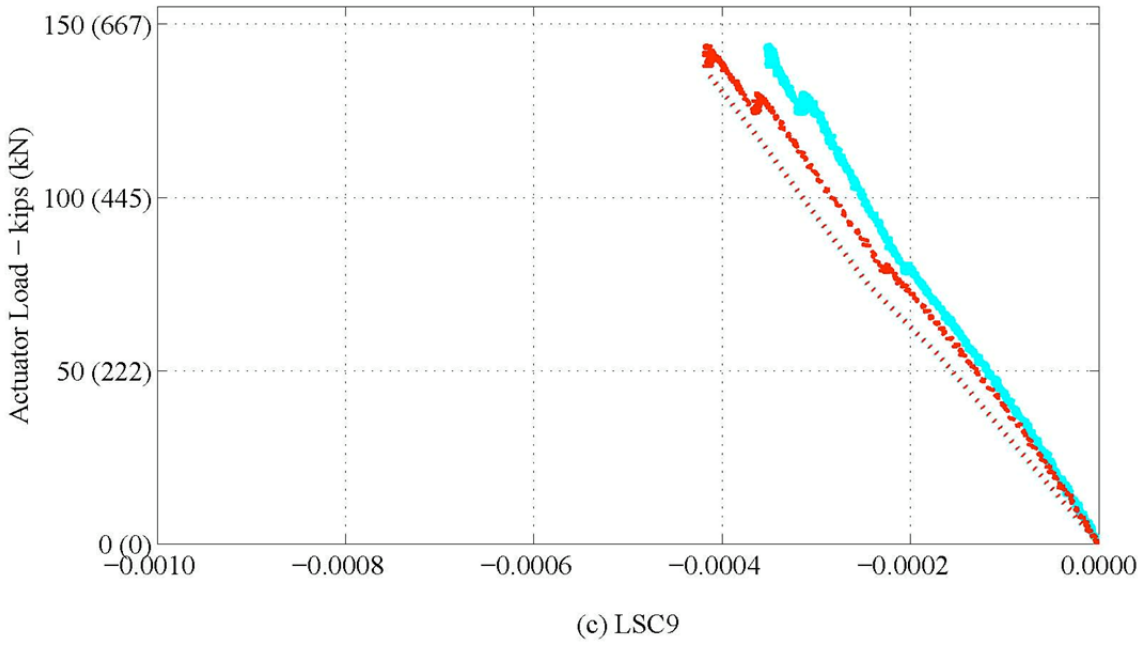

(c) LSC9

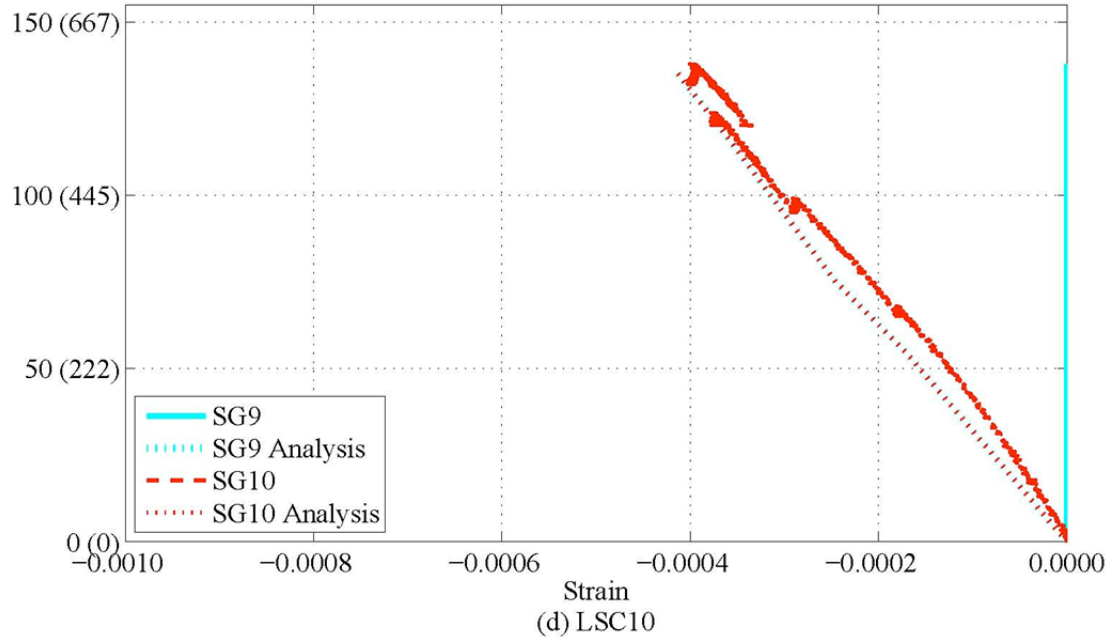

(d) LSC10

Figure 5-27. (Continued)

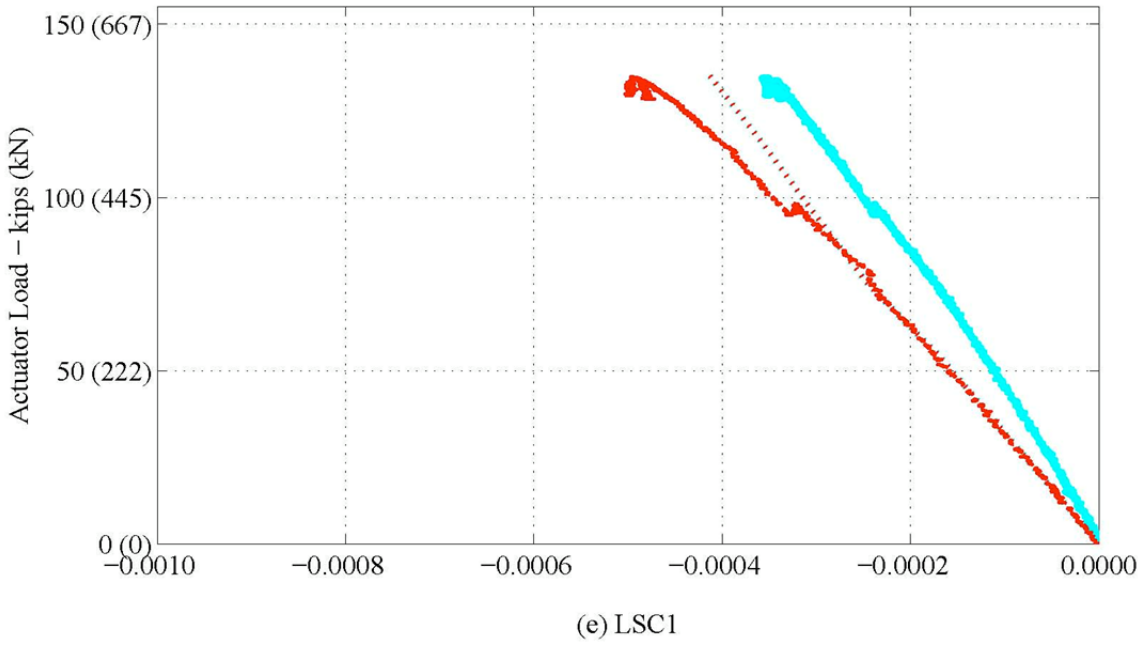

(e) LSC1

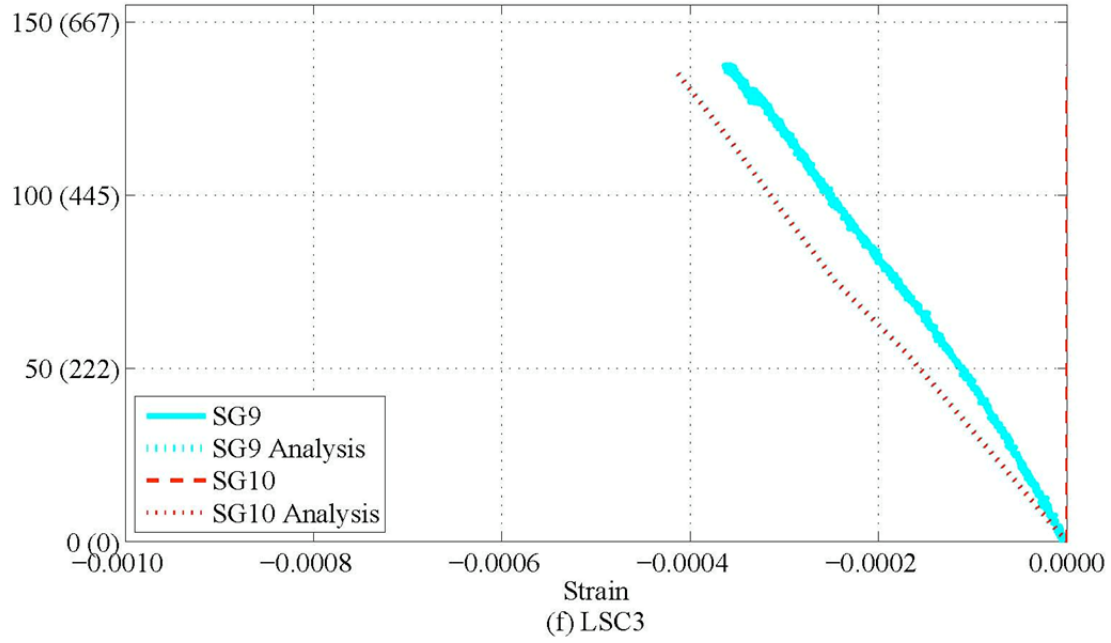

(f) LSC3

Figure 5-27. (Continued)

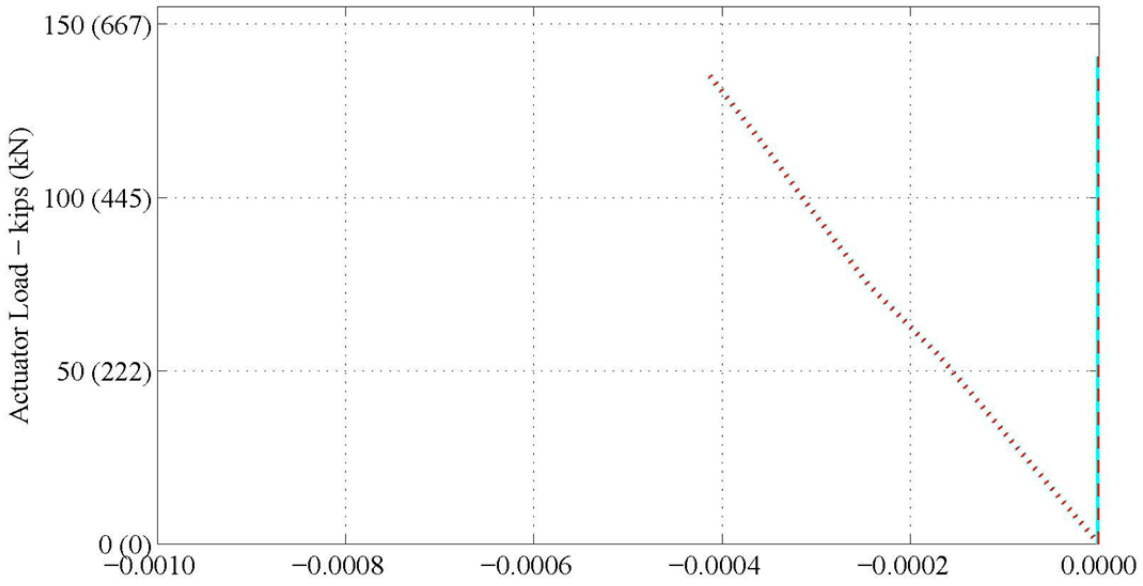

(g) LSC5

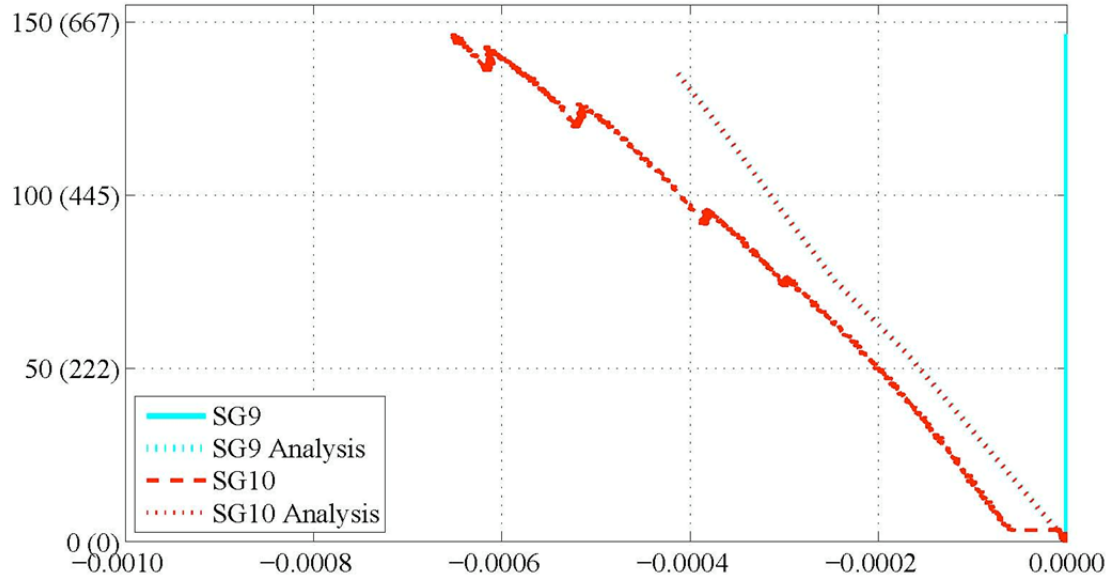

(h) LSC8

Figure 5-27. (Continued)

Figure 5-28 shows the measured external surface strains across the splice region at the same depth as the tension reinforcing steel as shown in Figure 5-11. LSC16 (Figure 5-28(a)) was instrumented with KM and LV gages on the tension regions of the specimen as shown in Figure 5-9. Figure 5-28(a) shows compression values recorded by KM14 and KM6 in the tension region of LSC16. The KM gages were not reliable in the tension region because the KM gages had a small gage length of 4 inches (102 mm) and some developing cracking did not form within the gage length of the instrument, but rather between gages. Since the LVDTs had a 12 inch (305mm) gage length, they were better able to capture the cracking within the specimen. The rest of the specimens were instrumented as shown in Figure 5-11. Note that LV1 and LV7 measured the strains at the sections directly under actuator 1 and actuator 2, respectively, and the others were within the splice region. The strains from the LVDTs were calculated using Eq. 5-10.

$$LV_{strain} = \frac{\Delta L_{LVDT}}{L_{LVDT}} \qquad \text{(Eq. 5-10)}$$

The LVDTs were positioned with 12 inches (305mm) between the couplers attached to the concrete. The increase in length, ΔL_{LVDT}, was recorded and divided by the length between the couplers, L_{LVDT}.

As shown previously, most of the plastic bending rotations within the specimen occurred only in the sections directly under each actuator. Figure 5-28(b) – (h) shows that the LV1 and LV7 measured surface strains were nonlinear and much larger than any other LV measurement within the splice region. Thus, this further confirmed that only the sections under the actuators were deforming plastically and those sections within the spliced region of the specimen remained within the elastic limits. Also it should be noted that the significant nonlinear response from the LV1 and LV7 gages started at a strain of about 0.002 for most specimens. The LV1 and LV7 gages on LSC9, LSC10, and LSC5 did not show yielding until a strain of about 0.0025 to 0.0030. This shows that it was reasonable to assume the rebar had yield strength of 70 ksi (783 MPa), instead of the specified 60 ksi (414 MPa), resulting in a theoretical yield strain of 0.0024. Also, this indicates that the plane sections remain plane modeling assumption is completely valid for the specimens tested in the four-point test setup.

Figure 5-29 compares the internal strains to the external strains across the splice length. LV1 and LV7 were removed from this figure since no internal gages were located at the splice ends. The closest SGs to the splice end were 18 inches (457mm) away. This figure better depicts the differences between LV2 through LV6 since the range of strains shown is smaller than Figure 5-28. This figure clearly shows that the response within the splice region remained in the elastic region and there was no sign of degradation within the splice region. In addition, the figure shows that the internal strain measurement and external surface strain measures were comparable; again validating the plane sections remain plane modeling assumption.

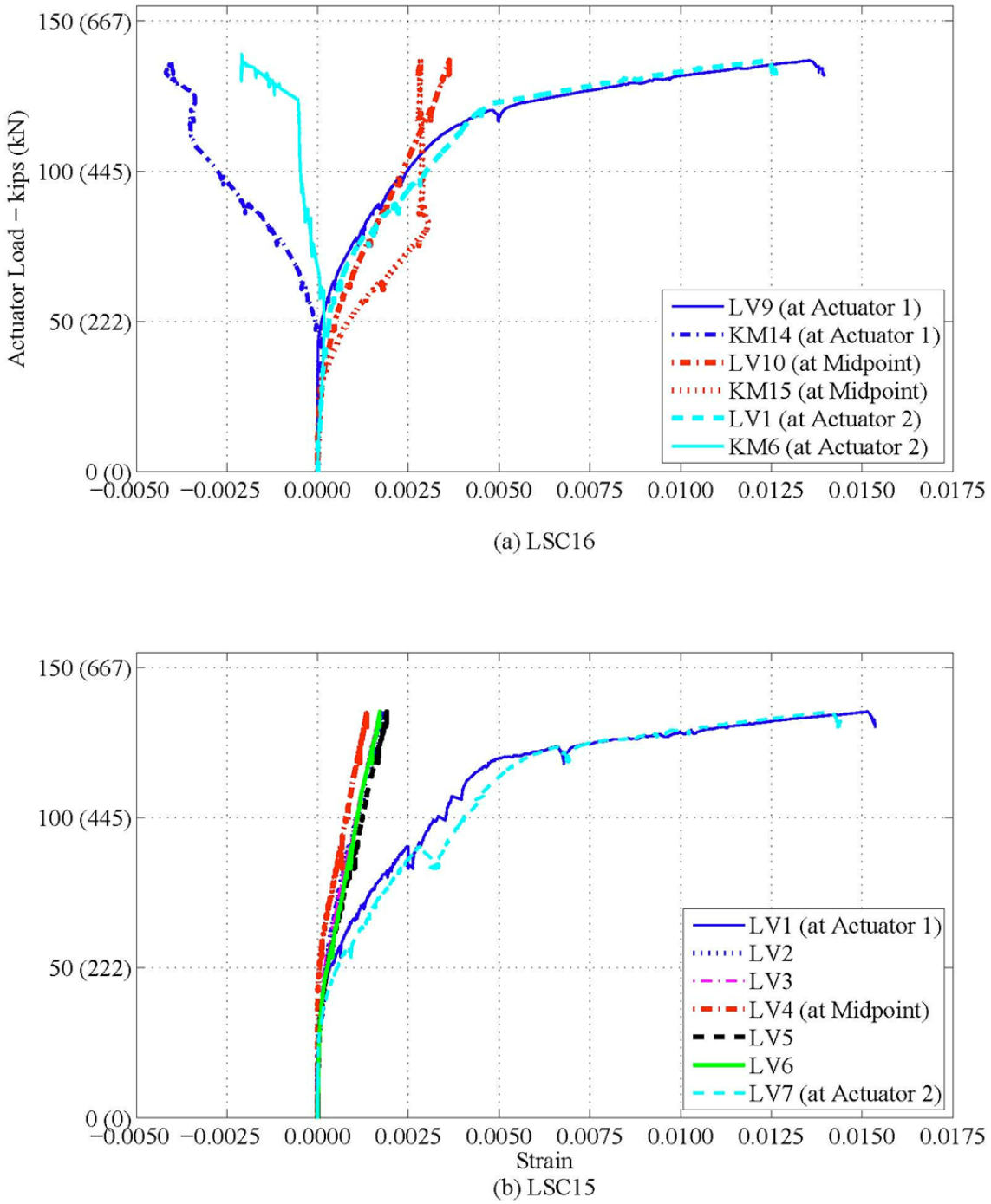

Figure 5-28. Experimental Load vs. Strain during Four-Point Test: LVDTs across the Splice Length in the Tension Region.

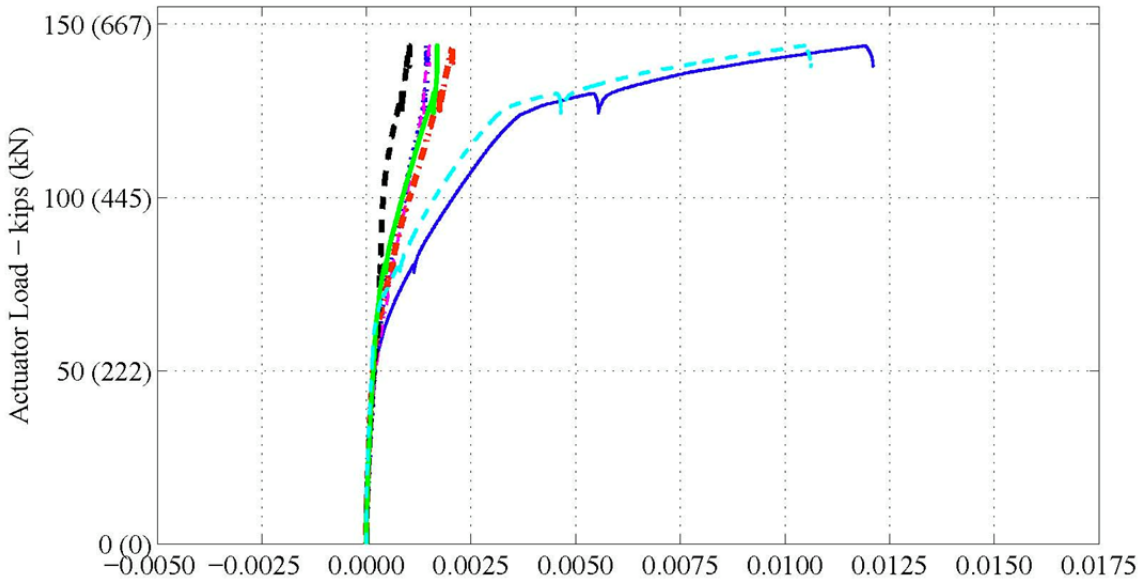

(c) LSC9

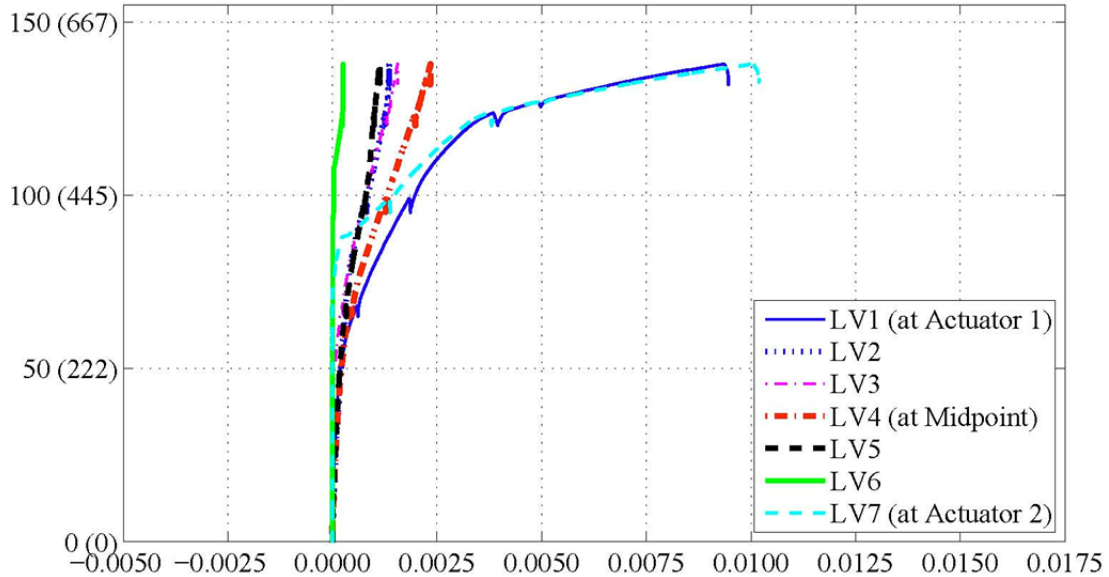

(d) LSC10

Figure 5-28. (Continued)

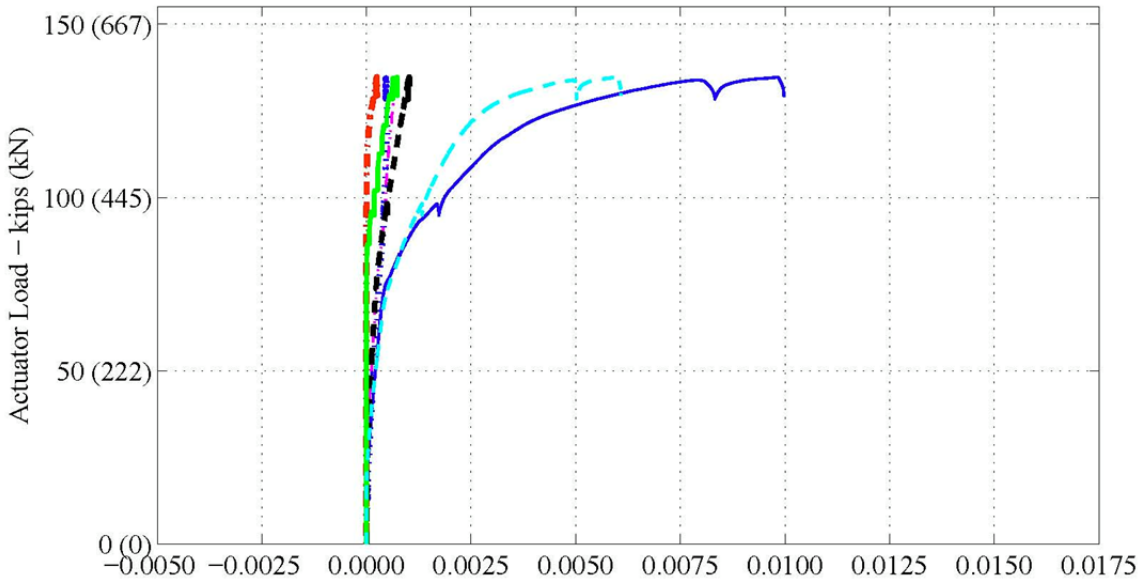

(e) LSC1

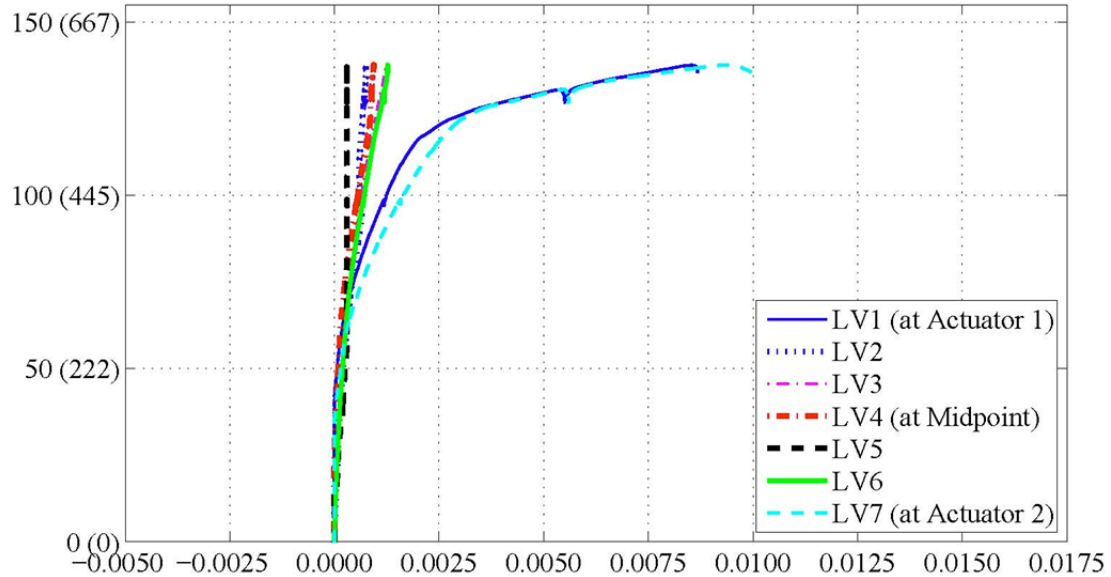

(f) LSC3

Figure 5-28. (Continued)

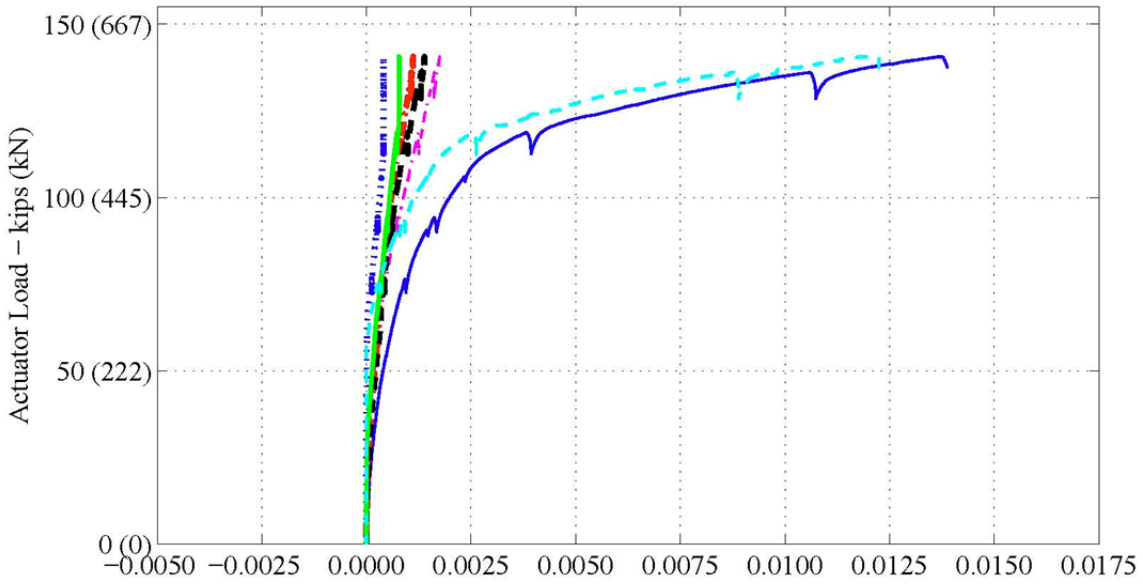

(g) LSC5

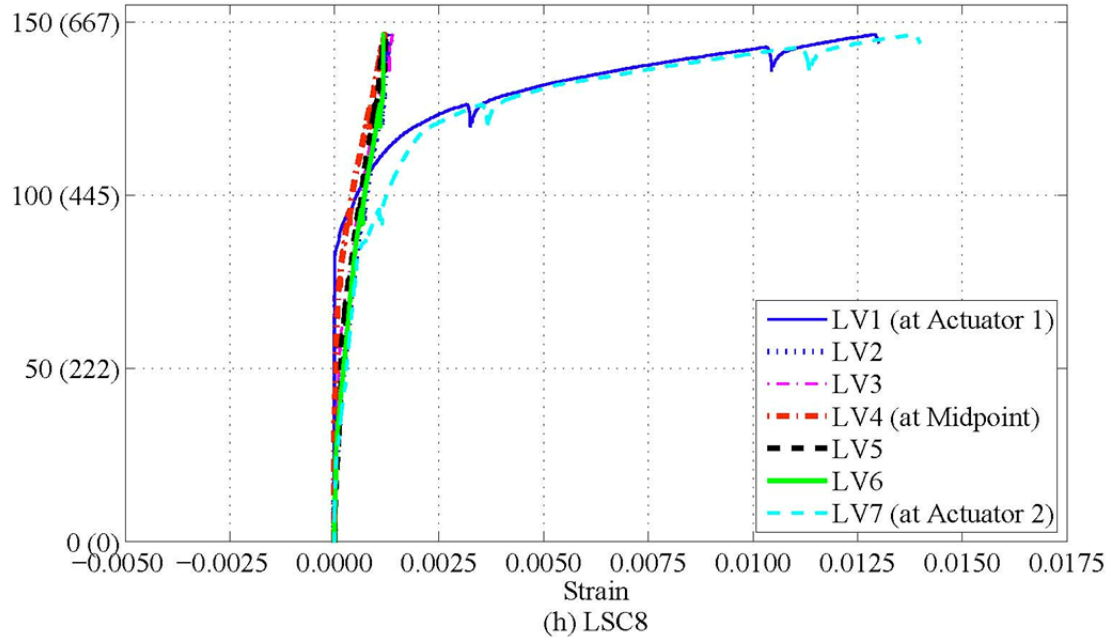

(h) LSC8

Figure 5-28. (Continued)

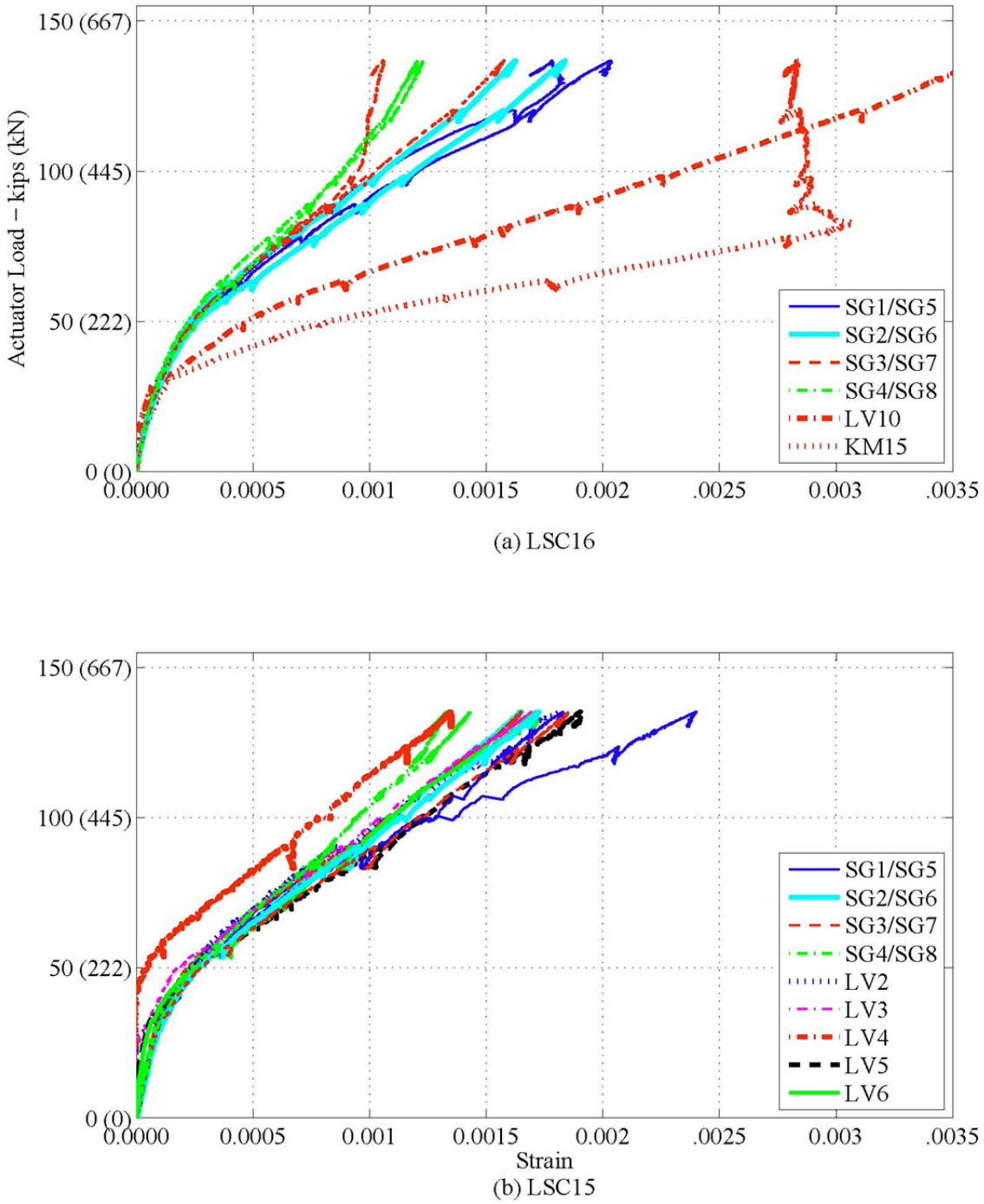

Figure 5-29. Experimental Load vs. Strain during Four-Point Test: Internal and External Strain Comparison across Splice Length.

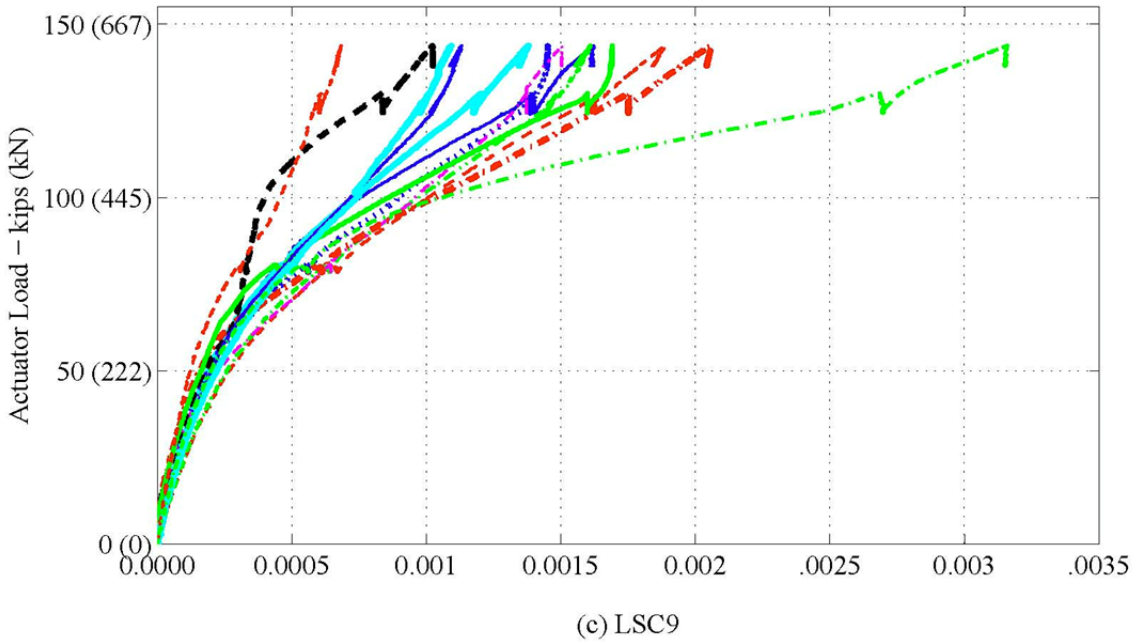

(c) LSC9

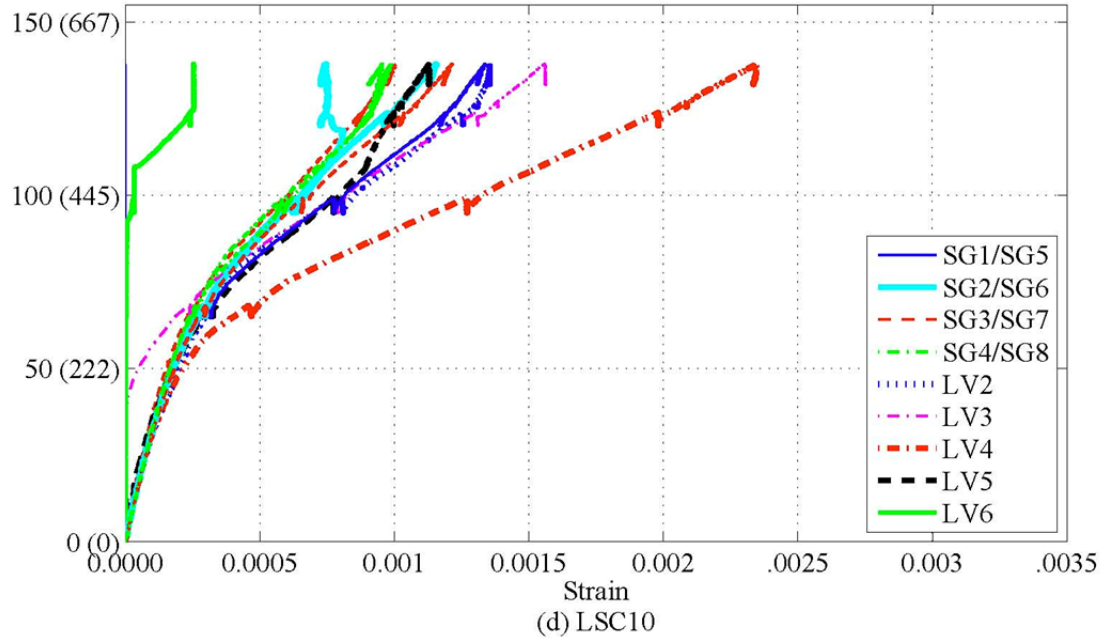

(d) LSC10

Figure 5-29. (Continued)

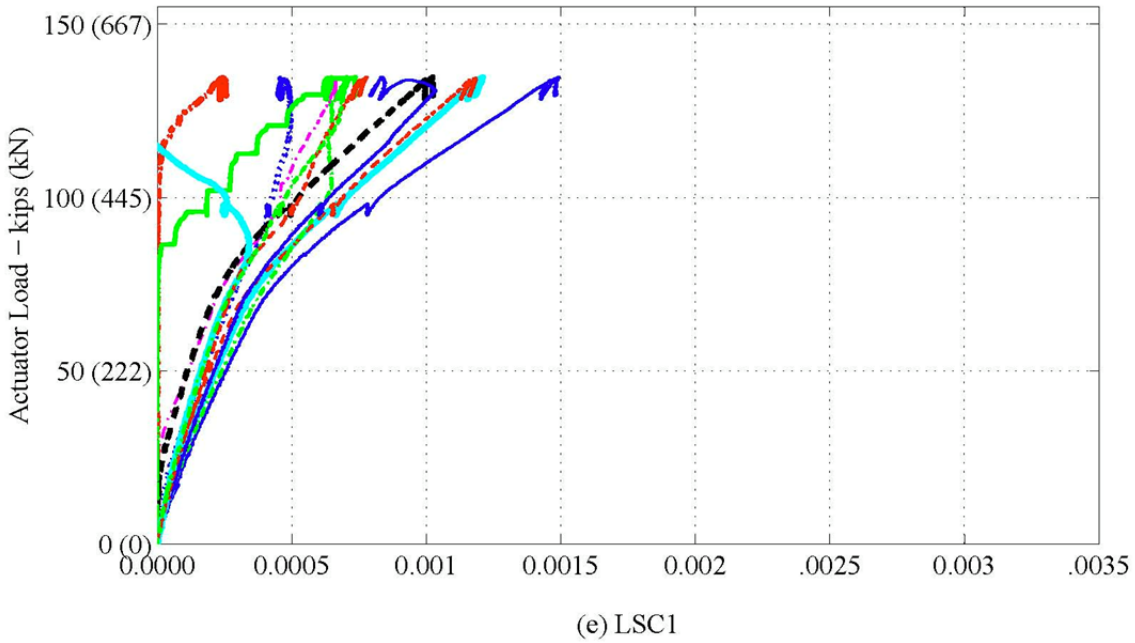

(e) LSC1

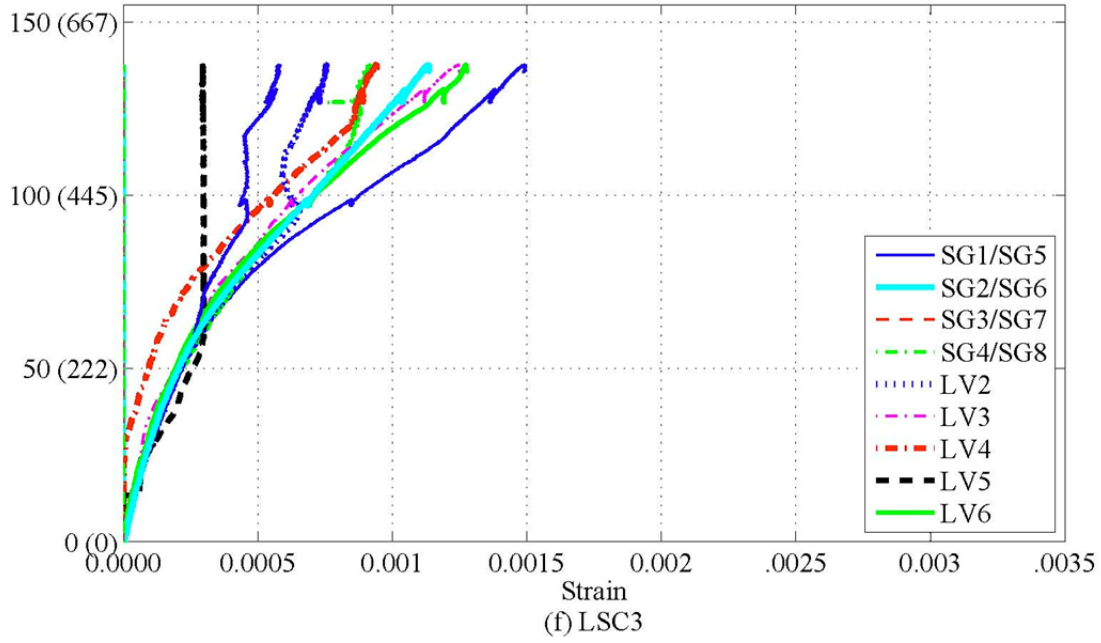

(f) LSC3

Figure 5-29. (Continued)

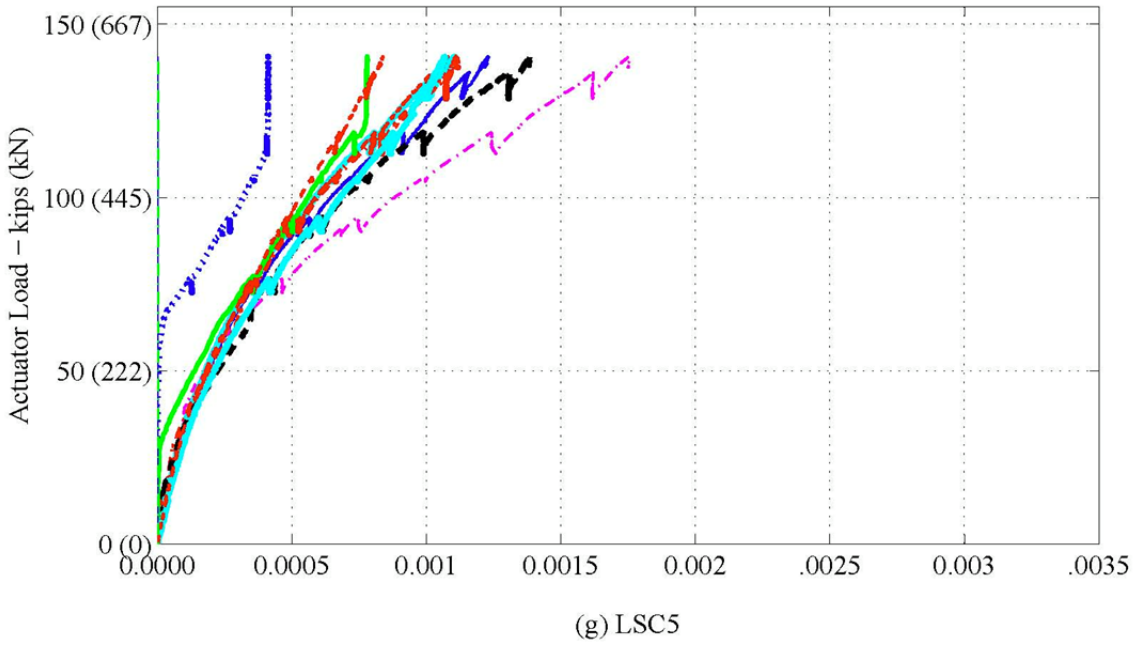

(g) LSC5

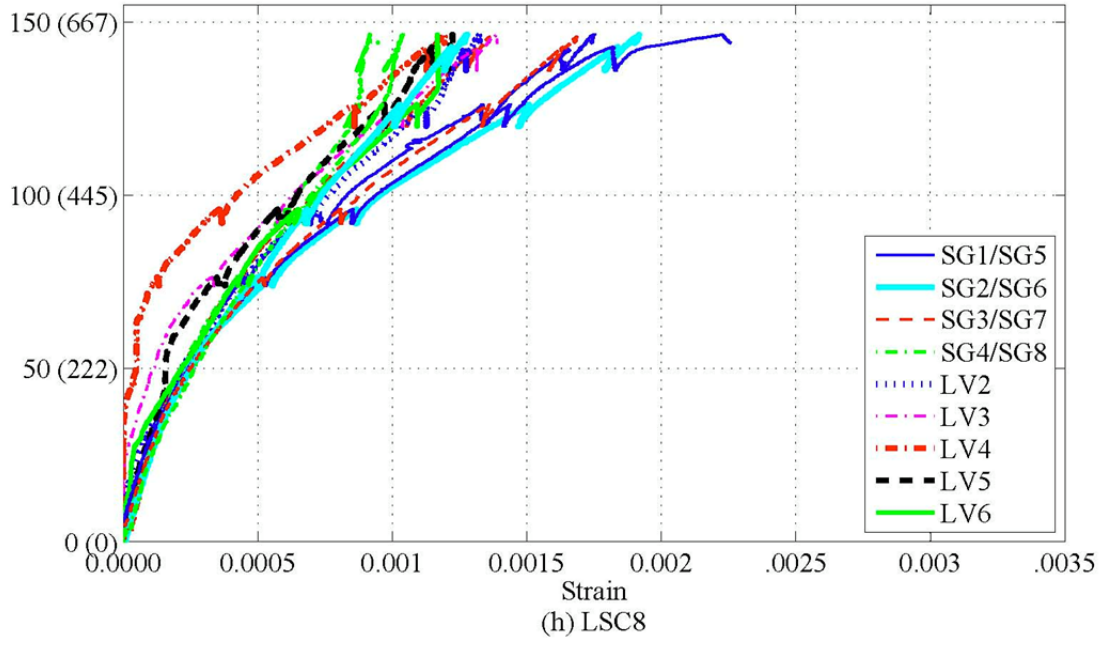

(h) LSC8

Figure 5-29. (Continued)

Figure 5-30 shows a large flexure crack (vertical crack in the figure) from the section directly under actuator 1 during the four-point test for LSC5 at the maximum load, 140 kips (623 kN). The crack width is approximately 0.25 inches (6.4 mm) at the bottom of the section and is within the gage length of LV1. Figure 5-30 also shows several cracks from premature concrete deterioration orthogonal to the bending crack from the load testing.

Figure 5-30. Flexural Crack under Actuator 1 during Four-Point Test for LSC5.

Figure 5-31 shows the actuator force vs. the measured strains at varying depths in the section directly below actuator 2. Figure 5-31(a) shows the strains in LSC16 using KM gages at the top of the section and LVDTs elsewhere (Figure 5-9). Although, Figure 5-30 shows cracks under Actuator 1, the cracking is very similar to the cracking under

actuator 2 with data presented in Figure 5-31. As discussed previously, the LVDTs and KM gages gathered better data in the tension and compression regions, respectively. Therefore, external location of the compression steel was instrumented with a KM gages for the rest of the specimens (Figure 5-11). No LVDT gages were placed on the bottom of LSC16 to measure the bottom strain, but two LVDTs were placed for the remaining specimens. Figure 5-31 also shows the actuator force vs. corresponding strains calculated from the analysis. The figure shows that the analytical response is comparable to the experimentally measured response up to yielding of the reinforcement, and misses the post-yield stiffness due to reasons explained earlier. Also, it is noticeable that the load at which the strains reached plasticity is almost constant throughout the section.

To compare the compression strains near the two actuators, Figure 5-32 shows the actuator force vs. strains from KM9, LV4, KM13, and LV8 for LSC16 and KM6, KM7, KM13, and KM14 for the other specimens. Figure 5-9 shows the KM locations on LSC16 and Figure 5-11 shows the KM locations for the other LSC specimens. About half of the specimens were loaded until the compression strain reached 0.003 (theoretical ultimate crushing limit). The figure shows that the experimental strains are smaller than the analytical strains similar to the internal compressive strains on the splice bar (Figure 5-27). The average load at yielding is the same for the analytical model and the control specimens (LSC15 and LSC16). However the analytical yielding load is higher than the experimental results for the non-control specimens varying up to about 20 kips (89 kN) larger than the experimental results.

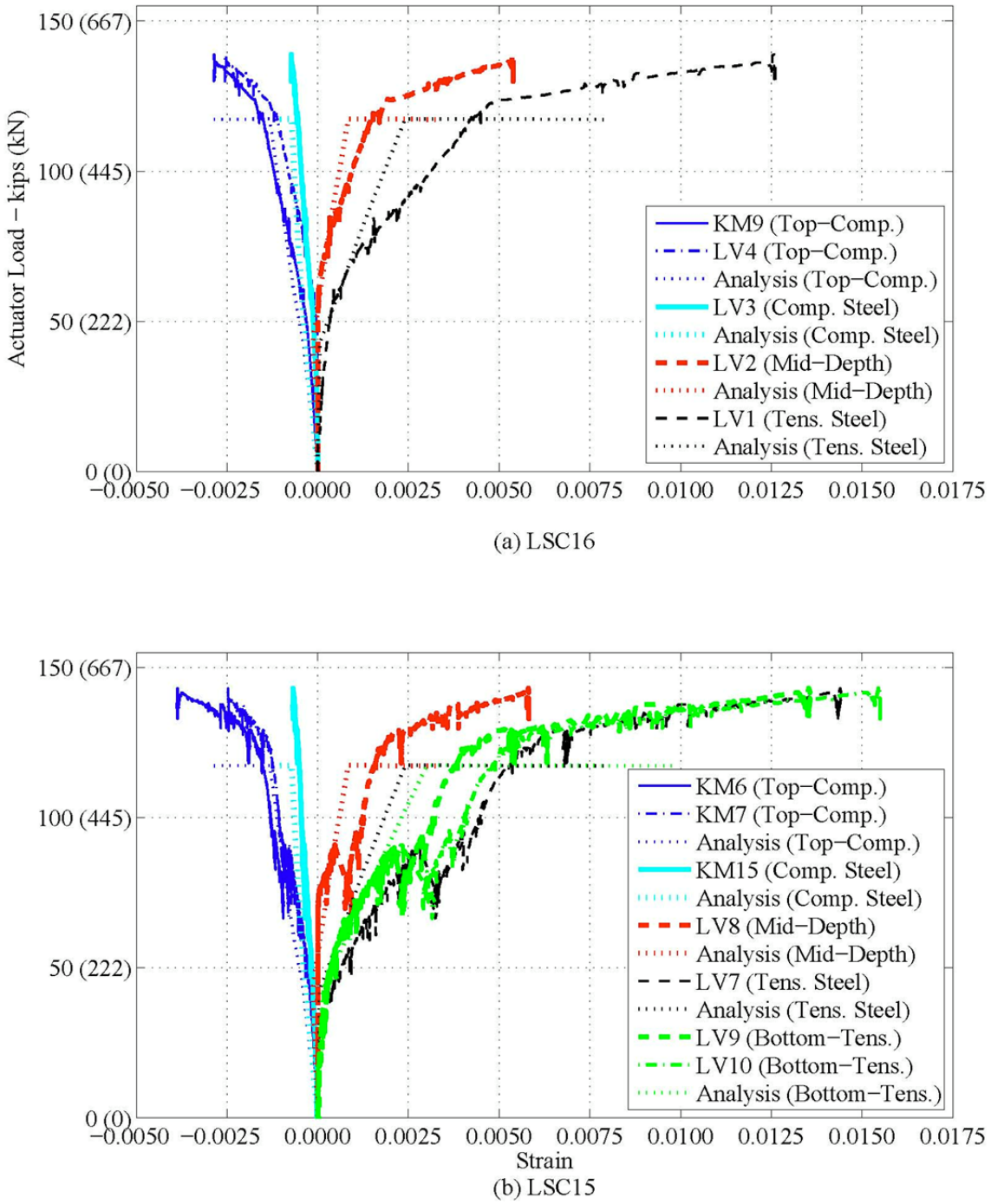

Figure 5-31. Experimental and Analytical Load vs. Strain during Four-Point Test: External Strain Gages across the depth of the Splice End.

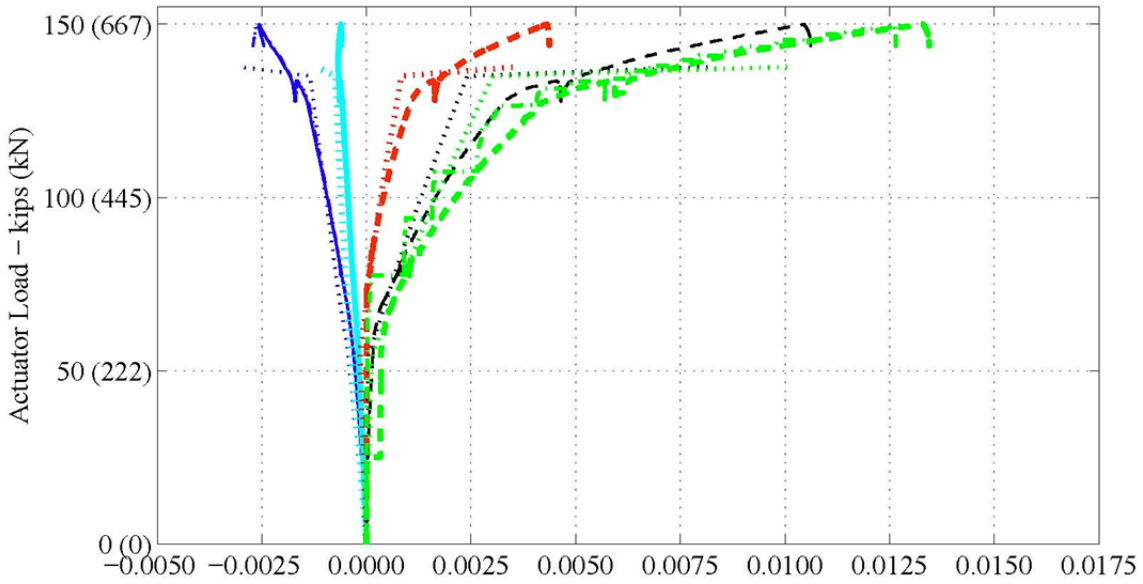

(c) LSC9

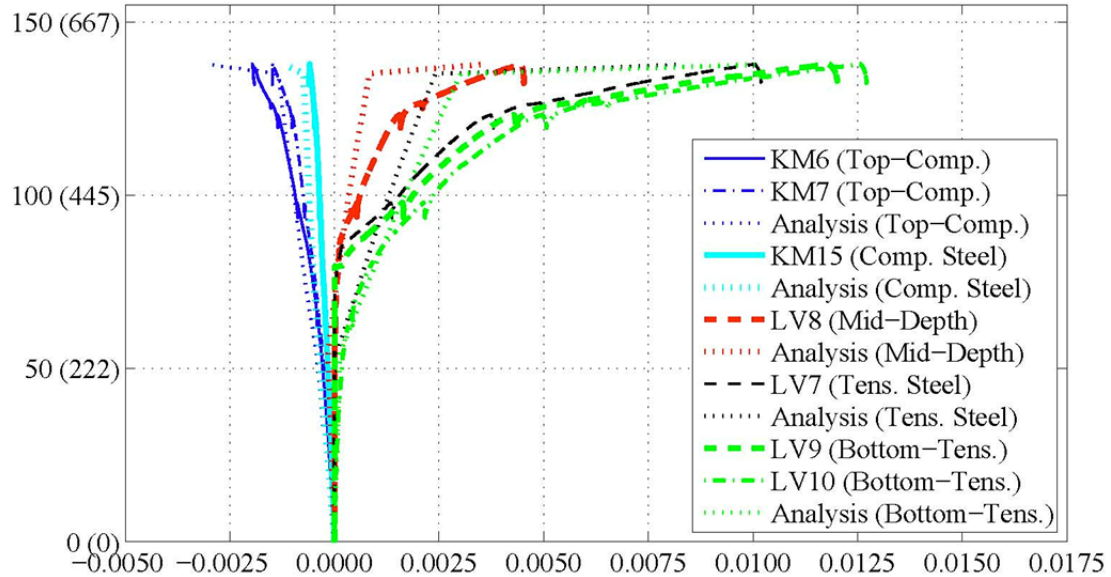

(d) LSC10

Figure 5-31. (Continued)

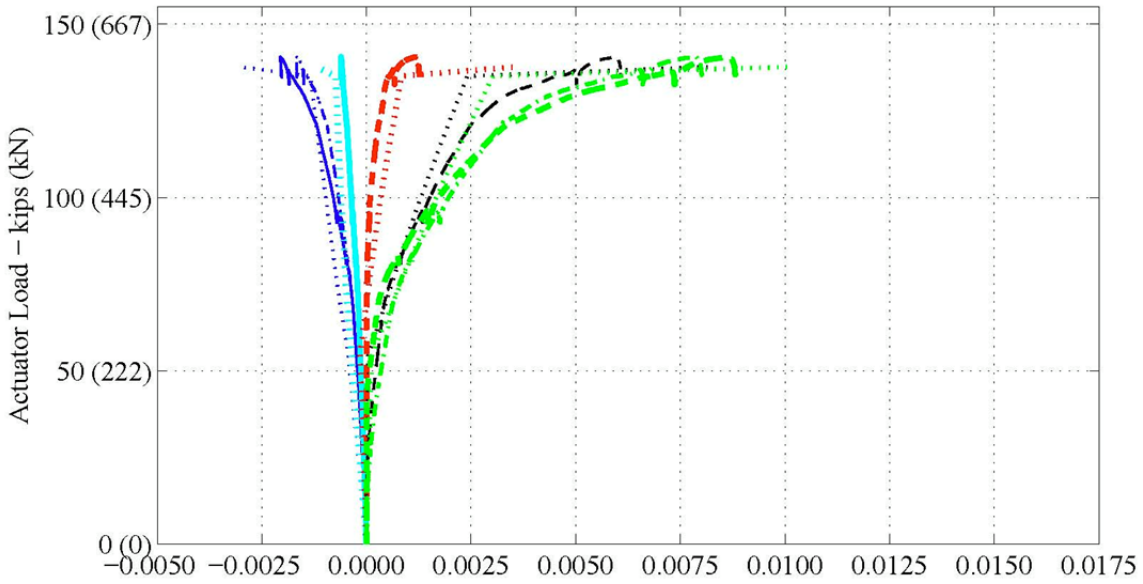

(e) LSC1

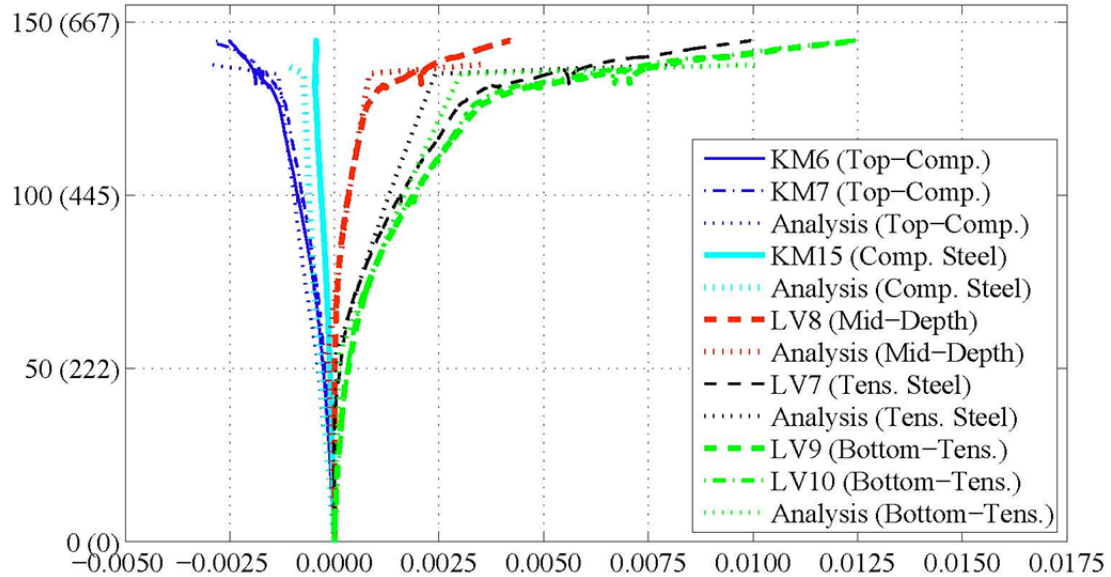

(f) LSC3

Figure 5-31. (Continued)

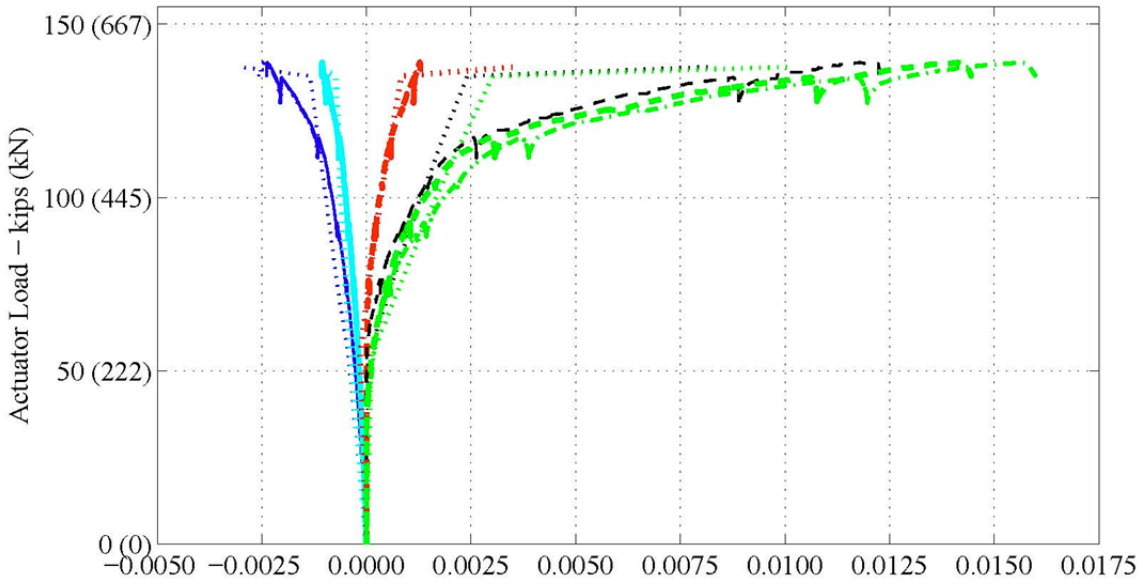

(g) LSC5

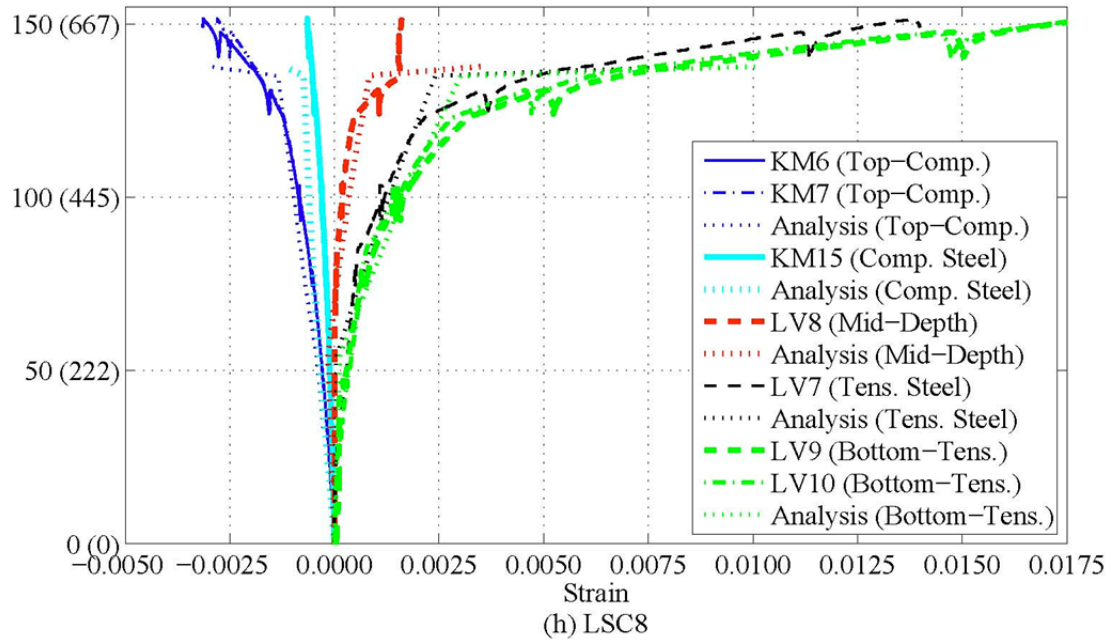

(h) LSC8

Figure 5-31. (Continued)

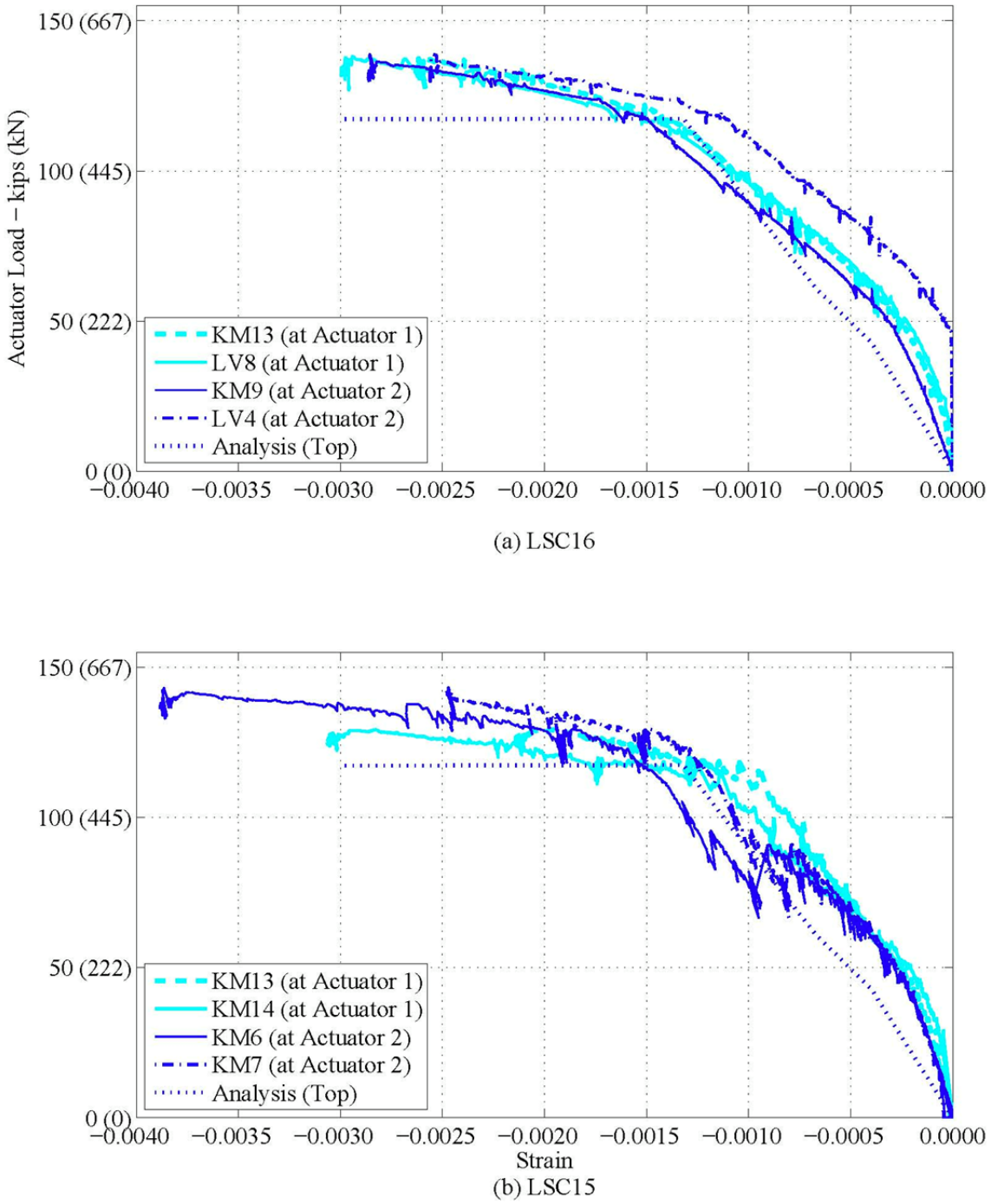

Figure 5-32. Experimental Load vs. Strain during Four-Point Test: KM gages at the Splice End in the Compression Region.

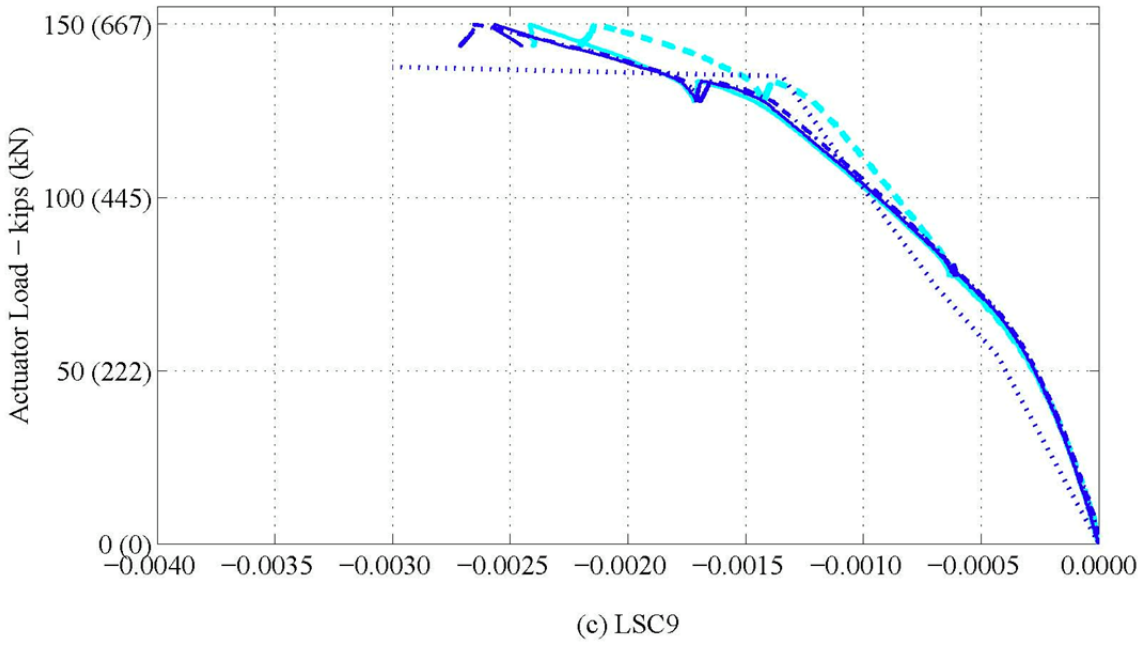

(c) LSC9

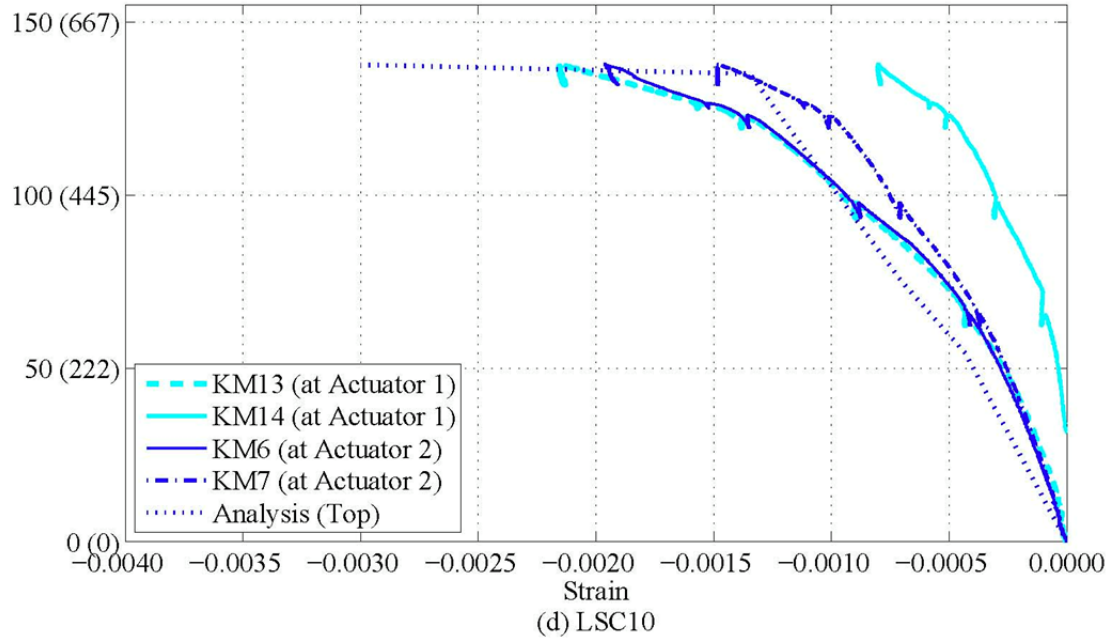

(d) LSC10

Figure 5-32. (Continued)

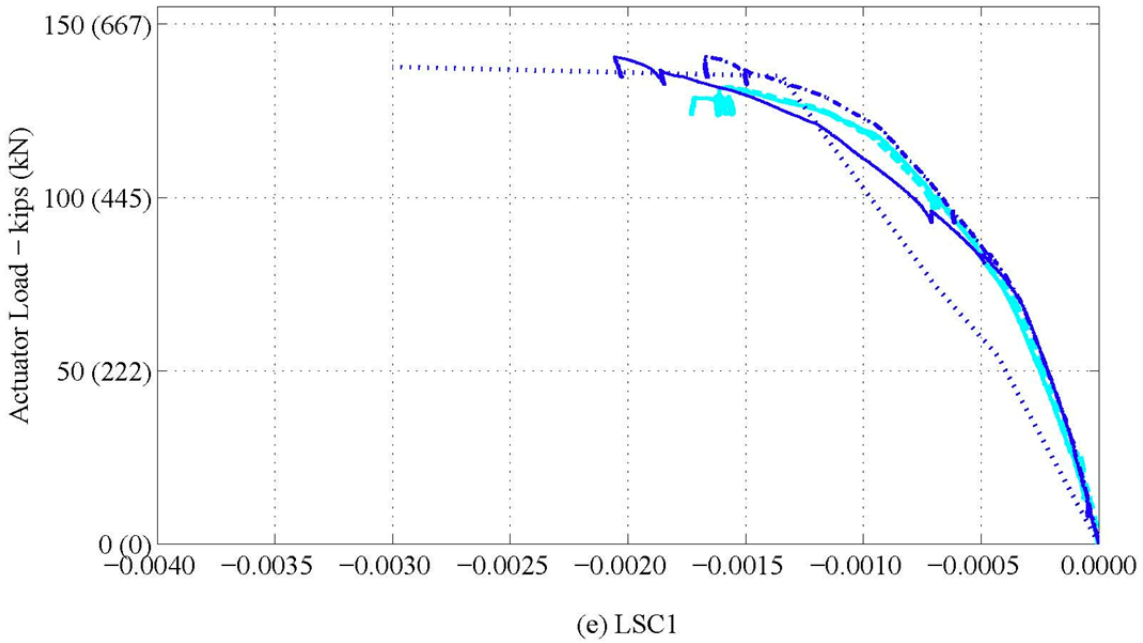

(e) LSC1

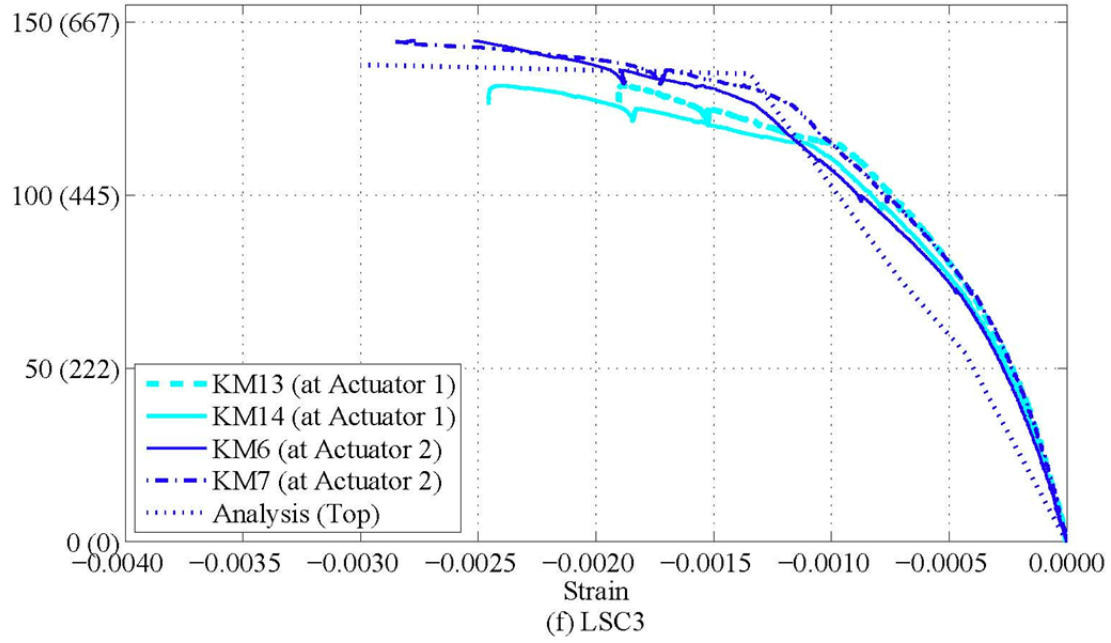

(f) LSC3

Figure 5-32. (Continued)

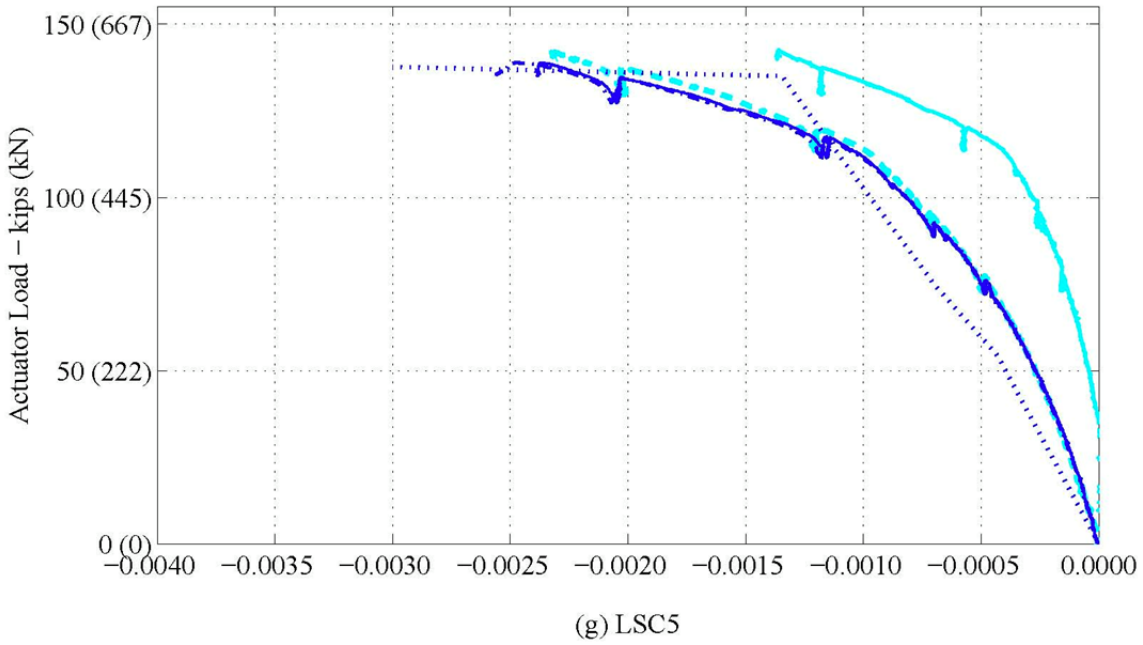

(g) LSC5

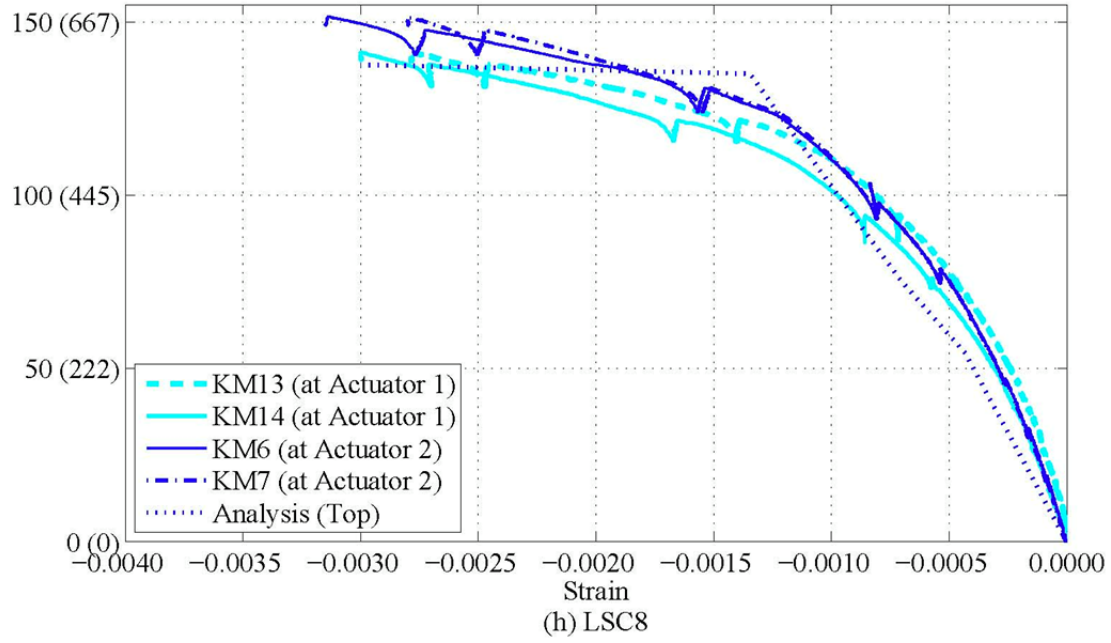

(h) LSC8

Figure 5-32. (Continued)

Figure 5-33 shows the compression surface strains across the splice length. Figure 5-33(a) compares the KM and LVDT gages in the compression region. This figure shows the compression strains at each actuator were very similar. KM gages were chosen to instrument the remaining specimens shown in Figure 5-33(b) – (h). The compression strains across the splice length were smaller and did not reach plasticity, unlike the compression strains at the actuator load point (Figure 5-32). This is same finding as the tension region, where the strains at the splice ends (actuator load points) deformed plastically and the splice region remained primarily elastic.

Figure 5-34 shows the transverse hoop strains from SG11, and comparable concrete cover and core from KM1, and KM2 near Small Face 1. These strains were measured during the deterioration process (section 3) and set to zero before the four-point test. Figure 5-35 shows the transverse hoop strains from SG12 and the comparable concrete cover and core strains KM3, KM4, and KM5 near Large Face 1, which were also set to zero before the four-point test,. The figures show some of the measured data had completely malfunctioned, and others gave inconsistent strain measurements. This most likely means that these measurements were not completely reliable following the large resulting strains during the deterioration program.

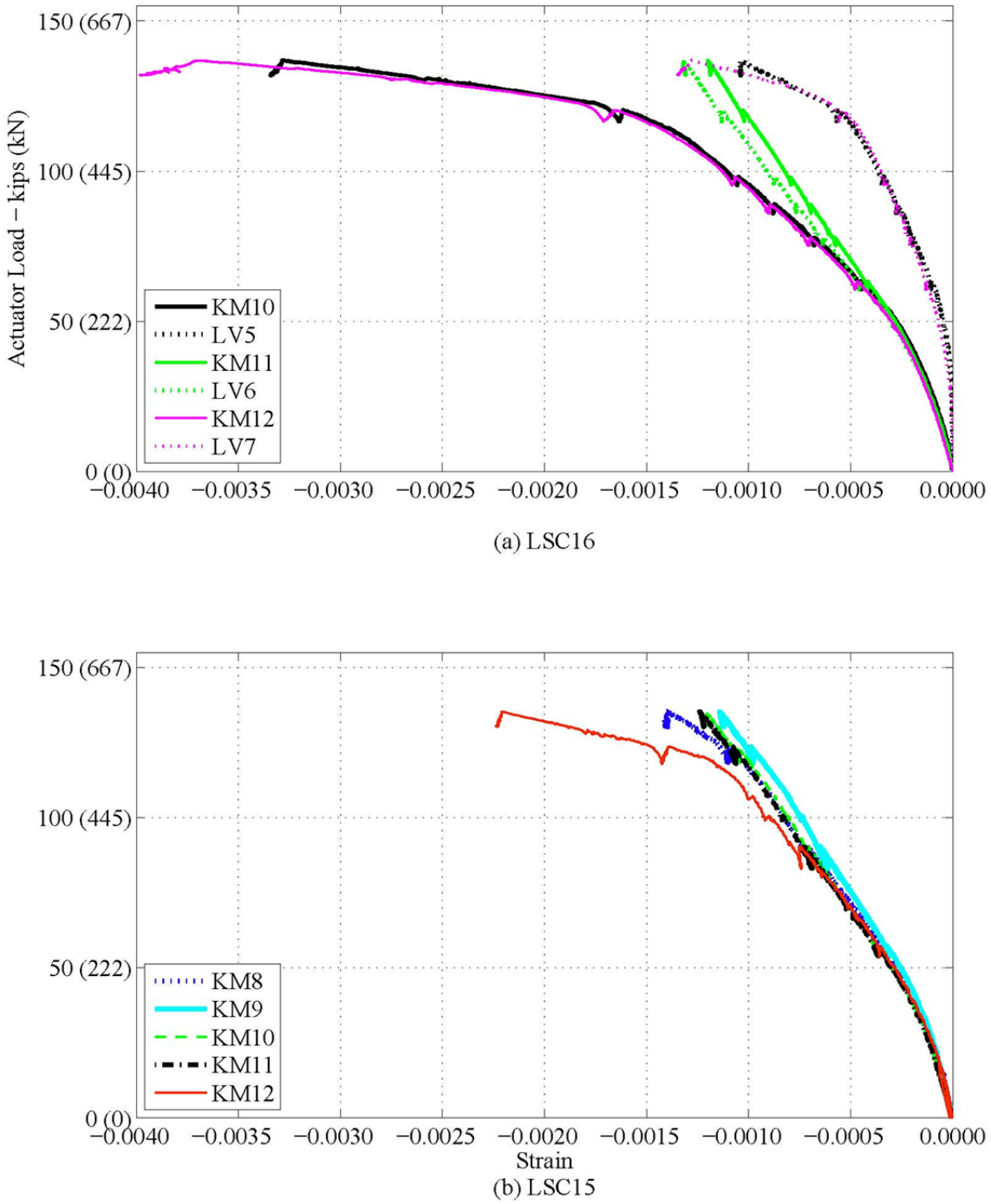

Figure 5-33. Experimental Load vs. Strain during Four-Point Test: KM gages across the Splice Length in the Compression Region.

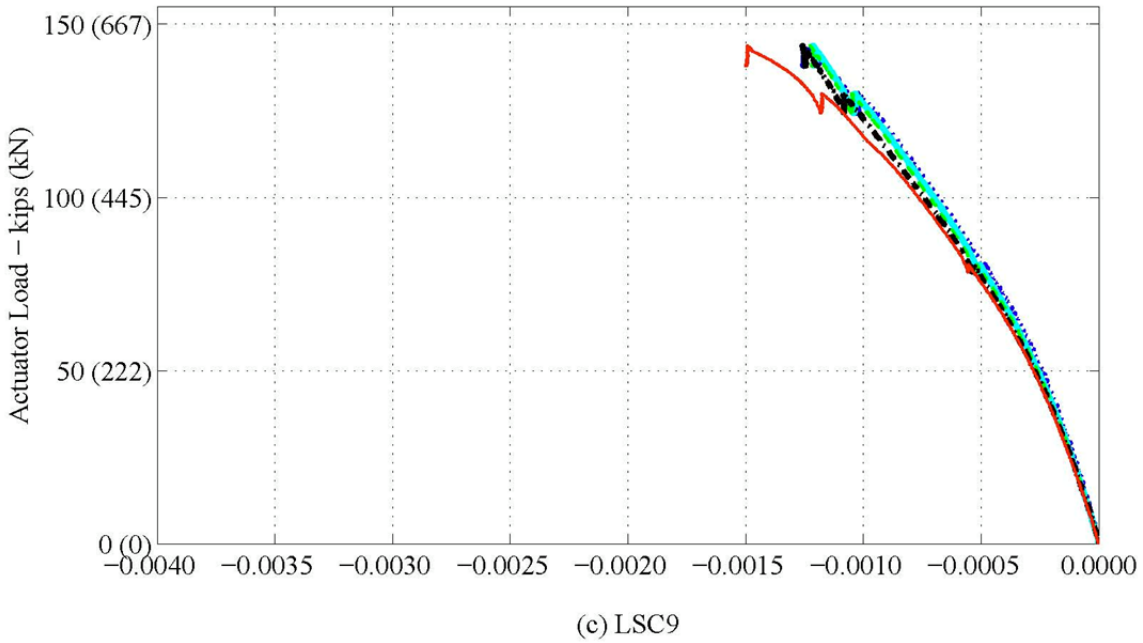

(c) LSC9

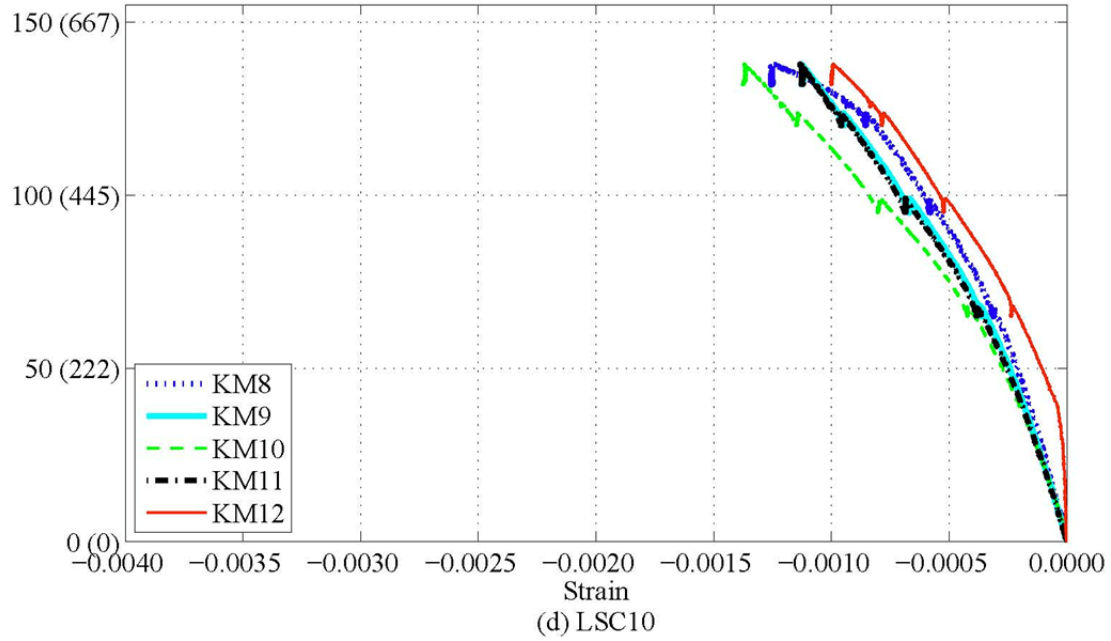

(d) LSC10

Figure 5-33. (Continued)

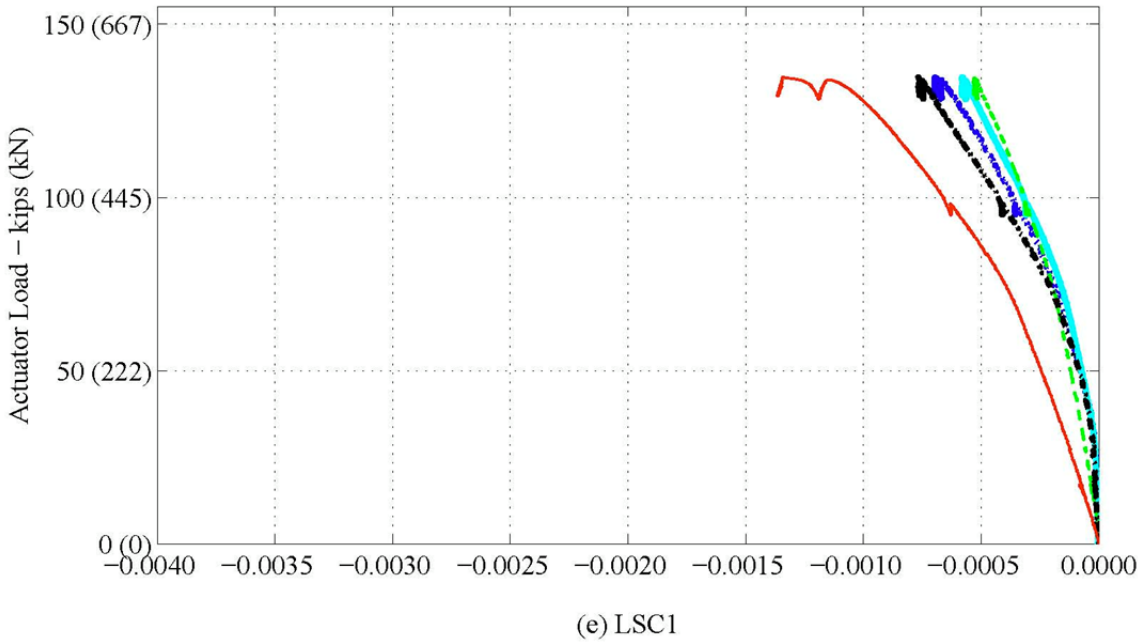

(e) LSC1

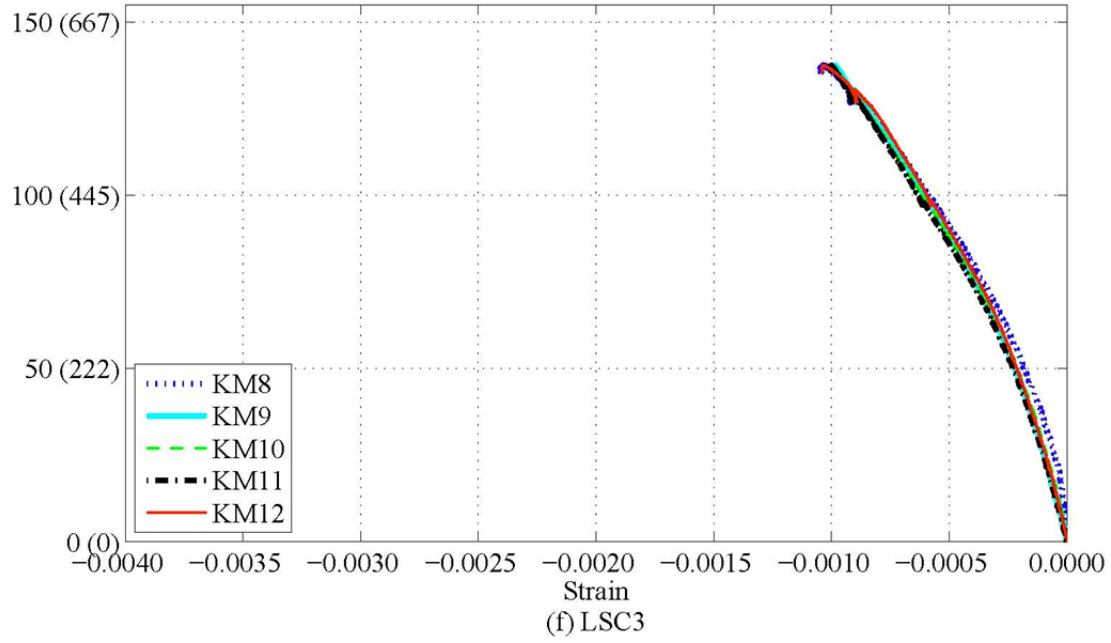

(f) LSC3

Figure 5-33. (Continued)

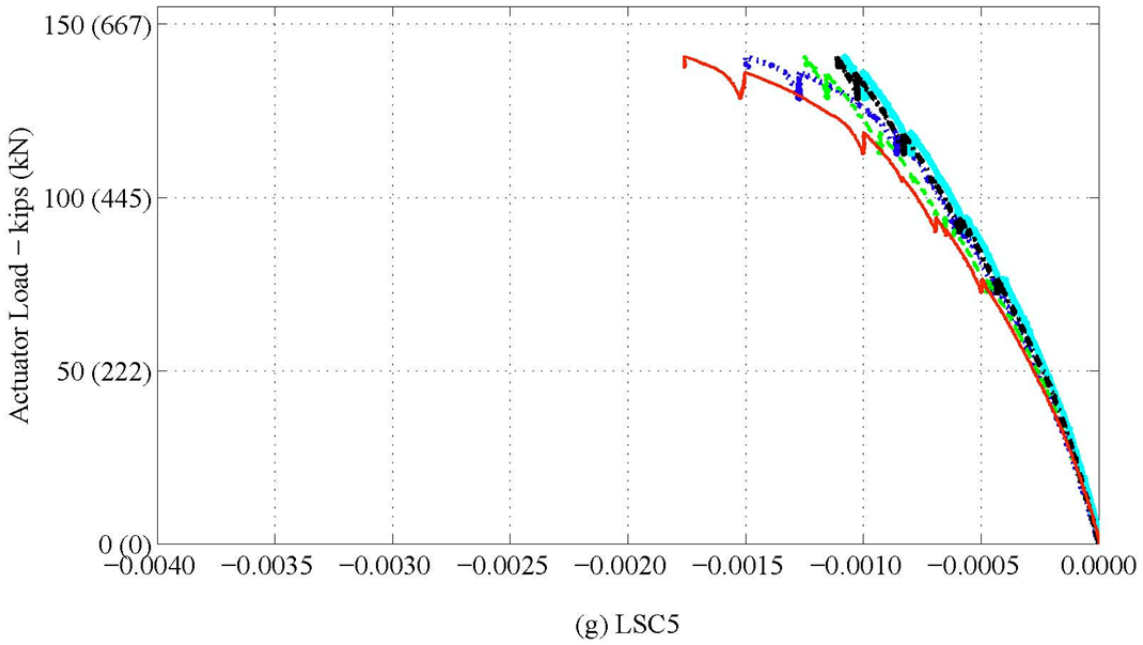

(g) LSC5

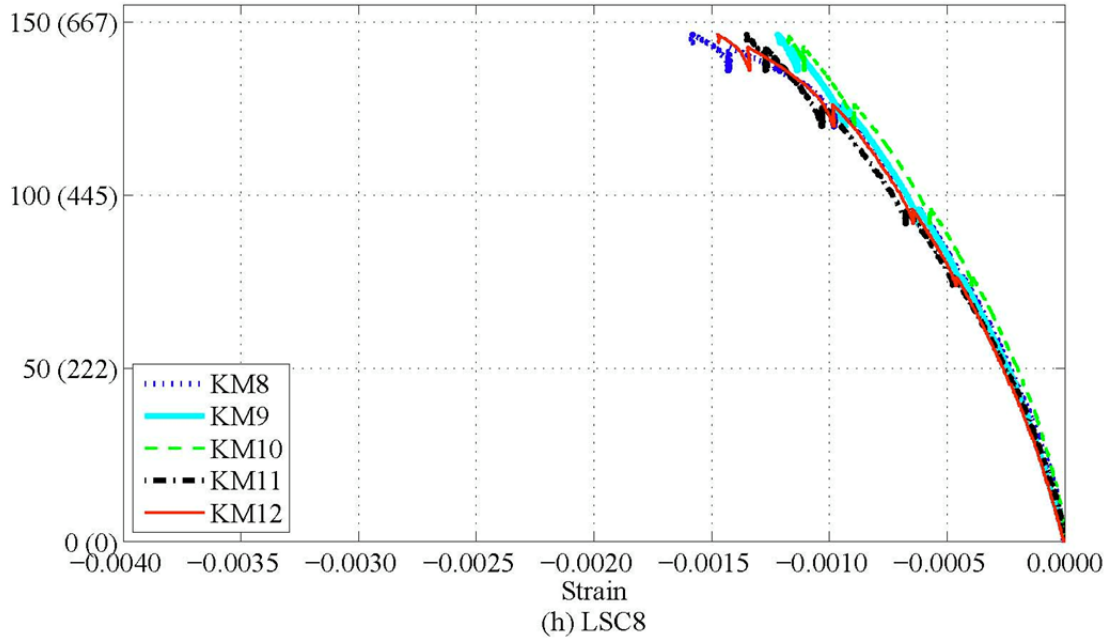

(h) LSC8

Figure 5-33. (Continued)

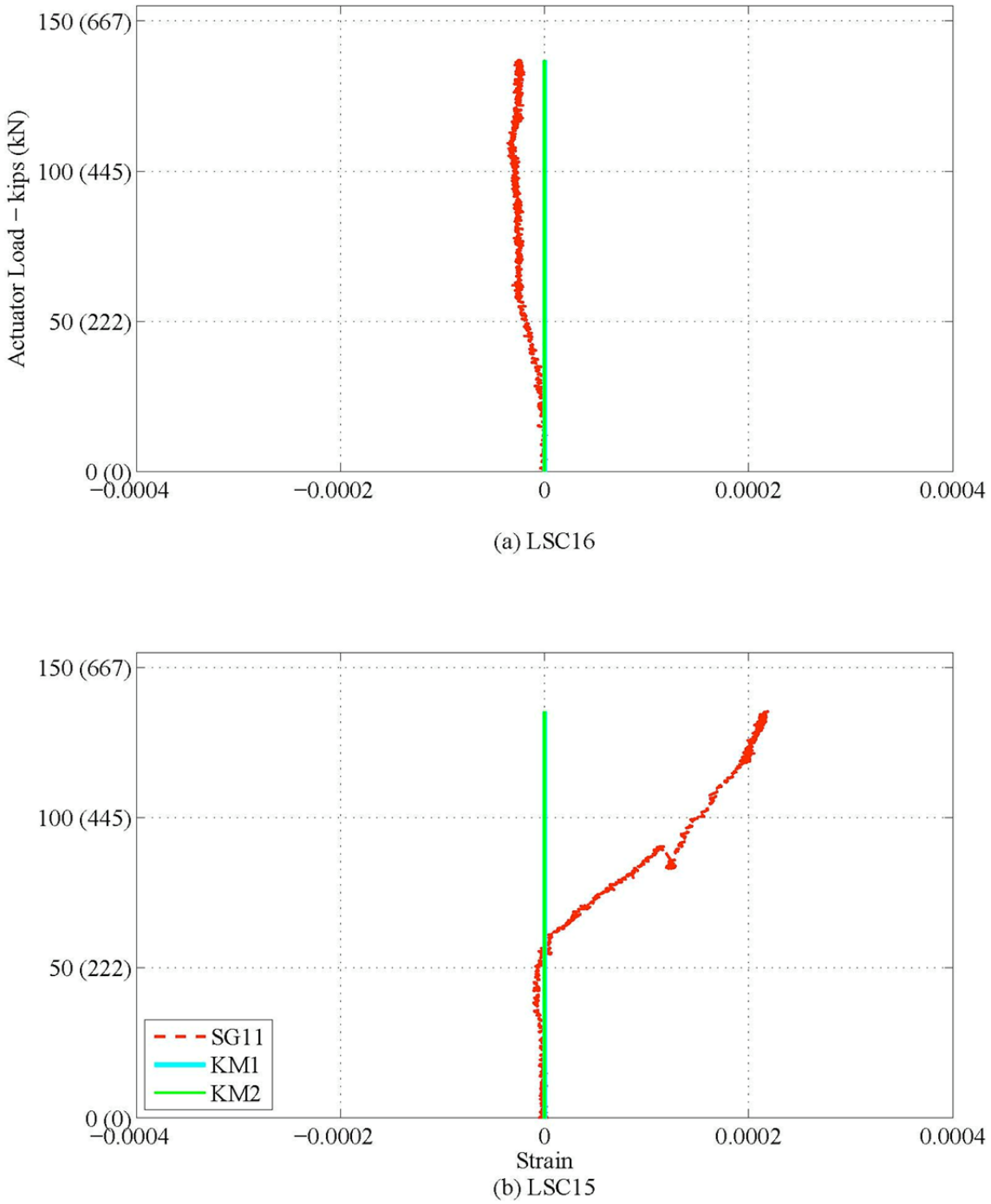

Figure 5-34. Experimental Load vs. Strain during Four-Point Test: Internal gages: SG11, KM1 – KM2 by Small Face 1.

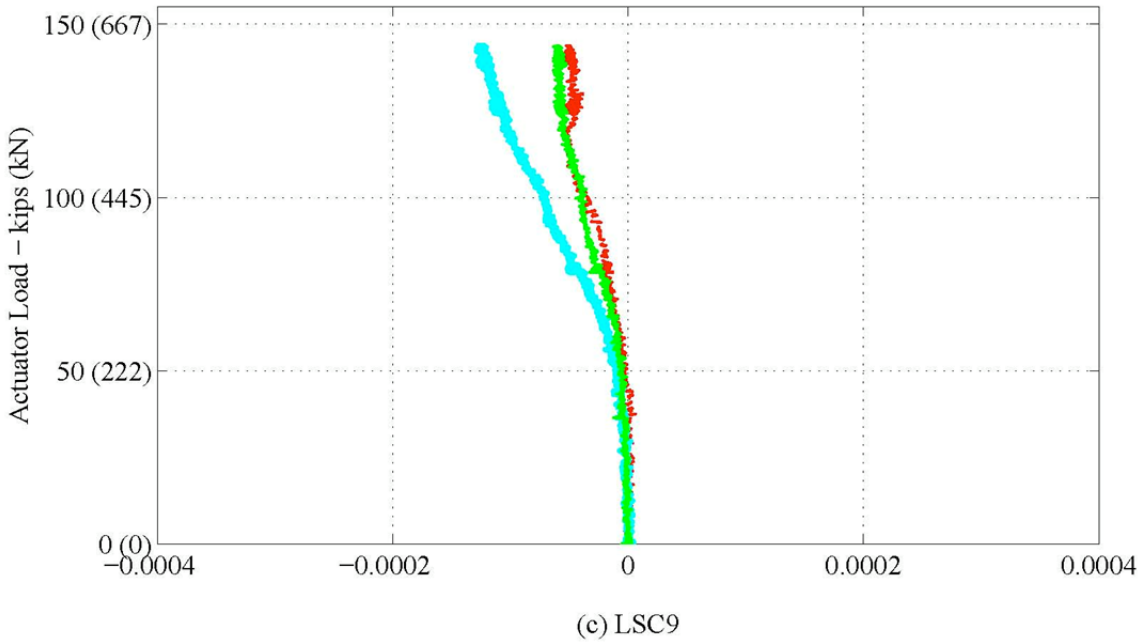

(c) LSC9

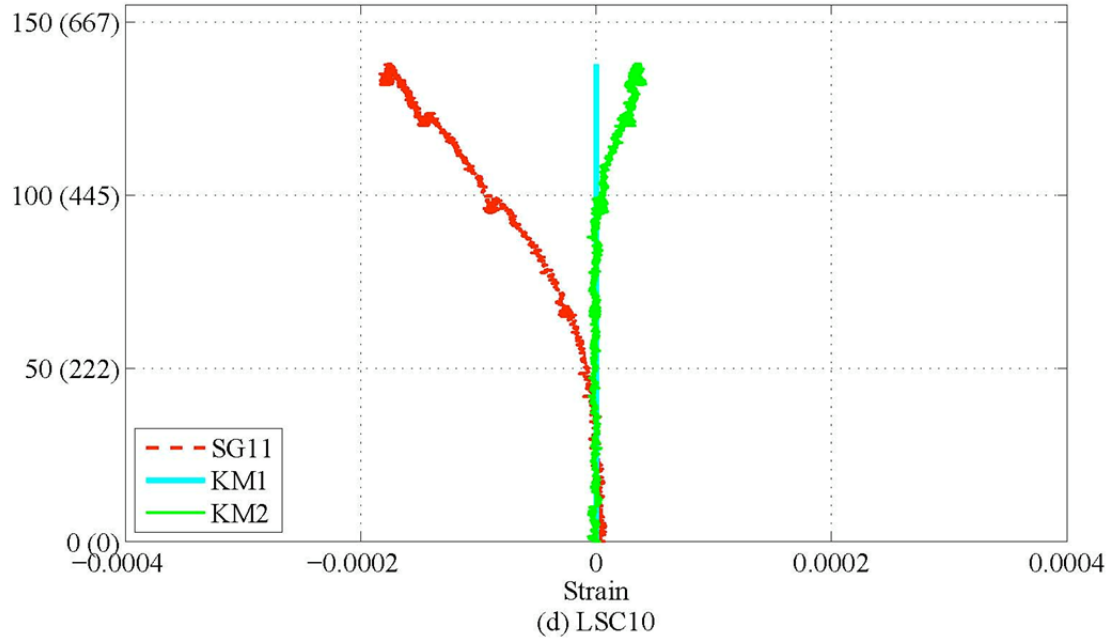

(d) LSC10

Figure 5-34. (Continued)

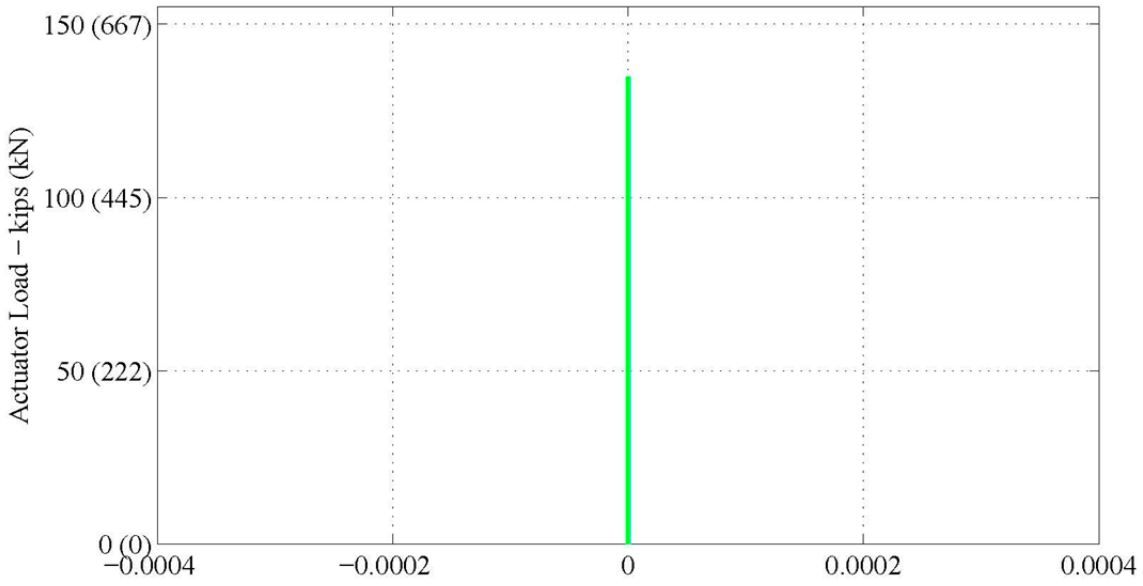

(e) LSC1

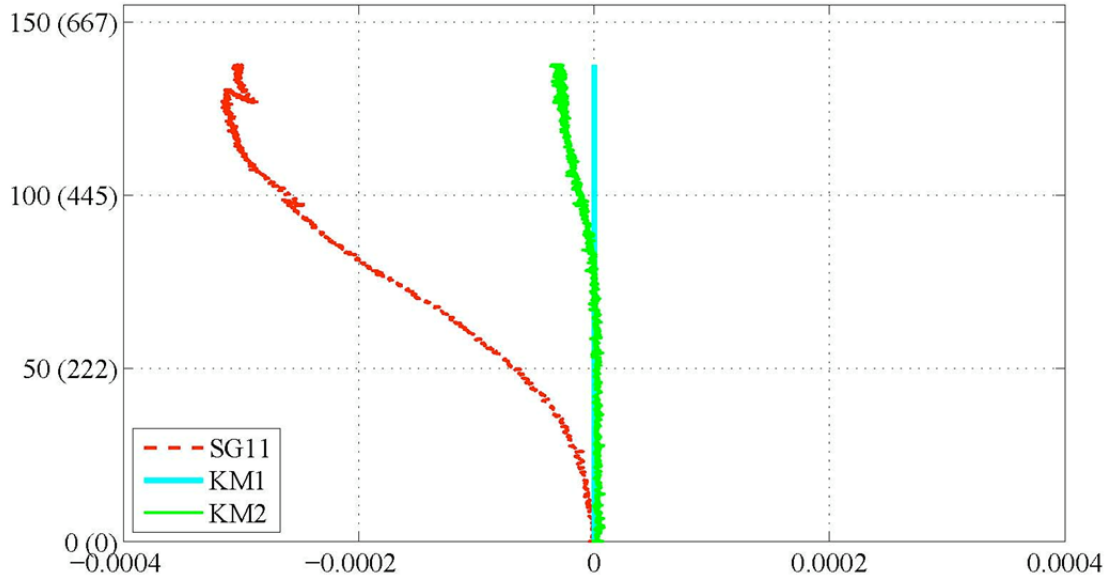

(f) LSC3

Figure 5-34. (Continued)

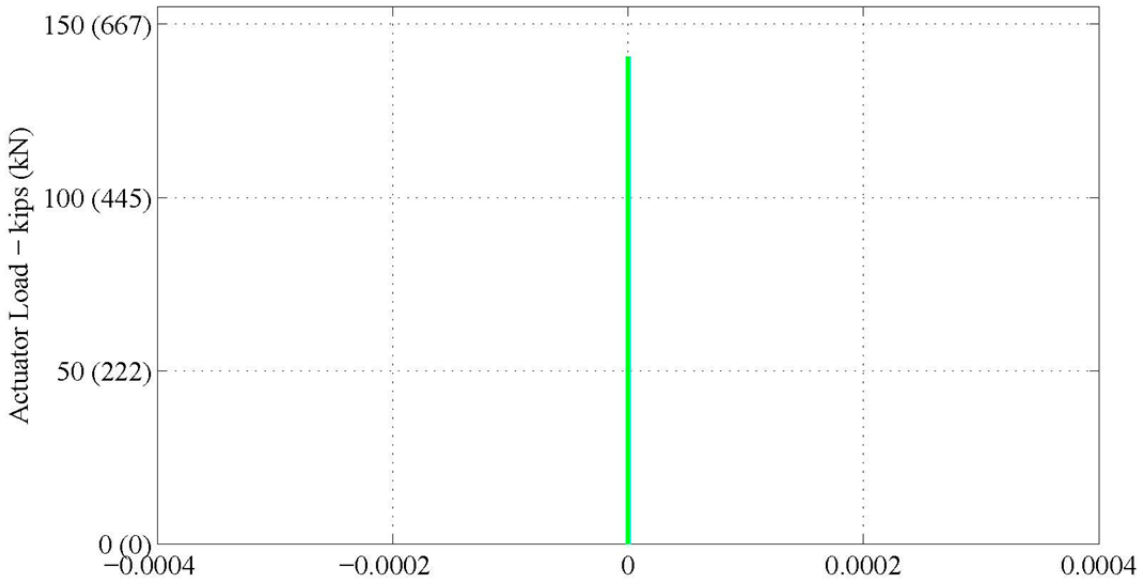

(g) LSC5

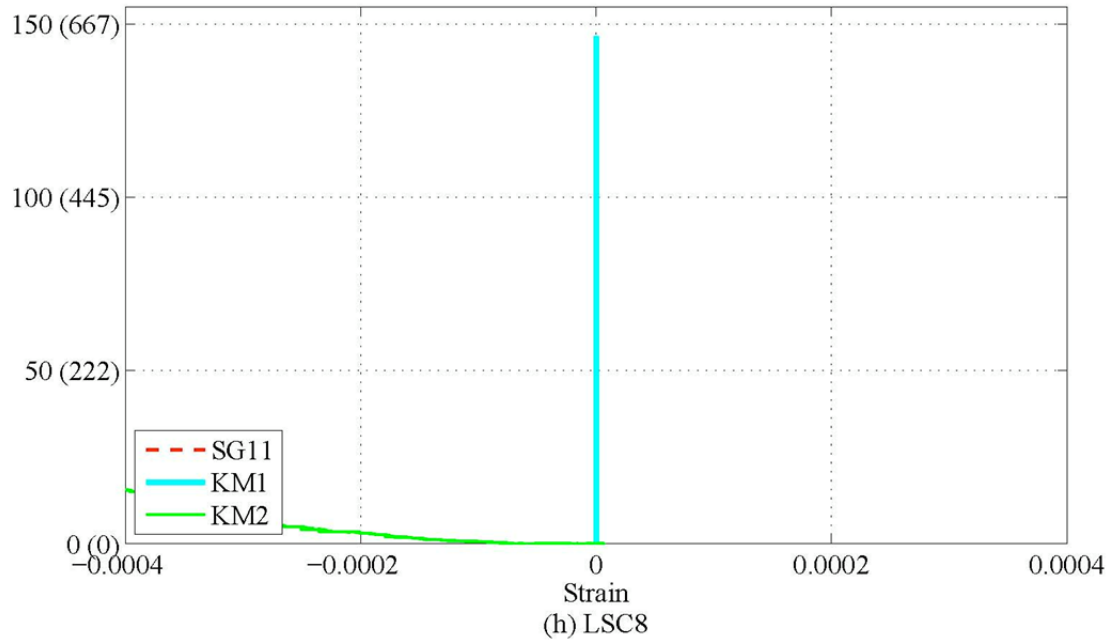

(h) LSC8

Figure 5-34. (Continued)

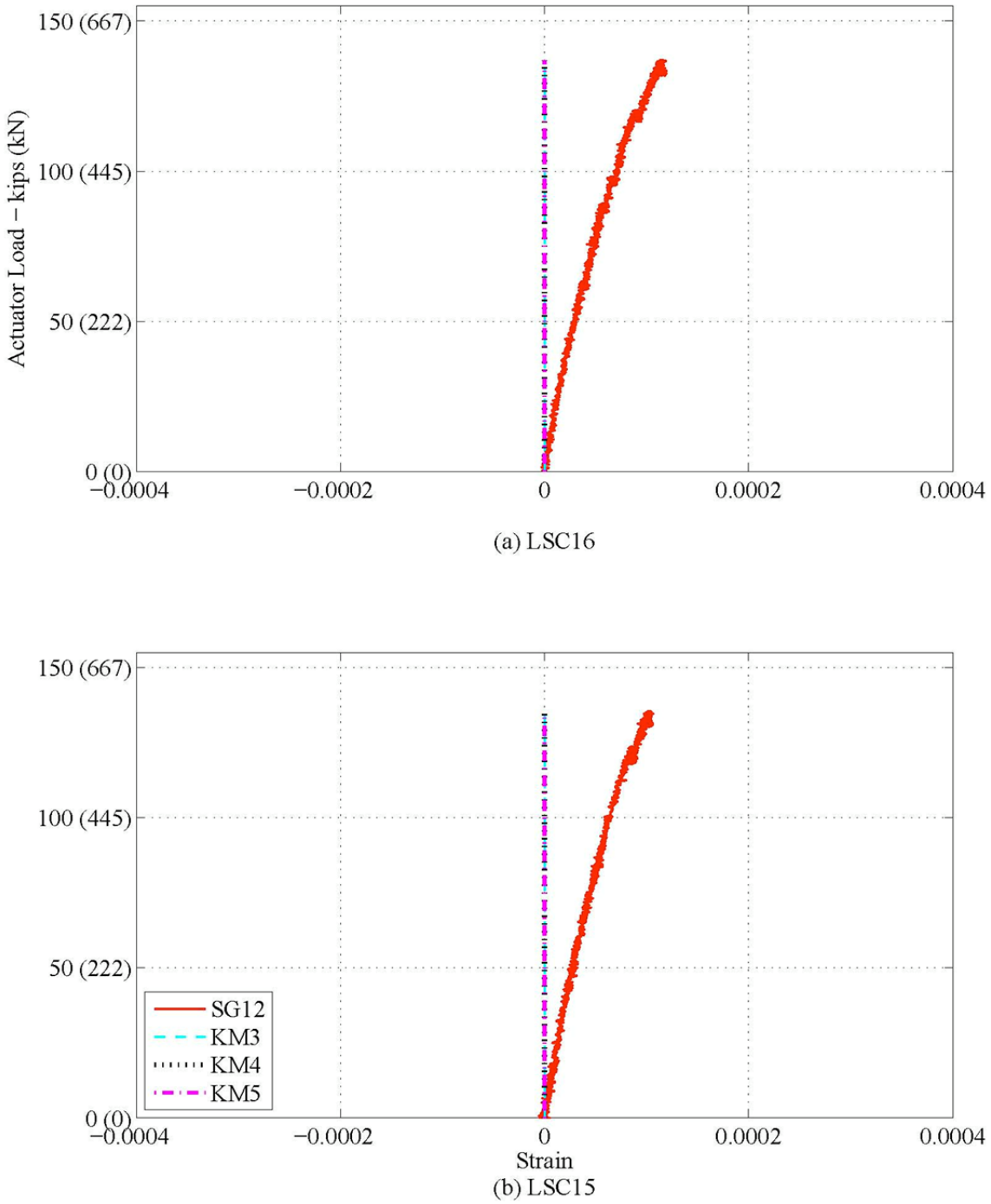

Figure 5-35. Experimental Load vs. Strain during Four-Point Test: Internal Gages: SG12, KM3 – KM5 by Large Face 1.

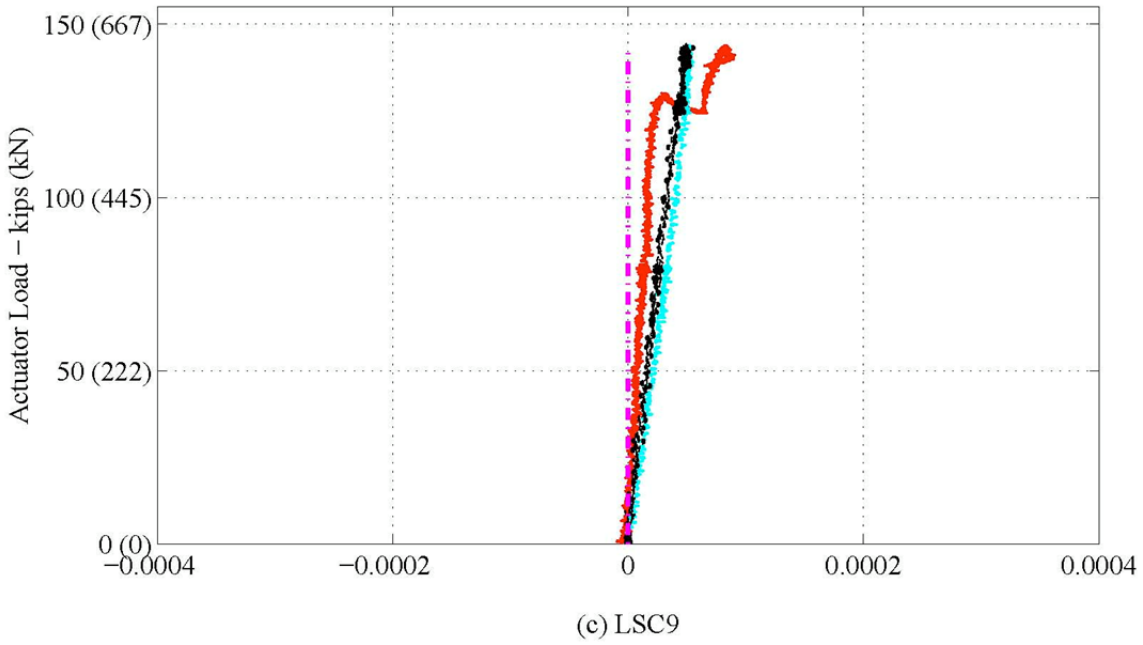

(c) LSC9

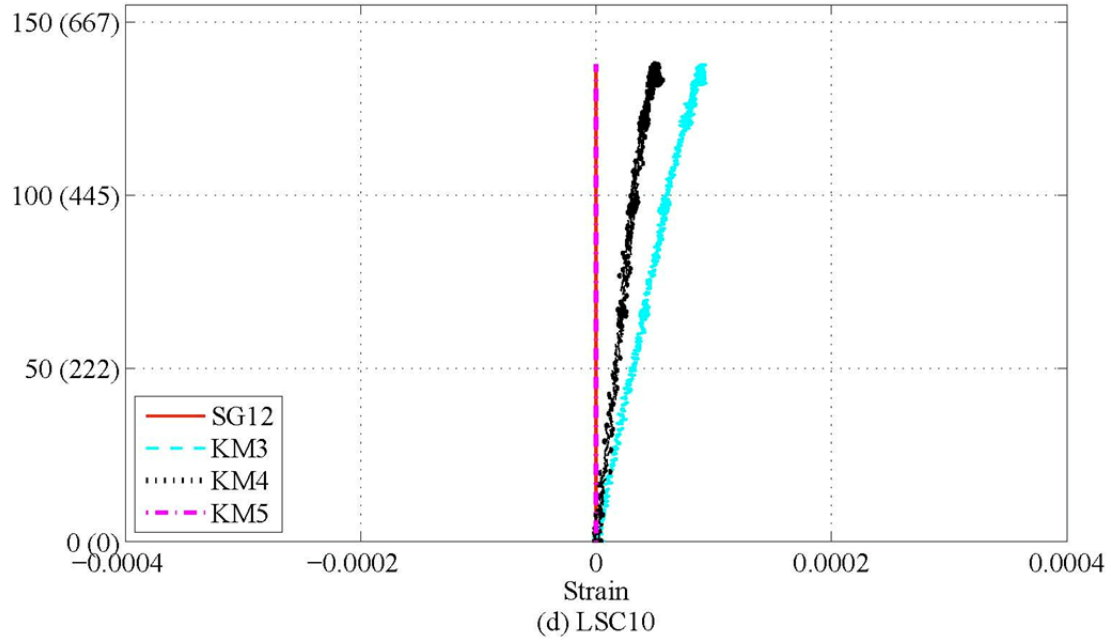

(d) LSC10

Figure 5-35. (Continued)

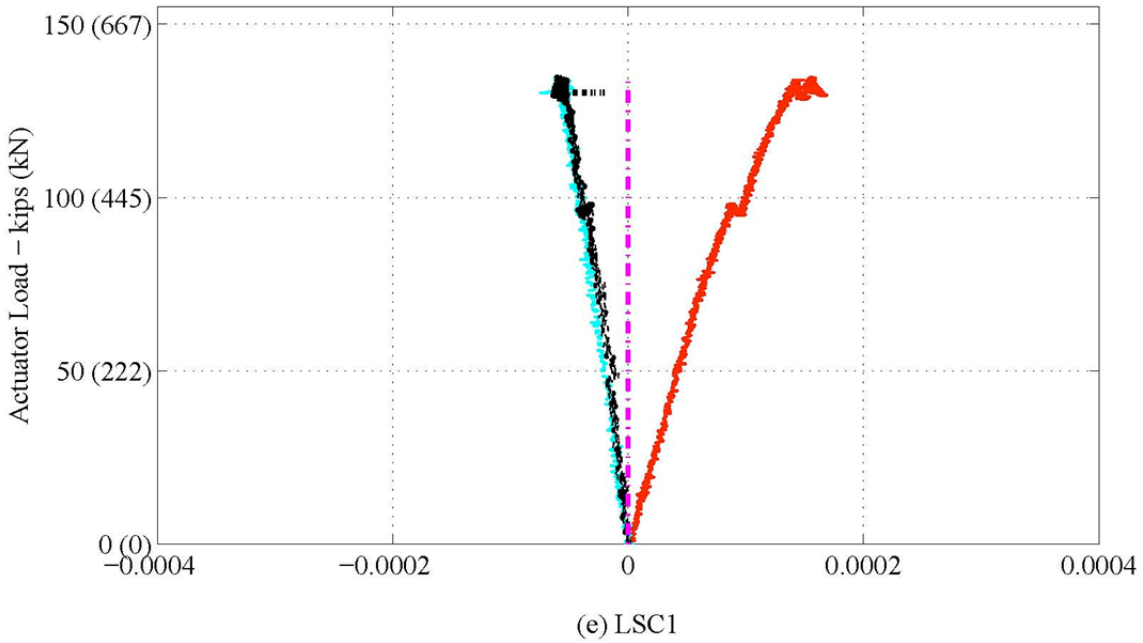

(e) LSC1

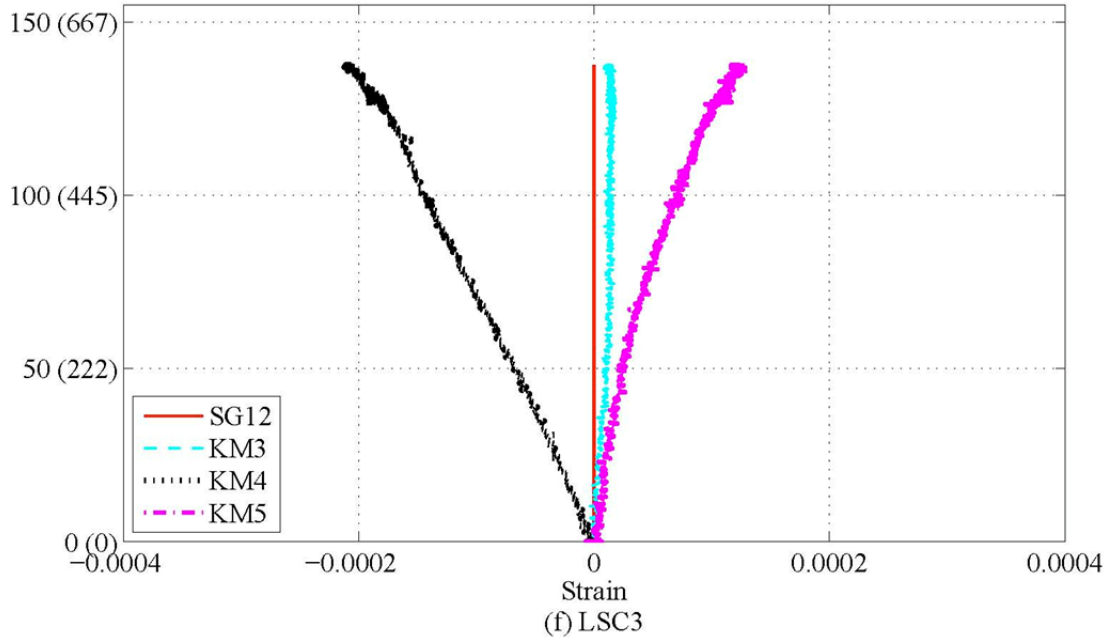

(f) LSC3

Figure 5-35. (Continued)

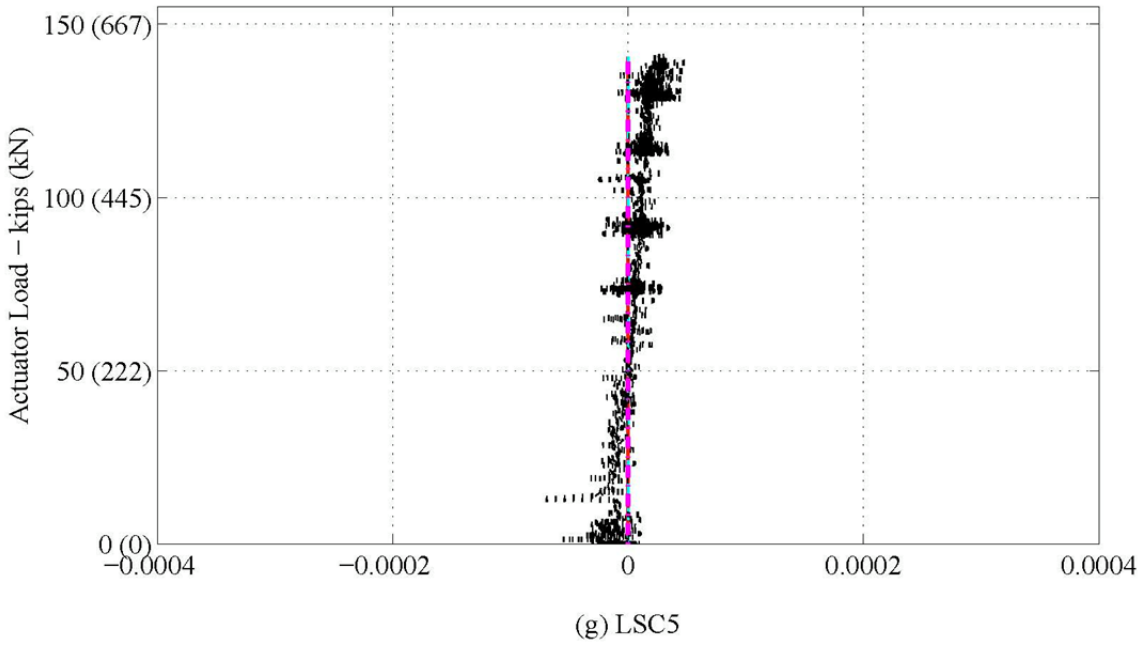

(g) LSC5

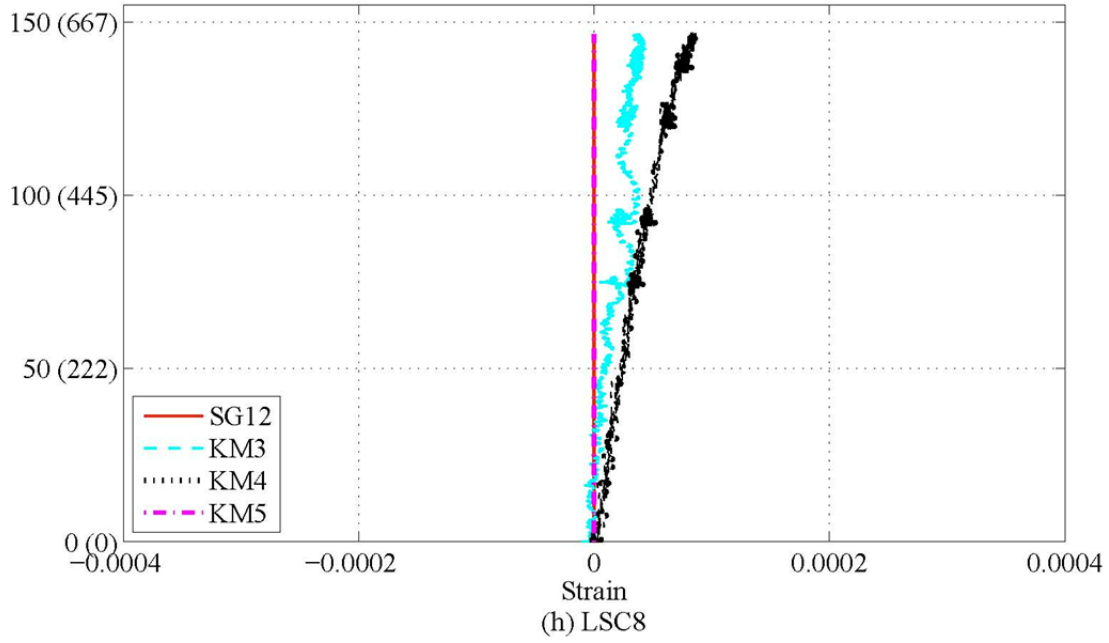

(h) LSC8

Figure 5-35. (Continued)

5.4.3 Three-Point Flexural/Shear Test Results

The specimen behavior from the three-point tests is presented below. As explained previously, the specimen was rotated such that the tension side on the four-point test was also the tension side on the three-point test. Figure 5-12 illustrates the three-point setup as well as the shear and moment diagrams for this test. The resulting damage from the four-point test that primarily developed at the splice ends had minimal impact on the performance of the specimen in the three point setup since the critical section for flexure is now at the center of the splice length region at the support reaction. The same internal gages as the four-point test were monitored during the test, however some of these gages proved to be unreliable from the previous deterioration program and four-point load testing. The internal gages were set to zero prior to the three-point test. External instruments, LVDTs, KM, and STR were reinstalled to measure the strains and deflections during the three point test as illustrated in Figure 5-13.

Figure 5-36 compares the actuator load vs. deflection response at the loading point from all tested specimens during the three-point test. Higher actuator loads were achieved during this test as compared to the previous four-point load test due to the different demand from the test setups and because these specimens were loaded to near failure since no further testing was planned. Note that LSC8 had the smallest measured load during the three-point test since severe cracking resulted and the test was terminated due to safety concerns. Similar to the four-point test, there are a few strain values that show a drop in load due to the halt in the loading to view cracks during the tests. Figure 5-36 shows that during the three-point test, the non-control specimens had about 5-15% higher yield strengths and were about 25-35% stiffer (similar to the four-point test) from post-cracking until yield than the control specimens (LSC15 and LSC16) for the same reasons as explained for the four-point test.

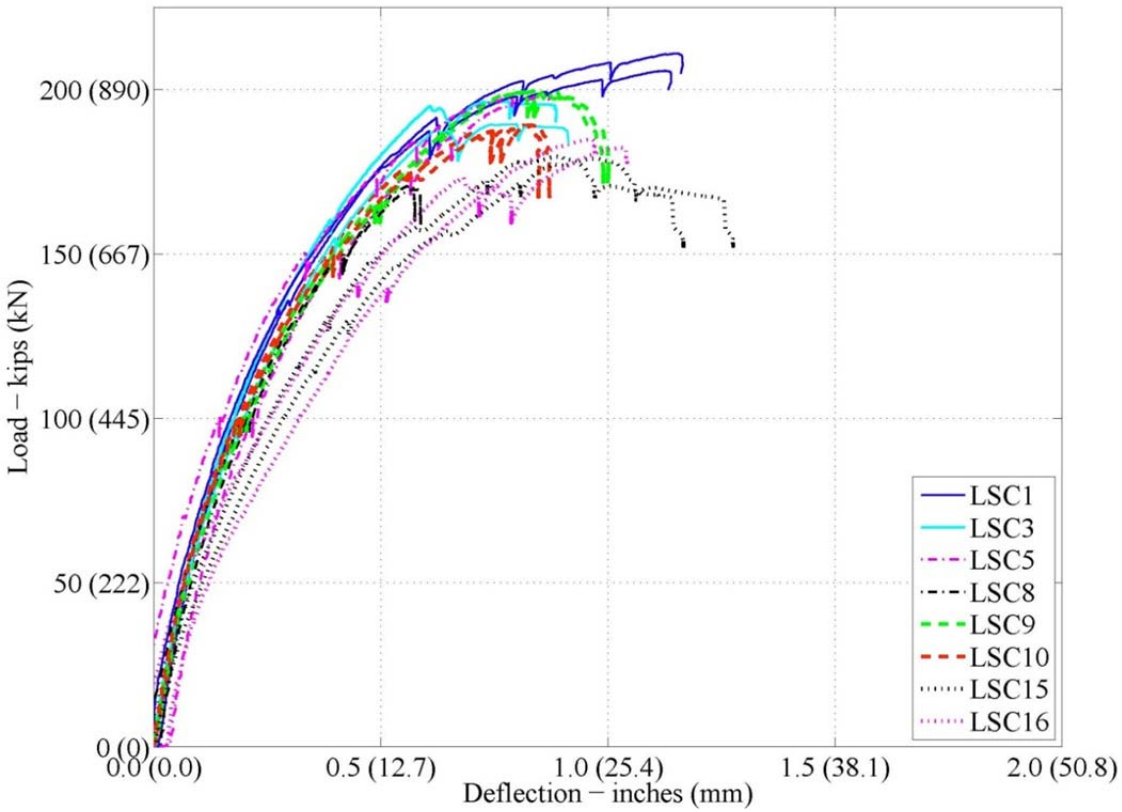

Figure 5-36. Experimental Load vs. Deflection during Three-Point Test: All Tested Specimens at the Actuator Load Point

Figure 5-37 shows the experimental and analytical load vs. deflection response for each specimen separately during the three point test. The analytical model also shows higher actuator loads during the three-point test than in the four-point test. The figure shows that the analytical model for the three-point test is fairly representative of the experimental data; however the analytical results are about 15% stiffer. This deviation can be explained because the analytical model did not account for the previous cracking and resulting in the specimen from the four-point load test, the modeling assumption that all plasticity occurred in the section at the support, and also because shear deformations were not accounted for in the analytical model and may be more prevalent in the three-point test setup since there are shear demands between the actuators in the three-point test setup.

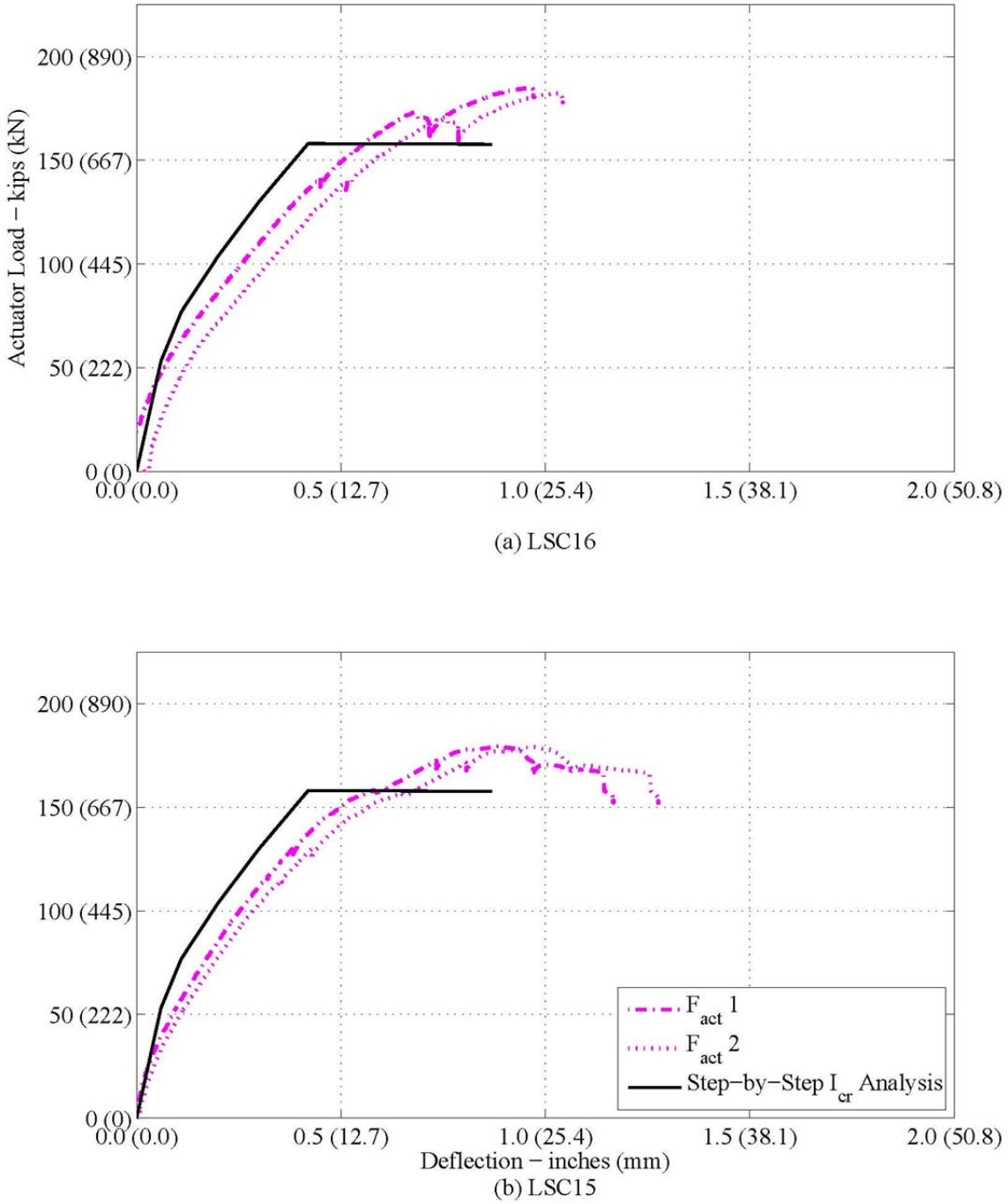

Figure 5-37. Experimental and Analytical Load vs. Deflection during Three-Point Test: At the Actuator Load Point.

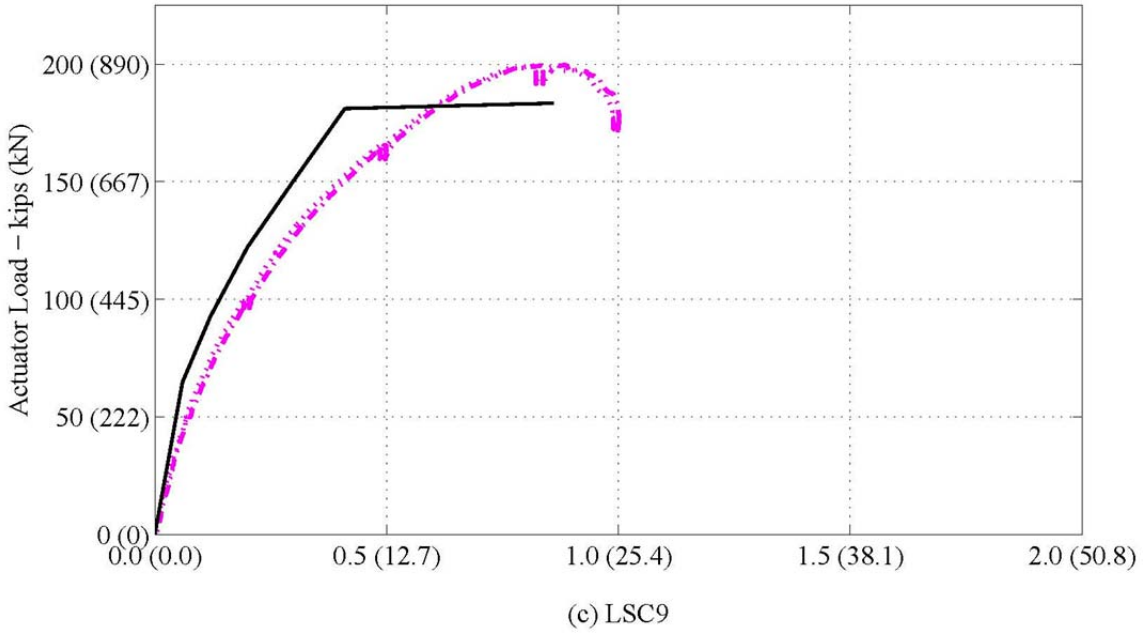

(c) LSC9

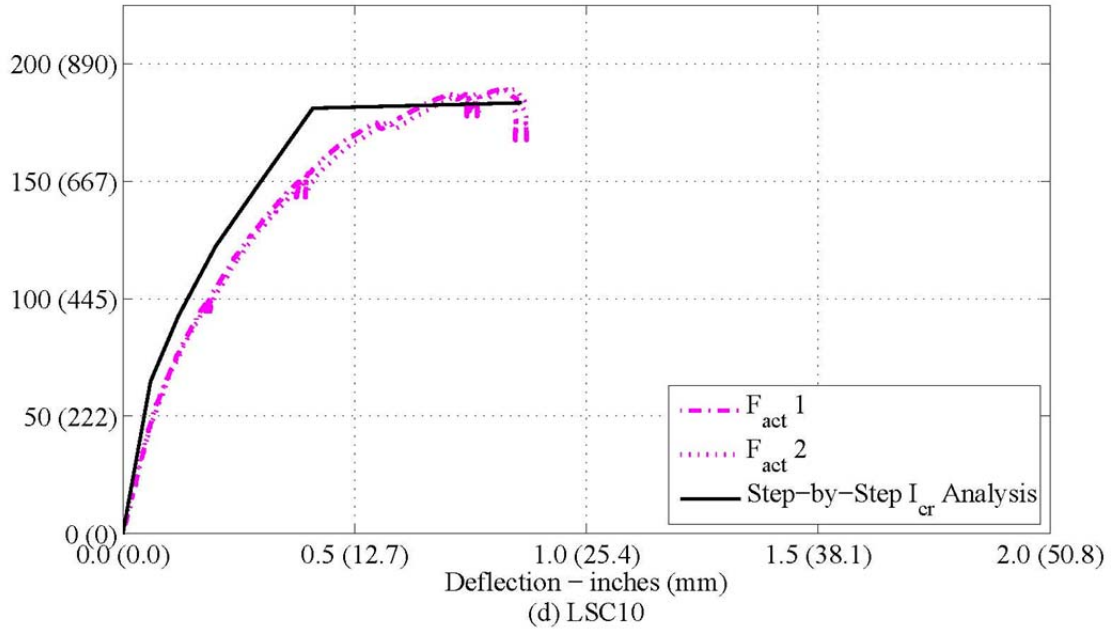

(d) LSC10

Figure 5-37. (Continued)

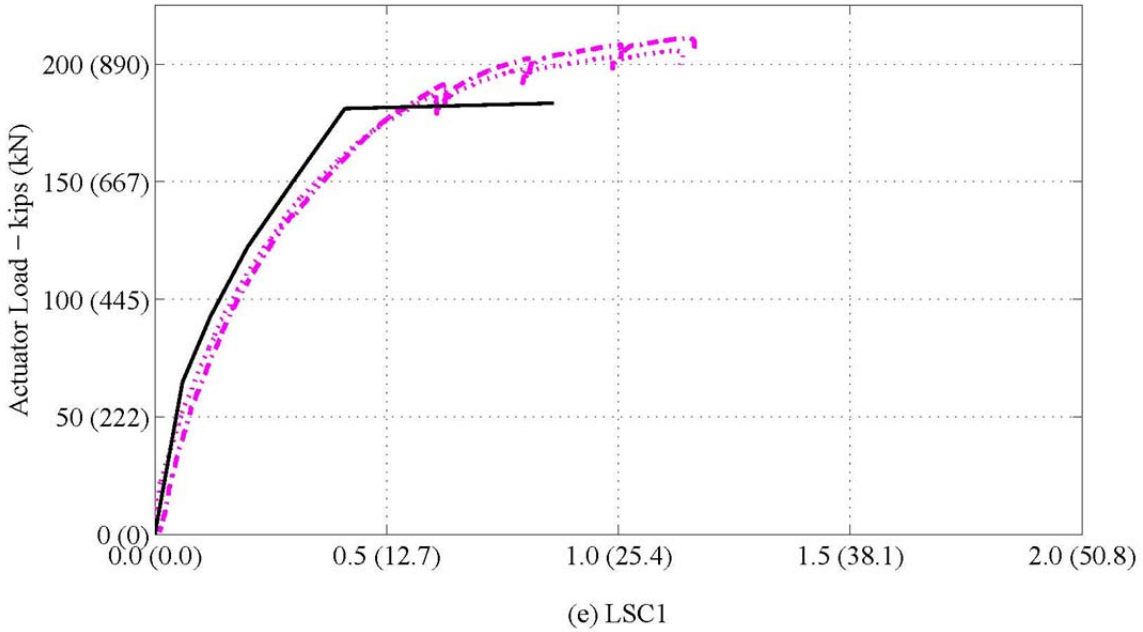

(e) LSC1

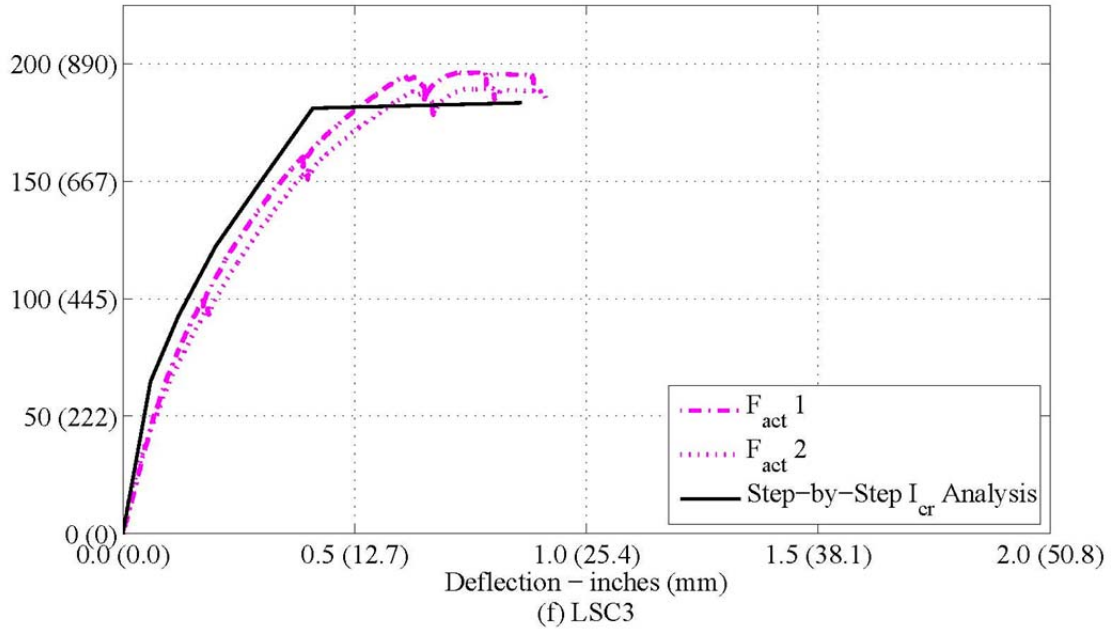

(f) LSC3

Figure 5-37. (Continued)

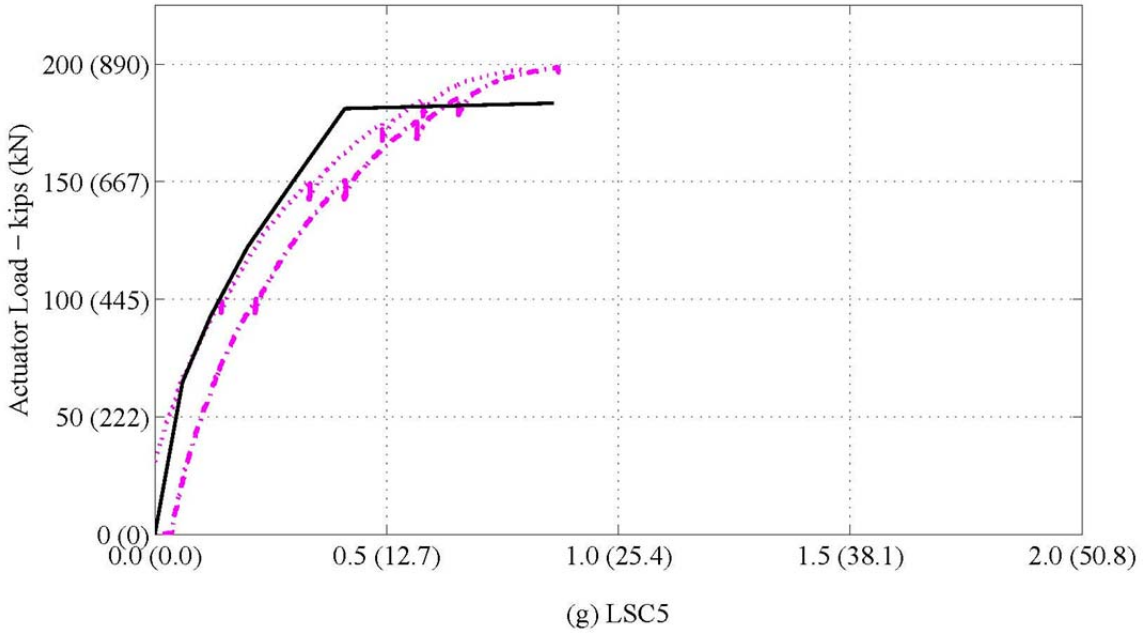

(g) LSC5

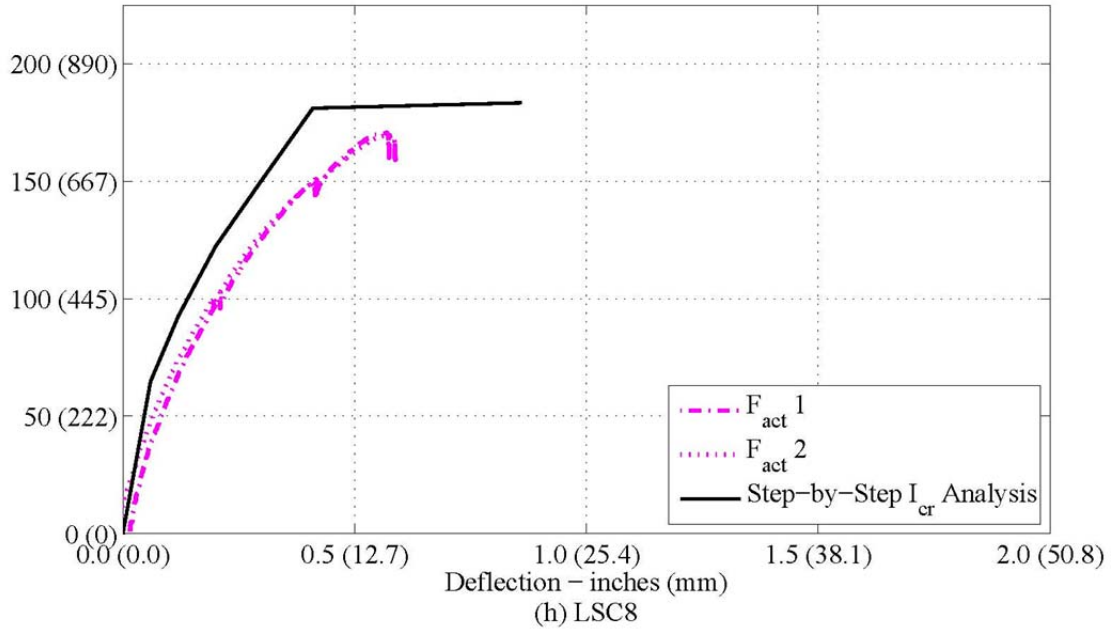

(h) LSC8

Figure 5-37. (Continued)

Figure 5-38 and Figure 5-39 show the total actuator load (sum of the two actuators) versus the internal strains in the reinforcing steel along the tension bars in the splice region. The total actuator load was used since this test is an inverted simply supported beam with one center point load. The strains on the splice bars reach yielding (0.002) about ¾ of the time and are close when yielding is not reached. However, SG4 and SG8 which are located at the end of the splice bars (little anchorage) only reached yielding on two specimens.

Figure 5-40 shows the same force versus the internal strains in the compression reinforcing steel. Internal compression gages on LSC16, LSC1, and LSC9 showed non-linear responses as early as first cracking in the concrete and proved to be unreliable in this test setup especially beyond the yield strains of steel of 0.002 inches/inches (mm/mm). LSC3, LSC5, LSC8, and LSC10 had SGs not functioning properly and recorded no strain during the three-point test.

Figure 5-41 and Figure 5-42 show the strain in the transverse reinforcing steel and surrounding cover and core concrete on Small Face 1 and Large Face 1 above the center support. Small Face 1 is on the side of the specimen and Large Face 1 is on the bottom, in compression during the three-point test.

Overall, the figures show that the longitudinal tension reinforcement throughout the splice region has yielded and that the analytical model reasonably correlates with the experimental behavior. However several internal gages showed non-linear responses as early as first cracking in the concrete and proved to be unreliable in this test setup especially beyond the yield strains of steel of 0.002. Also, several gages recorded no strain which shows these gages were not working properly. However they are shown here for completeness.

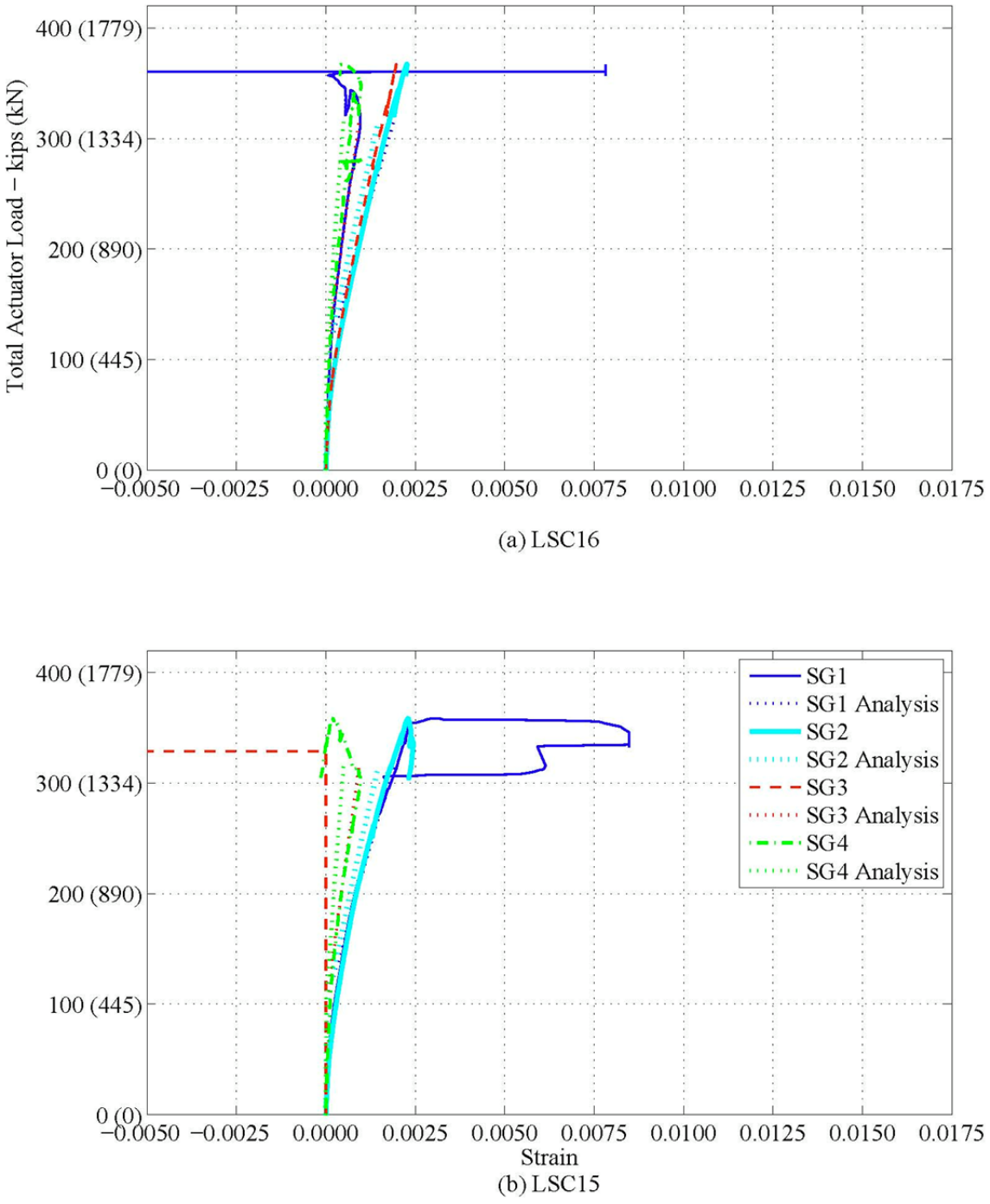

Figure 5-38. Experimental and Analytical Load vs. Strain during Three-Point Test: Internal Strain Gages (SG1–SG4) along the Tension Steel of the Splice Region.

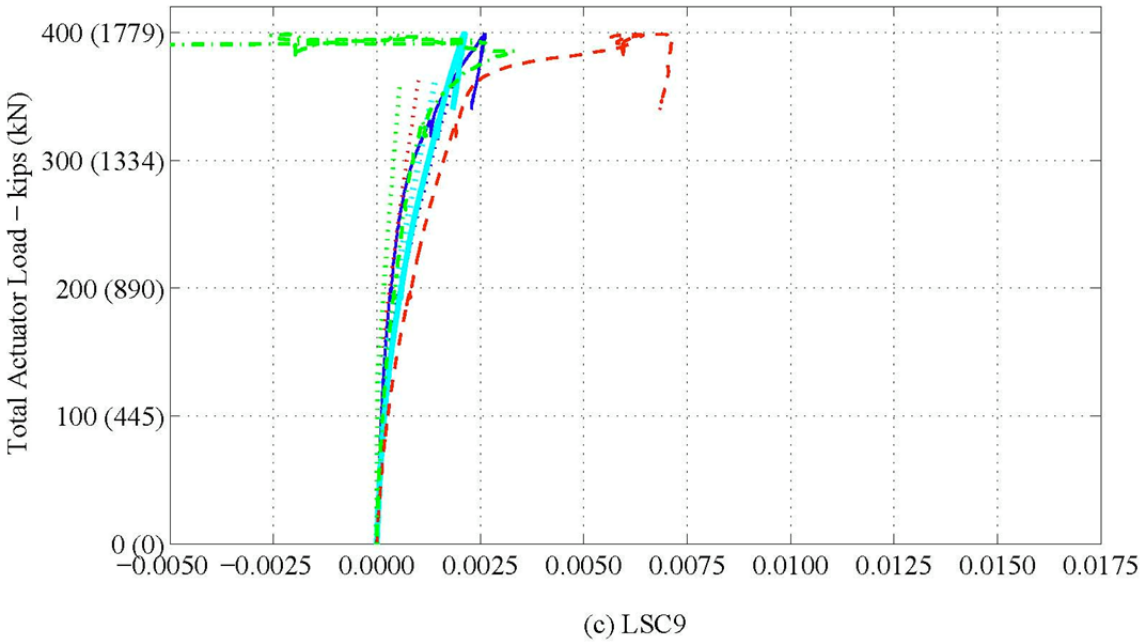

(c) LSC9

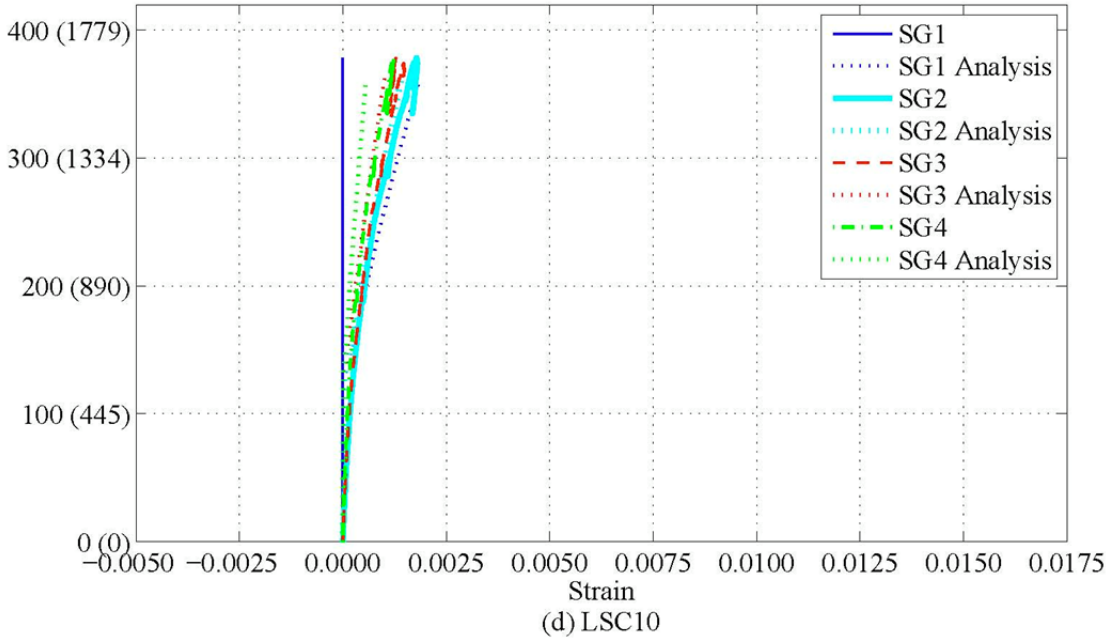

(d) LSC10

Figure 5-38. (Continued)

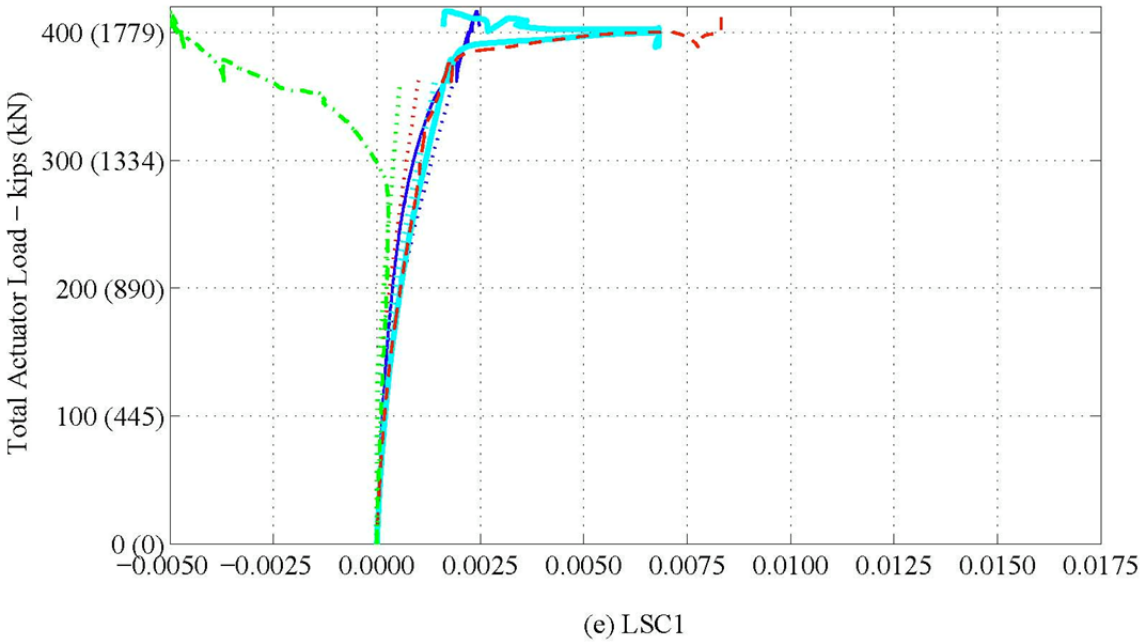

(e) LSC1

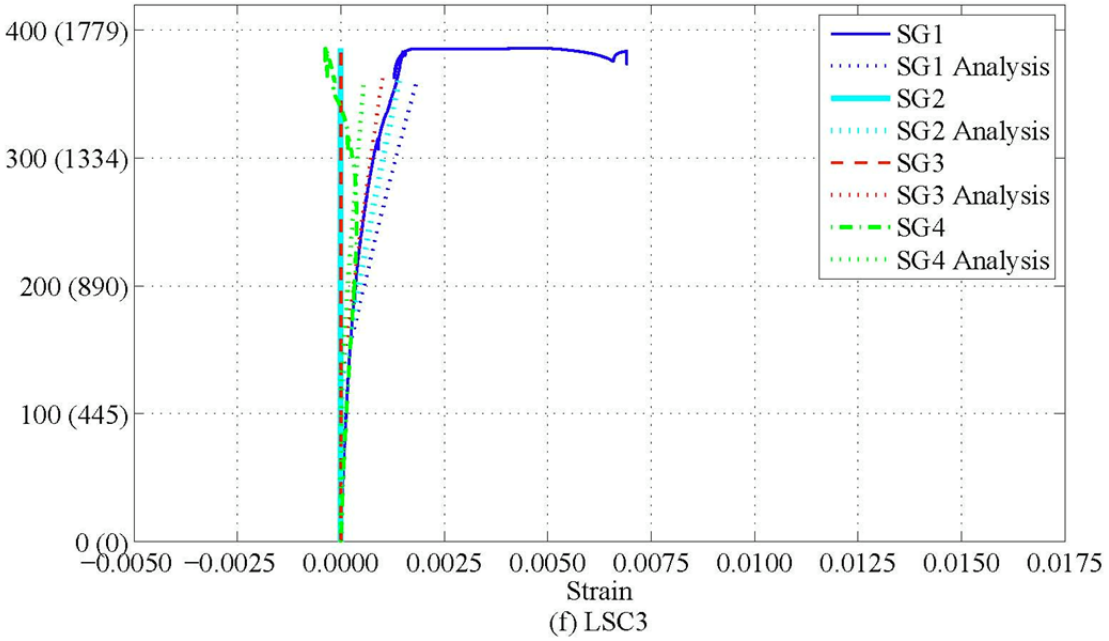

(f) LSC3

Figure 5-38. (Continued)

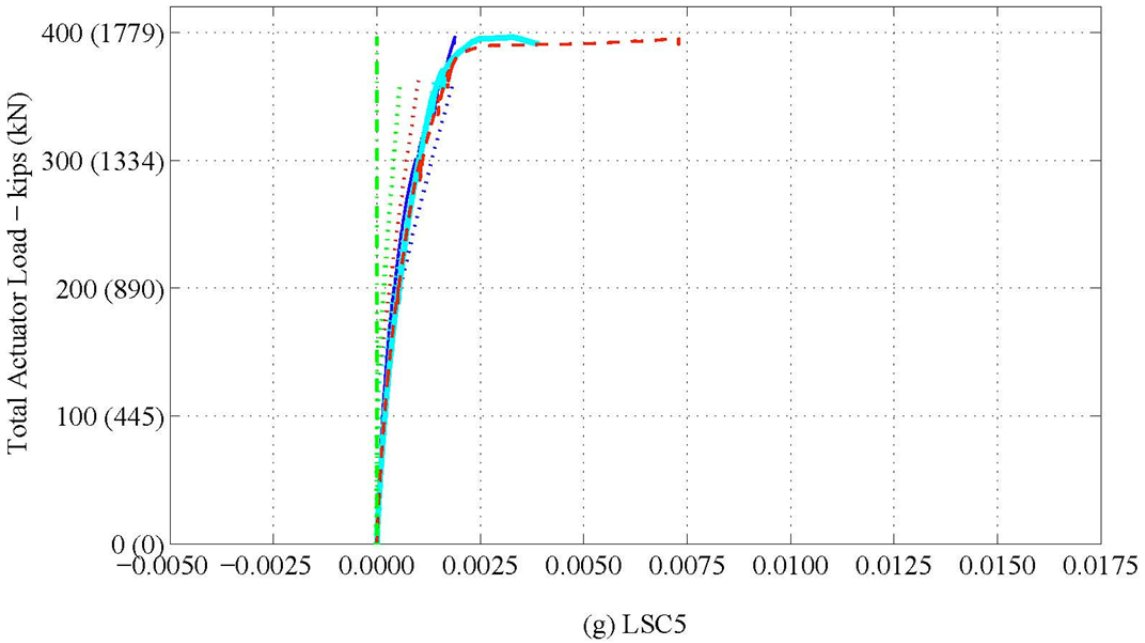

(g) LSC5

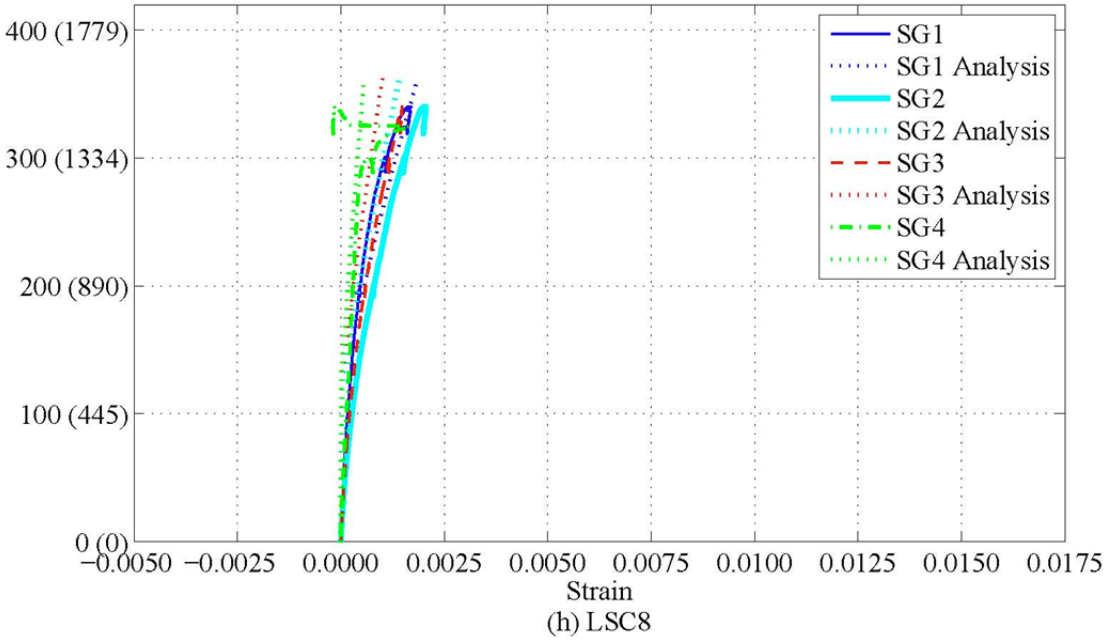

(h) LSC8

Figure 5-38. (Continued)

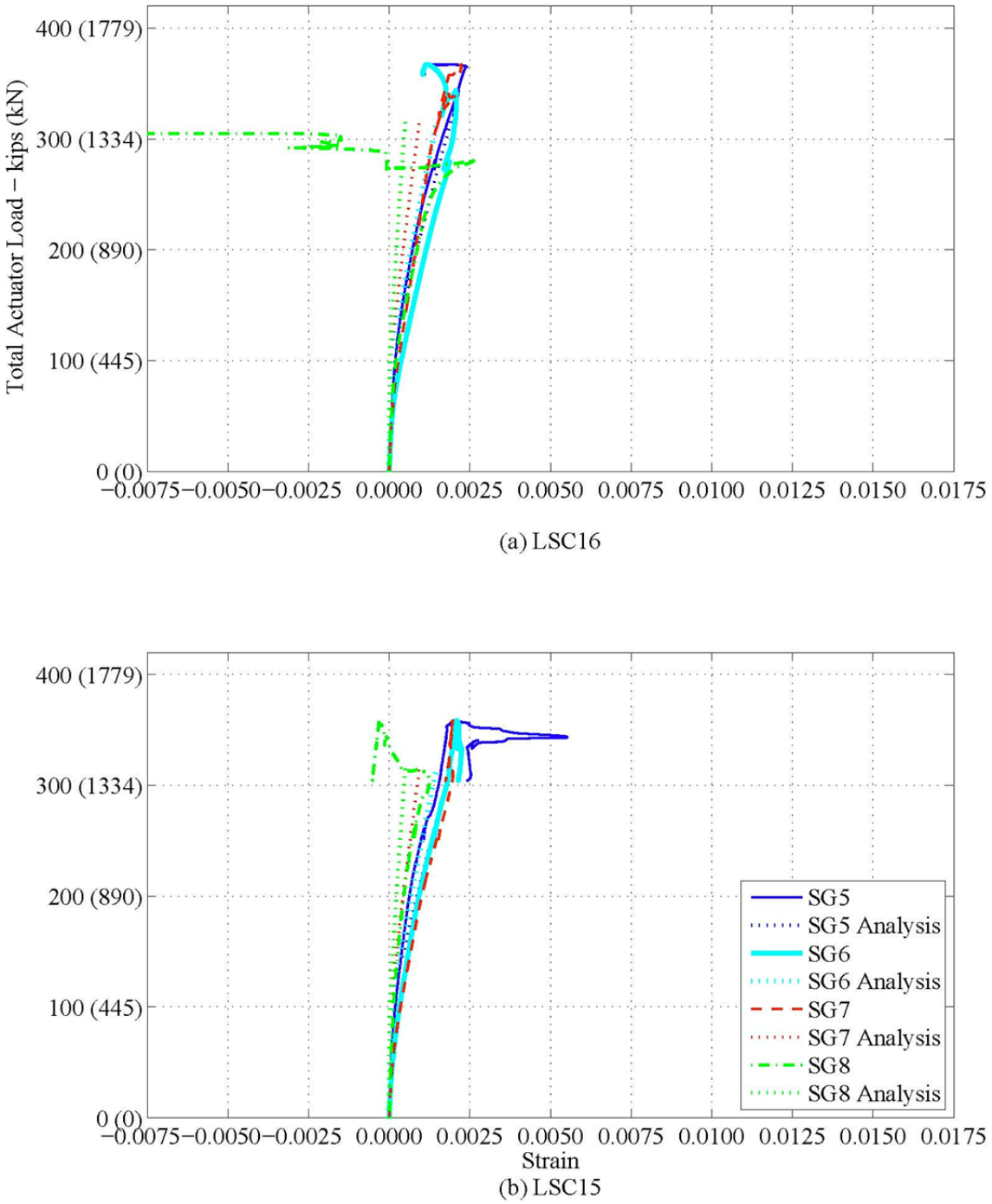

Figure 5-39. Experimental and Analytical Load vs. Strain during the Three-Point Test: Internal Strain Gages (SG5 – SG8) along the Tension Steel of the Splice Region.

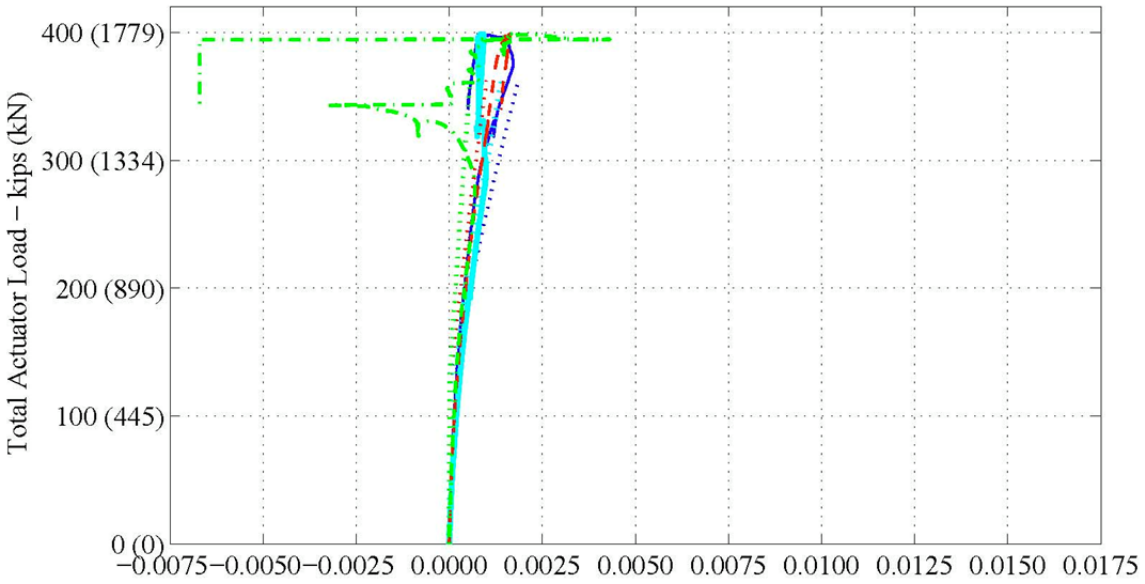

(c) LSC9

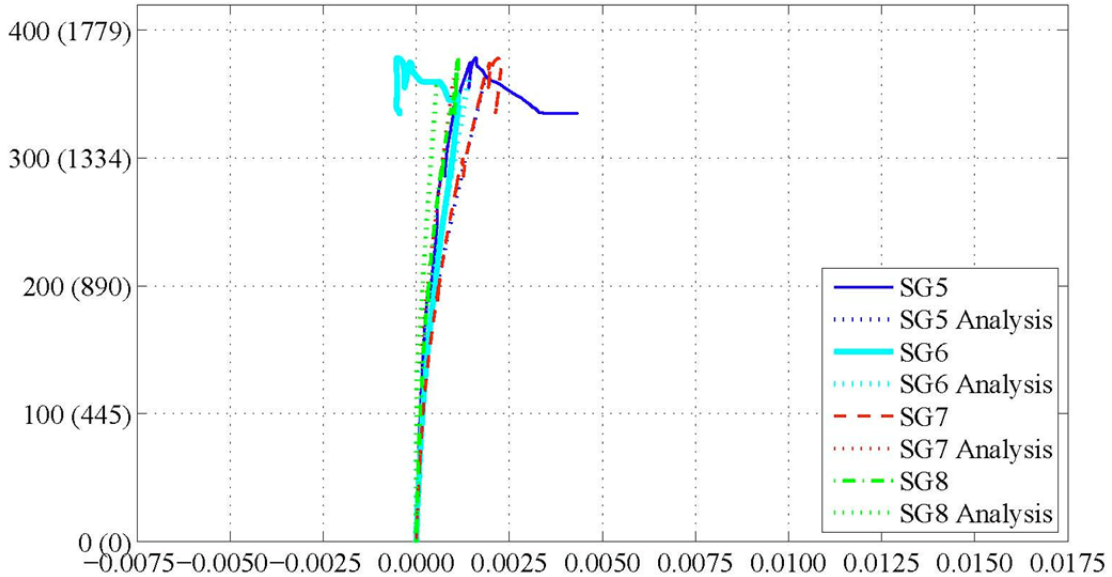

(d) LSC10

Figure 5-39. (Continued)

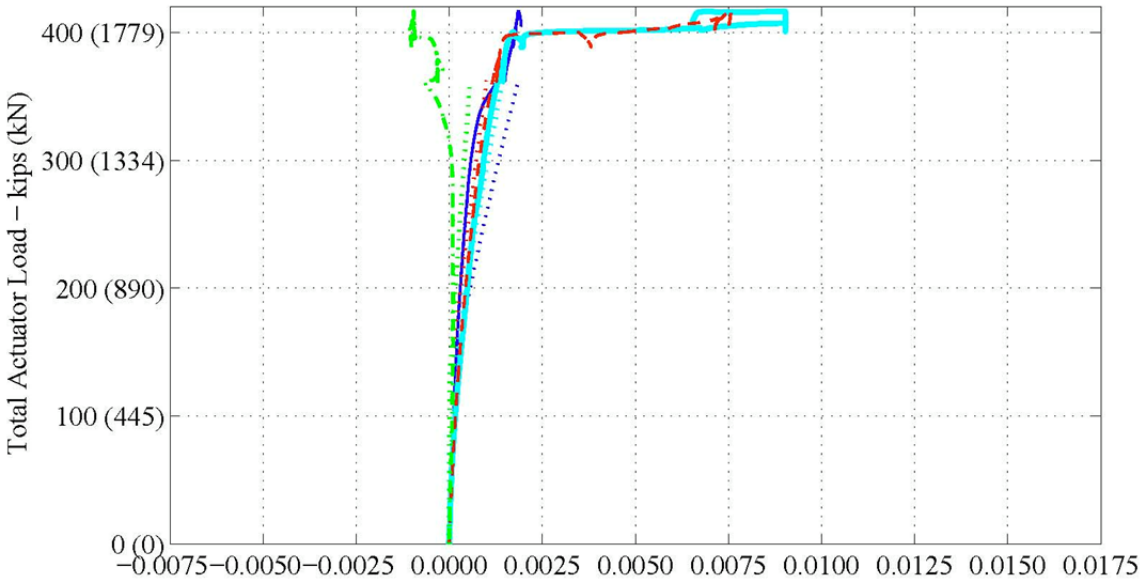

(e) LSC1

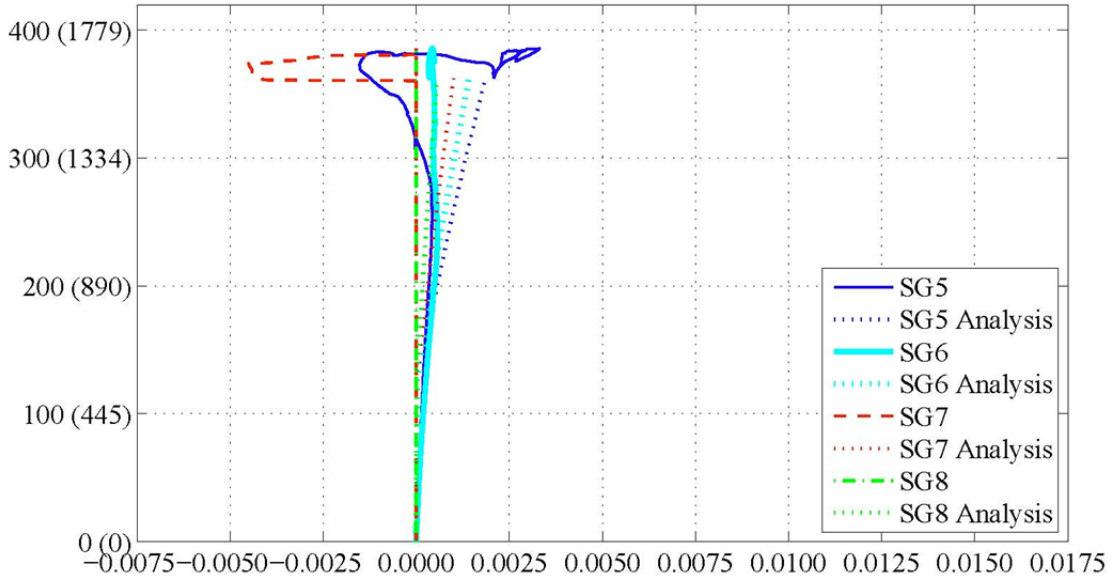

(f) LSC3

Figure 5-39. (Continued)

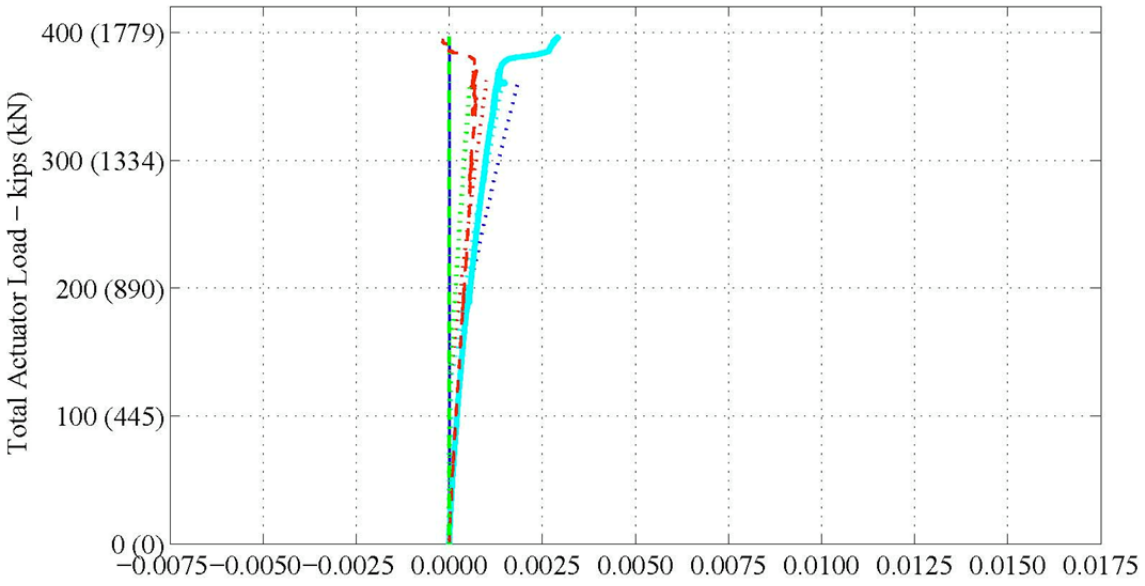

(g) LSC5

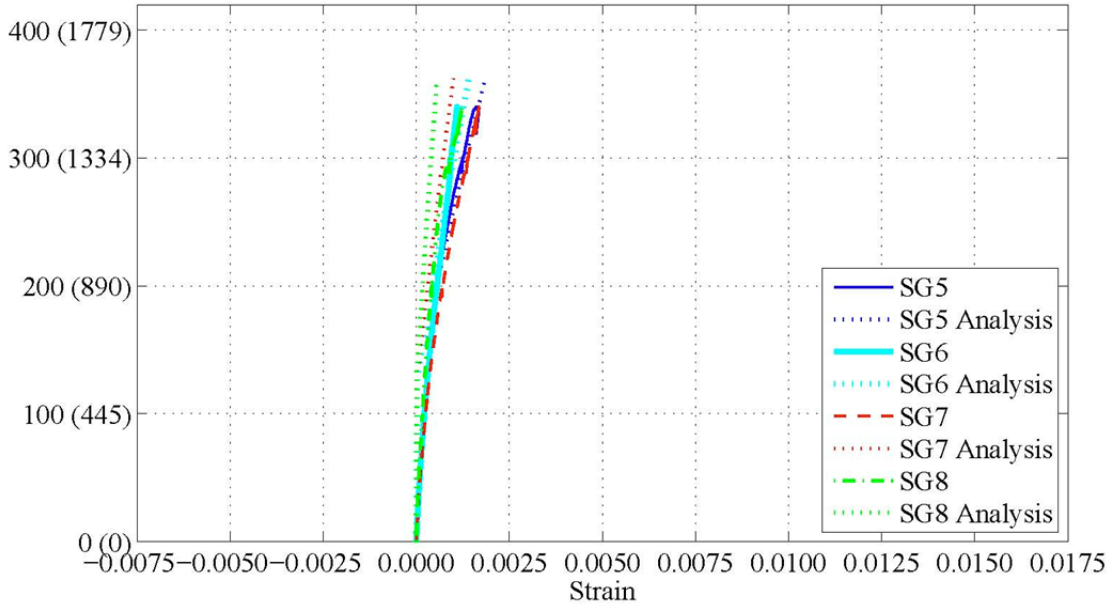

(h) LSC8

Figure 5-39. (Continued)

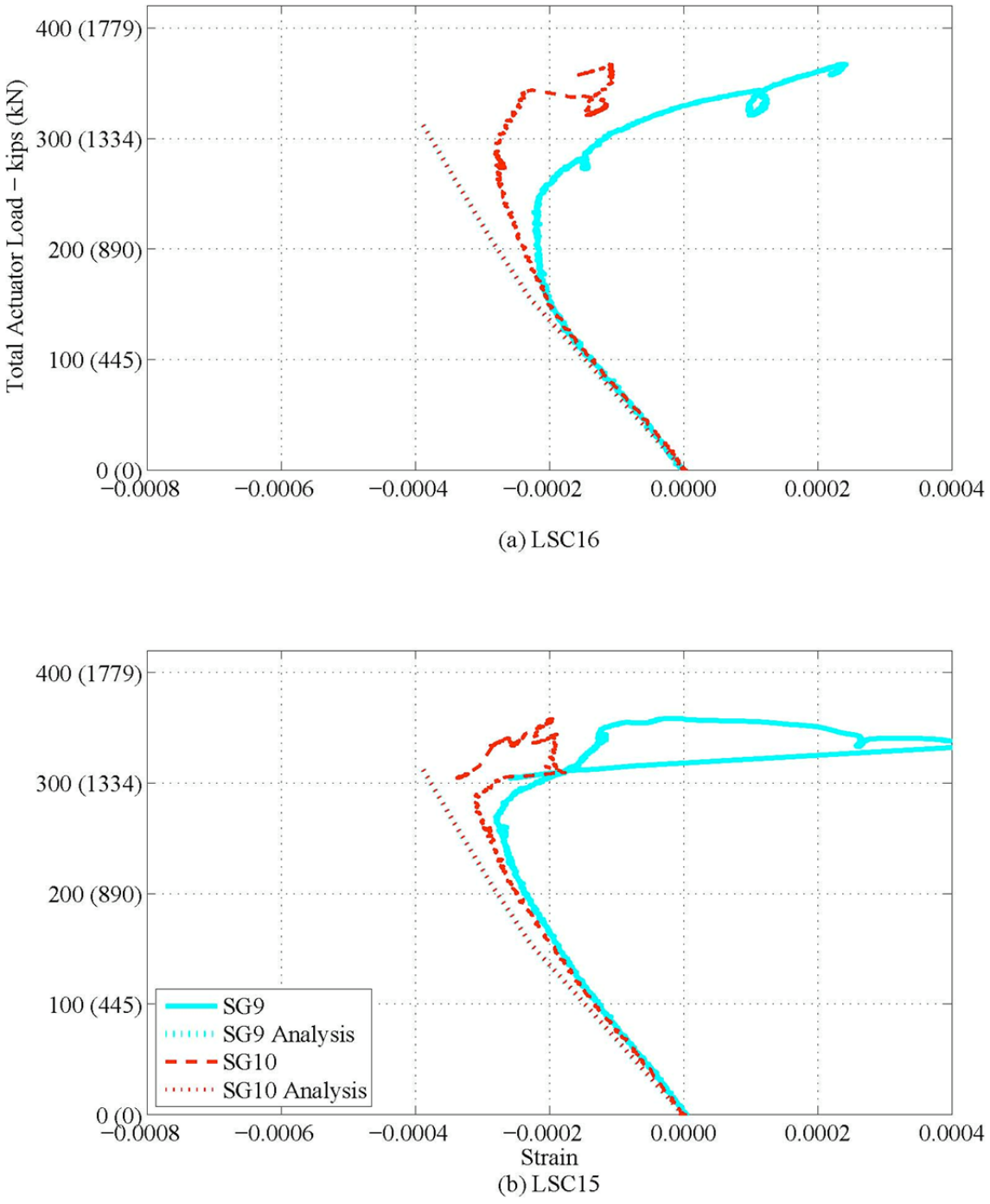

Figure 5-40. Experimental and Analytical Load. vs. Strain during the Three-Point Test: Internal Strain Gages (SG9 – SG10) along the Compression Steel of the Splice Region.

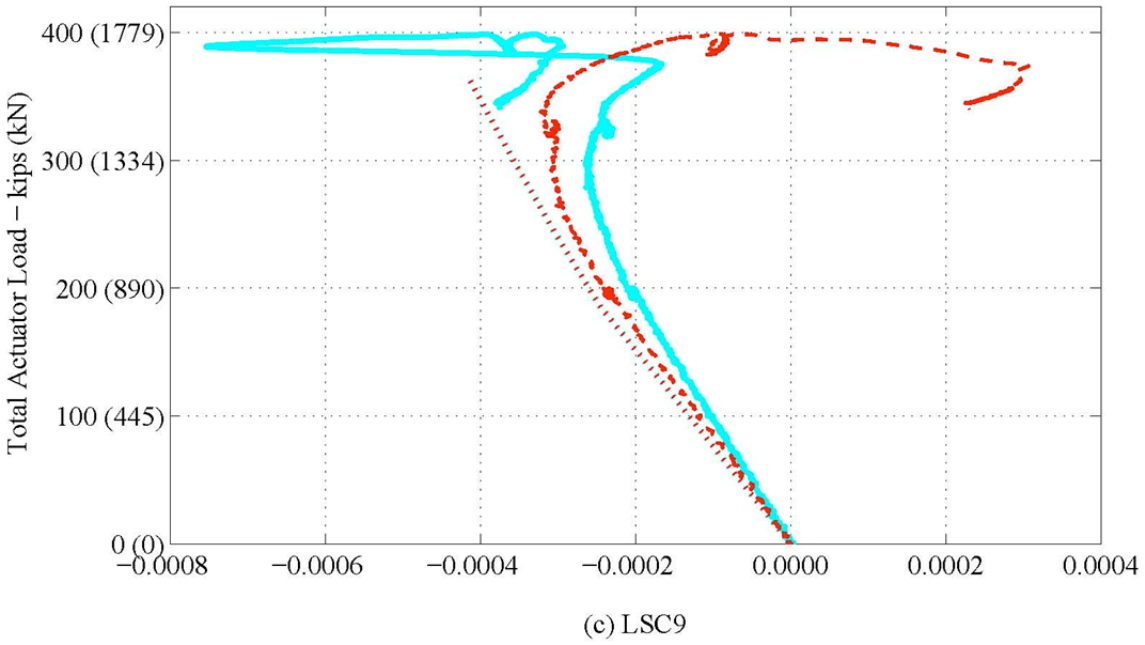

(c) LSC9

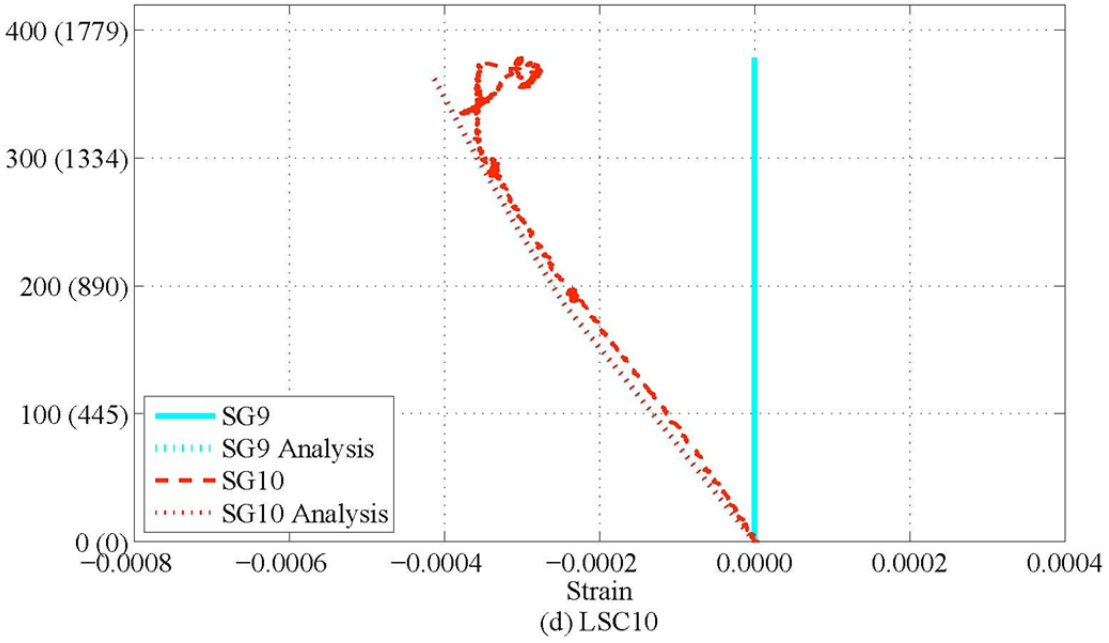

(d) LSC10

Figure 5-40. (Continued)

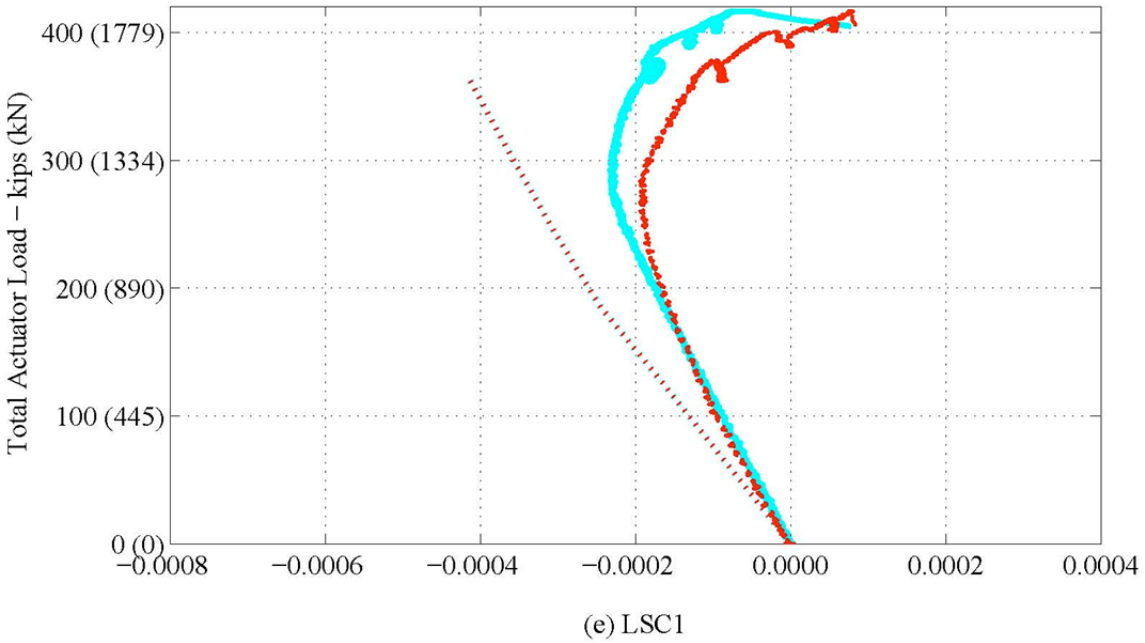

(e) LSC1

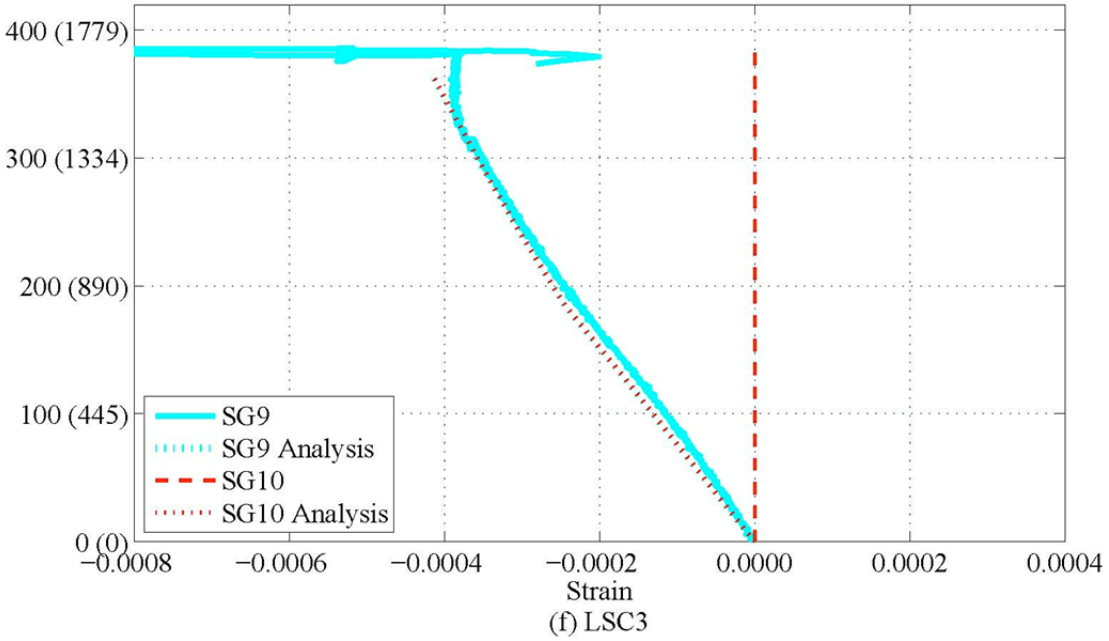

(f) LSC3

Figure 5-40. (Continued)

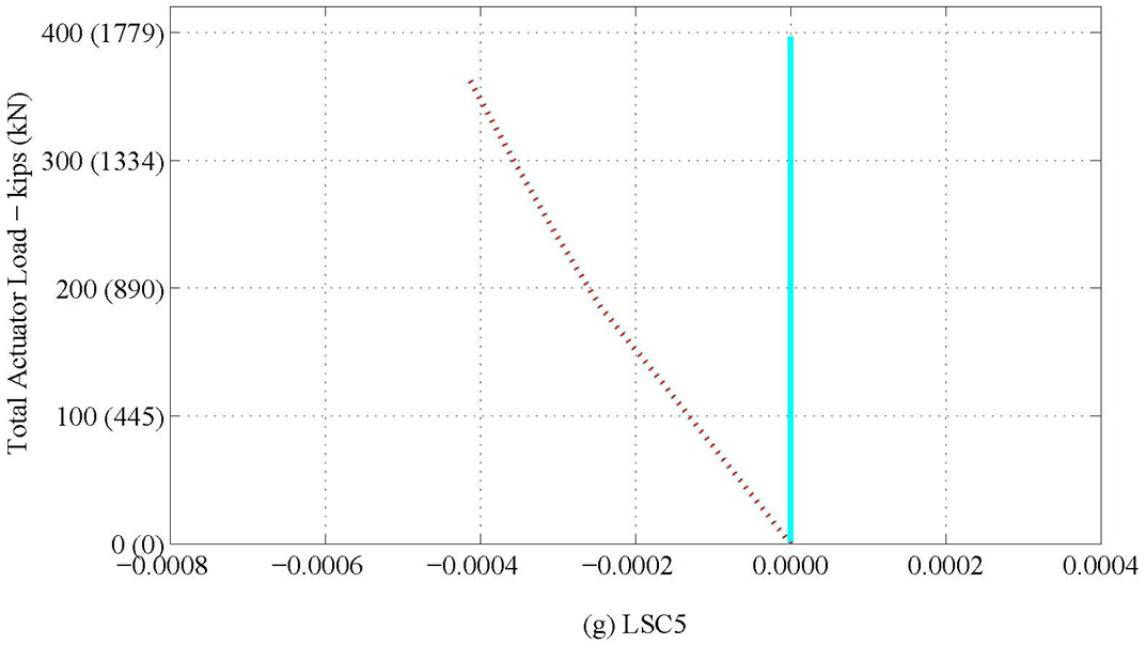

(g) LSC5

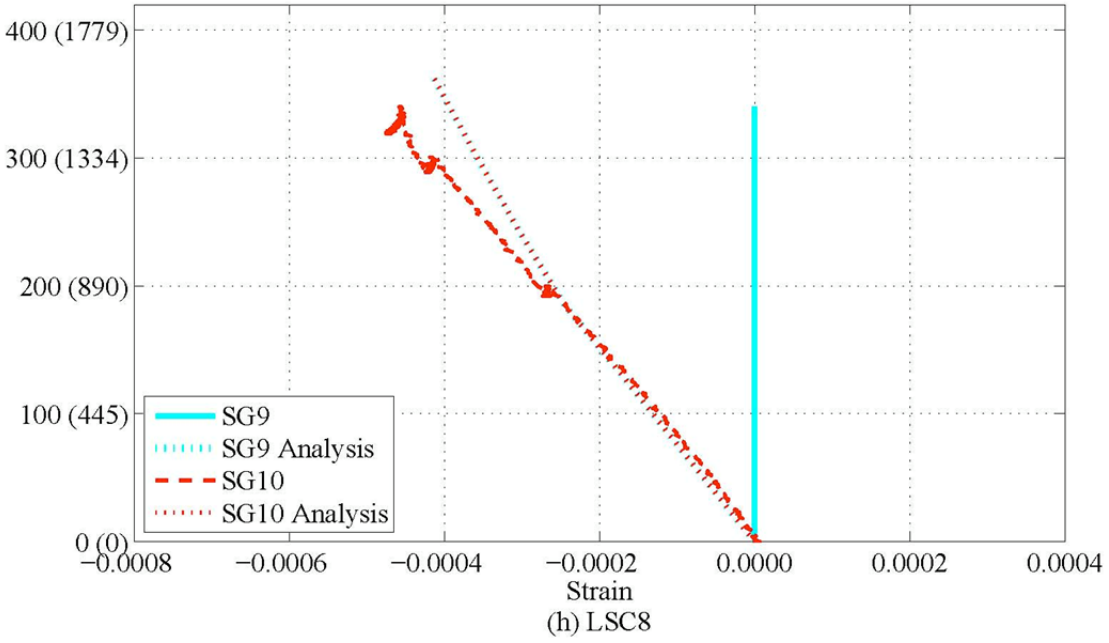

(h) LSC8

Figure 5-40. (Continued)

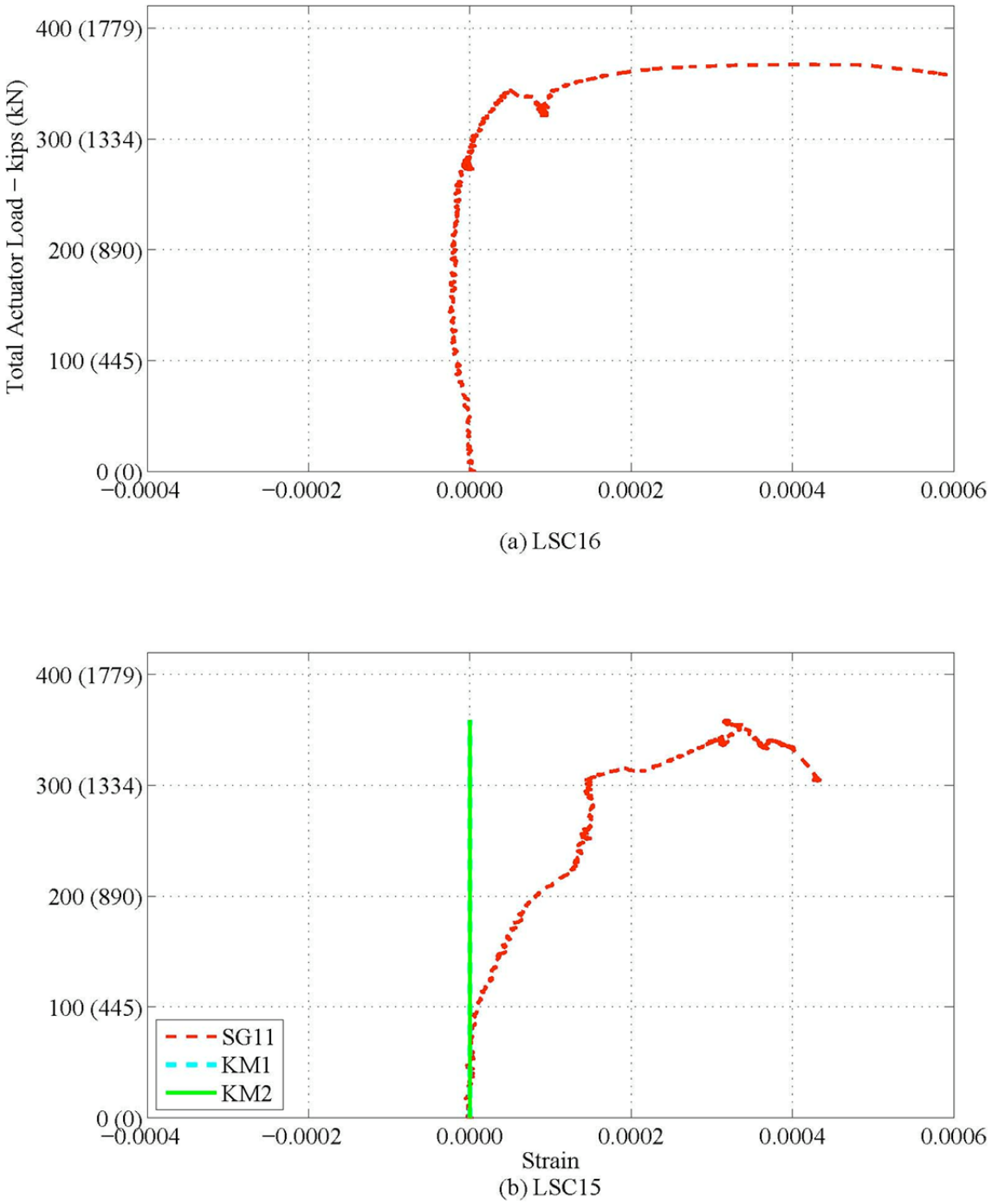

Figure 5-41. Experimental Load vs. Strain during the Three-Point Test: Internal Strain Gages (SG11, KM1 - KM2) on Small Face 1 above the Center Support.

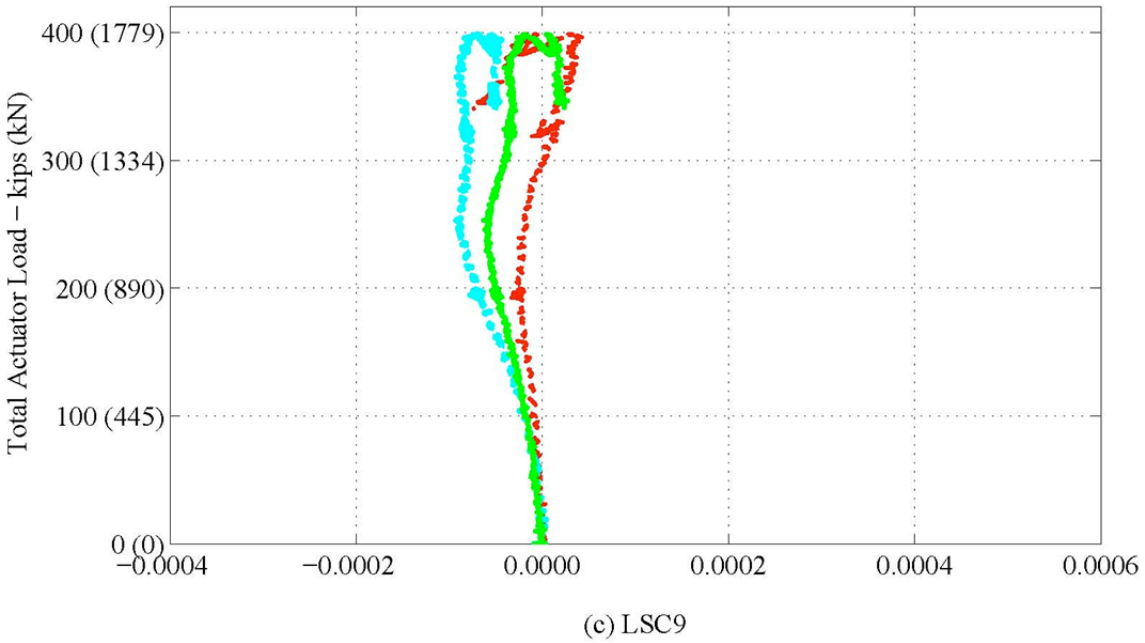

(c) LSC9

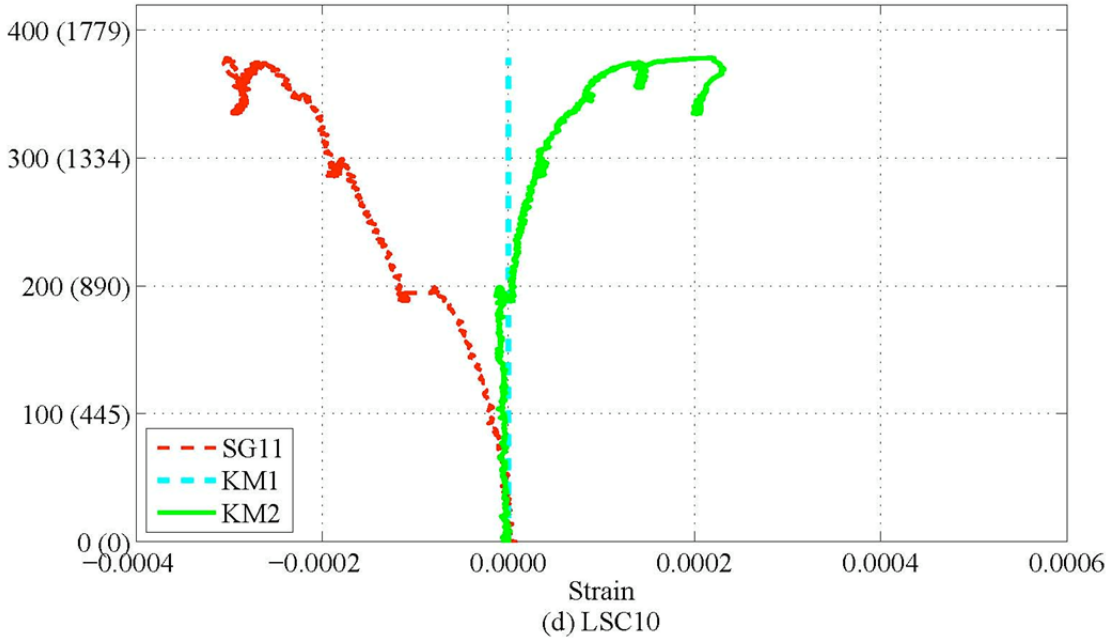

(d) LSC10

Figure 5-41. (Continued)

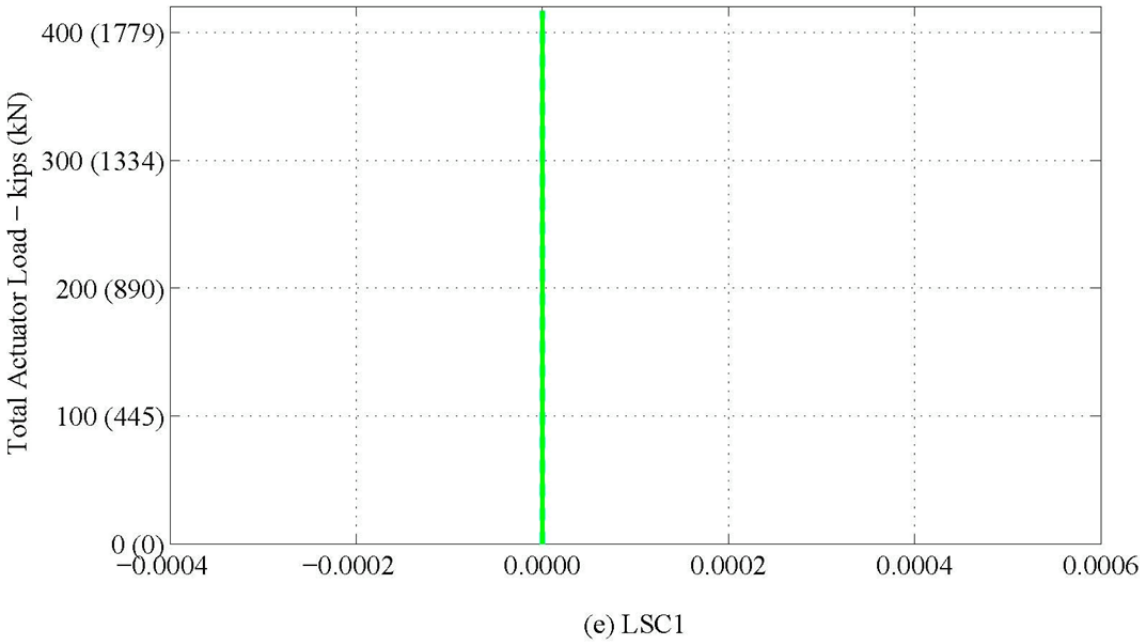

(e) LSC1

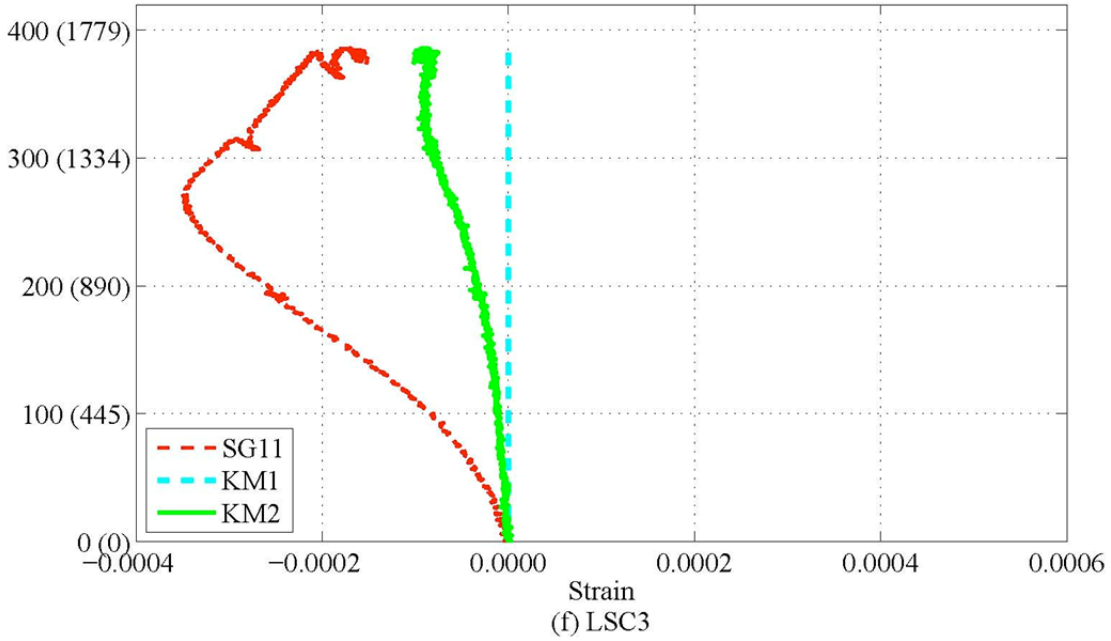

(f) LSC3

Figure 5-41. (Continued)

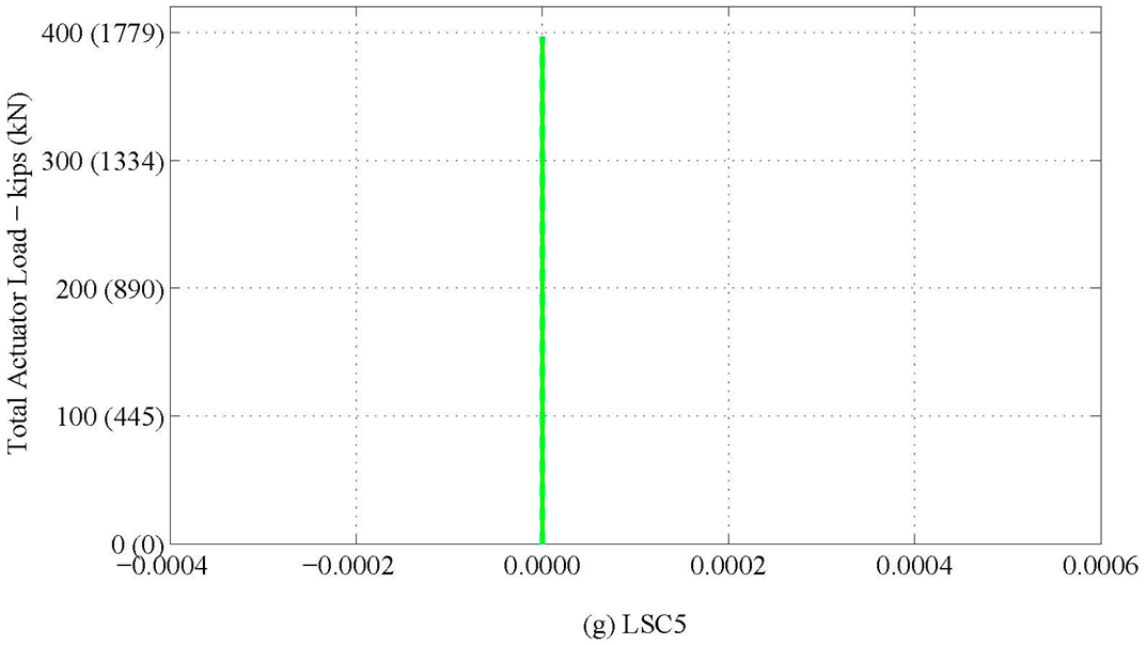

(g) LSC5

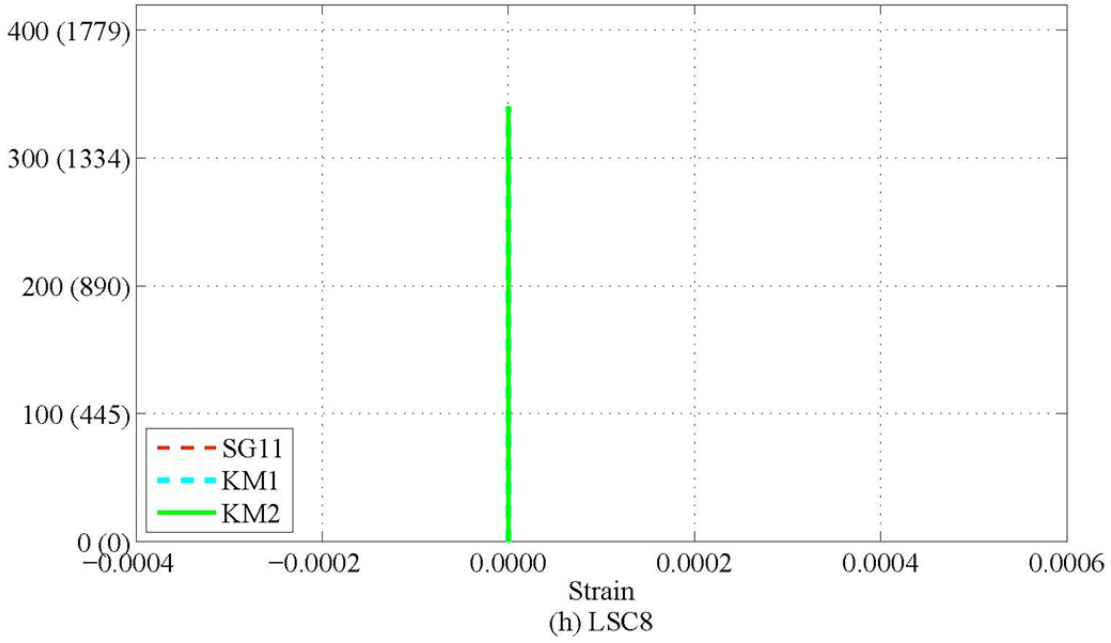

(h) LSC8

Figure 5-41. (Continued)

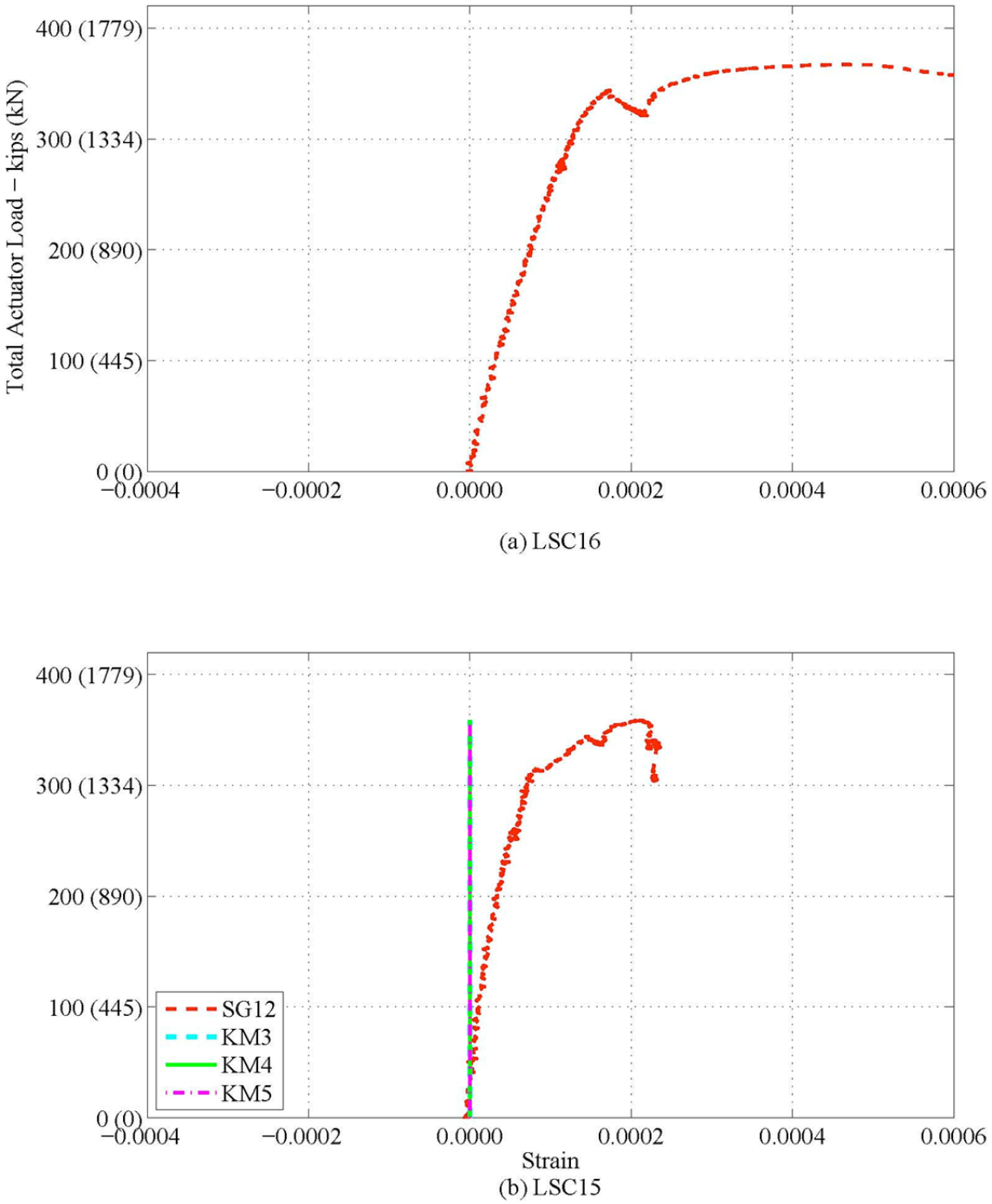

Figure 5-42. Experimental Load vs. Strain during the Three-Point Test: Internal Strain Gages (SG12, KM3 – KM5) on Large Face 1 above the Center Support.

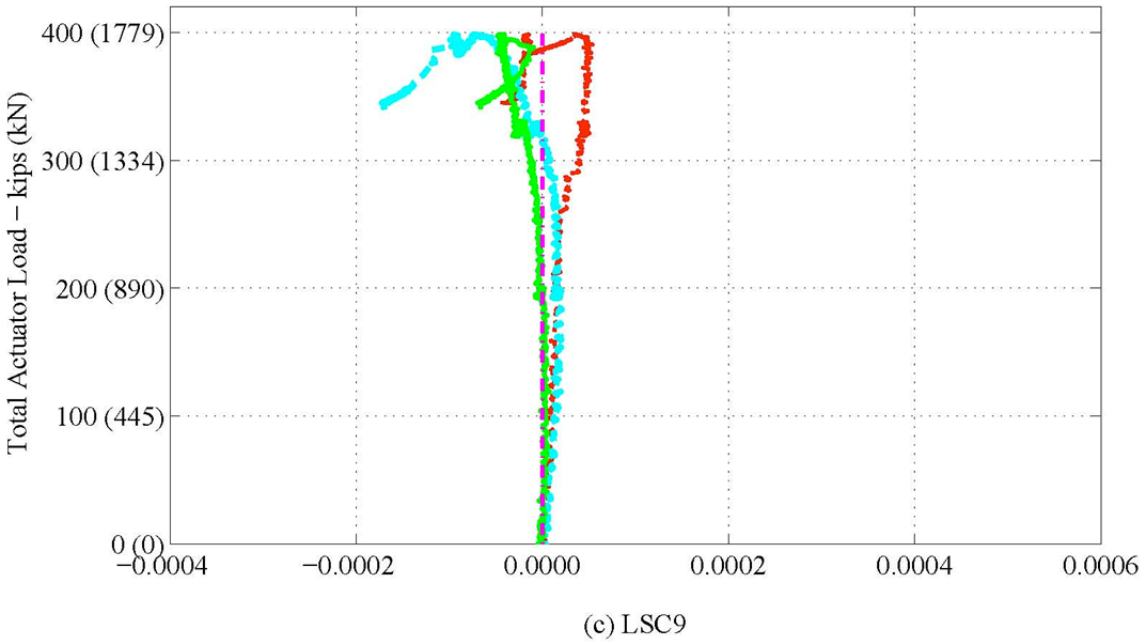

(c) LSC9

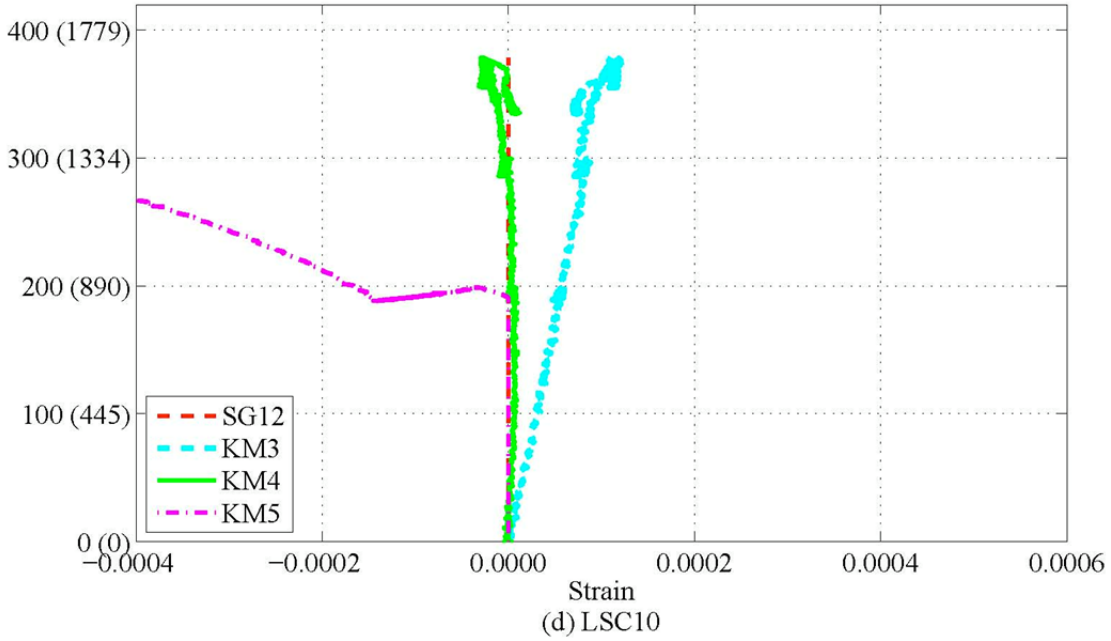

(d) LSC10

Figure 5-42. (Continued)

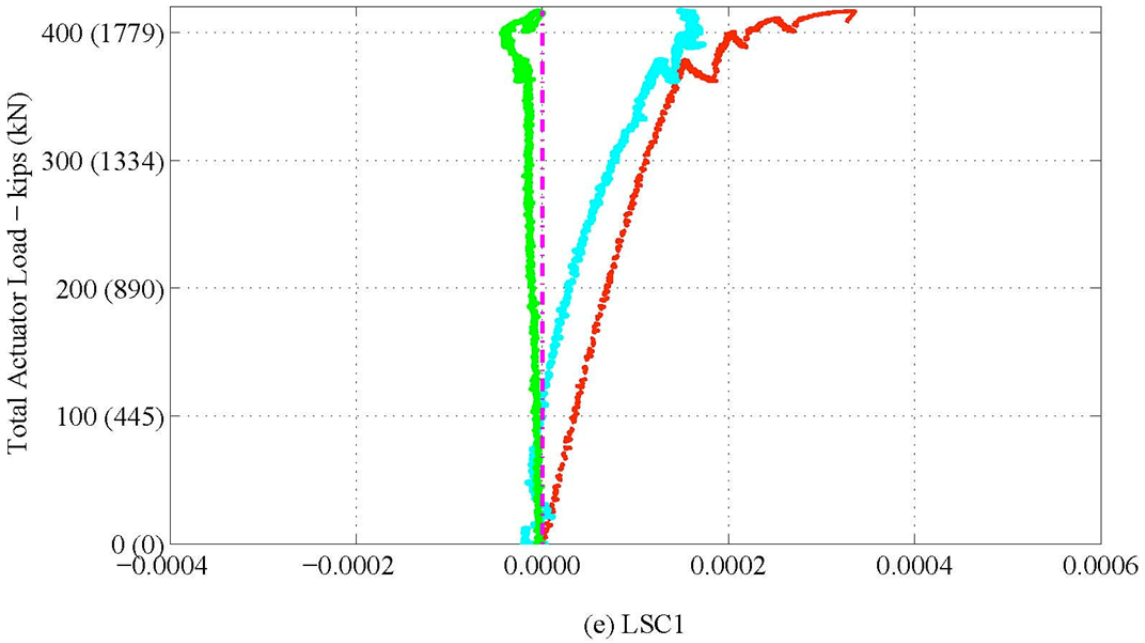

(e) LSC1

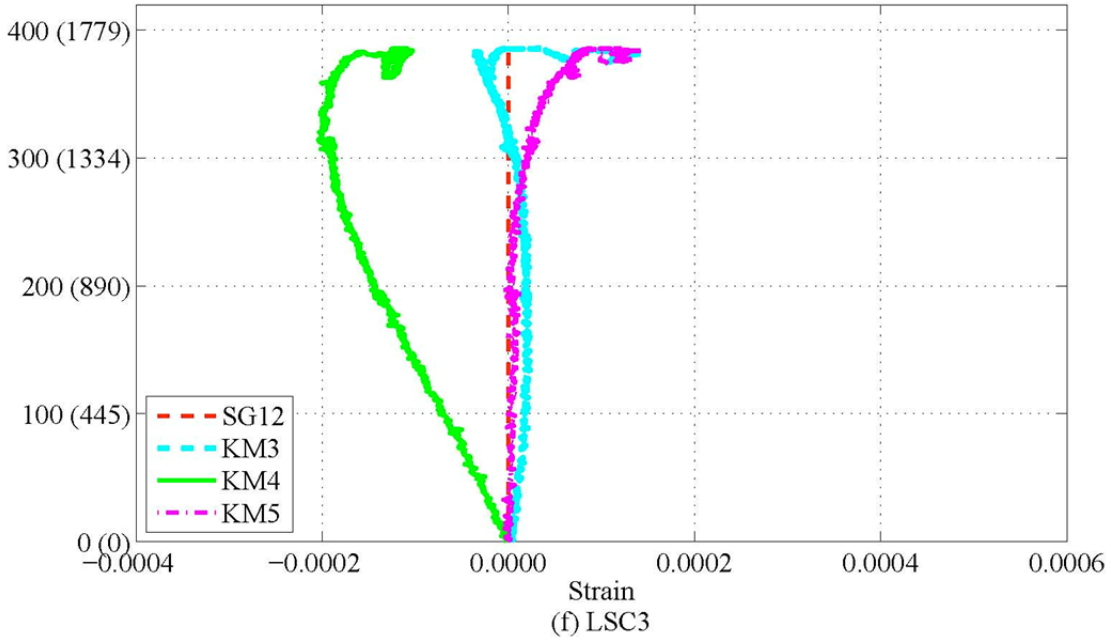

(f) LSC3

Figure 5-42. (Continued)

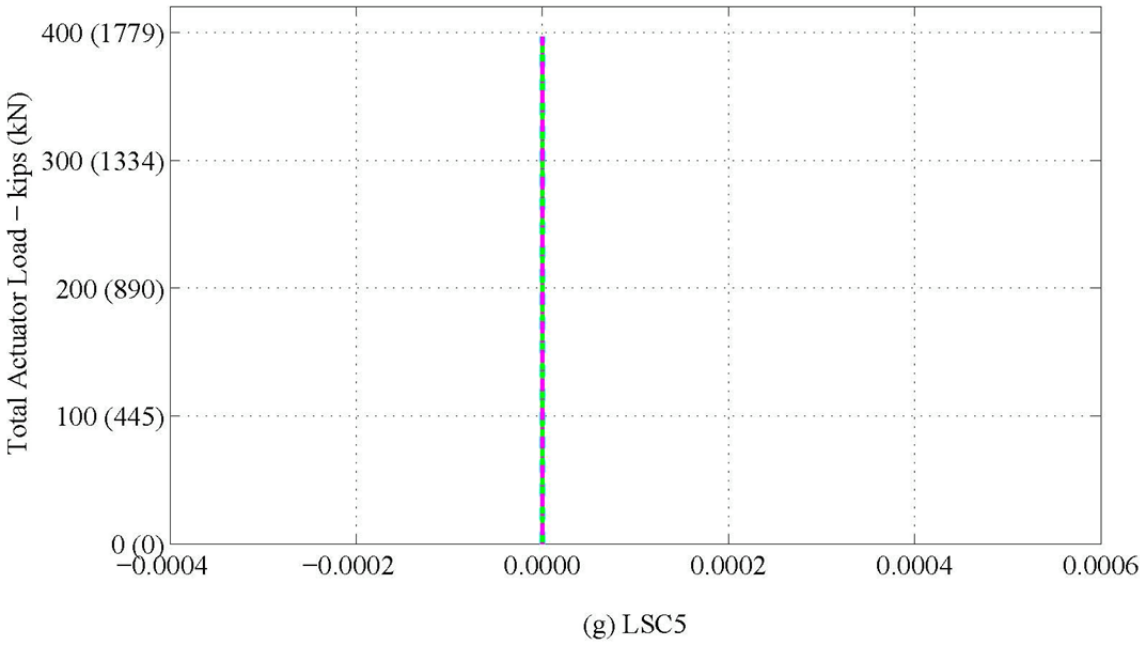

(g) LSC5

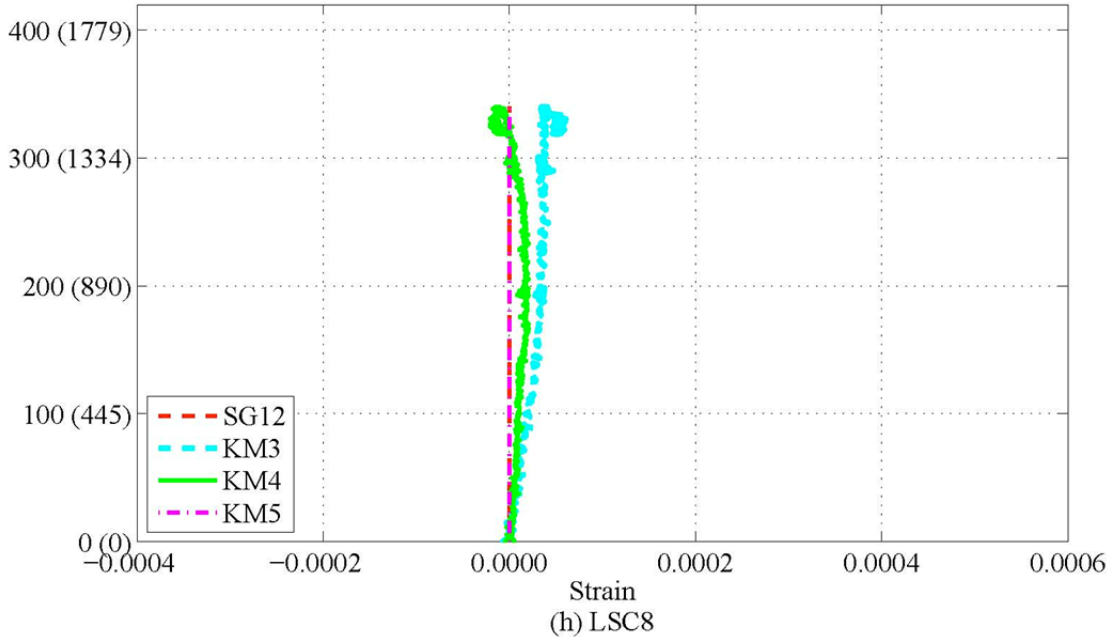

(h) LSC8

Figure 5-42. (Continued)

Figure 5-43 shows a crack and LV4 above the support during the three-point test on LSC8. The flexural crack width at the maximum actuator load of 195 kips (867 kN) was approximately 0.05 inches (1.27 mm). This crack is one fifth the width of the crack pictured in Figure 5-30 during the four-point test at near peak loading.

Figure 5-43. Flexural Crack above the Center Support from Three-Point Test (LSC5).

Figure 5-44 shows the external strain measurements in the splice region using the LVDTs. Note that LV1 and LV8 were closest to the actuators and not under the actuator as was the case for the four-point test. Therefore, the strains from LV1 and LV8 in the three-point test were not as large as the strains from LV1 and LV7 in the four-point test. LV4 measured the critical surface strains primarily from flexural deformations directly above the support. Either, LV1 or LV8 has the largest strain or begins plastic deformation first in all specimens. It is important to note that the LV above the support which resists the maximum moment does not have the largest strains.

Figure 5-45 shows the total actuator loading versus the internal and external surface strains in the splice region using the SG and LV data. This comparison is similar to the same comparison for the four-point test. The figure shows that the internal and external surface strains are comparable, implying a plane stress.

Figure 5-46 shows the total actuator loading versus the strains across the depth of the section directly above the support, which is the location of the largest moment demand. The strains follow the theoretical variation of large tension strains on top, very small strains in the midsection, and large compression strains on the bottom. The tension on top and compression on bottom is opposite from the four-point test, because of the specimen orientation in the test setup. The analytical model closely predicted the strains in this section. However, the experimental tension strain on the top is often greater than the analytical model and the maximum load is not accurately predicted as explained previously.

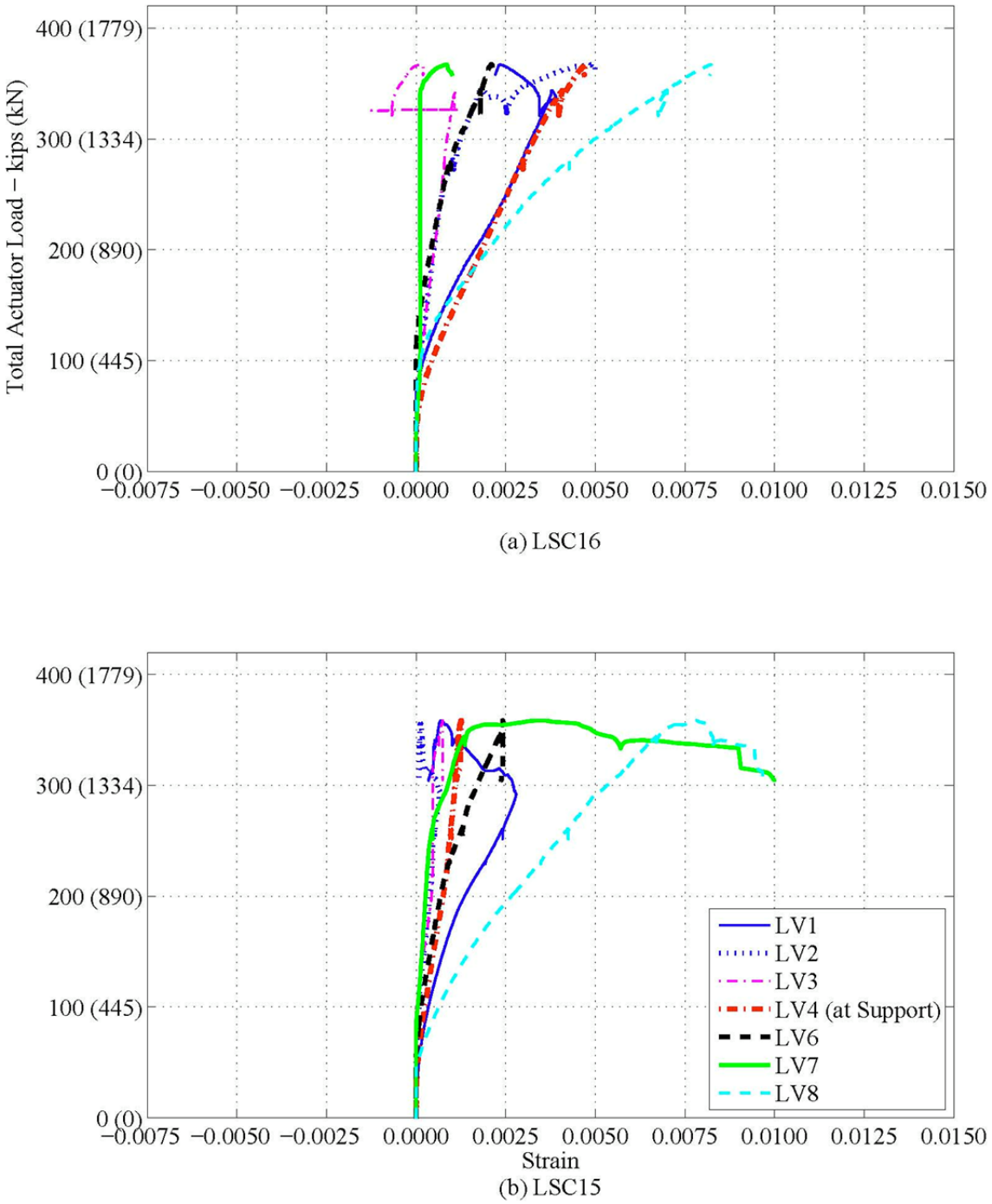

Figure 5-44. Experimental Load vs. Strain during the Three-Point Test: LVDTs along the Splice Region.

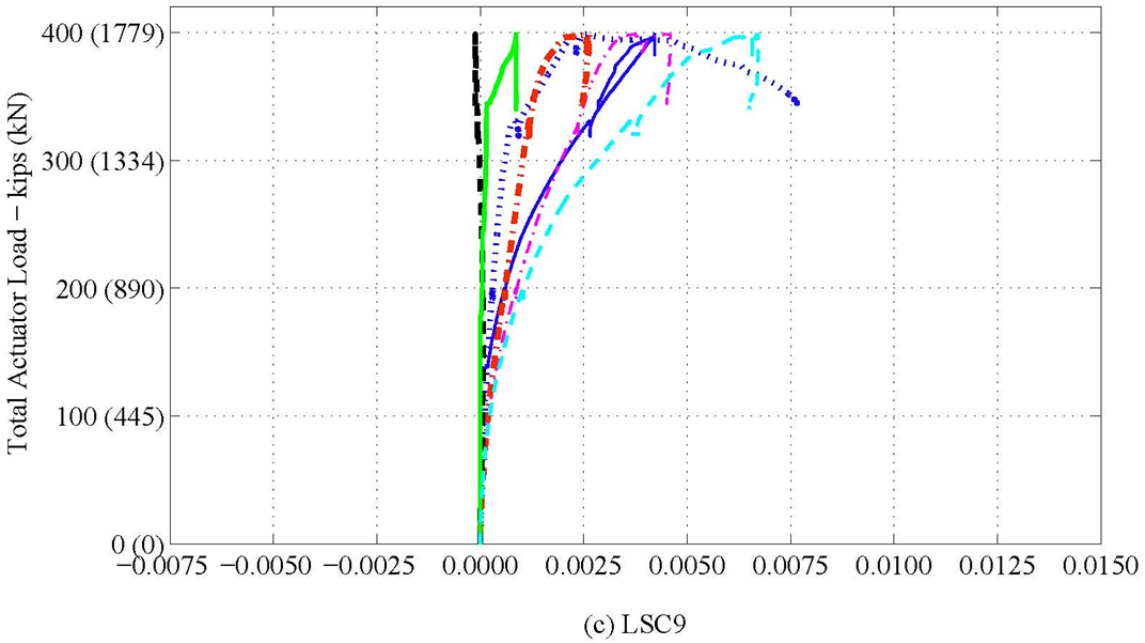

(c) LSC9

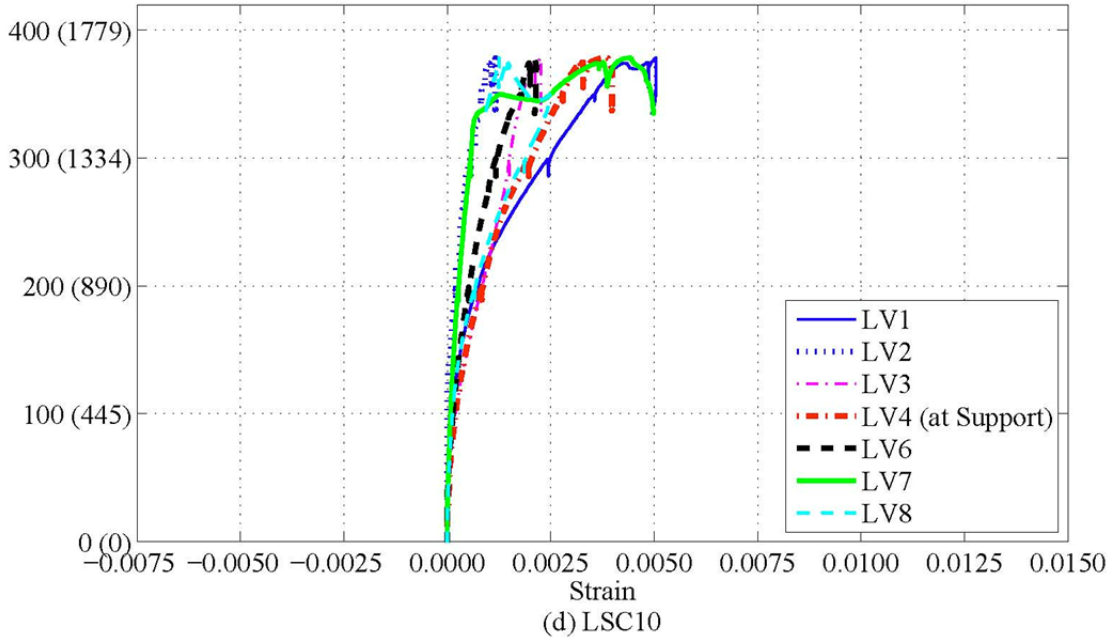

(d) LSC10

Figure 5-44. (Continued)

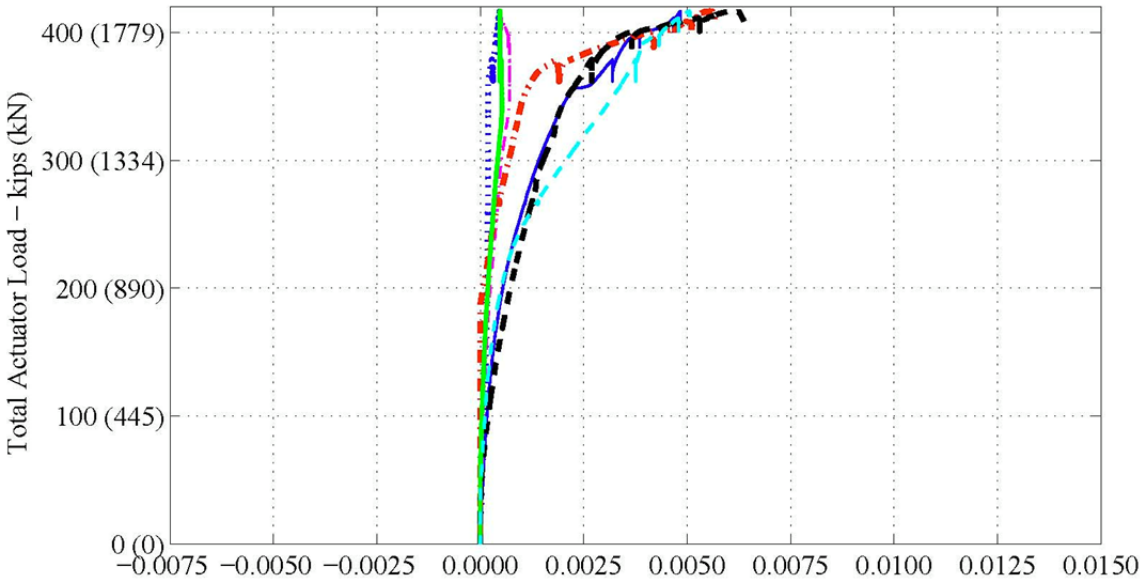

(e) LSC1

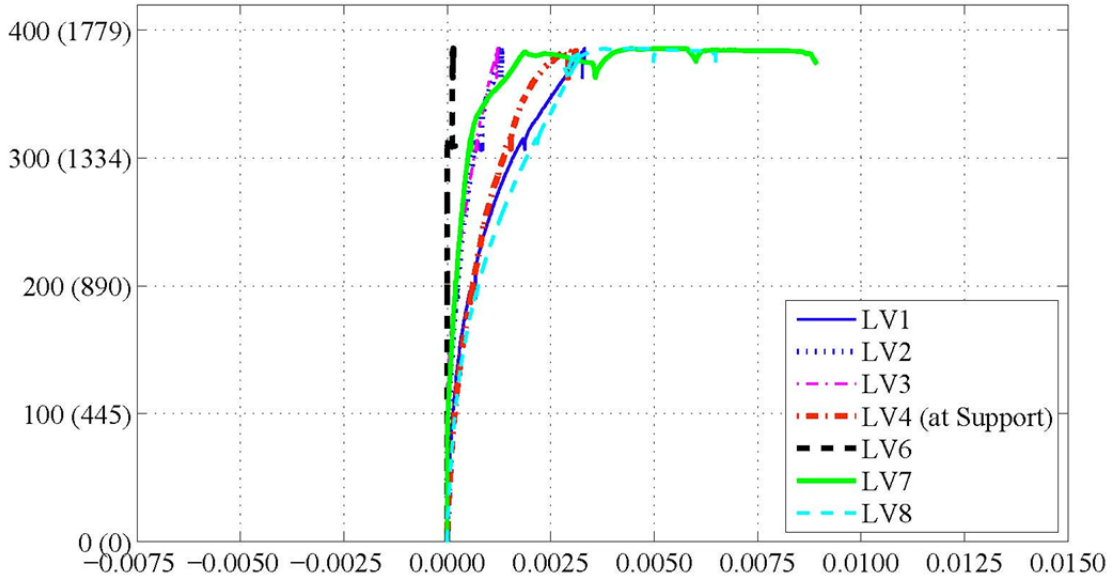

(f) LSC3

Figure 5-44. (Continued)

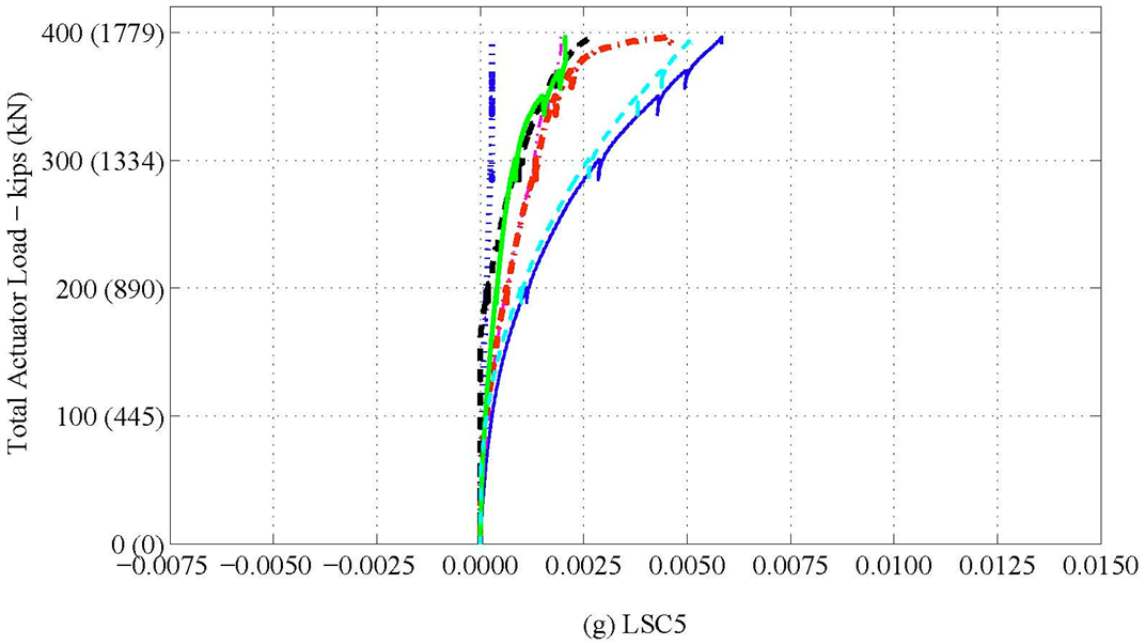

(g) LSC5

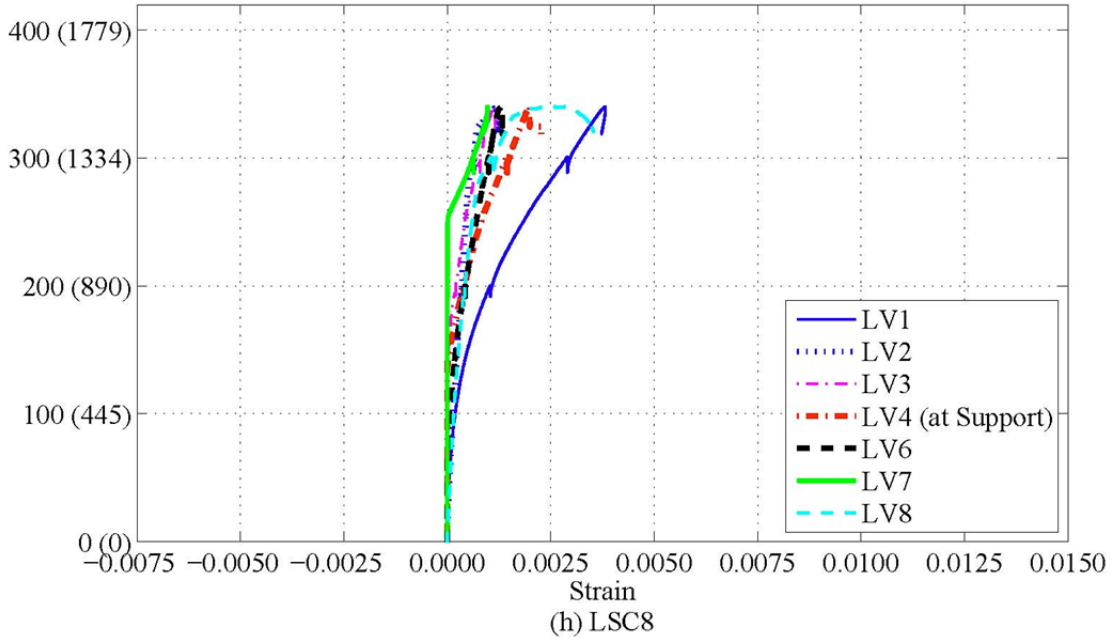

(h) LSC8

Figure 5-44. (Continued)

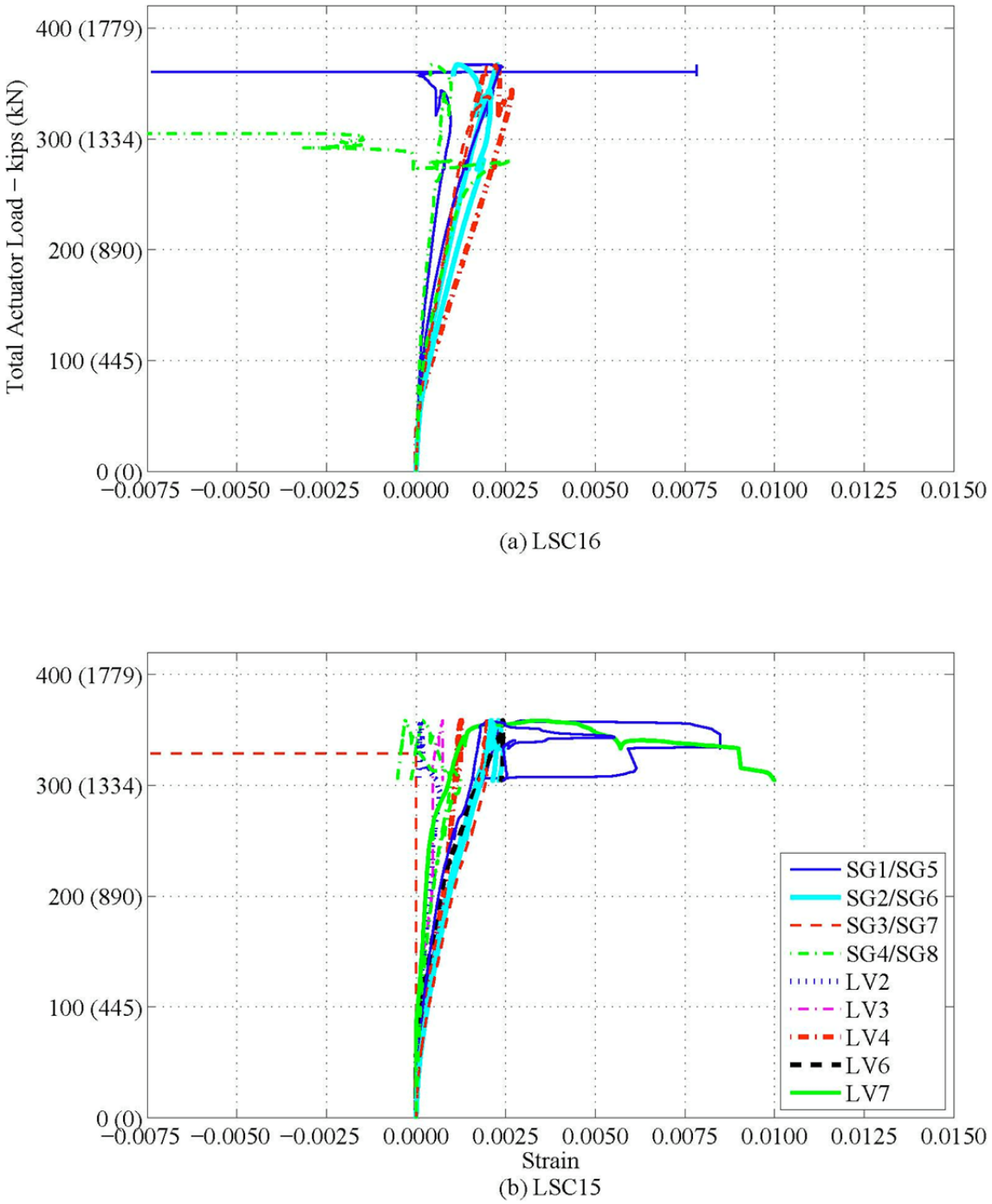

Figure 5-45. Experimental Load vs. Strain during Three-Point Test: Comparison of Internal and External Strains across Tension Region.

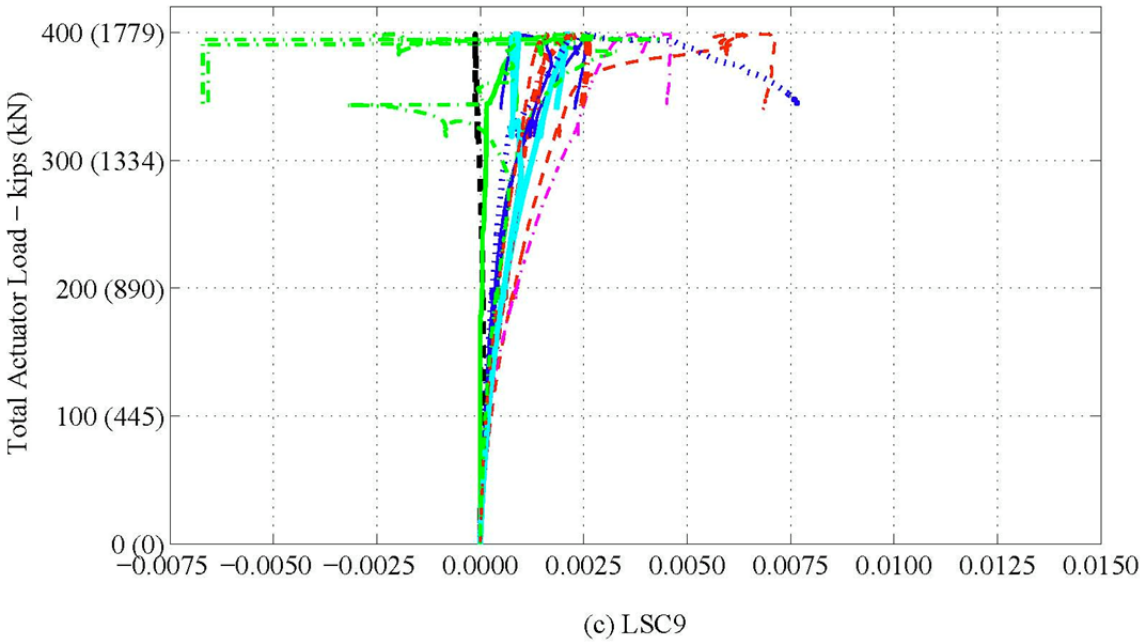

(c) LSC9

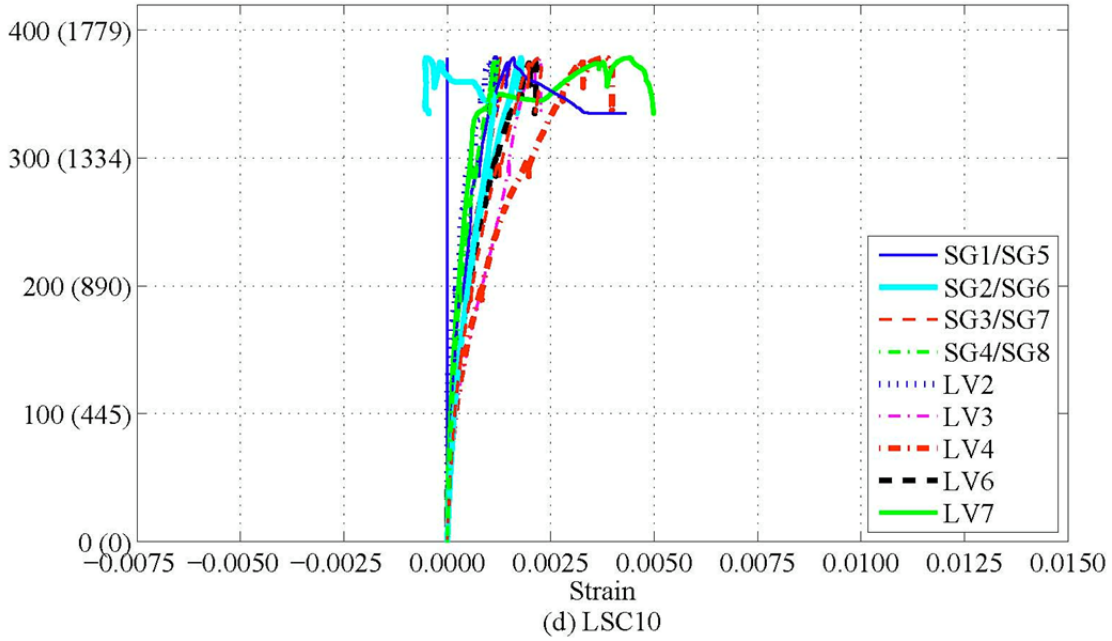

(d) LSC10

Figure 5-45. (Continued)

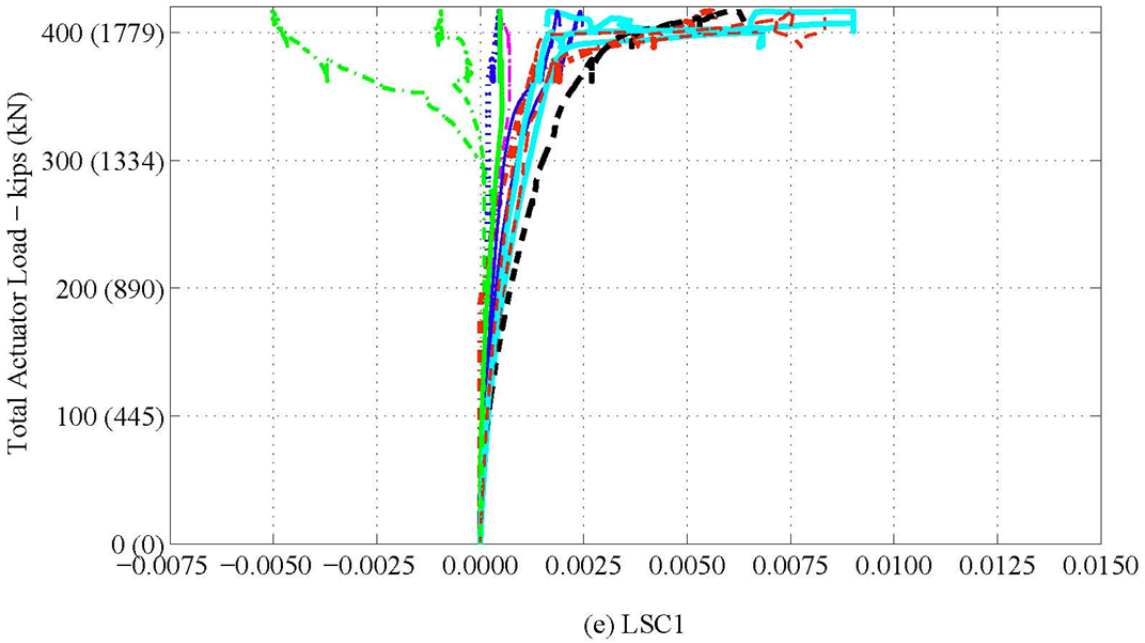

(e) LSC1

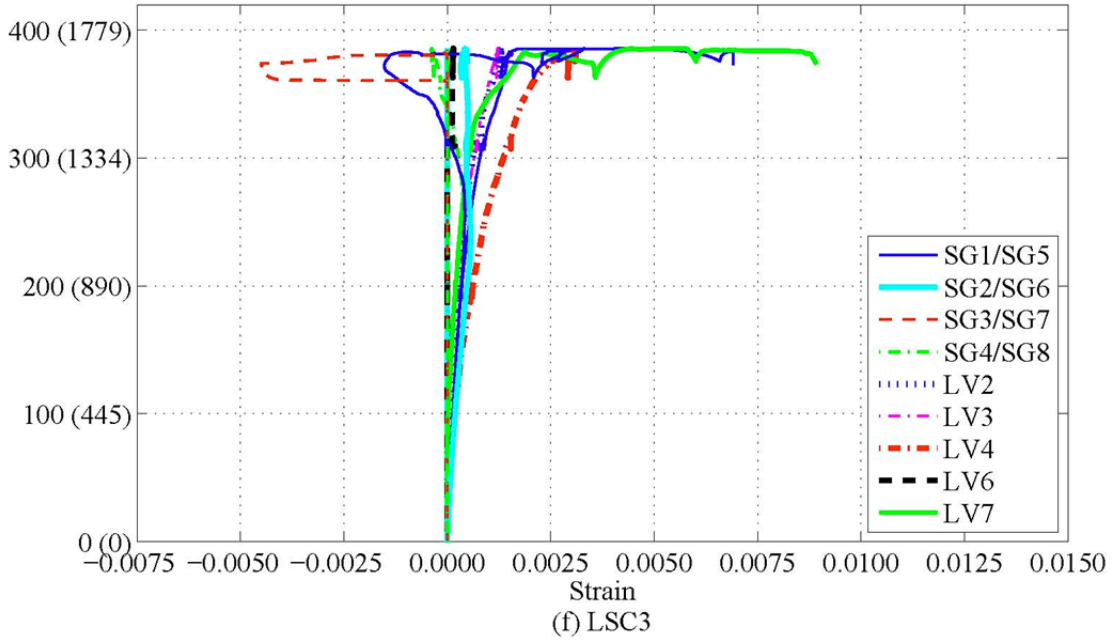

(f) LSC3

Figure 5-45. (Continued)

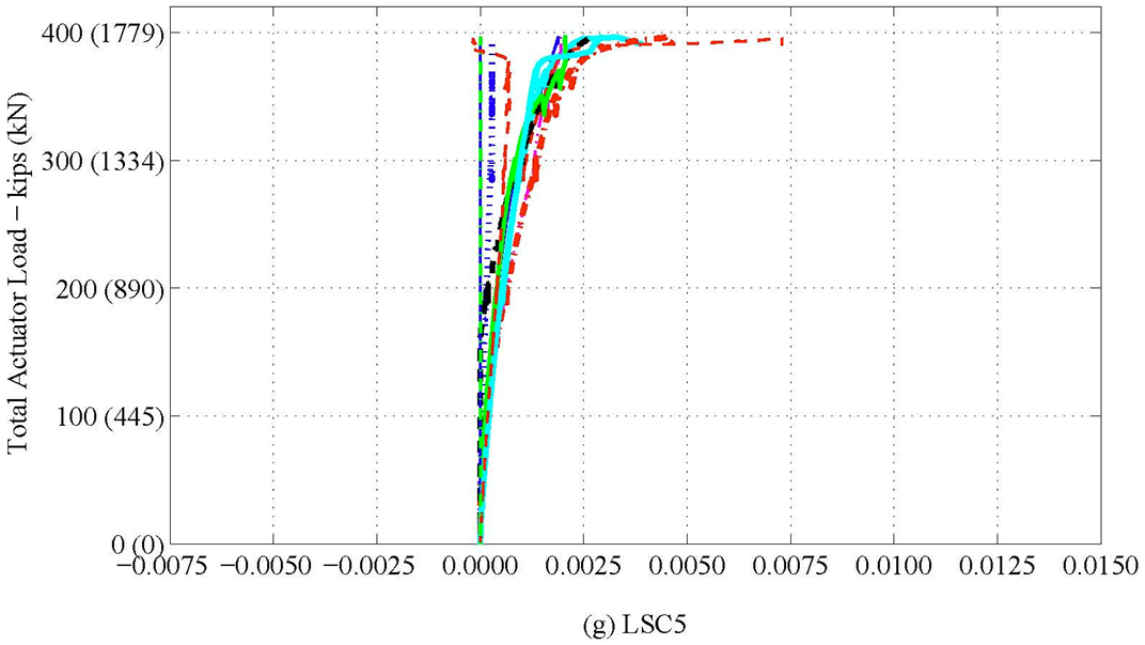

(g) LSC5

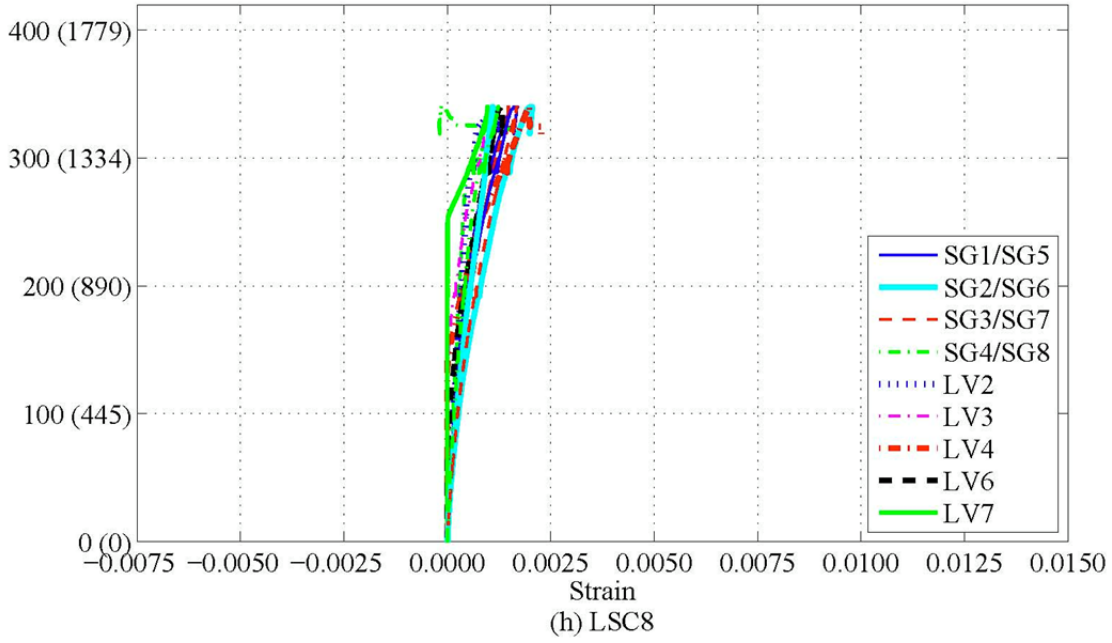

(h) LSC8

Figure 5-45. (Continued)

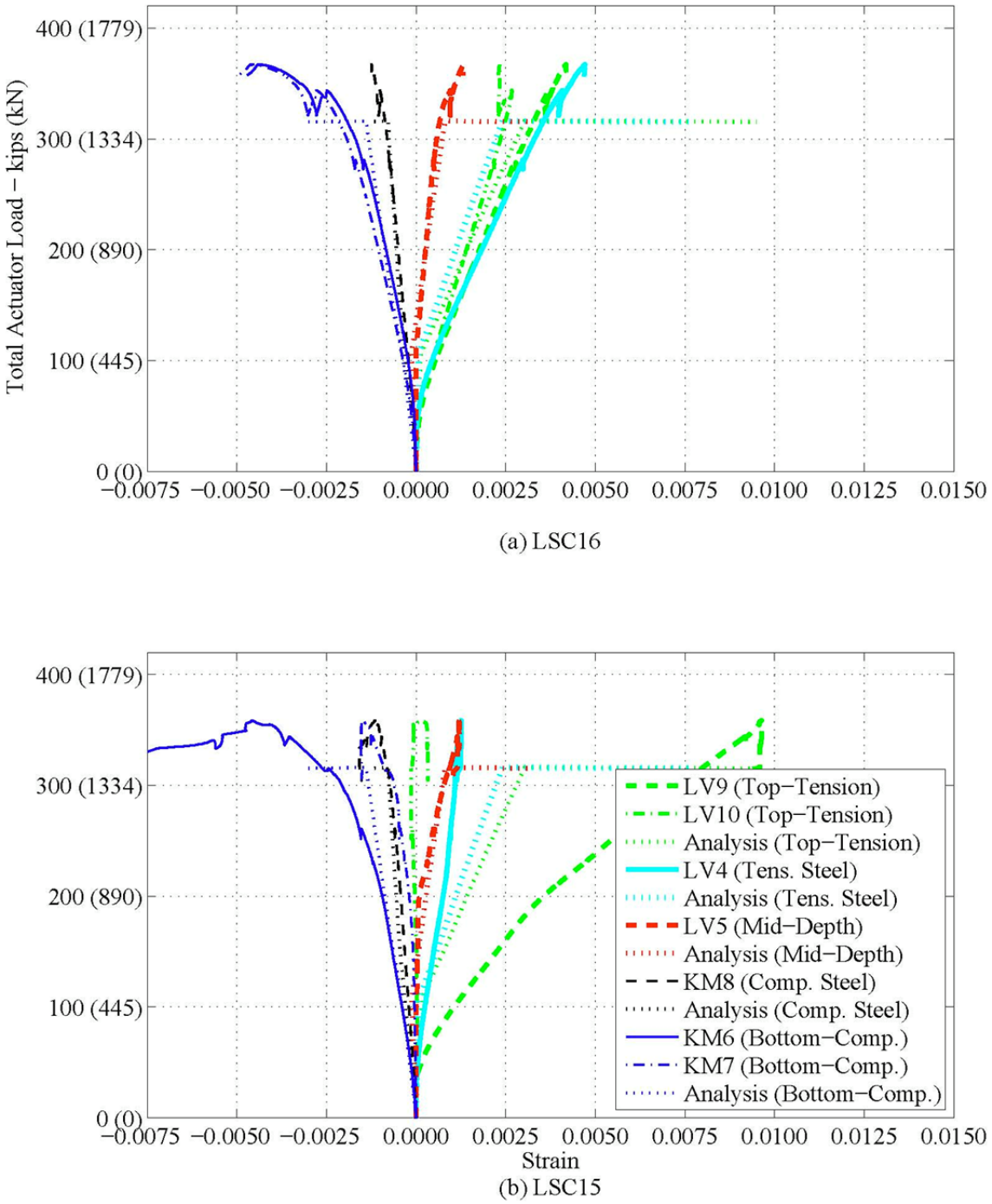

Figure 5-46. Experimental and Analytical Load vs. Strain during Three-Point Test: External Strain Gages across the Depth of the Specimen above the Center Support.

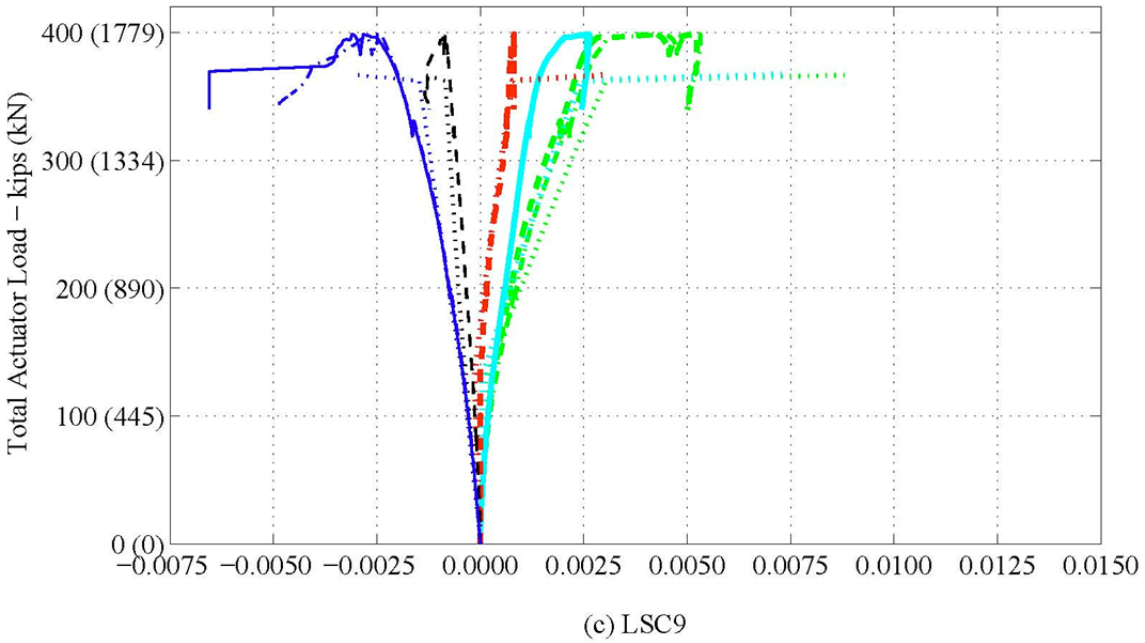

(c) LSC9

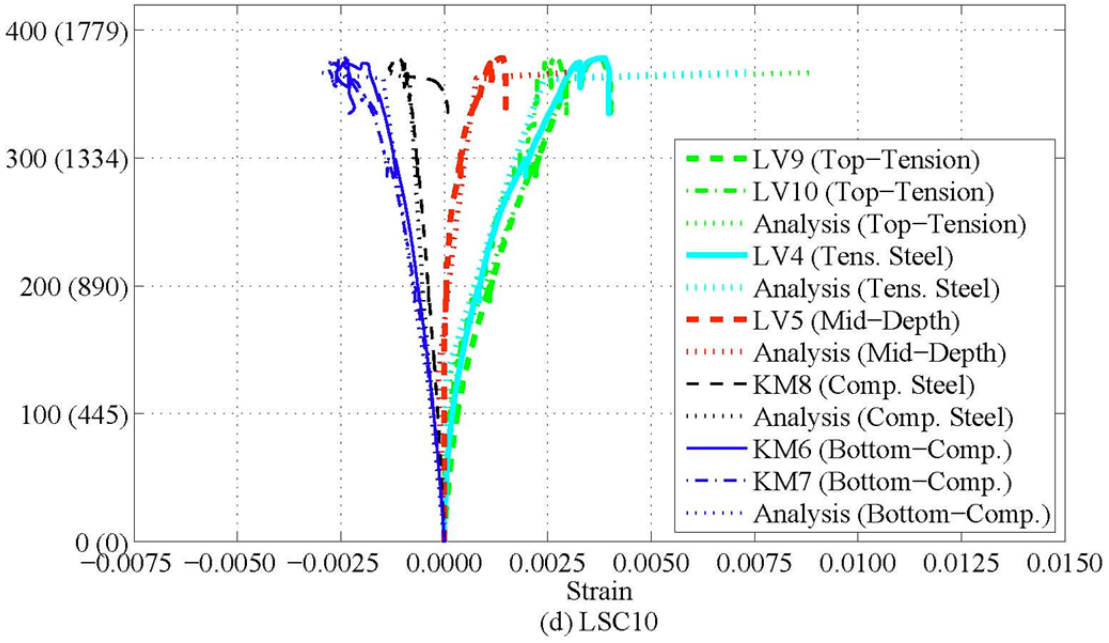

(d) LSC10

Figure 5-46. (Continued)

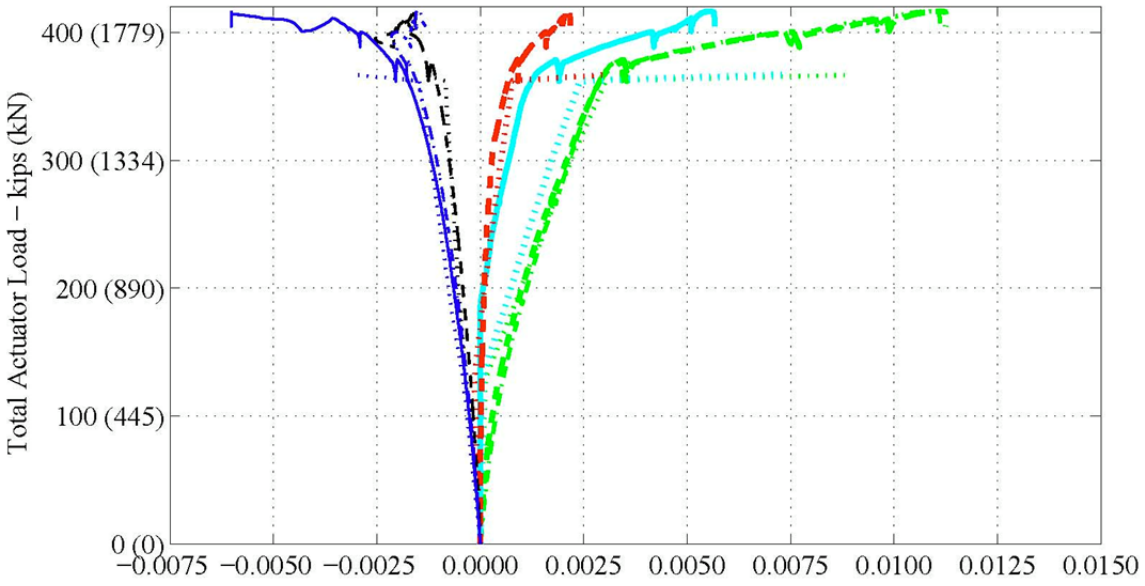

(e) LSC1

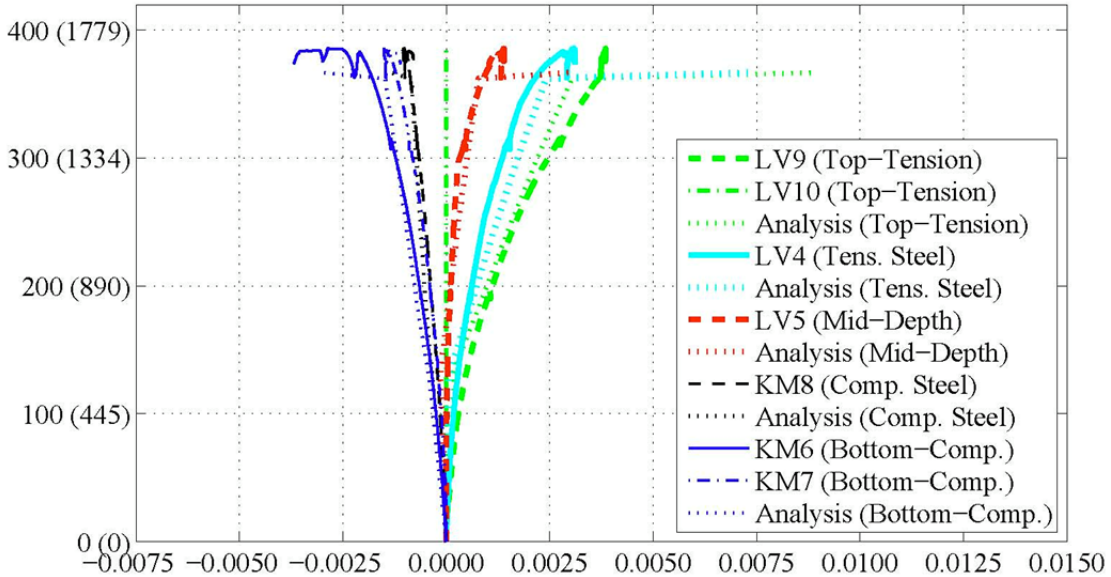

(f) LSC3

Figure 5-46. (Continued)

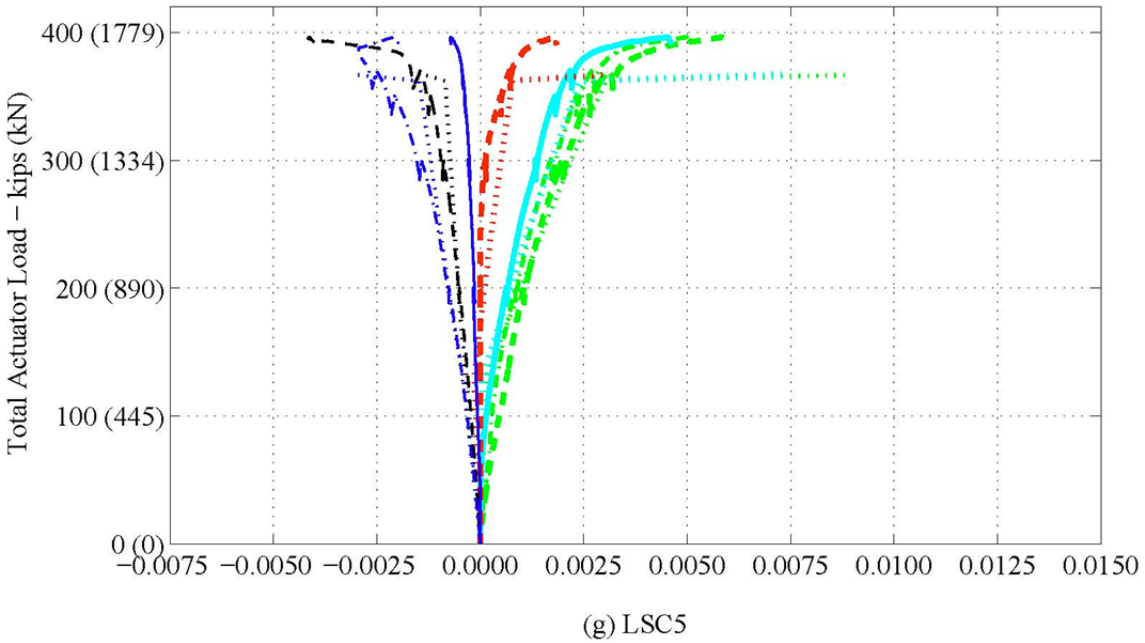

(g) LSC5

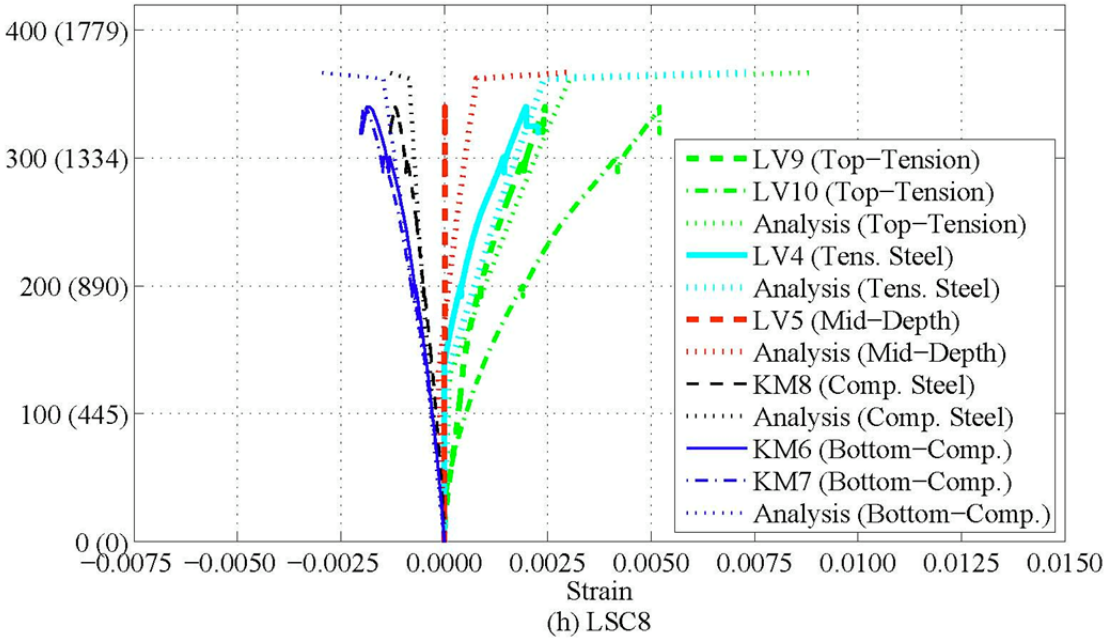

(h) LSC8

Figure 5-46. (Continued)

5.5 Summary and Key Findings

The experimental testing program in this research consisted of the design, construction, curing, deterioration, and structural load testing of 16 large scale column specimens with a critical lap splice region under varying degrees of premature concrete deterioration due to ASR/DEF. Of these specimens, two control specimens without any ASR/DEF deterioration and three groups of two specimens with varying levels of ASR and minimal DEF were structurally load tested in both the four-point and three-point load test setups to date. The remaining 8 specimens are still deteriorating under the environmental conditions and supplemental watering at the Texas A&M Riverside Campus with the hope of developing more severe damage from DEF, and will be structurally load tested at a later date.

The key findings from the experimentally measured structural force-deformation response, internal strain measurements, and developing failure mechanisms on the specimens tested to date are the following:

- Comparing the structural behavior of specimens with the varying degrees of ASR and minimal DEF deterioration to the control specimens with no ASR/DEF deterioration, it was found that they have similar initial stiffness and behavior up to first cracking, about a 25-35% increase in post-cracking stiffness up to yielding, 5-15% increase in yield strength, and showed no overall detrimental effects on the structural response. The increase in strength and stiffness can be explained by the resulting volumetric expansion of the concrete due to ASR/DEF that engaged the longitudinal and transverse reinforcement for better confinement of the core concrete and also further engaged the supplemental post-tensioning reinforcement and the longitudinal reinforcement to generate additional axial compression load.

- The Step-by-Step analytical modeling approach of the control and non-control specimens closely replicated the experimentally measured force-deformation behavior as well as internal strain measurements, in the two different test setups. However, the analytical load vs. deformation for the three-point test was about 15% stiffer than the experimental due to previous testing, some modeling assumptions, and intentionally neglected shear deformations. For the non-control specimens, the analytical model better fit the experimental behavior when the level of axial loading was increased as explained above.

- Although the structural performance of column splice regions with varying levels of ASR and minimal DEF showed no detrimental effects, the vulnerability of column splices with increased levels of DEF deterioration could not be evaluated to date. In spite of the research team's best efforts and the unprecedented rates of concrete expansion that were achieved, more time is needed to allow the remaining large-scale column splice specimens to further deteriorate in order to determine the performance of splice regions under severe DEF deterioration. The experimental testing of these specimens will be reported later.

6. SUMMARY, CONCLUSIONS, AND FUTURE WORK

6.1 Summary

Over the past 25 years or so, the Texas Department of Transportation (TxDOT) has had an aggressive construction program in place to accommodate the expanding population growth within the state of Texas. However, there is a significant amount of the reinforced concrete construction that has developed early cracking, termed premature concrete deterioration. Most of this deterioration has been identified or at least suspected to be from alkali silica reaction (ASR) and/or delay ettringite formation (DEF). Both deterioration mechanisms lead to volumetric expansion of the concrete due to ASR gel and/or the reformation of ettringite within the concrete, respectively. As such, the initial development of cracking from these mechanisms typically develops in the tension field of the concrete member due to gravity loading during service conditions. An area of concern for TxDOT is the performance of column splice regions when affected by varying levels of premature concrete deterioration due to ASR and/or DEF.

Therefore, the major objectives of this research program were to: (i) Evaluate the experimental behavior of critical column lap splice regions using large-scale specimens under varying levels of premature concrete deterioration due to ASR and/or DEF; and (ii) Develop an analytical model that can evaluate the behavior of a splice region under varying levels of concrete deterioration based on calibration with the experimental behavior.

In summary, the experimental testing program in this research consisted of the design, construction, curing, deterioration, and structural load testing of 16 large scale column specimens with a critical lap splice region under varying degrees of premature concrete deterioration due to ASR/DEF. Two of these specimens were constructed, preloaded to

simulate gravity load conditions and stored in the climate controlled structural laboratory without supplemental water, which basically eliminated the premature concrete deterioration. The experimental behaviors of these two specimens were considered as the undamaged control behavior. In addition, fourteen large-scale specimens were constructed, preloaded to simulate gravity load conditions, and then stored in an open field at the Texas A&M University Riverside Campus where they were exposed to wet-dry cycles and experienced ASR and minimal DEF deterioration. Data was recorded for surface expansions measurements in all specimens throughout the deterioration program. All specimens have successfully developed ASR/DEF deterioration (described as late stage ASR and minimal DEF from the measured instrumentation, crack width data and petrography analysis) in terms of internal concrete and reinforcing steel expansion, external surface expansion, and surface cracking that is representative of observations in in-service bridges.

Of the 16 specimens, two control specimens without any ASR/DEF deterioration and three groups of two specimens with varying levels of ASR and minimal DEF were structurally load tested in both the four-point and three-point load test setups to date. The remaining specimens are still deteriorating under the environmental conditions and supplemental watering at the Texas A&M Riverside Campus with the objective of developing more severe damage from DEF. These specimens will be structurally load tested at a later date.

To complement the experimental program, analytical models were developed based on flexure theory to characterize the force-deformation behavior and internal strains of the LSC specimens in both the four-point and three-point load test setups. Both in the critical splice region and the specimen end regions, the longitudinal reinforcing steel was assumed to develop tensile resistance linearly from zero resistance at the end of the bar to the yield strength at the code calculated development length of the bar. The results from these models were compared with the experimental response of undamaged LSC

specimens and then adjusted for the increased axial load due to the longitudinal expansion from ASR and minimal DEF.

6.2 Conclusions

The conclusions and key findings from each phase of the research program are presented in this section.

6.2.1 Deterioration Program

In summary, 14 large-scale specimens stored at the Riverside Campus were exposed to the outdoor weather conditions of Bryan, TX and to wet-dry cycles using supplemental water to accelerate the ASR and minimal DEF deterioration mechanisms. Internal instrumentation and external surface measurements were continually recorded for all specimens throughout the deterioration program. It can be concluded that all specimens have successfully developed significant premature concrete deterioration due to ASR and/or DEF in terms of concrete expansion and surface cracking that is representative of observations in in-service bridges. In addition, the deterioration mechanism is continuing. To develop more severe damage states, additional exposure time is required. Therefore eight untested specimens continue to deteriorate at the Riverside Campus.

The following highlights some of the findings derived from the deterioration program to date:

- The direct sunlight on the specimens made a large impact on the expansion due to ASR and minimal DEF. The transverse surface strain on the side of the specimen were as larger as 61% of the transverse surface strain on the top surface with direct sunlight and some were less than 20% the top surface strain.

- The LSC specimens expanded at a higher strain rate during the summer months (May through September); therefore, the high temperatures accelerate and increase the deterioration. The increase in the average strain/month on the top surface was calculated to measure this. The rate of increase was different for the three groups of specimens first exposed to the high temperatures and supplemental water at different times, May, July, and September. The strain rate on the first six specimens, which were exposed during all of the summer of 2008, was 1.7 larger during the summer of 2009 than the non-summer months of 2008 and 2009. The next four LSC specimens were only exposed during half of the 2008 summer. The average strain rate of the transverse strain on the top was 2.7 times as large during the summer of 2009 than the non-summer months. The last four specimens were not exposed to the environmental conditions during any of the summer in 2008. The strain rate increase during the first summer months on these LSC specimens was 6.5 of that during the initial strain rate prior to the summer months.

- The transverse surface strains were about 10 times larger than the longitudinal surface strains due to the longitudinal restraint from the axial post-tensioning steel and longitudinal column reinforcement and the transverse tension field induced by Poisson's effect under post-tensioning.

- The average strains calculated from measuring the sum of the crack widths between DEMEC points were about 50% of the surface strains calculated from measuring the distance between DEMEC points.

- The measured strains were larger on the surface than inside the specimen with the strain in the cover reaching about 58% and the strain in the core concrete reaching about 52% of the surface strain. The strain on the steel hoop in the middle of the splice region ranged from 0.0036 and 0.0054. The hoop strain percentage of the surface strain was 40% on Small Face 1 at the time of the first rotation. The Large

Face 1 hoop strain percentages of the surface strain were 83% and 78% at the first two rotations.

- Using measured internal and external concrete expansion data throughout the deterioration program, measured crack widths and lengths throughout the deterioration program, and from petrography analysis of concrete cores taken from the specimens after they were structural tested, the three groups of tested specimens were categorized as having varying levels of primarily ASR deterioration ranging from none to late stage and none/minimal levels of DEF.

6.2.2 Experimental Testing Program

Comparing the structural behavior of specimens with the varying degrees of ASR and minimal DEF deterioration to the control specimens with no ASR/DEF deterioration, it was found that they have similar initial stiffness and behavior up to first cracking, about a 25-35% increase in post-cracking stiffness up to yielding, 5-15% increase in yield strength, and showed no overall detrimental effects on the structural response. The increase in specimen strength and stiffness can be explained by the resulting volumetric expansion of the concrete due to ASR/DEF that engaged the longitudinal and transverse reinforcement for better confinement of the core concrete and also further engaged the supplemental post-tensioning reinforcement and the longitudinal reinforcement to generate additional axial compression load.

6.2.3 Analytical Modeling

The Step-by-Step I_{cr} analytical modeling approach for the column splice region in the control and non-control specimens in the two different test setups close to accurately replicated the experimentally measured force-deformation behavior, as well as internal strain measurements. For the non-control specimens, the analytical model better

correlated with the experimental behavior when the level of axial loading was increased to account for the engagement of the reinforcement and additional post-tensioning load due to the volumetric expansion of the concrete as a result of ASR and minimal DEF. Based on these findings, no modification factors are currently necessary for the analytical modeling to account for deterioration of the column splice regions. However, if future testing results in bond-slip issues of the spliced longitudinal reinforcement and warrants such modifications of the analytical modeling, a simple procedure will be implemented such that the longitudinal reinforcing steel develops at reduced development length of the bar compared to the code calculated development length of the bar.

6.3 Future Work

In spite of the research team's best efforts and the unprecedented rates of concrete expansion due to ASR/DEF that were achieved, more time is needed to allow the remaining large-scale column splice specimens to further deteriorate in order to determine the performance of splice regions under severe DEF deterioration. Currently, eight specimens remain at the Texas A&M University Riverside Campus and exposed to supplemental water from a sprinkler system four times a day and for 15 minutes each watering. The measured concrete expansions and surface cracking during the further deterioration program and the subsequent experimental testing of these specimens will be reported later.

REFERENCES

AASHTO. (2010). "AASHTO LRFD Bridge Design Specifications," American Association of State Highway and Transportation Officials, Washington, DC.

ACI committee 318. (2008). "Building code requirements for structural concrete and commentary." *ACI 318-08*. American Concrete Institute, Detroit.

Alberson, R. M. (2009) "Capacity prediction of reinforced concrete column cap splices." M.S. thesis, Texas A&M University, College Station, TX.

American Society for Testing and Materials. (2001) ASTM C39-01 Standard test method for compressive strength of cylindrical concrete specimens, Annual book of ASTM standards: Volume 04.02, Concrete and Aggregates. West Conshohocken, PA.

Bauer, S.; Cornell, B.; Figurski, D.; Ley, T.; Miralles, J.; and Folliard, K.; Alkali-silica reaction and delayed ettringite formation in concrete: A literature review. Report No. FHWA/TX-06/0-4085-1. Center for Transportation Research, The University of Texas at Austin, 2006.

Berube, M.-A.; Chouinard, D.; Pigeon, M.; Frenette, J.; Boisvert, L.; and Rivest, M. (2002) "Effectiveness of sealers in counteracting alkali-silica reaction in plain and air-entrained laboratory concrete exposed to wetting and drying, freezing and thawing, and salt water," Can. *J. Civ. Eng*. 29:289-300.

Bracci, J. M., Gardoni, P., Eck, M. K., and Trejo, D., "Performance of Lap Splices in Large Scale Column Specimens Affected by ASR and/or DEF," Report 0-5722-1, Texas Transportation Institute, Texas A&M University, Dec. 2011

Folliard, K.J., Barborak, R., Drimalas, T., Du, L., Garber, S., Ideker, J., Ley, T., Williams, S., Juenger, M., Thomas, M., and Fournier, B. (2006) "Preventing ASR/DEF in new concrete: Final Report," Technical Report No. 0-4085-5, The University of Texas at Austin, Center for Transportation Research.

Gardoni, P.; Nemati, K. M.; and Noguchi, T. (2007). "Bayesian statistical framework to construct probabilistic models for the elastic modulus of concrete," *Journal of Materials in Civil Engineering*, 19(10), 898-905

Liu, Shih-Hsiang (2012) "Structural assessment of "D" region affected by premature concrete deterioration," Ph.D. disertation, Texas A&M University, College Station, TX.

MacGregor, J. G., and Wight, J. K. (2009). *Reinforced concrete mechanics and design*, Fifth Edition, Prentice-Hall Inc., Upper Saddle River, NJ.

Mander, J.B., Bracci, J.M., Hurlebaus, S., Grasley, Z., Karthik, M.M., Scott, R.M., Liu, S.-H., "Structural assessment of "D" region affected by premature concrete deterioration," Report 0-5997, Texas Transportation Institute, Texas A&M University, Oct. 2011

Naaman, A. (2004) *Prestressed concrete analysis and design*, Second Edition, Techno Press, Ann Arbor, Michigan

PCI. (2004) "PCI design handbook precast and prestressed concrete", Precast/Prestressed Concrete Institute, Chicago.

Petrov, N., M. Thibault, and A. Tagnit-Hamou. (2006) *Expansion due to DEF in normally-cured concrete heated by cement hydration*. ACI Special Publication. Vol. 234: 239-250.

The Weather Channel. “Monthly Weather for Bryan, TX.”. Web. 9 May 2011. http://www.weather.com/outlook/homeandgarden/home/wxclimatology/monthly/graph/77801

Supplemental Source Consulted

Park, R. and Paulay, T. (1975) *Reinforced concrete structures*. John Wiley & Sons, Inc. New York.

VITA

Name:	Mary Kathleen Eck
Address:	Department of Civil Engineering
	Texas A&M University
	3136 TAMU
	College Station, TX 77843
Email Address:	kleen10@gmail.com
Education:	B.S., Civil Engineering, Texas A&M University, 2010
	M.S., Civil Engineering, Texas A&M University, 2012